Understanding the effect of surface generation rates for finish milling of Ti-5Al-5Mo-5V-3Cr aero-structural components

Adam Cox

The University Of Sheffield.

Department of Materials Science and Engineering

University of Sheffield

A thesis submitted for the degree of Engineering Doctorate of The University of Sheffield

November 26, 2017

Acknowledgements

For my Father. I would like express my up-most thanks to my supervisors, Martin Jackson, Sam Turner, Germain Forgeoux and Jean-Phillippe Villain-Chastre for their continued support and passion towards my research and personal development. My thanks to all of the staff, students and engineers at The University of Sheffield, The AMRC with Boeing, Safran Landing Systems and LMT Cachan for their influence, friendship and team work. A special thanks goes to my colleagues, but most importantly my friends from D1 and the IDC, without all of them the last 4 years would not have been anywhere near as enjoyable as it has been. Finally, to my family and friends, who without their unfaltering love and support, I would not be where I am today.

Abstract

A detailed investigation into the influence of cutting parameters on the surface integrity, subsurface microstructure, tool wear and fatigue performance for finish milling of Ti-5Al-5Mo-5V-3Cr landing gear components. Low cost, small scale testing methodologies have been developed to replicate complex machining strategies employed in aerospace manufacturing, to understand and develop an improved processing window. Machinability trials identified the influence of cutting speed (V_c), feed per tooth (f_z) and surface generation rates (SGR) on surface roughness and subsurface deformation. The detrimental impact of f_z can be offset somewhat by comparable increases in V_c. The subsequent reduction in imposed cutting forces, increased coolant delivery and improved chip evacuation achieves moderate responses in surface integrity and subsurface deformation. Severe plastic deformation at the near surface, exacerbated by increased cutting parameters, is accommodated through dislocation slip along basal, prismatic and pyramidal planes of primary alpha (α_p) grains. Deformation modes, which are intensified by increased tool wear. A transition from abrasive to adhesive tool wear mechanisms have been identified and shown to be accelerated by increased f_z. Through the application of a bespoke four point bend test rig, low cycle fatigue testing at R=0.1, has proposed some important observations for fatigue performance of machined high strength titanium allows. Cycles to failure were shown to be reduced for identical applied stress for increased SGR. Fatigue cracks has been identified within the severe plastic deformation region of the subsurface, as a result of machining. Initiation was produced through quasi-cleavage along dislocation slip planes of α_p and propagated in a mixed mode, significantly influenced by bulk β grains. A competing mechanism between initiation influenced by machining damage and propagation retardation as a result of machining induced compressive residual stresses has been postulated.

Contents

List of Figures

List of Tables

Nomenclature

In order of appearance in text:

- α Titanium beta cubic phase or grains
- β Titanium beta cubic phase or grains
- α_{GB} Titanium grain boundary alpha hexagonal phase or grains
- K_1 Twinning plane
- η_1 Shear direction
- **S** Shear strain
- **m** Schmid factor
- **CRSS** Critically resolved shear stress
- γ Declination angle
- **r** Cutting edge radius
- t_o Uncut chip thickness
- **a** Flank angle
- t_c Segmented chip thickness
- **y** Rake angle
- **f** Feed rate
- **Z** Number of teeth of a milling tool
- f_z Feed per tooth
- V_c Cutting speed
- D_e Effective cutting diameter
- **n** Spindle speed
- a_p Axial depth of cut
- a_e Radial depth of cut
- Ψ_r Lead angle
- Ψ_t Tilt angle

- ϕ Shear angle
- F_x Normal force
- F_y Vertical thrust force
- F_z Horizontal cutting force
- F_s Resultant force
- C_r Cutting resistance
- P_c Power consumption
- l_n Roughness measured length
- l_r Roughness sample length
- R_a Arithmetic centre line average roughness
- R_q Root mean squared roughness
- R_sk Skewness
- R_ku Kurtosis
- V_{ceff} Effective cutting speed
- **VB** Flank wear
- VB_{max} Maximum flank wear
- **C** Tool wear constant
- α_p Titanium primary alpha hexagonal grains
- α_s Titanium secondary alpha hexagonal grains
- l_c Cutting length
- **B** Wedge angle
- **R** Stress ratio
- σ Stress
- σ_{min} Minimum stress
- σ_{max} Maximum stress
- σ_m Mean stress
- σ_{alt} Alternating stress
- **M** Bending moment
- **y** Centroid of area
- I_z Moment of inertia

- S_a 3D Arithmetic centre line average roughness
- S_q 3D Root mean squared roughness
- S_sk 3D Skewness
- S_ku 3D Kurtosis

Chapter 1

Introduction

1.1 Motivation

With orders for the previous generation of large super-jumbo jet aircraft like the twin aisle Airbus A380 and Boeing 747 dwindling [1], such programmes are forecast to be scrapped. With the focus of high volume domestic air travel tending towards shorter point to point routes in versatile and efficient single aisle wide body aircraft [1]. The outlook for the global commercial aircraft market is positive, with increasing demand driven from emerging economies, population growth and reduced oil prices. Air traffic is set to double over the next 15 years with demand on the industry totalling 4.9 trillion dollars [2].

(a) Photograph of Boeing 787 Dreamliner commercial aircraft [3].

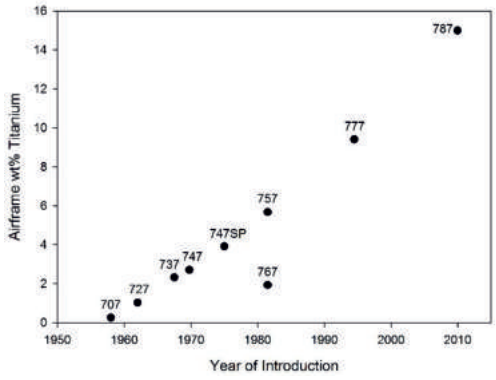

(b) Commercial trend for titanium application in Boeing aircraft construction [4].

Figure 1.1: Titanium usage in commercial aircraft.

To enable point to point journeys and ease the congestion at major aviation hubs, an increase in production by 30,000 passenger aircraft over the next two decades is predicted. Whilst production grows, restrictions on the average kilograms of fuel per passenger continue to be tightened. To meet these demands of increased fuel efficiency, noise reduction and aircraft versatility, significant weight reduction is required. This has led to the increase in the utilisation of lightweight materials, especially within components that account for significant proportions of the total aircraft weight, such as the airframe and fuselage. Fig.1.1 shows the increase in airframe construction by weight percentage comprising of titanium. Next generation

commercial aircraft platforms such as the Boeing 787 Dreamliner boast weights comprising of 50% composites and 15% Titanium alloys [5].

The aerospace industry continues to be a source of consistent growth for the titanium market, with the industry accounting for over 60,000 tonnes of titanium metal in 2012. Despite this expansion of over 60% from 2009 [6], pressures on the security of supply and cost of fabrication for titanium components continues to strain the market. These pressures are exacerbated as Boeing overcome delays in development with an increased production rate of 12 aircraft per month for the 787 Dreamliner [7]. With production rates already reaching 10 aircraft per month in early 2014 and over 70% of all production activities outsourced to the supply chain [8], this demand is felt directly by tier 1 suppliers.

Titanium accounts for 17 of the 260 million dollar cost for which Boeing makes a loss of 30 million dollars for each Dreamliner produced [9]. To reach these required production rates cost reduction is a must and titanium is at the centre of these cost reduction activities due to the metal respective costs.

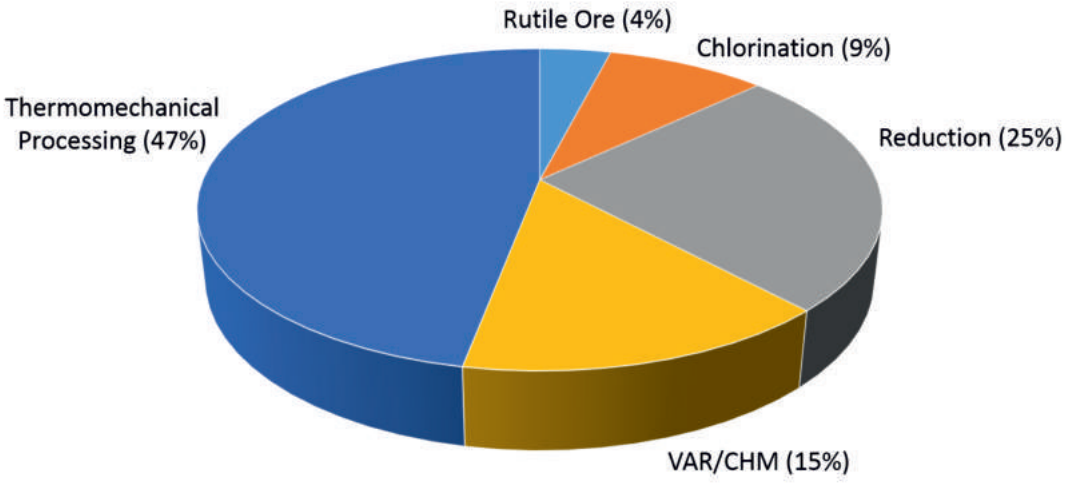

Figure 1.2: Cost distribution for production of titanium sheet [10].

A typical cost distribution for production of titanium alloy plate material can be seen in Fig.1.2. It can be seen that thermomechanical processing accounts for almost half of all fabrication costs [10], for which material removal processes such as machining can be considered. In many cases machining can account for almost 60% of wrought titanium metal costs [11] and with up to 95% of the starting material removed, optimising the efficiency, cost and impact of such operations on the final in service performance is crucial to secure the future of titanium components on next generation aircraft

The comparably low machinability of titanium alloys is well reported in the literature. High mechanical strength and low thermal conductivity of such alloys results in greater tool wear and temperature generation when compared to steel or aluminium. Therefore, titanium is considered to be a difficult to machine metal. This increases the complexity and cost of material removal processes for titanium alloys and results in a need for innovation and integration of advanced manufacturing techniques for the production of such components.

A fundamental way in which to improve productivity without inferring increased production costs is to increase the material removal rate of machining operations. For conventional alloys significant research has been conducted and correlations be-

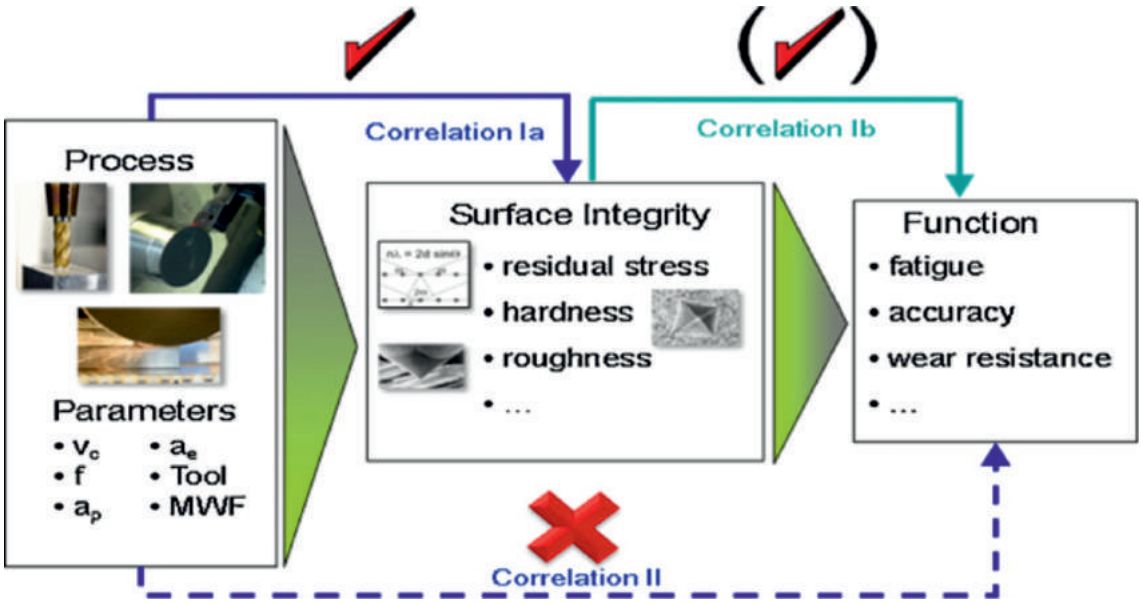

Figure 1.3: Schematic representation of fundamental correlations in machining research [12].

tween the effects of increased material removal rates and the response of the workpiece material have been defined. The associated effects of cutting conditions and tooling parameters on the surface integrity; defined in terms of roughness and the presence of defects and the subsurface; defined in terms of microstructural deformation and residual stresses, have been correlated. Similar correlations have been successfully drawn between the influences of individual defects on in-service performance. However, the correlations and understanding between the effect of machining parameters and the in-service performance for example fatigue is limited.

Machining, conventionally a topic for the field of mechanical engineering, now requires an expansion into advanced analytical techniques from a variety of engineering disciplines to accurately characterise the microstructural phenomena related to the correlations identified in Fig.1.3 [13, 14].

Through exploitation of small scale testing, finite element analysis and advanced characterisation techniques gaps in the knowledge can be interrogated in a manner that can be applied into real world engineering applications and drive cost reduction in the machining of aerospace components. Through this process, the application of titanium alloys in the construction of critical airframe structures can be secured.

1.2 Industrial Context

Safran Landing Systems (SLS) is a world leading landing gear, braking and ground movement system original equipment manufacturer (OEM). Employing over 60,000 professionals in over 50 countries, SLS supplies landing systems for approximately 22,000 aircraft, accounting for 35,000 landings globally, every single day [15]. SLS supplies the nose and main landing gear systems for the next generation commercial aircraft platform the Boeing 787 Dreamliner.

Major structural components on Boeing 787 landing gear assemblies are constructed from high strength titanium alloys offering weight reduction benefits and removing the requirement of coatings due to the materials inherent corrosion resistance. Titanium landing gear components such as the truck (or bogie) beam are

(a) Photograph of Boeing 787 Dreamliner main landing gear.

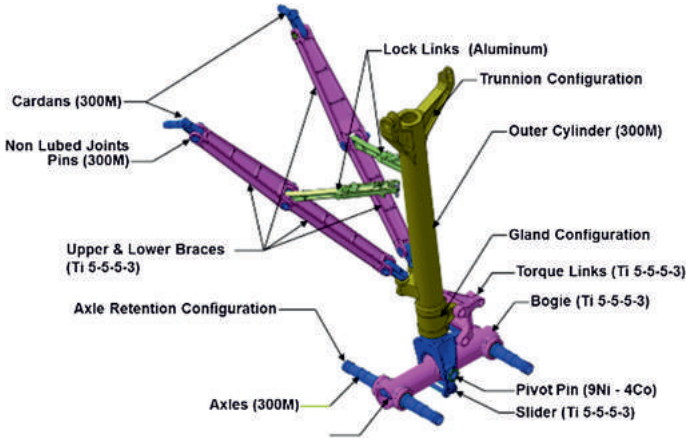

(b) Schematic representation of the Boeing 787 Dreamliner main landing gear components [16].

Figure 1.4: Boeing 787 Dreamliner main landing gear.

the focus of substantial industrial and academic research as OEM's like SLS aim to drive down production costs.

1.3 Aims & Objectives

The research presented in this thesis focusses on the machining operations performed in the production of Titanium 5Al-5Mo-5V-3Cr (Ti-5553) truck beam components for the Boeing 787 Dreamliner Fig.1.4. The aims of this research are summarised below:

- Develop small scale testing methodologies to provide a cost effective means of technical exploration.
- Reduction of the production time for Ti-5553 aero-structural components through increased surface generation rates for machining operations.
- Test 1: Understand the relationship between the surface integrity and subsurface microstructure with the increase of surface generation rates.
- Test 2: Understand the relationship between tool wear behaviour and the increase of surface generation rates.
- Test 3: Understand the relationship between the fatigue performance and the increase of surface generation rates.

1.3.1 Research Strategy

This research programme was conducted in partnership with SLS and the Industrial Doctorate Centre (IDC) in Machining Science at the Advanced Manufacturing Research Centre (AMRC) with Boeing and the Department of Materials Science and Engineering at The University of Sheffield. Due to the complexities and magnitude of the topics explored throughout this work, the dominant experimental activities

can be categorised into three topics as summarised below. In combination these topics of study address the aims and objectives detailed in section. Each topic is related to the other through the iterative and exploitative nature of academic research.

- Test 1: The effect of surface generation rates on surface integrity and subsurface microstructure for finish milling of Ti-5553
- Test 2: The effect of surface generation rates on tool wear for finish milling of Ti-5553
- Test 3: The effect of surface generation rates on fatigue performance for finish milling of Ti-5553

1.3.2 The effect of cutting parameters on the surface integrity and subsurface microstructure for finish milling of Ti-5Al-5Mo-5V-3Cr

The growth in the application of β alloys in aero-structural components over recent decades remains limited due to their inherent high processing costs when compared to well established alloys like Ti-64 [16, 17]. The low machinability of titanium alloys is well reported [13, 14, 16, 18–23], but due to the respective infancy of Ti-5553, limited research into its machinability exists in the public domain. Early research has shown, even for a titanium alloy, Ti-5553 offers low machinability in comparison to Ti-64 [20, 24]. For industrial machining operations there is a clear drive to identify and maximise existing capabilities to improve operational efficiency. Following on from the industrial investigation, ball nose finish end milling of Ti-5553 landing gear components investigated. Studying the effect of increased V_c and f_z on quality measures. A great deal of attention must be paid to the programming tool paths. Accurate replication of SLS machining strategies for milling of contoured external surfaces of the B787 truck beam are required to ensure the applicability of obtained results. Development in machining parameters can be iterative and conducted in time and cost intensive manner. The work presented in this chapter details the development of accurate small scale testing methodologies. Achieved through detailed reproduction of machining strategies, design of custom fixtures, parameter control and application of advanced monitoring techniques. Critical aero-structures are conventionally characterised through standardised quality measures such as stylus roughness techniques. All specimens produced during this investigation were characterised through such techniques in line with quality standards set by SLS and the wider aerospace manufacturing. This work was also supplemented with advanced characterisation techniques including, XRD, SEM and EBSD, in order to provide a higher resolution information about microstructures.

1. Study the effect of increased V_c, f_z and surface generation rates during ball nose finish end milling on the surface integrity and subsurface microstructure of Ti-5553 forgings.
2. Production of applicable and repeatable small scale testing methodologies for the investigation of industrial milling processes.
3. Identify a potential wider and economical processing window for further investigation.

1.3.3 The effect of cutting parameters on tool wear for finish milling of Ti-5Al-5Mo-5V-3Cr

The investigation presented in Test 1 will determine the influence of cutting parameters: V_c, f_z and SGR on the surface integrity and subsurface microstructure during finish end milling processes for Ti-5553 components. However, this work was carried out utilising only new cutting tools in a manner that isolated the influence of tool wear. Tool wear is a subject of great interest in industry and the research community, [25–33]. Predominantly it is turning trials that are utilised for studying tool life for machining of titanium alloys. Milling possesses greater complexity, due to the interrupted nature of the cutting process and the subsequently elongated tool life when compared to turning. In order to develop a thorough understanding of this finish end milling process and to accurately determine an improved processing window, it is expected that tool wear is considered. Any utilisation of increased cutting parameters cannot be at the expense of tool life, as cutting tools contribute significantly to the cost for any machining processes particularity when up to half of Ti-5553 forgings are machined away to swarf. The work presented in this chapter details an investigation into tool wear for solid carbide ball nose end milling tools for finish machining of Ti-5553. Small scale testing methodologies, developed in Tests 1 and 2, were used to study the effect of cutting parameters on tool wear and subsequent surface integrity and subsurface microstructure. Tool wear, as a result of increased cutting parameters was characterised using advanced techniques. The number of cutting conditions were downselected for increased duration tool wear trials. Trials were interrupted at increasing durations of use and the tools were used to produce experimental coupons, as shown in Fig.3.3b and 3.4. This was in order to characterise the influence of progressive tool wear on surface integrity and subsurface microstructure. Through advanced characterisation, tool wear mechanisms were studied an approach not currently undertaken for such industrial processes.

1. Determine the effect of increased V_c, f_z and SGR during finish end milling on tool wear of 20 mm solid carbide ball nose milling tools.

2. Determine the effect of tool wear on the surface integrity and subsurface microstructure in the finish milling of Ti-5553

3. Understand the relationship of surface roughness and tool wear measurement parameters in the finish milling of Ti-5553

4. From tool wear trials recommend an improved processing window for finish milling of Ti-5553.

1.3.4 The effect of machining induced deformation on fatigue performance for finish milling of Ti-5Al-5Mo-5V-3Cr

For finish end milling of Ti-5553, cutting parameters and tool wear influence surface and subsurface deformation. The results presented in Tests 1 and 2, have expanded knowledge of Ti-5553 response to machining. These studies utilised small scale testing methodologies that can be utilised to investigate a wide variety of industrial and experimental machining strategies for an array of aerospace materials. In service, such critical aero-structural components are subject to complex loading

conditions and can be acutely susceptible to fatigue failures. In agreement with literature, [13, 22, 31, 34–38], increases in V_c and f_z, play a significant role in component integrity, increasing cutting forces, imparting compressive residual stresses, SPD and the propensity for the activation of dislocation slip. Preceding research for machined titanium has focused on the importance of surface condition on fatigue life [39–42]. However, this approach is limited and does not consider the subsurface condition, nor the interaction with surface roughness. Work has postulated that such an interaction exists [12], but there has been insufficient work that provides an holistic assessment of fatigue performance post machining. The present study is an investigation into the influence of machining on induced deformation and the subsequent fatigue performance. The work in this chapter aims to address the issues discussed and exploit opportunities to advance the application of metastable titanium β alloys alloys in aero-structural applications [16]. Through the application of low cost small scale testing, the inherent expensive and iterative nature of development will be addressed. A bespoke 4 point bend fatigue test has been designed with the assistance of commercial FEA package Ansys, to isolate and investigate the effect of machining induced deformation on the fatigue performance of finish end milled Ti-5553. A variety of monitoring data was recorded throughout the duration of all low cycle fatigue tests. Advanced characterisation techniques were employed to study the machined and subsequent fatigue failed test coupons.

1. Production of repeatable small scale testing methodology for the investigation of industrial milling processes on low cycle fatigue performance.

2. Study the effect of increased SGR during ball nose finish end milling on the surface integrity, subsurface microstructure and subsequent fatigue performance of Ti-5553.

3. Determine the driving mechanisms in fatigue performance for finish end milled Ti-5553.

Chapter 2

Literature Review

2.1 Titanium alloys

2.1.1 An Introduction

Constituting of up to 0.6% of the earth's crust, titanium is the ninth most abundant element on the planet and fourth most abundant structural metal [18]. Titanium has high affinity for gases, namely oxygen. As a metal, titanium therefore requires complex and laborious reduction processes, such as Krolls method, which produces metal from an intermediate substance titanium tetrachloride ($TiCl_4$) [18, 19].

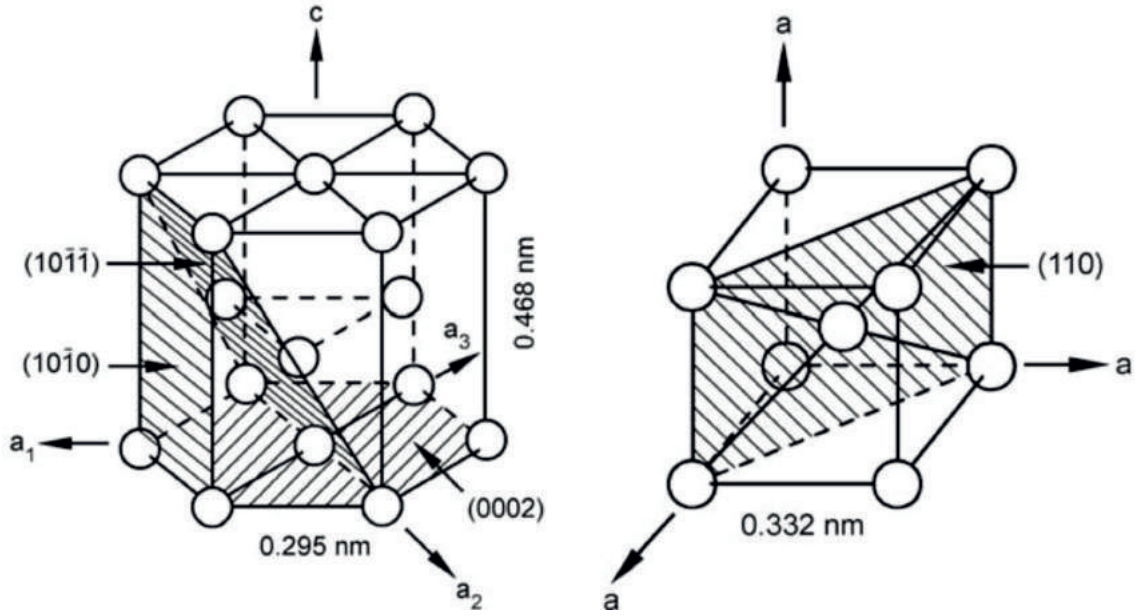

Figure 2.1: Crystal structures of the α and β titanium phases [18]

.

As an engineering metal, Titanium is present in two forms of crystal structures Fig.2.1. For commercially pure (CP) titanium, the low temperature alpha (α) hexagonal-close-packed (HCP) phase undergoes an allotropic transformation at approximately 882°C to the body-centre-cubic (BCC) beta (β) phase. At room temperature, the α face c/a lattice ratio is 1.587 nm, with the β phase ratio experimentally obtained at 900°C to be 0.332 nm Fig.2.1.

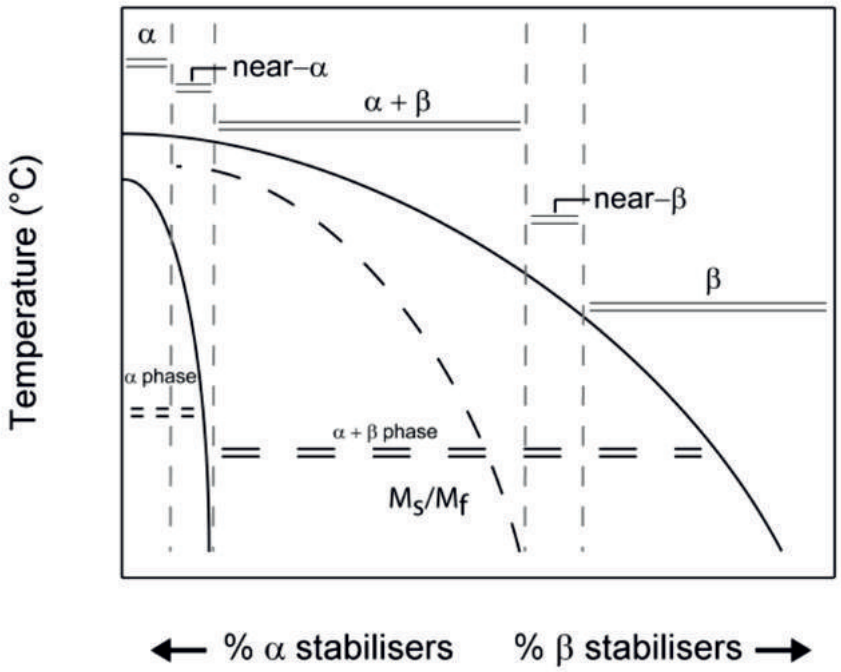

Figure 2.2: Pseudo-phase diagram for titanium alloys with respect to transformation temperature as a result of wt% of phase stabilisers [18, 43].

The addition of solute alloying elements has the effect of modifying the temperature at which this transformation occurs allowing for phases to be thermodynamically stable within greater operating temperatures. This can be observed in the pseudo phase diagram Fig.2.2. The quantities of the constitutive alloying elements determine the classification of the resultant alloy. Alloying elements such as Oxygen, Nitrogen, Carbon and Aluminium stabilise the α phase, such alloys (CP grades 1-4) are typically not employed as structural materials due to their low mechanical strength, though do offer excellent corrosion resistance (grades 7 & 12) [18,19]. The dominant commercial alloy with regards to aerospace applications for over 60 years is Ti-6Al-4V (Ti-64) due to the excellent complimentary tensile and fatigue properties achieved through the balanced phase presence. Ti-64, an α+β alloy, contains α stabilising elements and at room temperature and significant proportions of β stabilising elements, specifically between the α transus and the martensitic transformation temperature [18, 19]. Alloys that contain significant concentration of β stabilising elements such as Iron, Chromium and Manganese above the martensitic transformation temperature are known as near or metastable β alloys due to the remnant presence of an α phase [18, 19].

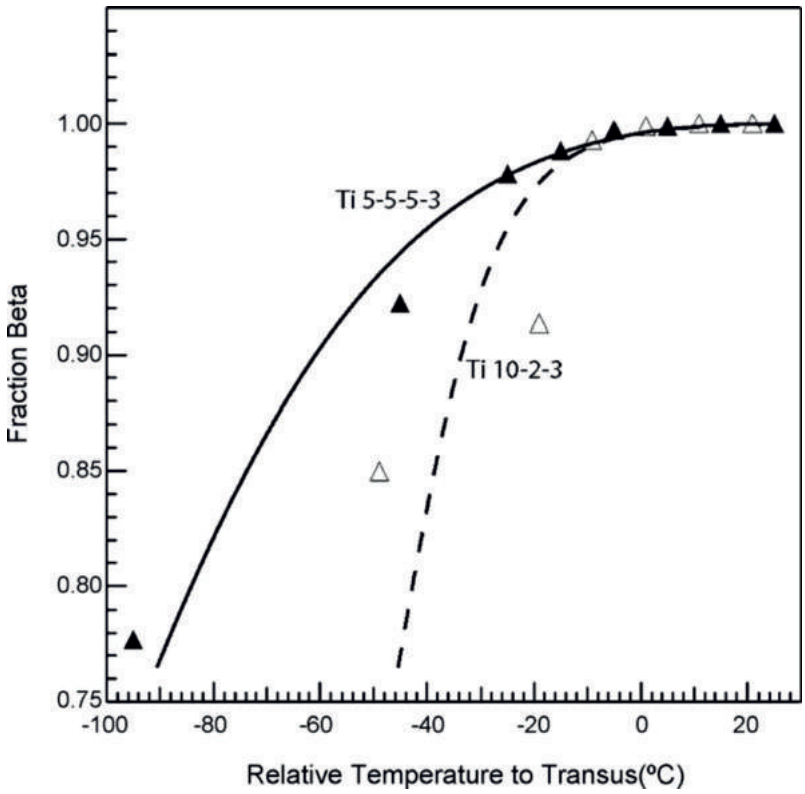

Figure 2.3: β Transus approach curves for Ti-5553 and T-10-2-3 [44].

Ti-5553 is a metastable β alloy with a lower β transus temperature and shallower beta approach curve, Fig.2.3 than the preceding Ti-10-2-3 allowing for a wider processing window and thus lower production costs [45, 45]. The nature of the alloy also allows for heat treatment of larger components to higher strengths than that of Ti-10-2-3 [44, 45]. With the elimination of Fe, Ti-5553 has also negated issues of β fleck formation as found in Ti-10-2-3 [45]. When processed well above the β transus temperate stable β alloys are produced. Though alloys such as Ti-13V-11Cr-3Mo have been applied to military aircraft, the deleterious effect of high temperatures on mechanical properties have limited this classification of alloys applicability [18, 19, 46, 47].

2.1.2 Beta Alloy Microstructural Processing

Within the aerospace industry β alloys first appeared on the Lockheed SR-71 "Blackbird" military platform in the 1960s [46, 47]. The high strength β alloy Ti-10-2-3 was first employed by Boeing in the early 1990s for landing gear components on the aircraft platform 777. Ti-5553 has now taken over in many applications on aircraft landing gear [46, 47] most significantly for Boeing 787 Dreamliner platforms. These β alloys offer a range of advantages over other titanium alloy classifications including a high H tolerance, higher corrosion resistance and with suitable heat treatments higher strength, ductility and fatigue life. This combination of excellent mechanical properties along with a wide processing window and high strength to weight ratio mean β alloys are an attractive material of choice for a variety of applications within the aerospace industry [47]. The mechanical properties in beta titanium alloys are a result to the microstructure produced from thermomechanical processing Fig.2.4. Variations in process conditions during deformation and heat treatment can produce either lamellar or equaixed phase arrangements [3]. Lamellar microstructures

offer high fracture toughness are achieved through cooling from the β field, the rate of which determines the fine or course nature of this structure [18]. Equiaxed structures are produced by recrystallization and high levels of deformation with subsequent and lengthy annealing to achieve high creep and fatigue strength and improved ductility [18, 19].

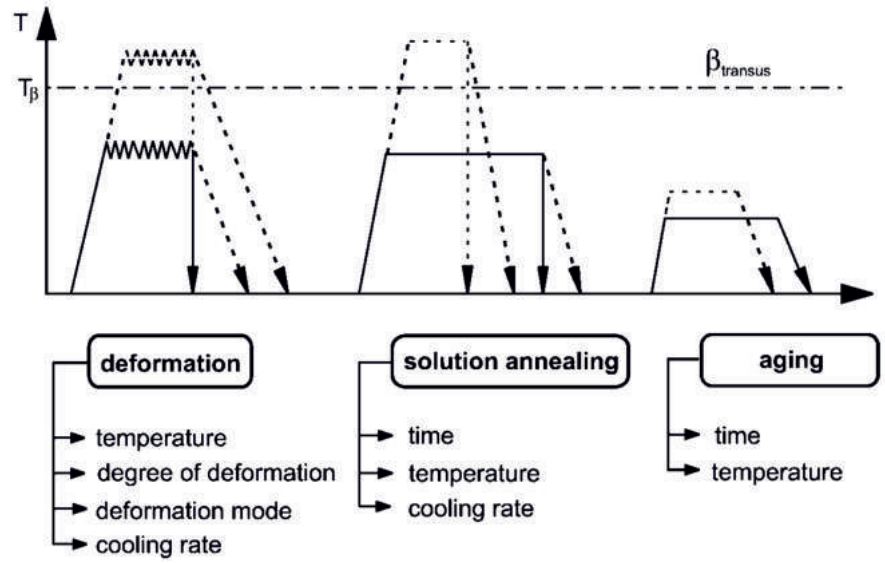

Figure 2.4: Schematic representation of thermo-mechanical processing of titanium alloys [19].

Processing of β alloys can be simplified, into three fundamental stages; deformation, heat treatment and ageing with the β transus as a thermal control point for these processes , as shown in Fig.2.4 [19]. The mode and extent of deformation is used to determine the un-recrystallized microstructure and therefore determines the size and shape of parent β grains [18]. This typically is carried out in the $\alpha + \beta$ phase field for near β alloys [19]. Primary hot work for Ti-5553 is carried out super-transus followed by a secondary forging to 15% reduction within the $\alpha + \beta$ phase field [19]. This secondary hot working operation has be shown to result in lower strain rate dependancy when compared to Ti-10-2-3 and improved elastic strength in the sub-transus state [44]. Ti-5553 has been shown to posses significantly less sensitivity with regards to microstructure with strain, strain rate and temperature than Ti-10-2-3 and can be considered to be easier to control during hot working [44, 45].

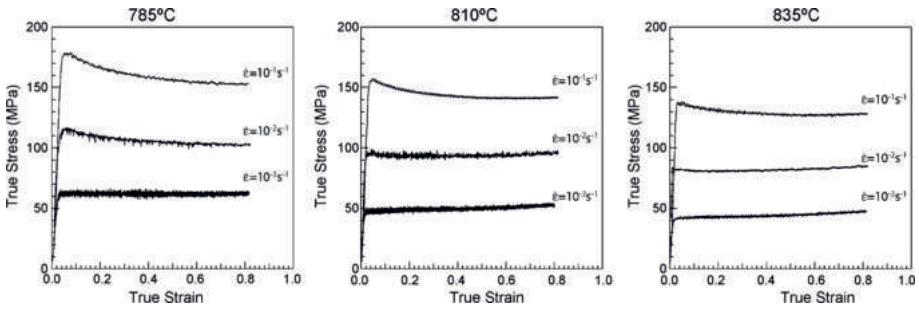

Figure 2.5: Flow stress behaviour for isothermal forging of Ti-5553 near transus [44].

The heat treatment followed by a quench and solution annealing stages control the transformation and growth of the α phase. This is a achieved with sub-transus heat treatment which allows for preferentially precipitation of the α phase at β grain

boundaries as continuous layers. Ageing allows for growth of α platelets which, due to the diffusion gradient formed by the precipitate free zone (PFZ) in the centre of β grains undergo dendritic growth inwards [18]. Substantial ageing times will produce an equiaxed α phase structure and aid in precipitation of the α phase. The temperature of this process will determine the volume fraction (vol%) of this α [18]. Through the alteration of this thermo-mechanical processing an array of microstuctures can be produced including β-annealed, β-processed and through transus microstructures.

2.1.3 Ti-5553 Microstuctural Development

The manufacturing processes critical aero-structural components are substantial and complex. An investigation and modification to any stage of this process must be studied in isolation. But it is important to consider the prerequisite and subsequent effects of other operations.

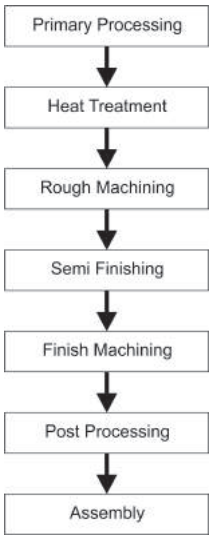

Figure 2.6: Schematic overview of the fundamental Ti-5553 truck beam processing stages.

A simplified schematic representation of the Ti-5553 B787 truck beam production route can be seen in Fig.2.6. Upstream operations; from primary processing through to rough machining are carried out by the forging company, VSMPO-AVISMA. Primary processing or billet manufacture involves several stages rotational deformation known as cogging, of a cast ingot at elevated temperatures within the $\alpha + \beta$ phase field, followed by air cooling. The formed billet is then heated in a horizontal furnace and held within the $\alpha + \beta$ phase field for several hours. The billet is subjected to several stages of high tonnage open die forging to meet the final as forged geometry. An overview of typical thermo-mechancial processing of β alloys is described in Chapter 2. The effects of forging, deformation, strain paths and heat treatments on the microstructure and mechanical properties of metastable β alloys have been explored in literature [44, 45, 48, 49].

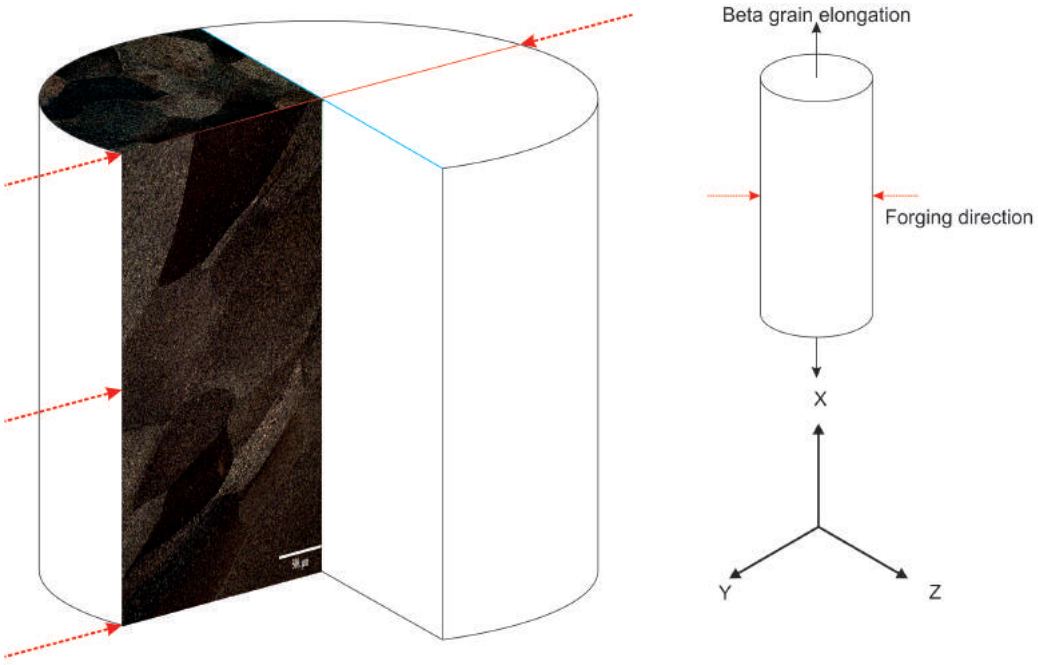

Figure 2.7: Schematic representation with super-imposed light micrographs (x5 magnification) of the β grain orientation as a result of open die forging.

Fig.2.7 is a schematic illustration of the effect of the forging direction on the elongation of β grains within a forged Ti-5553 billet. The high strain and plastic deformation imparted by the act of open die forging has extruded the grain structure perpendicular to the forging axis. When observed in this orientation, the grains appear as narrow, elongated plates. Observed along this elongation axis (parallel to the forging axis) the grains appear equiaxed. This behaviour is evident even after heat treatment operations.

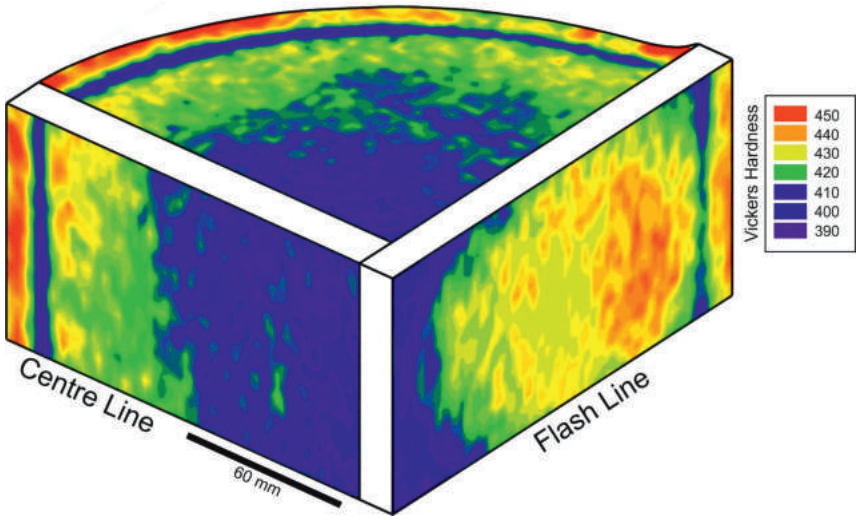

Figure 2.8: Schematic contour plot of the Vickers hardness variation in an as forged Ti-5553 B787 truck beam billet prior to heat treatments [49].

Fig.2.8 is a schematic representation of a large scale indentation contour map through thickness and around the circumference of the as forged Ti-5553 billet [49]. A significant variation in micro-hardness can be observed through the radius of the billet in directions both parallel and perpendicular to the flash line. The centre of the

billet is approximately 60 H_v lower than the outer diameter (OD). An interesting behaviour can be observed in the outer regions of the circumference of the billet where a band of low hardness material is present. The same behaviour is observed in microstructural analysis of the billet where a region of low % of retained β is found. This is an important observation as a global variation in mechanical properties will have an impact on machinability during cutting trials.

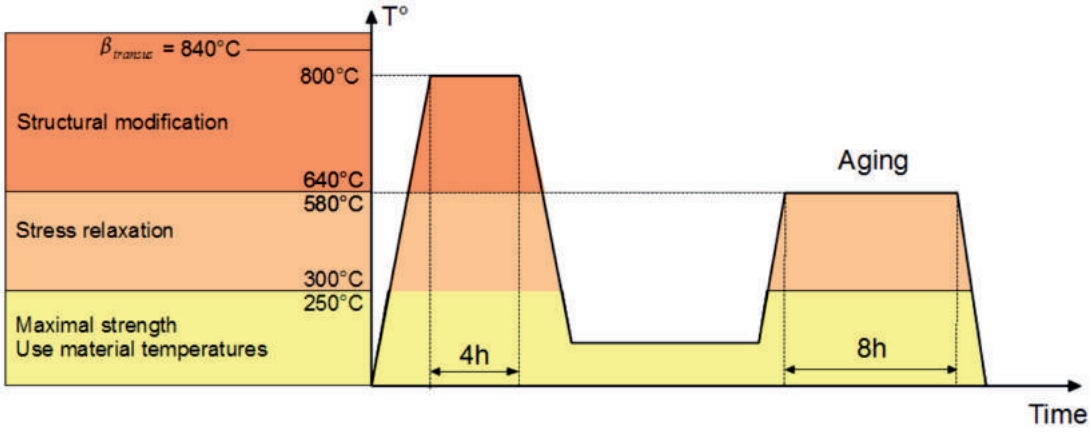

Figure 2.9: Graphical representation of the heat treatment operation for the production of Ti-5553 B787 truck beam components [50].

Solution heat treatment is then used to normalise this forged microstructural variation. The motivation and influence on microstructure and mechanical properties of temperature, duration and cooling rates employed in the heat treatments is discussed in Chapter 2. Fig.2.9 is a graphical representation of heat treatment regime applied to the forged and rough machining Ti-5553 billet after secondary processing. This involves fist a solution heat treatment, sub-β transus for 4 hours and an air cool for structural modification of the α_p volume fraction. Followed by a 8 hour age and air cool for stress relaxation and strength improvement in the retained β phase.

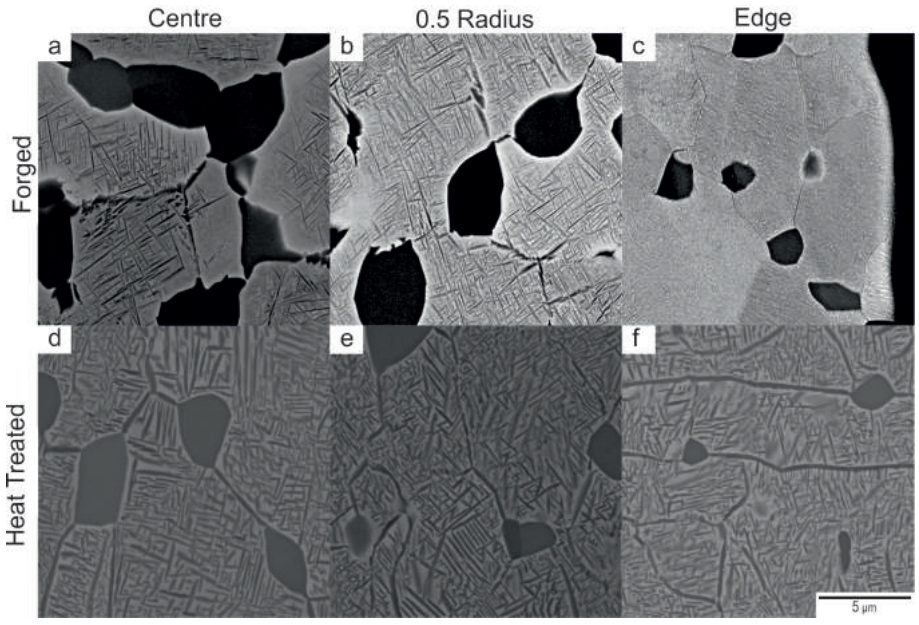

Figure 2.10: BSEI x 16,000 magnification of forged (a-c) and heat treated (d-f) Ti-5553 at the centre, half radius and edge of the face parallel to the forging axis.

The effect of heat treatment on the microstructure of Ti-5553 can be observed in Fig.2.10. This illustrates the grain structures found in identical locations of a forged and heat treated Ti-5553 section, located at the OD and centre of the sections both parallel and perpendicular to the forging axis. A detailed study in to the effect of this microstructural variation on the mechanical, namely tensile and ductility properties can be found in literature [49]. It can be clearly observed that α_p grain size and volume fraction is normalised throughout the radius of the section as a result of the heat treatment. The dissolution of α_s during the solution heat treatment is then mitigated through the precipitation of a finer and more regular or homogenised α_s phase. This through radius normalised α_s phase structure is responsible for the uniformity of mechanical strength and fatigue performance of Ti-5553 when compared to previous generation; VT-22 and Ti-10-2-3 metastable β alloys.

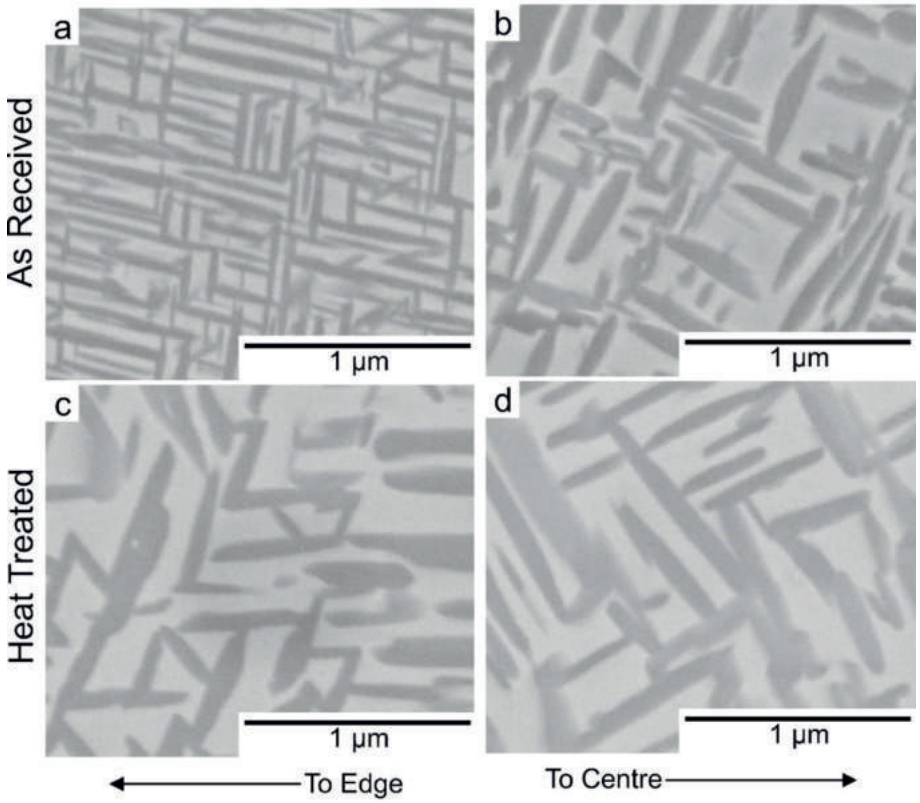

Figure 2.11: BSEI x 16,000 magnification of forged and heat treated Ti-5553 at the centre, 0.5 radius and edge of the face parallel to the forging axis [49].

The critical factor on mechanical properties identified [49] is the influence the α_p volume fraction has on the volume fraction of retained β and therefore the strength. Fig.2.11 shows BSEI micrographs for the forged and heat treated conditions along the flash line at the centre of the billet and the OD. It can be seen that the affect of the ageing process and the homogenisation of the retained β volume fraction through the radius and thus the homogenisation of mechanical properties. However, localised variation in inferred strength from micro-hardness indentation is observed due to local variation in α_s density [49].

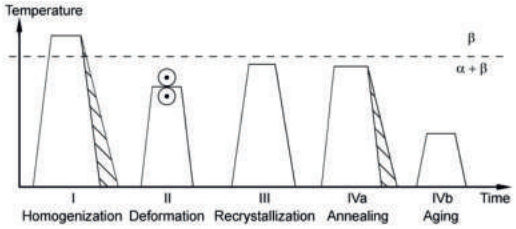

(a) Schematic representation of thermo-mechanical processing of bi-modal titanium alloys.

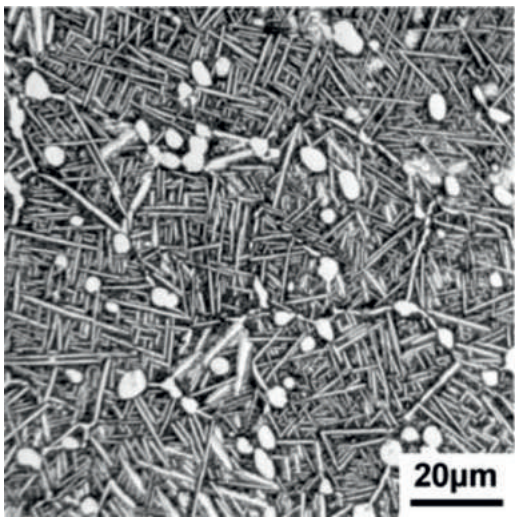

(b) Light micrograph of a representative bi-modal microstructure (β-CEZ alloy).

Figure 2.12: Bi-modal titanium alloy thermo-mechanical processing and microstructure [19].

Ti-5553 is bimodal metastable β alloy possessing the combined effects of a lamellar and equiaxed structures producing well-balanced mechanical properties [1]. Bi-modal structures are produced through careful control of the annealing process just below the β transus. Annealing temperature provides control the (vol%) of α. Careful control of the cooling rate post homogenization will limit the formation of the grain boundary α_{GB} while the cooling rate post annealing will control the size and (vol%) of α platelets within parent β grains [18]. The target for such a processing route is to limit β grain growth and to limit the precipitation of α_{GB} and thus limit crack propagation [18, 51].

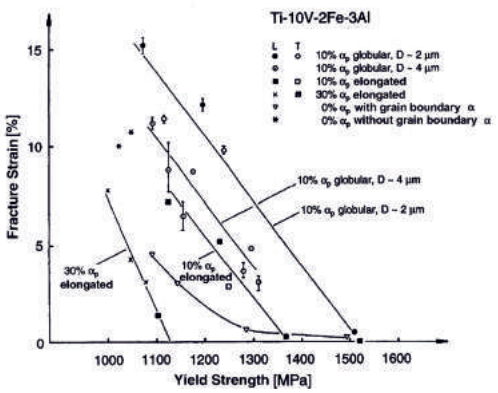

(a) Effect of microstrucuture on strength for Ti-10-2-3.

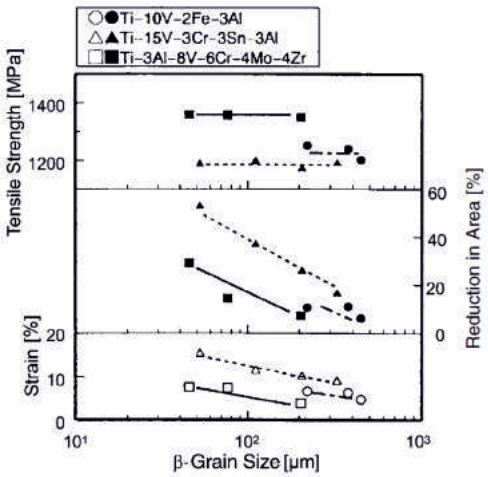

(b) Effect of β grain size on tensile strength.

Figure 2.13: Effect of parent β grains and precipitated α in β alloys on mechanical properties [19].

The formation of these α platelets is of great importance for high strength β alloys as is the β grain size. Precipitation of the α phase impede dislocation motion and strength β alloys [52]. The grain boundaries of β grains are pinned and grain

growth limited by α platelets [52]. Over-aging causes local inhomogeneity within the β matrix and thus a reduction in ductility, as depicted in Fig.2.13a [19]. Reduction in ductility is also observed in β alloy as a result of increased vol_f or change in form (acicular or elongated) of the α phase precipitates [19]. It has been experimental shown that grain refinement can negate this affect in many β alloys, Fig.2.13b.The strengthening effect of α particles is a result of the aforementioned precipitation hardening along with a dislocation strengthening which is a result of fine dispersal of α particles within the β matrix [18]. This relationship can be described through an inversely proportional "Orowan" relationship between interparticle spacing of α and β phases and yield strength [16, 49].

2.1.4 Deformation Behaviour in Titanium alloys

Dislocation slip

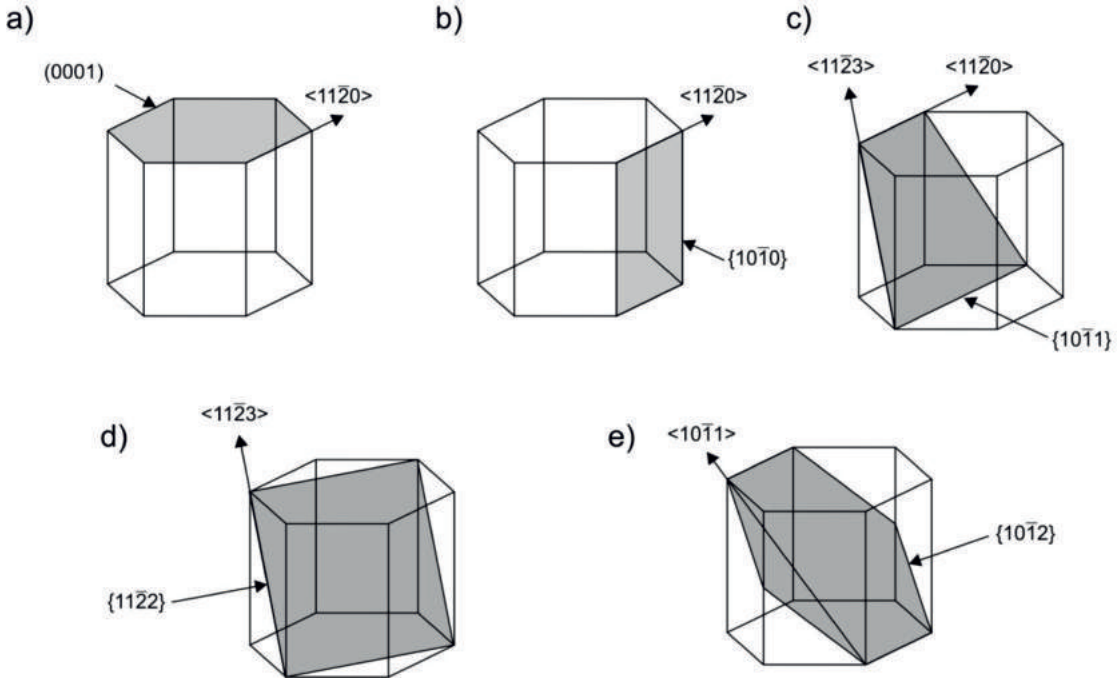

Figure 2.14: Major slip planes and associated directions; a. basal, b. prismatic and c &d. pyramidal slip with e. twinning plane and associated directions [18, 19, 53].

Within the α HCP crystal structure, plastic deformation is accommodated through the activation of dislocation slip and mechanical twinning along slip planes and associated directions as depicted in Fig.2.14. Though deformation can also activate the β slip and twinning modes in metastable alloys like Ti-5553 the precipitation hardening achieved through heat treatment can significantly if not completely suppress these deformation modes [18, 19, 22, 53].

Table 2.1: SLIP SYSTEMS FOR ALPHA TITANIUM CYRSTAL [18].

Slip system	**Burgers vector**	**Slip direction**	**Slip plane**	**Systems**
1	a	<11$\bar{2}$0>	(0002)	2
2	a	<11$\bar{2}$0>	{10$\bar{1}$0}	2
3	a	<11$\bar{2}$0>	{10$\bar{1}$1}	4
4	c + a	<11$\bar{2}$3>	{11$\bar{2}$2}	5

Slip within the α crystal is accommodated along the most close packed planes; described by the $< a >$ type Burgers vector, being basal and prismatic with three slip systems each in Fig.2.14 [18, 19]. However, only two planes are independent resulting in four independent slip systems [19, 22]. According to the Von Mices criterion to fully describe the deformational behaviour of a polycrystal five systems are required. To satisfy this the a <c+a> Burgers vector is included.

Mechanical twinning

At room temperature and under stress applied parallel to the c-axis dislocation motion is restricted and deformation can not be accommodated via slip so is accommodated through mechanical twinning mechanism [18]. Twinning influence mechanical properties acting as dislocation motion barriers and as crack initiation sites [54].

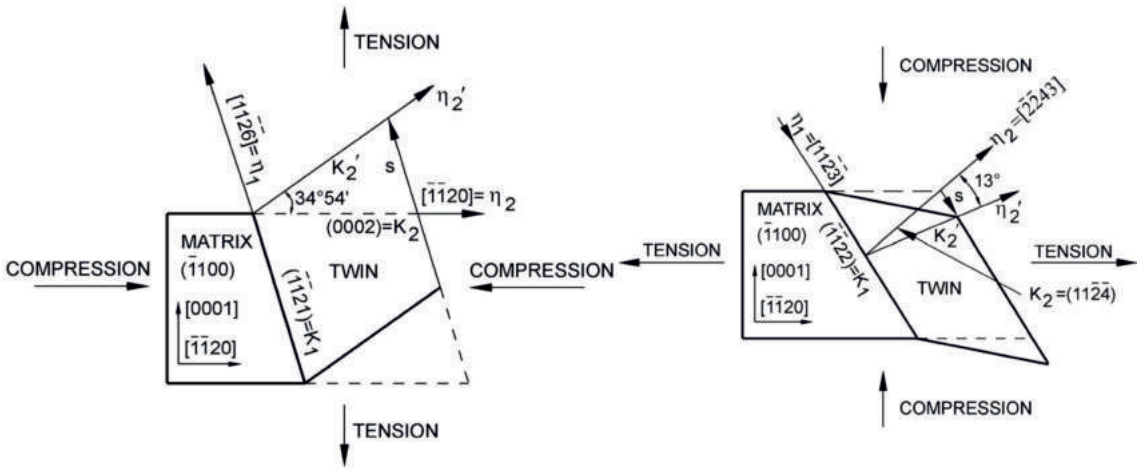

Figure 2.15: Schematic representation of the shape change occurring from $\{11\bar{2}1\}$ and $\{11\bar{2}2\}$ mechanical twinning [18].

Twinning in titanium is more prone in pure α alloys as increased quantities of O and Al and the low symmetry and anisotropy of the α HCP crystal suppress this deformation mode [18]. The major twinning modes for α titanium have been determined experimentally [54] summarised in the Table.2.2.

Table 2.2: MECHANICAL TWINNING MODES FOR ALPHA TITANIUM HCP CRYSTAL [54].

Mode	K_1 **Plane**	η_1 **Direction**	**Angle (°)**	**Shear**
Tension 1	$\{10\bar{1}2\}$	$<\bar{1}011>$	85 $<1\bar{2}10>$	0.171
Tension 2	$\{11\bar{2}1\}$	$<\bar{1}\bar{1}26>$	$35<1\bar{1}00>$	0.629
Compression 1	$\{11\bar{2}2\}$	$<11\bar{2}\bar{3}>$	$65<\bar{1}100>$	0.221
Compression 2	$\{10\bar{1}1\}$	$<10\bar{1}\bar{2}>$	54 $<\bar{1}2\bar{1}0>$	0.101

The twinning (K_1) plane and shear (η_1) direction for each of the 4 major tensile and compression twinning modes can be associated to one another by their respective misorientation angles and the axis of rotation. Twinning is an extension or contraction of a crystal depending on the applied stress direction [18, 55]. Twinning can be thought of as a reorientation of the crystal structure [22] in which a shear of the lattice occurs along the K_1 plane in a given η_1 direction parallel to crystallo-

graphic planes producing a twinning plane K_2 [18, 55]. The associated shear strain as shown in Table 2.2 can be calculated via Eqn. 2.1.

$$S = [\frac{c}{a} - 3]\frac{\sqrt{3}a}{3c} \tag{2.1}$$

The shear strain (S) accommodated by a twin is calculated by measurements of the lattice parameters of the twinned crystal structure and depending on whether this value is greater or less than 0 dictates whether the crystal is extended or contracted respectively [18, 53, 55]. Both dislocation slip and mechanical twinning have an Schmid factor associated with them. Schmid factors (m) are measures of the tendency for a given deformation mode to be activated and is related to the critically resolved shear stress (CRSS) required to activate that mode [22, 56].

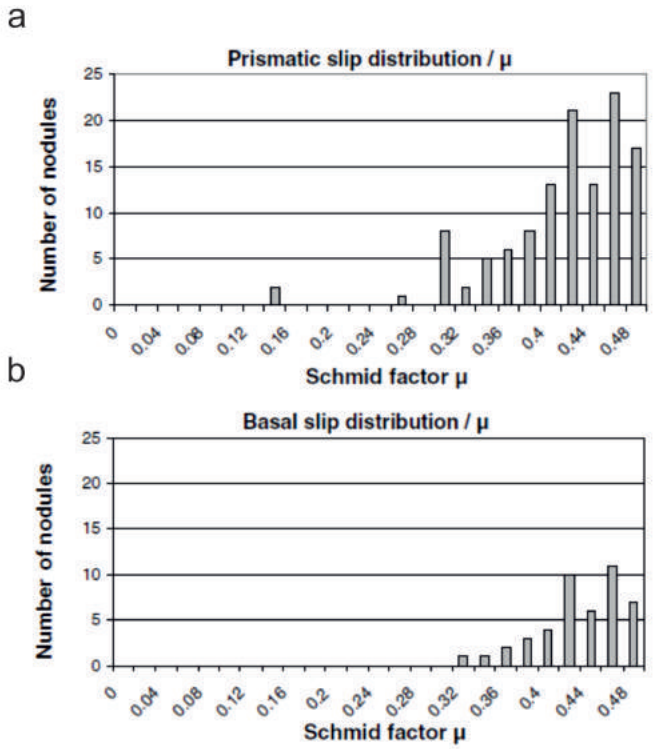

Figure 2.16: Distribution of Schmid factors associated with a) prismatic slip and b) basal slip in Ti-6Al-4V [57].

Schmid factors describe the geometric relationship between the direction and mode of deformation ranging from m= 0-0.5 where m= 0.5 is the maximum applied stress [22, 56]. As can be seen in Fig.2.16, the frequency of grains within a deformed Ti-64 specimen present with prismatic and basal slip [57]. It can be seen that both deformation modes have higher associated m values ($m > 0.3$) with grains inhabiting prismatic slip greater in frequency at the highest m values [57].

Characterisation of deformation modes

Historically, characterisation of deformation modes has been the domain of transition electron microscopy (TEM). The application of this established technique has been described in academic investigations of deformation modes within titanium alloys in a variety of applicaitons [58–61]. With the advancement of scanning electron microscopy (SEM) based systems the utilisation of electron backscatter diffraction (EBSD) allows for detailed qualitative and quantitative analysis of deformation

modes. SEM based EBSD allow for characterisation of larger regions of subsurface material without the extensive sample surface preparation required for TEM [22,56].

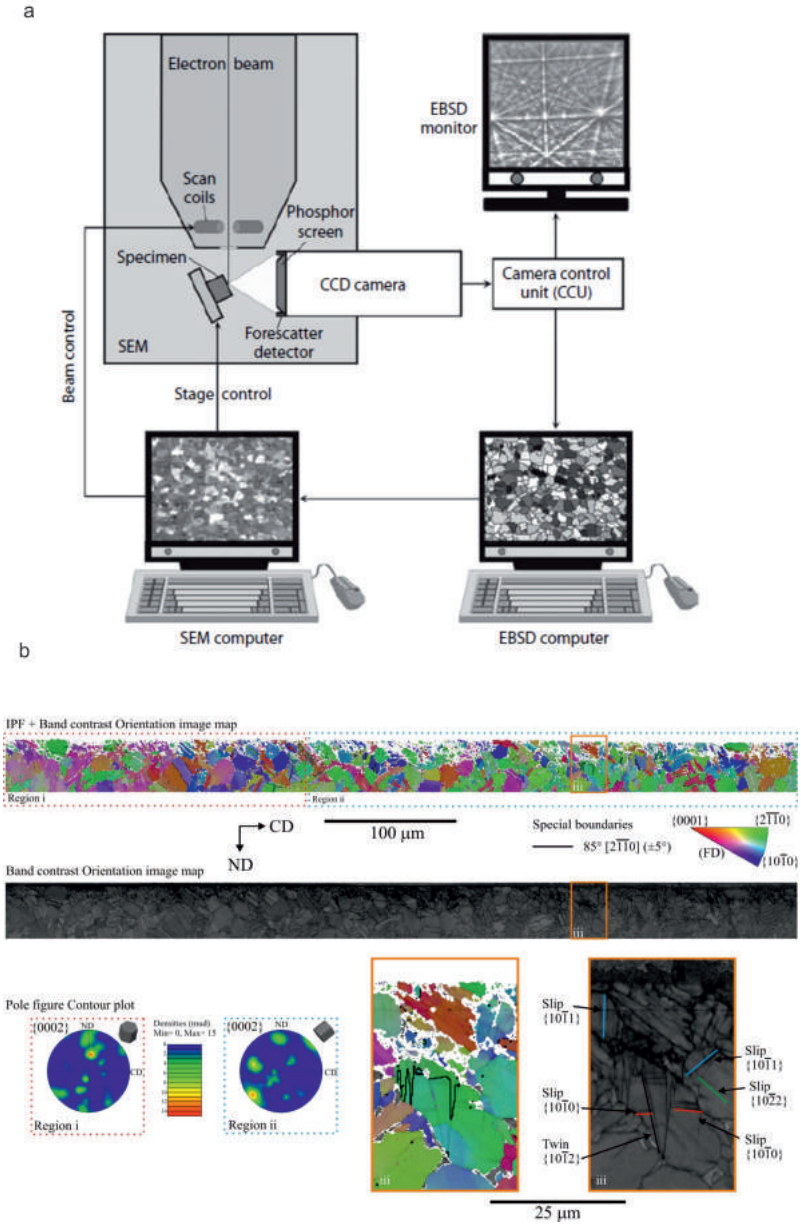

Figure 2.17: a. Schematic depiction of a typical SEM based EBSD system [56] and b. a detailed overview of SEM based EBSD deformation mode analysis of a Ti-834 [22].

A thorough description of the technique including data aquisition and analysis of deformation modes with application towards titanium alloys can be found in literature [22, 53, 56, 57, 62–64]. A schematic representation of a typical SEM based EBSD system is shown in Fig.2.17a [56]. Through the utilisation of the Bragg's angle (70°) the interaction volume of the electron beam can identify the crystallographic orientation of the region of the specimen under investigation. The diffracted electron beam is received by a forescatter screen, typically phosphor, which is inserted into the SEM chamber at a tilted orientation typically 10-15 mm from the specimen surface [56]. Acquisition software post-processes this interaction and interprets crystallographic planes from Kikuchi patterns as displayed on the EBSD monitor as an electron backscatter pattern (EBSP) in Fig.2.17 [56]. Fig.2.17b. shows an

example of a orientation image map (OIM) which is a representation of the quality of the indexed points from the area of investigation. The orientation of a given indexed point is inferred from the Kikuchi bands when compared to the Euler angles that describe the orientation of a reference crystal of the same structure [22, 56].. The deviation from the reference Euler angles to those characterised from the given indexed point is given as a mean angular deviation (MAD) number which is represented in the OIM [22, 56]. The average orientations of individual grains within the indexed region can be described through a graduated colour scheme and displayed on an inverse pole figure (IPF) map as shown in Fig.2.17b [22]. The pole figure of an individual grain or region can be imposed onto a 2D stereographic projection representing the orientation of a given plane in 3D space based on the respective Euler angles, as can be seen in the pole figure contour plots in Fig.2.17b. [22]. Based on the misoriation angle about the C-axis of a given twin plane for specific crystallographic structures as shown in Table.2.2, a user subroutine can be applied to the EBSD data to delineate the IPF map and identify twin planes. Such an operation has been conducted on the red highlighted sub-region of the OIM in Fig.2.17b. [22].

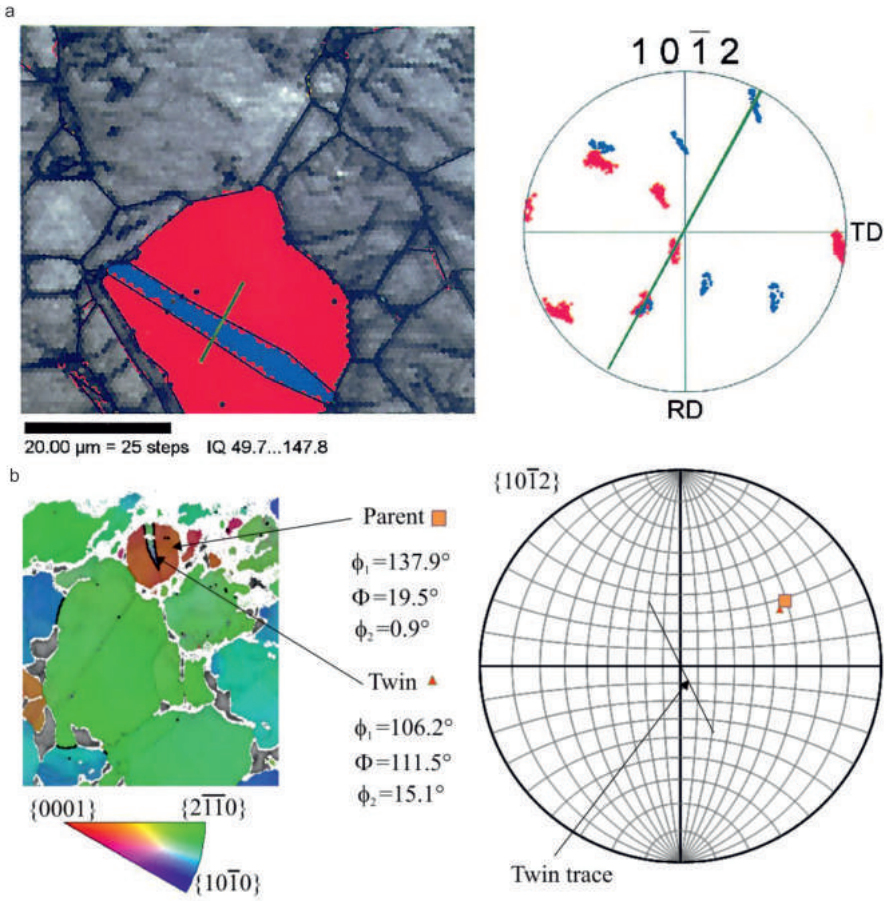

Figure 2.18: a) a. Analysis of a $\{10\bar{1}2\}$ twin in Zr with corresponding K_1 plane and b) analysis of a $\{10\bar{1}2\}$ twin in Ti-834 with corresponding K_1 plane [22].

In Fig.2.18 examples of tensile $\{10\bar{1}2\}$ mechanical twins in (a) a Mg alloy and (b) Ti-834. The pole figure projection show that the orientation of the twin plan (η_1) and parent grain plane (K_1) are normal to one another. This methodology of twin trace analysis is described in literature [22].

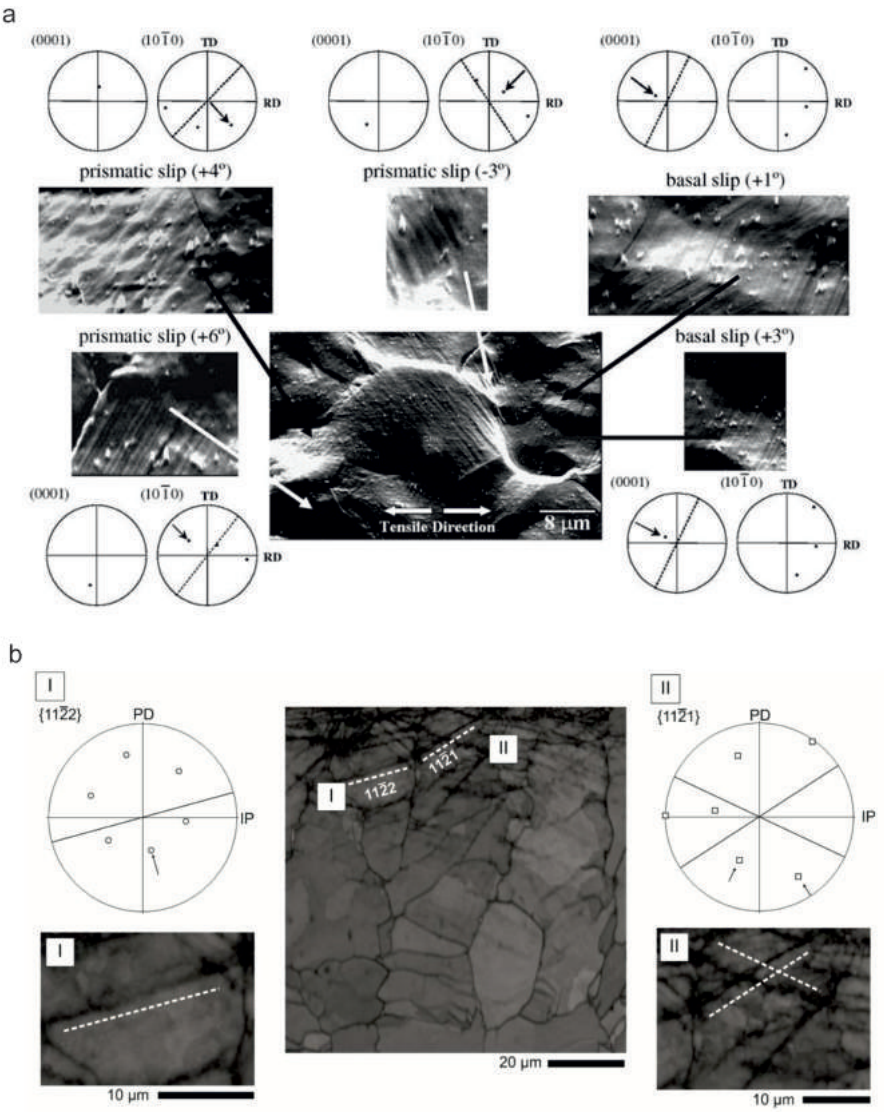

Figure 2.19: Slip trace analysis within a) a Mg-3Al-1Zn alloy [65] and b) a shot peened Ti-834 alloy [53].

A similar procedure for identification of the dislocation slip planes from SEM based EBSD techniques was proposed in literature [65], in which traces for prismatic and basal slip planes in a Mg alloy were presented [65]. Slip lines can be identified from the OIM as displayed by the dashed white lines in Fig.2.19b and the orientation of the slip line superimposed onto the stereographic pole figures [53]. An accurate trace is dependant on the known orientations of the specimen with respect to loading direction and the known available slip plane directions for the crystal structure under investigation. Through the application of a slip trace analytical tool, the recorded trace can be coincided with all available slip directions for that given crystal and loading direction and the specific slip direction identified. This methodology is best described in literature [22], which explores the mathematical functions required to produce accurate tensile and compressive slip plane orientation traces within the stereographic pole figures for a given crystal structure. Further detailed discussions into the above techniques can be found in literature [22, 53, 56, 58].

Influence of phase transformation on deformation

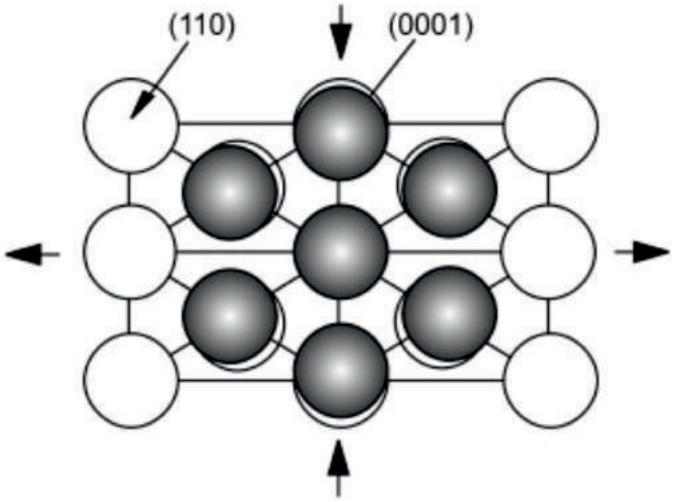

Figure 2.20: Schematic representation of the $\beta \rightarrow \alpha$ transformation [19].

The phase transformation during primary processing from the BCC β phase to the HCP α crystal structure described in Fig.2.20 occurs along the close packed planes $\{100\}_\beta \| \{0001\}_\alpha$ and associated directions $\langle 111 \rangle_\beta \| \langle 1120 \rangle_\alpha$ [18, 56]. This Burgers relationship describes the orientational relationship between the β and α phases, through the use of EBSD techniques [62, 66, 67] has been shown to persist through secondary processing and can be determined as the DNA or fingerprint of the alloy [22]. The parent β structure produces 12 variants in the α HCP crystal [18, 56].

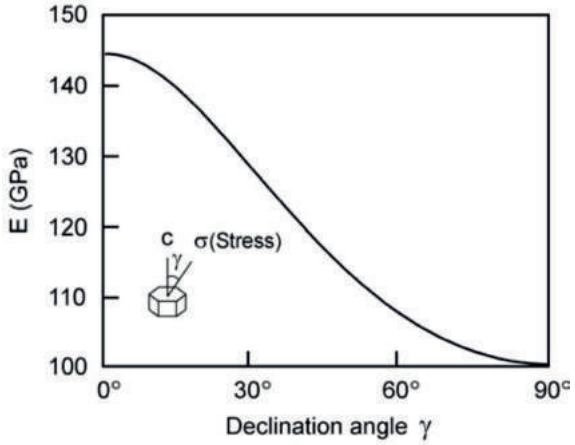

Figure 2.21: The affect of the applied stress with respect to the C axis or declination angle (γ) on elasticity of a single α crystal [18].

Due to the intrinsic anisotropy of the HCP crystal, the effect of the resultant α C axis orientation with respect to applied stresses (declination angle (γ) can be traced back to the parent β texture through this Burgers relationship Fig.2.21.

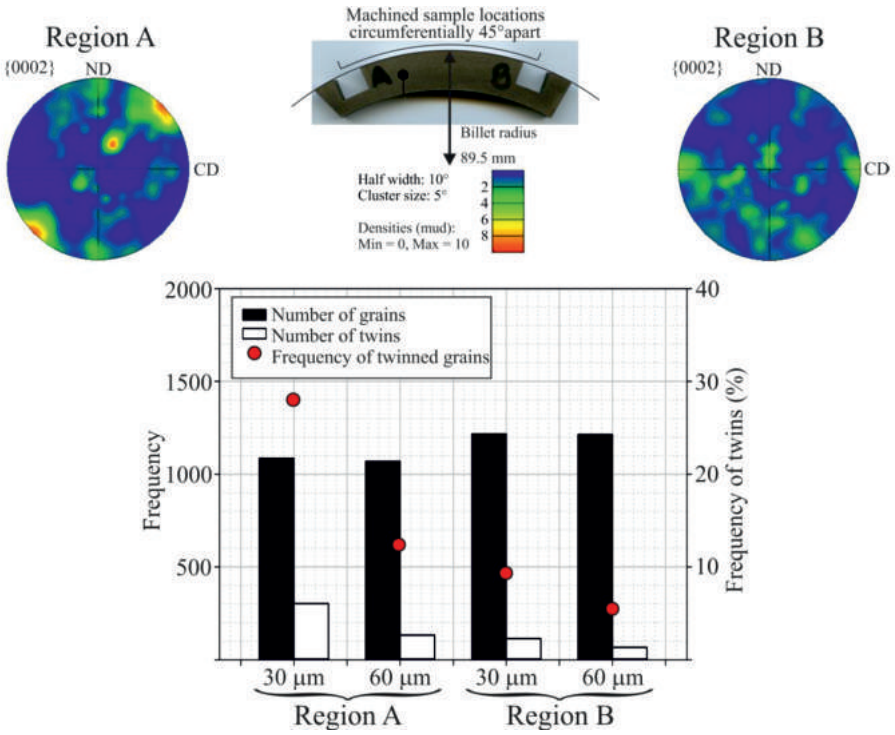

Figure 2.22: Comparison between 2 regions (a and b) of a forged Ti-54M billet with different micro-textures and the relationship with the extent of machining induced mechanical twinning deformation [22].

The influence of this Burgers relationship on the propensity for deformation shown in Fig.2.22 [22]. Regions from two different positions 45°apart along the outer diameter (OD) of a forged Ti-54M specimen was characterised through EBSD and shown to possess differing microtextures as a result of primary forging operations. Subsequent turning operations resulted in significant differences in the induced mechanical twinning frequency. This behaviour can be related to the effect of induced stress of along the respective declination angle of the α crystals which in turn is consequential to this Burgers relationship and the parent β texture from primary processing [22]. From these results it can be inferred that the texture and Burger relationship will have an influence on the machinability of titanium alloys.

2.2 Fundamentals of machining

2.2.1 Mechanics of Machining

Machining, employed following primary and secondary forming operations is a material removal technique achieved through high strain rate plastic deformation and chip formation utilising high hardness and wear resistant cutting tools. Turning operations involve the rotation of a workpiece about a static tool with continuous interaction between said workpiece and tool. Milling operations involve the relative motion between a workpiece and a rotating tool involving interrupted cutting action between the tool and workpiece.

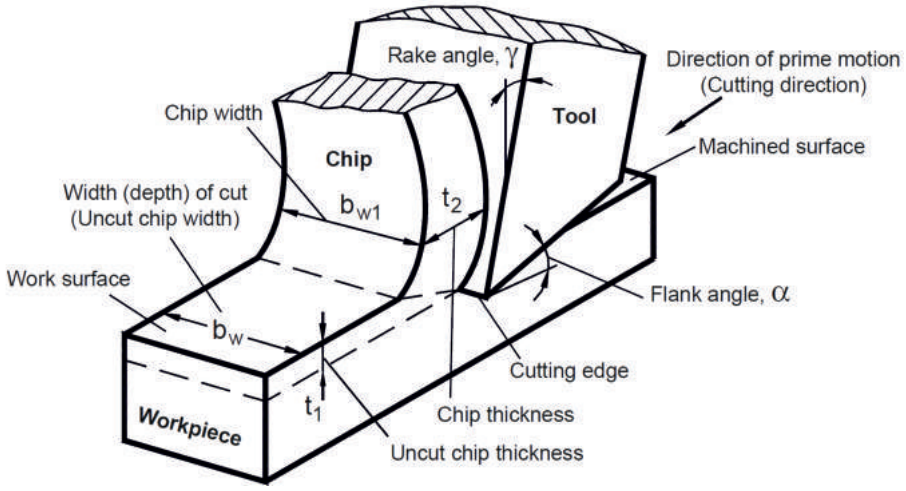

Figure 2.23: Schematic representation of orthogonal cutting terminology [68].

The fundamental terminologies can be identified and the mechanics of machining operations understood, in a simplified 2D representation of orthogonal cutting as depicted in Fig.2.23. Orthogonal cutting is a useful approach for determining the basic nomenclature for machining operations such as turning and milling. Conventionally, two standards are used for cutting tool nomenclature; the American National Standard B94.50-1975 and ISO 3002/1. The cutting edge or nose of a tool of a specified radius r (μm) interacts with the workpiece at a depth t_o known as the uncut chip thickness (μm). This is subject to the cutting edge angle and the angle between the work piece and flank face of the tool known as the flank angle a ($^\circ$) behind which the newly produced machined surface is exposed. The segmented chip of thickness t_c is removed at an angle with respect to the rake face of the tool known as the rake angle y ($^\circ$). Ahead of the nose of the tool is where the greatest plastic shear strain occurs and the behaviour of which results in segmentation of the chip to differing extents.

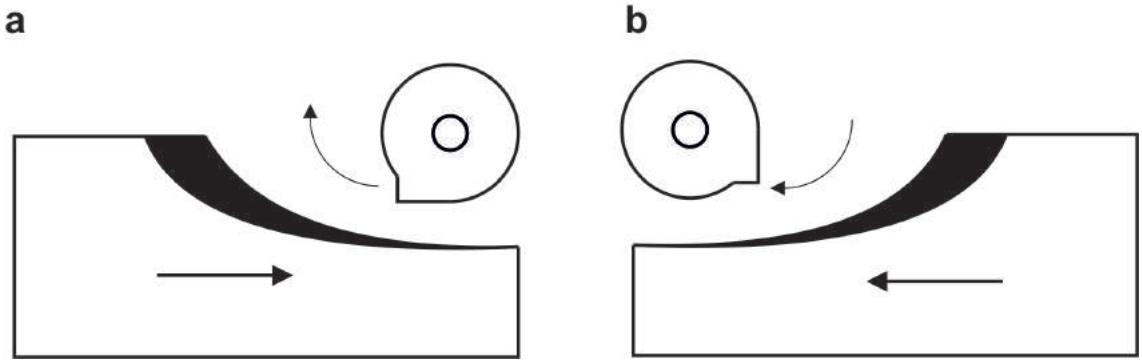

Figure 2.24: Schematic representation of milling directions. a. Conventional milling formation of a thin to thick chip and b. climb milling formation of a thick to thin chip.

Milling operations can be first sub-categorised into conventional or climb milling as depicted in Fig.2.24. Conventional milling Fig.2.24a is as a result of contradictory interactions between the tool rotation and workpiece feed direction. This produces an increasing chip thickness and chip loading on the rake face of the tool. Climb milling Fig.2.24b is as a result of complimentary interactions between the tool rotation and workpiece feed direction. This produces a decreasing chip thickness and

chip loading on the rake face of the tool. Machining processes can be then further sub-categorised into applications, which describe the nature of the cutting action. Though many variations and descriptions exist, the most widely adopted applications include face, profile, slot and end milling. All of which have many further variations dependant on the tooling options available and the exact relationship between the cutter and workpiece surface.

$$f = RPM \times Z \times f_z \tag{2.2}$$

For all milling applications the relative velocity of the cutting edge with the workpiece is the feed rate f (mm/min) expressed in eqn.2.2 in which RPM, Z and F_Z are revolution per minute of the spindle, the number of teeth on the cutter and feed per tooth or chip load (mm) respectively.

$$V_c = \frac{D_e \times \pi \times n}{1000} \tag{2.3}$$

Cutting speed (m/min) is the speed of the cutting edge relative to the workpiece and is expressed in eqn.2.3 in which D_e and n are the effective cutting diameter at a given depth of cut a_p (mm) and the spindle speed (rpm) respectively. The D_e and a_p parameters depicted in Fig.2.25.

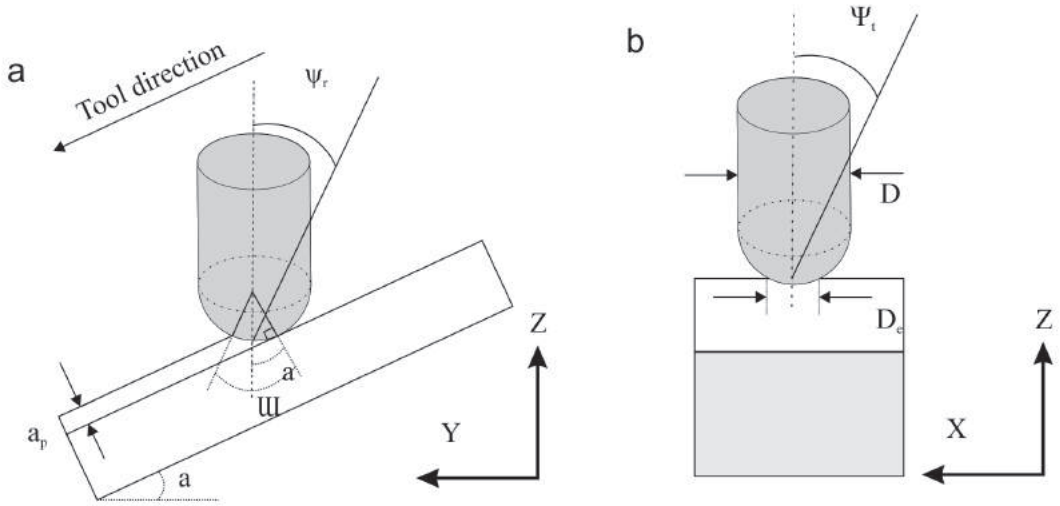

Figure 2.25: Schematic representation of end milling. a. YZ plane showing lead angle Ψ_r and b. XZ plane showing tilt angle Ψ_t.

End milling, classified as such due to the cutting action of the end of a solid tool on the surface of the workpiece offers a range of possible profiles to be produced through careful control of key machining parameters Fig.2.25. On cutting a workpiece at an inclined angle of a and at a given depth of cut a_p (mm) an effective cutting diameter D_e (mm) is produced. A range of D_e can be achieved through varaition of α and a_p up to the diameter of the tool D (mm). The same variation can be achieved through the alteration of the lead angle Ψ_r (°). The ability to affect the Ψ_r is subject to the available axes of movement within the machining centre. Along with traversing the workpiece and or tool in the X, Y and Z axes, the Ψ_r results in a 4th axis of movement. The ability to rotate the workpiece about the Z axes produces a 5th axis. Fig.2.25b shows how in the XZ plane a tilt angle Ψ_t (°) can be produced and again will affect the D_e.

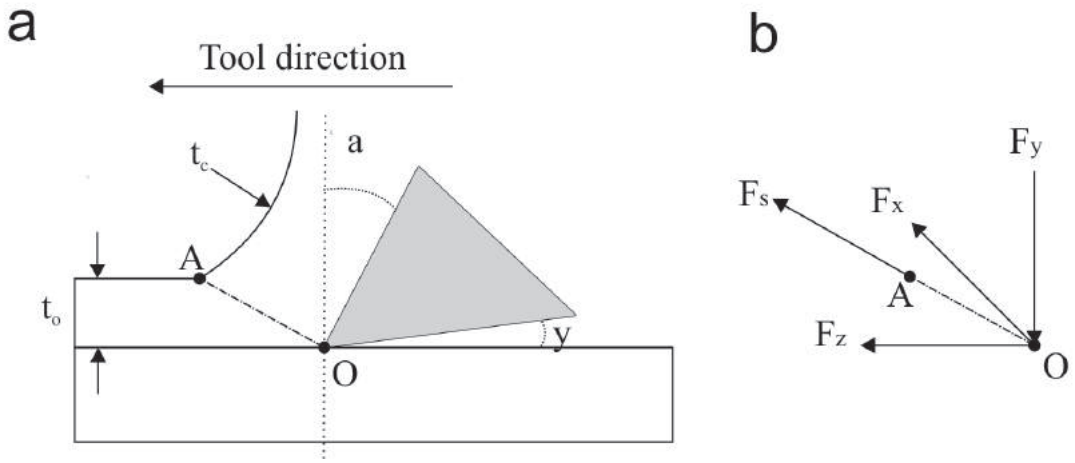

Figure 2.26: Schematic representation of a. the idealised cutting process with b. the cutting force components [55].

Upon studying an idealised model of the localised cutting action of a single flute from Fig.2.26a, the importance of the uncut chip thickness and a angle can be understood.

$$r = \frac{t_o}{t_c} = \frac{sin\theta}{cos(\theta - a)} \tag{2.4}$$

Eqn.2.4 shows how the ratio of the uncut chip thickness t_o and the thickness of the segmented chip formed ahead of the tool rake face *(t_c)* is dependant upon the rake a and relief y angles of the cutting tool flute. The *(t)* is in turn dependant on a_p and the Ψ_r and Ψ_t angles described in Fig.2.25. Variation of *(r)* changes the shear angle *(ϕ)*, which is the angle between the workpiece surface and the plane OA or shear plane, where the largest intensity of plastic shear and chip segmentation is localised. Variation of *(ϕ)* determines the resultant stress components at the point of chip segmentation Though these stress components are complex and dynamic, they can be experimentally obtained through the use of strain dependant force dynomometer and can be simplified into three components as shown in Fig.2.26b. The horizontal cutting force F_z, the vertical thrust force F_y and the normal force F_x. The resultant force component acting within the shear plane OA is F_s can then be formulated 2.5.

$$F_s = F_z cos\phi - F_y sin\phi \tag{2.5}$$

The dynamic nature of the chip formation process during intermittent machining such as milling, induces variations in cutting force measurements.

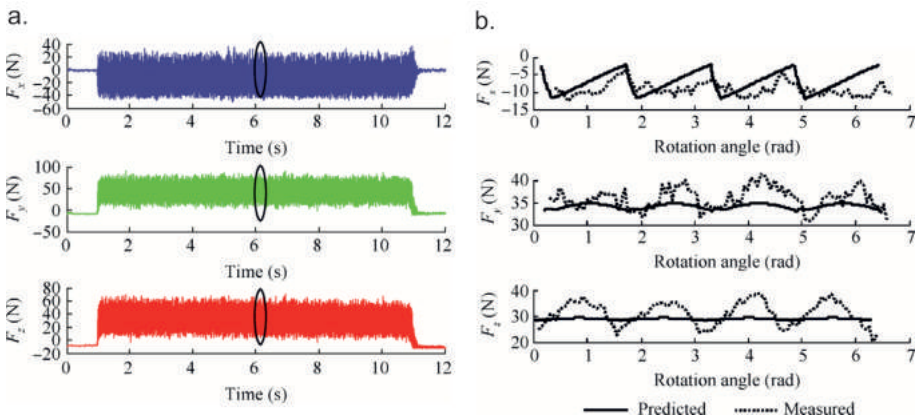

Figure 2.27: Schematic representations of the cutting forces for an intermittent process a. against time and b. against rotational angle [69].

A simplified representation of the recorded dynamic cutting forces for milling operations is shown in Fig.2.27 against time and with respect to rotational angle.This process can be distinguished by 4 fundamental stages. I, entry phase, during tool engagement, chip loading rapidly increases as full t is achieved. The rate of increase is highly dependant on the cutting tool geometry, machining parameters and material properties. Average cutting forces in milling typically peak at the end of stage I prior to achieving stability in stage II the stationary phase due to a final initial engagement of the flank face of the cutting edge. For intermittent cutting process there is greater variation in the stationary phase than those found in turning for example. This is due to the dynamic nature of milling that involves variations in chip thickness, chip loading and tool-workpiece interaction parameters such as lead angles. Therefore, stage II is dependant on the relationship between the tool and the workpiece. The intermittent contact between cutting flutes and the workpiece also results in fluctuations in localised friction and temperatures as coolant delivery and chip removal varies with the rotation of the tool. Stage III, the exit phase involves a rapid reduction in cutting forces as the chip thickness is reduced to 0 and the tool becomes disengaged. During this process the shear plane and direction of the applied shear stress is reversed as the final chip is removed from the workpiece surface via either ductile or brittle failure. Due to rapid cooling at the point of tool disengagement, sharp burrs are often produced which can affect surface finish. The final stage IV, the free phase involves no cutting forces, only thermal stresses from induced heating remains within the workpiece.

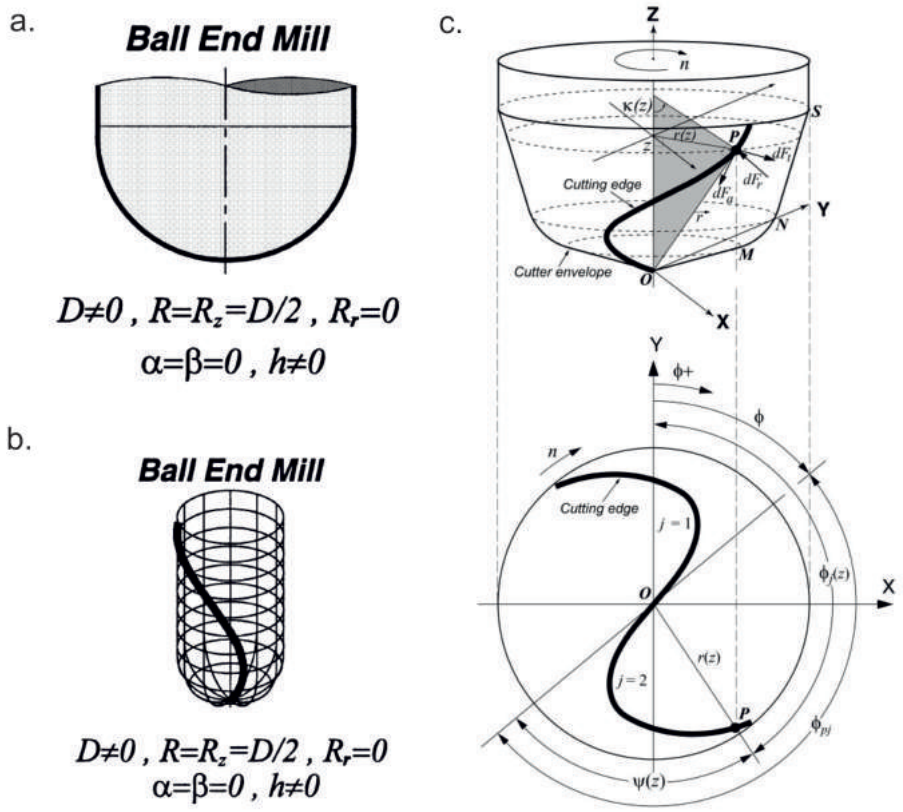

Figure 2.28: Schematic representations of the fundamental geometric parameters for a and b. ball nose milling tools and c. the angular considerations for ball nose cutting flutes [70].

Compared to the simplistic 2D models for cutting mechanics found in orthogonal cutting descriptions, ball nose cutting tools produce complex 3D geometric behaviours during cutting. An example of the models utilised to describe the characteristics of ball nose milling as shown in Fig.2.28 [70].A variety of nomenclature is employed to describe complex cutting tools such as the ball nose, shown in Fig.2.28a and b a summary of independent parameters are simplified in a manner to best describe the tool geometry and assist in formulation of cutting mechanics in both 2D and 3D, Fig.2.28a and b respectively [70]. The influence of the helical cutting flutes which wrapped around the tool diameter is further expressed in Fig.2.28c [70]. Fig.2.28 show how at any given point P, at a position along the helical cutting flute at a distance from the workpiece plane, the coordinates, cutting edge geometry, chip loading, and the three cutting forces can be forumlated. A point along the helix exists within one of the fundamental zones, OM, MN and NS which influences the effective cutter radius.

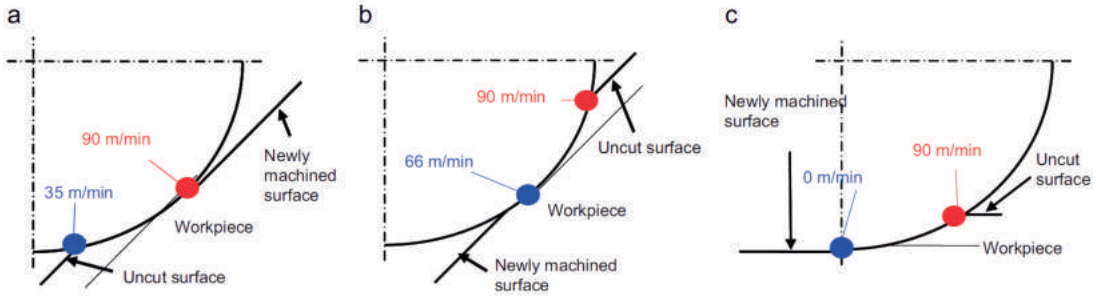

Figure 2.29: Schematic representations of the influence of effective cutting radius and tilt angle for a. positive tit, b. negative tilt and c. no tilt [71].

The influence of this effective cutter edge radius is represented schematically in Fig.2.29 [71] in which at a given rotational speed the instantaneous cutting edge velocity varies along the cutter helix. At a given instant, this means that along the chip formation plane the cutting speed varies influencing tool wear and the chip morphology. This behaviour is influenced by other cutting parameters, as in Fig.2.28, the influence of tilt angle, both positive, negative and 0; a, b and c respectively. The later of which shows how at the lowest cutter radius the effective cutting velocity is 0 resulting in a ploughing rather than a cutting action [71].

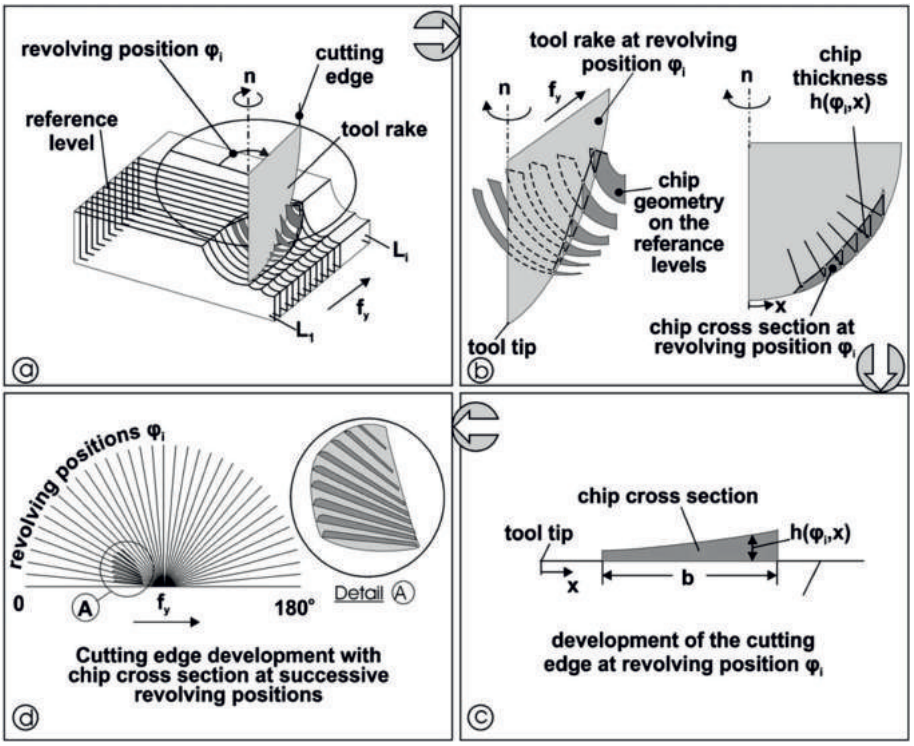

Figure 2.30: Schematic representations of chip formation process for ball nose milling processes [72].

The aforementioned factors can be utilised to understand the chip formation process for ball nose milling. Fig.2.30a. isolates the 3D ball nose into a 2D cutting edge plane interacting with a 3D workpiece surface at a resolved position [72]. It is shown that along the rake face formed chip vary in thickness as a result of the effective cutter radius and cutting velocity as shown in Fig.2.30b resulting in a thin to thick chip. This thickness behaviour is subject to the exact resolved position or

point along the rotation of th tool cutting edge as shown in Fig.2.30c and d [72].

$$C_r = \frac{F_z}{t \times b} \tag{2.6}$$

Cutting forces are directly related to the cutting resistance (C_r) (N/mm^2) imposed by the total area of the chip engaged with the cutting tool. Eqn.2.6 shows that the static cutting resistance is dependant on the cutting force F_z, the uncut chip thickness (t_o) and the area of the rake face in contact with the chip (b). Therefore, the C_r is highly sensitive to cutting parameters and tool wear. As the cutting resistance affects the F_z, it can be concluded that this behaviour has a direct effect on power consumption during machining operations.

$$P_c = V_c \times f \times a_p \times C_r \tag{2.7}$$

The cutting power (W) scan be formulated from the cutting speed, DOC, feed and cutting resistance as shown in Eqn.2.7.

2.3 Influence of machining

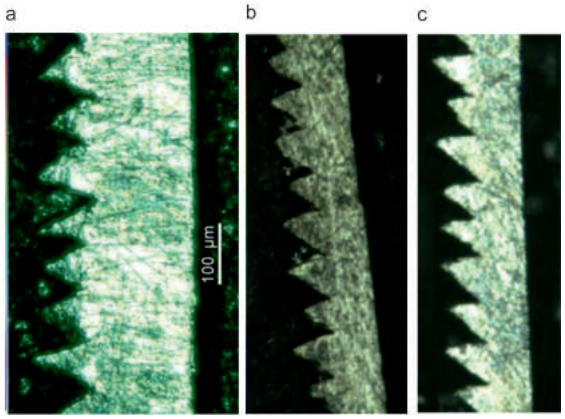

Figure 2.31: Chip segmentation of turned Ti-64 at a. V_c 121.9 m/min and f 0.127 mm, b. V_c 240.8 m/min and f 0.1 mm and c. v_c 240.8 m/min and f 0.127 mm [73].

The dynamic nature of the induced stress, temperature generation and friction during machining can be directly observed in the segmentation of chips. Variation in cutting parameters such as V_c and f, affect the distribution and magnitude of cutting forces which inferred by the material properties. The direction and magnitude of localised shear band formation is evident in the variation of chip morphology, see Fig.2.31.

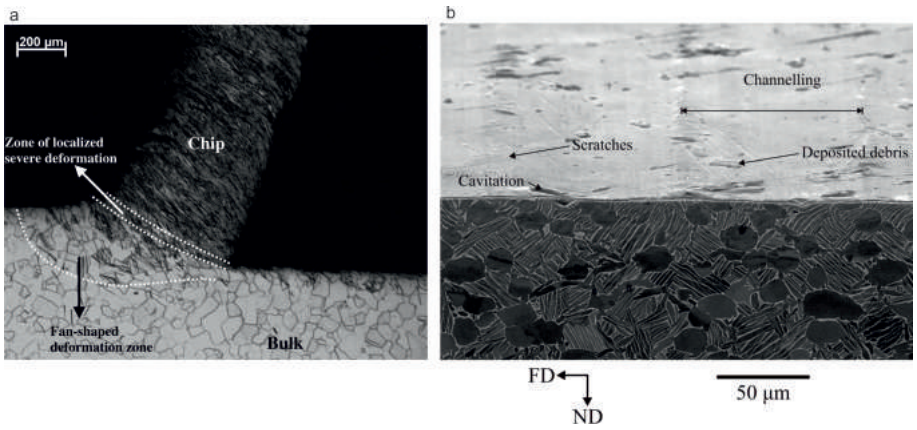

Figure 2.32: a. OM of deformation ahead of chip formation in orthogonal cutting of CP titanium [74] and b. a composite BSEI of Ti-54M surface and subsurface response to turning [22].

The same can be said for the newly generated material surface and near subsurface material as shown in Fig.2.32a, ahead of the cutting rake face a region of severe plastic deformation (SPD) is produced below the intense shear band. Within this region, high localised stresses and temperatures activate deformation modes, as discussed in Chapter 2. Upon chip removal, the workpiece subsurface contains remnant deformation, induced through the process of chip formation. In addition localised heat and stress induce tool wear and instability that can produce surface defects as observed in Fig.2.32b. Many factors can affect the surface and subsurface condition including; tool wear, temperature, dynamic stability and machining parameters, the latter of which is the focus of this study.

2.3.1 Surface response to machining

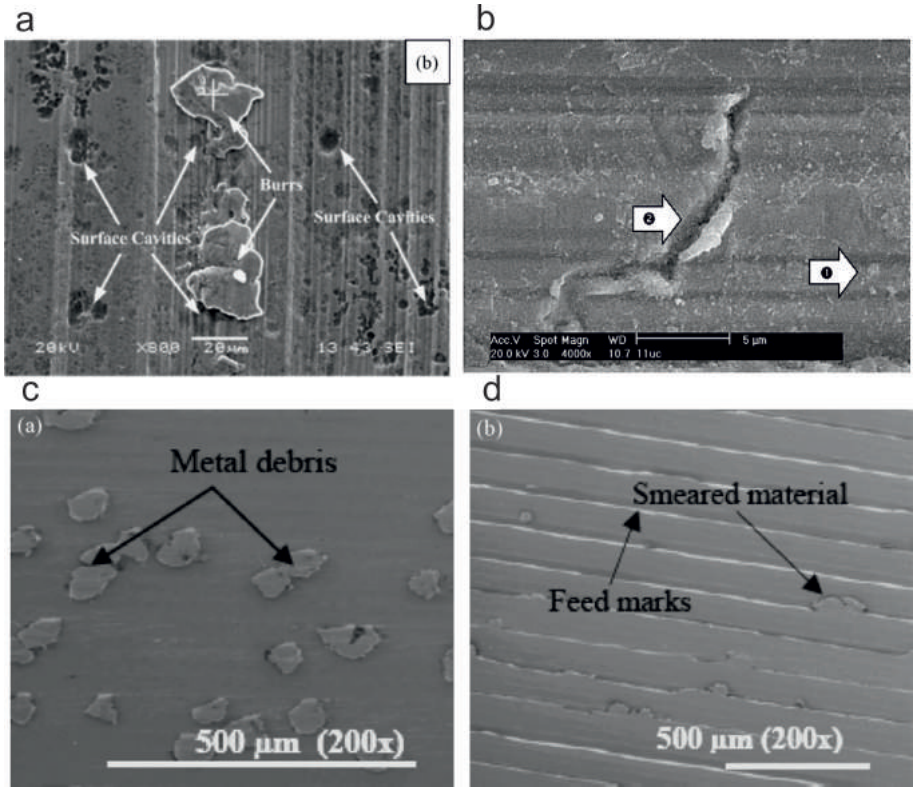

Figure 2.33: BSEI of surface defects including a. surface cavities and burrs from turning of a NiCrTiAl alloy [75], b. tearing during milling of Ti-6242 [29] and c. metal debris, d. feed marks and smeared material during turning of Inconel 718 [76].

A variety of surface defects can be induced during the cutting of high strength materials, typical examples are presented in Fig.2.33. Such defects are a direct result of tool and workpiece condition. Cavities, burrs, smearing and debris are dependant on tool wear, temperature and material ductility. These defects typically occur during the use of worn tools for cutting of ductile materials at low V_c. This produces a built up edge (BUE), an accumulation of material between the chip and rake face in a ploughing type process. This transports material and tool fragments, disturbing the newly generated material surface. These defects will result in aero-structural components potentially failing to satisfy quality standards and requiring further surface preparation. It has been shown that defects will influence in-service performance [77–81].

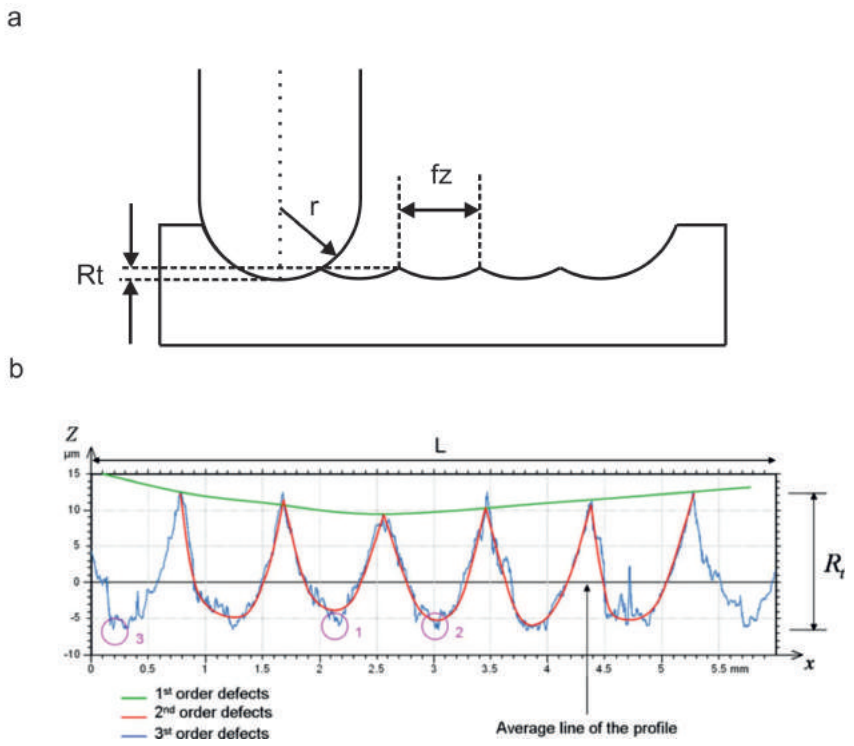

Figure 2.34: Schematic representations of a. the theoretical roughness produced in end milling operations, adapted from [82] and b. the 1^{st}, 2^{nd} and 3^{rd} order defects a milled surface [42].

Defects can be considered as 1^{st} order surface deviations, or form errors [82]. The theoretical roughness for end milling processes can be seen in Fig.2.34a, in which the radial step over (a_p) and axial depth of cut (a_e) with respect to the tool radius (r) produces the waviness or 2^{nd} order defects. This surface is defined by the machined cusp height and width [82]. The surface generated by the intersection peaks of these cusps shown in Fig.2.34b, produce the 1^{st} order profile, or geometric surface [82]. The true surface produced by machining operations is the 3^{rd} order roughness profile [42,82]. This roughness is determined by the chip formation process, material properties and dynamic stability of the system. It is from these three profiles that the quality of the surface produced can be defined by ISO 4287.

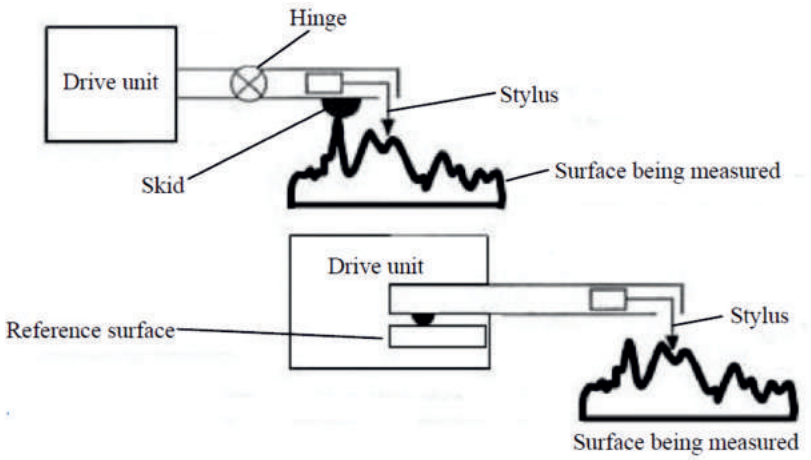

Figure 2.35: Schematic representation of skid and skidless roughness profilometers [82].

Surface roughness is typically a primary indicator of component quality, conventionally a field for mechanical engineers. Surface roughness can be characterised through a variety of technologies, but the most commonly employed are roughness profilometer, as shown in Fig.2.35 [82]. In accordance to the ISO 4288 standard, a 2D roughness profile is evaluated over a given length (ln) divided by 5 sample lengths (lr) dependant on the expected arithmetic centre line average (R_a) (μm).

$$R_a = \frac{1}{l_n} \int_0^{l_n} |Z(x)| dx \tag{2.8}$$

R_a is calculated from the average vertical distance Z over the ln as shown in Eqn.2.8. R_a, the most prominent roughness parameter, due to the ease of computation, is limited due to the insensitivity to local deviations. Other commonly employed measures include R_t, the maximum valley to peak height, which shows significant sensitivity to large deviations in roughness, see Fig.2.34b. This sensitivity can be reduced through the calculation of the average peak to valley of the largest 5 peaks over the ln R_z [82].

$$R_q = \sqrt{\frac{1}{l} \int_0^{l_n} Z^2(x) dx} \tag{2.9}$$

The root mean squared (RMS) roughness parameter (R_q) is more sensitive to low order deviations than R_q and is calculated by Eqn.2.9 [82]. Over recent years, the application of third and forth order measures have been used to characterise surface forms and found to be especially descriptive when considering the effect of roughness on fatigue performance [12, 40, 42, 83].

$$R_{sk} = \frac{1}{n} \sum_{i=1}^{n} (\frac{x_i - \overline{x}}{SD(x)})^3 \tag{2.10}$$

$$R_{ku} = \frac{1}{n} \sum_{i=1}^{n} (\frac{x_i - \overline{x}}{SD(x)})^4 \tag{2.11}$$

Skewness (R_{sk}), Eqn.2.10 and kurtosis (R_{ku}), Eqn.2.11 [82], enable classification of the isotropic nature of machined surfaces describing the shape, distribution and symmetry of the l_n [82].

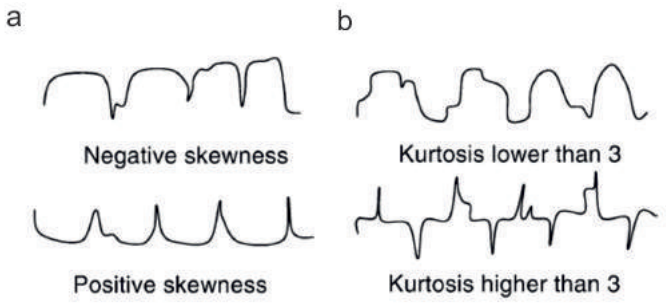

Figure 2.36: Schematic representations of a. a negative and positive skew and b. a kurtosis above and below the coefficient of 3 for machined surfaces [84].

Skewness can be considered to be a measure of asymmetry where a negative skew describes surfaces with a greater number of peaks or a full surface, where an empty

surface possesses many valleys where are positively skewed [82,83]. Surfaces characterised through the R_{ku} measurement can be described in terms of their sharpness of the distribution [82]. Surfaces with R_{ku} values below 3 can be thought of as having smooth peaks and are platykurtic in nature. Those with values above 3 are dominated with sharp peaks and are leptokurtic. R_{ku} values of zero describe normally distributed peaks or mesokurtic in nature. Representations of machined surfaces with the extremes of these high order measures can be seen in Fig.2.36 and have significant influence on tribology and wear behaviour of surfaces [84].

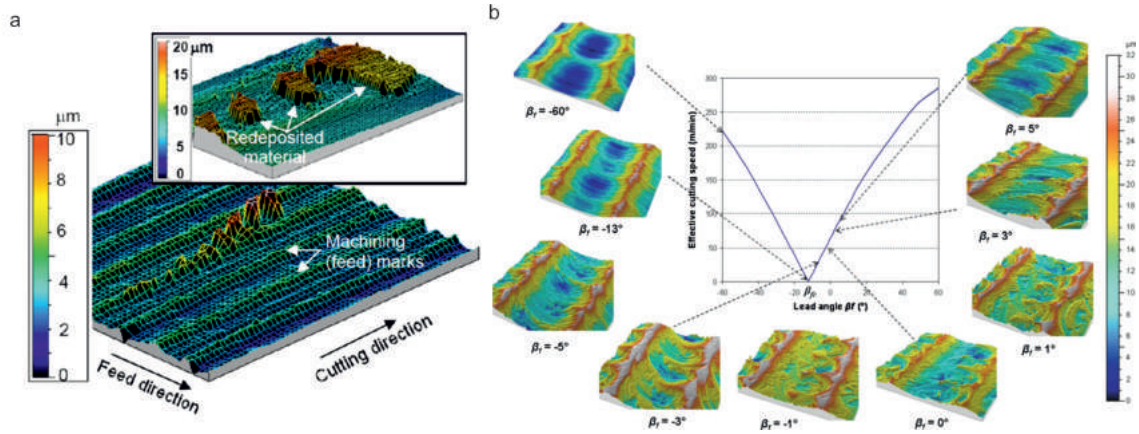

Figure 2.37: 3D light roughness representations of a. surface defects from turned Ti-64 [85] and b. the effect of lead angle during ball nose end milling of 25MnCrSiVB6 bainitic steel [42].

The aforementioned roughness parameters are all obtained from a 2D plane of the machined surface. This has limited application for complex processes, such as end milling and especially so when considering ball nose tools. Fig.2.37b shows how the variation of lead angle (Ψ_r) significantly affects the 3D surface roughness produced from ball nose end milling of a 25MnCrSiVB6 bainitic steel [42]. It can be seen that surface is affected significantly by Ψ_r, both in quantitative roughness [72] and qualitative topography. The mechanics of contact between a spherical tool and a flat surface produces complex contact radii, influenced by the elasticity of the respective materials [86]. The addition tool rotation produces a variation in D_e and contact radii, as discussed in Chapter 3 [72,86]. Fig.2.37b shows how at acute Ψ_r, the effective cutting speeds $V_{c_{eff}}$ is reduced to 0 m/min. Rather than inducing a cutting action, at these angles, the tool is dragged across the surface causing ploughing behaviour and inducing a poor surface finish. Methods for 3D surface characterisation also offer the advantage of producing a visible representation of the surface, introducing a higher level of understanding of machining marks and surface defects as shown in Fig.2.37a [42].

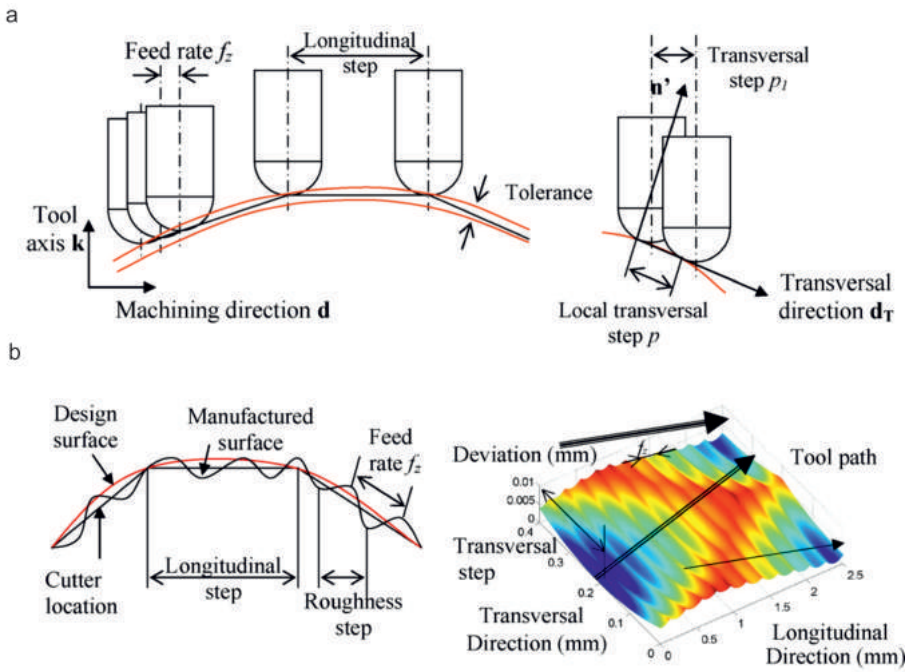

Figure 2.38: Schematic representations depicting a. the importance of 5-axis milling programming tolerances and b. the influence of programming tolerances on 3D roughness [87].

A determining factor of surface roughness from ball end milling is the accuracy of the machining strategy. Many aerostructural components utilise ball end milling to produce complex surfaces. Fig.2.38a and b show how the longitudinal and transversal steps influence the tolerance between the programmed tool path and the actual surface produced [87]. The machining strategy is characterised as a series of points in a co-ordinate system, within which movements are linearly interpolated [87]. These translations along the programmed path, influence the surface produced, in which a tighter tolerance results in improved surface roughness. The tolerance is subject to the accuracy of the numerically controlled (NC) programme produced on CADCAM software and the resolution of the co-ordinate system of the machining centre. Surface topographies and roughness in 3D can be accurately predicted for ball end milling in 3-5 axes, when NC tolerances, machining strategies and cutting parameters are known [72, 87, 88].

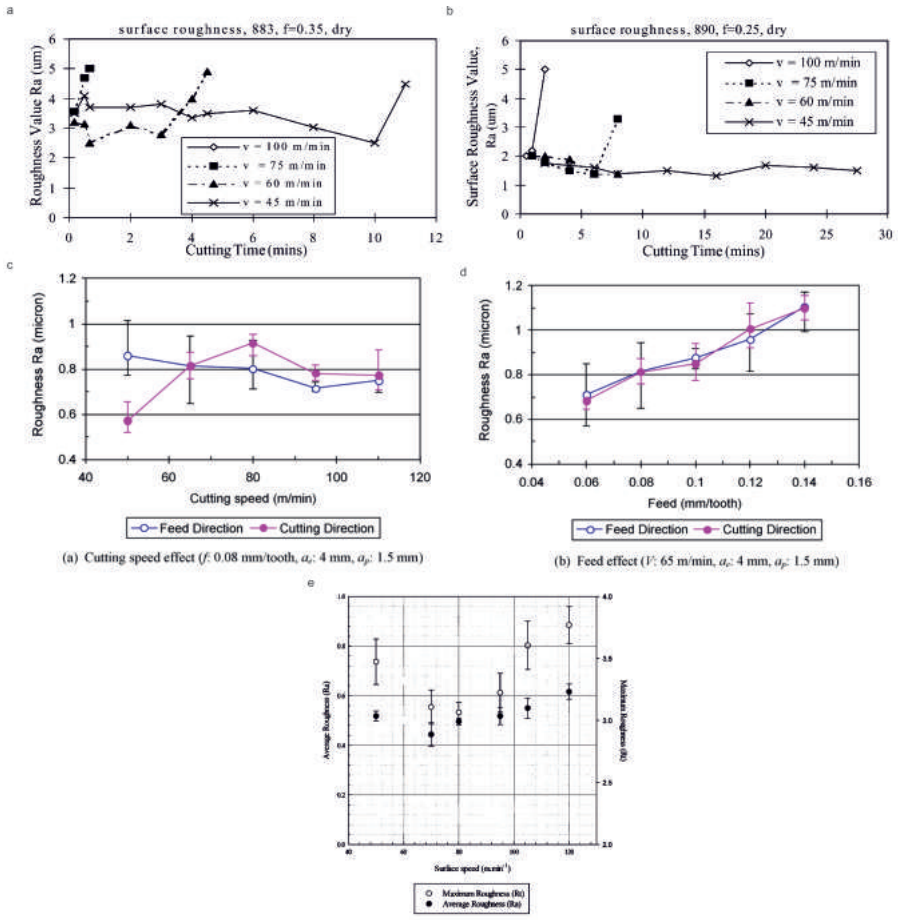

Figure 2.39: Investigations into the effect of V_c on R_a for feed rartes f of a. 0.35 mm/min and b. 0.25 mm/min for turning of Ti-6246 [31,34], the effect of c. V_c and d. f_z on R_a for end milling of Ti-64 [35] and e. V_c on R_a and maximum roughness R_t for turning of Ti-834 [22].

Cutting parameters including V_c, f_z and DOC have been proven to effect the surface roughness of machined high strength titanium alloys. An array of research presented in Fig.2.39, has shown for turning and milling of titanium alloys, these cutting parameters can produce increases in surface roughness measures to differing extents [22, 31, 34, 35]. The affect of cutting parameters have however proven not to be consistent over a range of materials nor cutting operations. It can be seen be comparing Fig.2.39a and c, for two different titanium alloys over a comparable range of V_c, the effect on R_a is significantly different [31, 34, 35]. In some cases the effect of increased V_c has been shown to have a minimal impact on R_a, see Fig.2.39c and e [22, 35].

$$R_a = f_z^{0.55} V_c^{-0.14} a_e^{0.28} \tag{2.12}$$

The effect of increased f_z has been proven to influence surface roughness considerably, as depicted in Fig.2.39d. Eqn.2.12 shows the weighting of specific cutting parameters influence on R_a, calculated experimentally for turning of Ti-64 over a range of V_c, f_z and DOC [35]. For an identical cutting environments of Ti-6246, at two different f_z, the results in Fig.2.39a and b highlight the influence of tool wear on surface roughness. At greater V_c, the rate of tool wear increases and the rate at which surface roughness deteriorates follows. This behaviour is exacerbated when the increased V_c is accompanied by an increased f_z, thus significant increase

in MRR the rate of tool wear and surface roughness deterioration is increased too. As previously discussed, with milling operations, the 3D nature of the surface must be considered. This fact is illustrated in the deviation in roughness measurements with respect to cutting direction, in Fig.2.39c and d [35].

2.3.2 Subsurface response to machining

The act of chip formation in Fig.2.32, depicts the mechanism behind subsurface deformation of workpiece material during machining. A variety of subsurface defects have been defined for machining of titanium alloys.

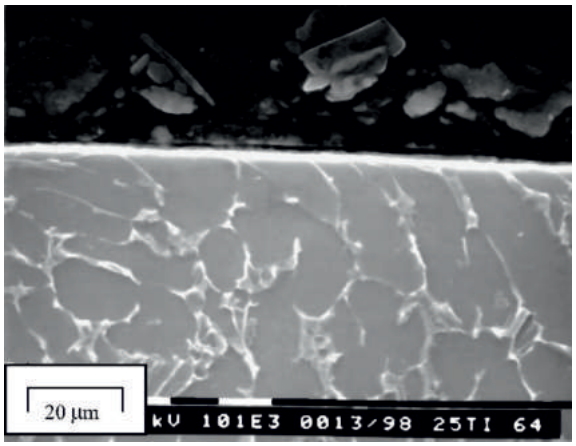

Figure 2.40: White layer formation from turning of Ti-64 [34].

Strain ageing as a result of machining often leads to the formation of a white layer, so called due to its appearance under light microscopy [85]. These white layers result in differing mechanical properties at the near surface to that of the bulk material and can influence the mechanical performance of components. Though less pronounced and severe when compared to the white layers induced in nickel superalloys, studies have found white layers to be produced in the upper 10-20 μm of the machined surface of Ti-6Al-4V [34]. White layers are potential crack initiation sites and can influence crack propagation. Therefore limiting the propensity for white layer formation is of great importance, in relation to in-service performance [85]. White layer formation is believed to be dependent on localised temperatures, plastic deformation and flank wear as a result of tool wear [85].

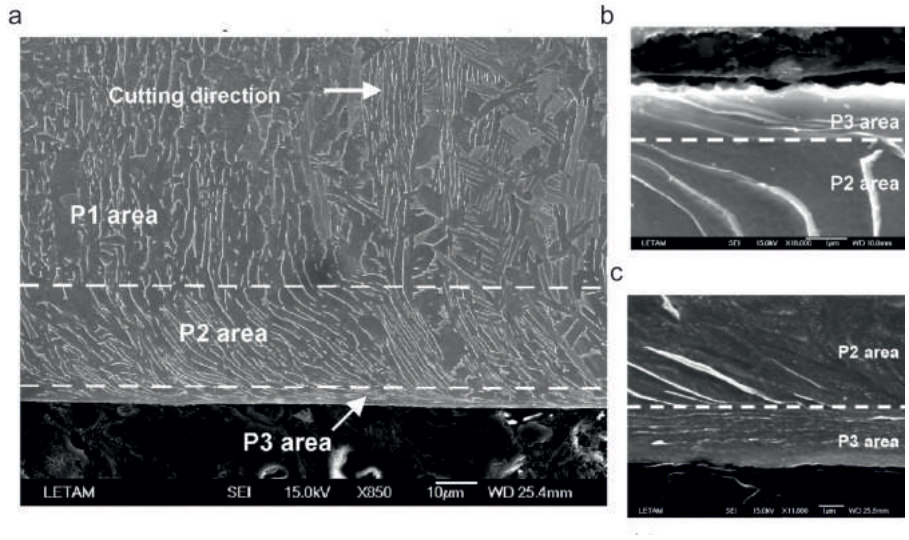

Figure 2.41: Subsurface microstructural alteration for orthogonal cutting of Ti-64 a. low magnification overview of regions 1-3 and regions 2 and 3 for V_c of b. 20 m/min and c. 260 m/min. [89].

Localised temperature and stress during cutting imparts strain into the material. The level of strain is dependent on the cutting conditions and the susceptibility to deformation or machinability of the workpiece material. Microstructural alteration and deformation as a result of machining operations have been a topic of research over the last few decades. Initial investigations focussed on simple characterisation operations, such as the grid technique, used to qualitatively identify the direction and magnitude of microstructural deformation [90, 91]. For titanium alloys, imparted strain is observed as microstructral alteration, as the softer β phase plastically deforms. The magnitude of stress required to produce this matrix phase distortion can be observed as region P2 in Fig.2.41 [89]. Below the boundary of this region, the imparted stress is not satisfactory to induce any observable plastic deformation, although elastic deformation could be imparted, the microstructure is representative of the bulk or material state prior to machining. In the near surface P3 region, Fig.2.41, the induced stress is significant enough to induce severe plastic deformation (SPD) in which elongation and distortion is evident in the brittle α_p phase [22, 89]. The direction of this elongation and distortion is relative to the cutting direction. The maximum resultant stress direction, which is 45°from the machined surface was determined from quick stop tests and examination of chip formation mechanisms [22, 92].

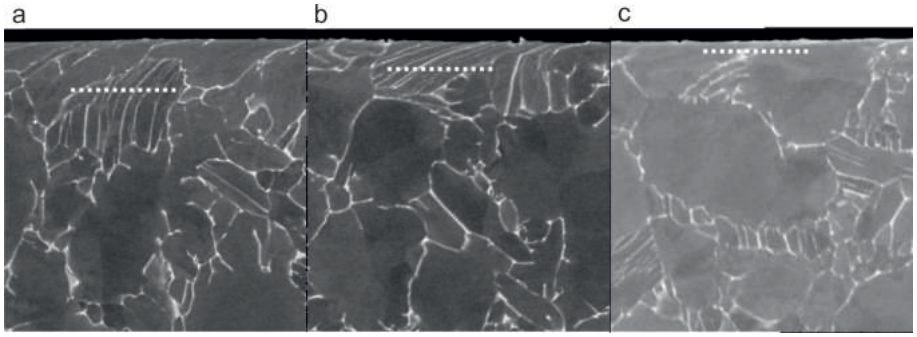

Figure 2.42: The effect of increased V_c on the depth of SPD from turning of Ti-834 at a. 50, b. 85 and c. 120 m/min [22].

The depth of this SPD layer for a given material is dependent on a number of factors and has been shown to vary with respect to cutting parameters. Fig.2.42 shows how the depth of the SPD layer decreases from 10 to 3 μm with increased V_c during turning of Ti-834 [13].The driving force for SPD in metal cutting is localised temperature and induced stress [93]. Induced stress, which is dependant upon the specific cutting parameters, tool condition and workpiece mechanical properties are related to dynamic cutting forces as discussed in Chapter 2.

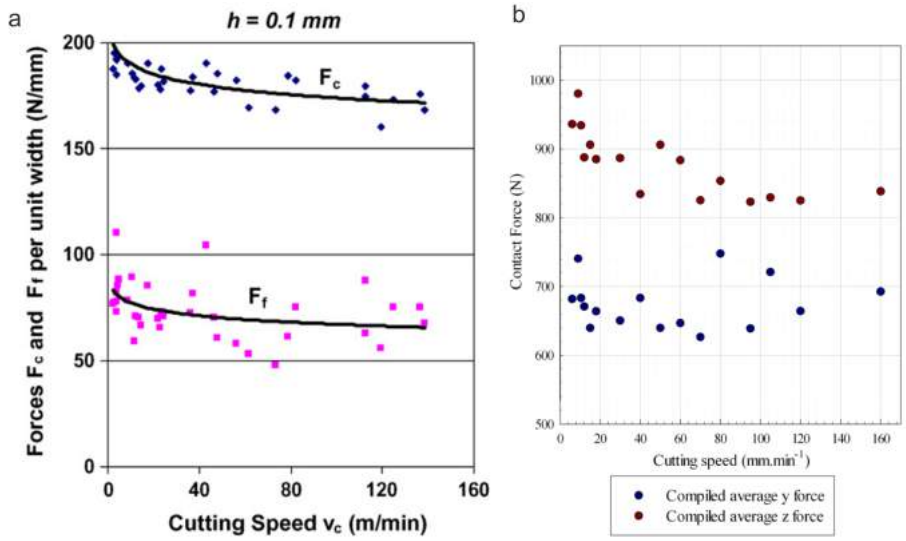

Figure 2.43: The effect of increased V_c on the average cutting force (F_c) and the feed force (F_f) in the Y and Z directions respectively for a. orthogonal cutting for Ti-64 and [94] b. turning of Ti-834 [22].

The influence of increased V_c on average cutting force (F_c) and the feed force (F_f) as shown in Fig.2.43, for orthogonal cutting of Ti-64 and turning of Ti-834 [22, 94]. It can be seen that after an initial decrease, above 40 m/min cutting forces plateau. This goes some way to explain the behaviour observed in Fig.2.42, in which the depth of SPD regions have limited susceptibility to increased V_c, as there is limited increase of induced stress on the workpiece. However, there is evidence that at high V_c, >80 m/min for turning of both Ti-54M and Ti-64, a further increase in specific F_f and F_c [95]. It is believed that this is due to the significant increase in flank wear at high V_c. It is postulated this would induce increased localised temperature and prevalence for SPD.

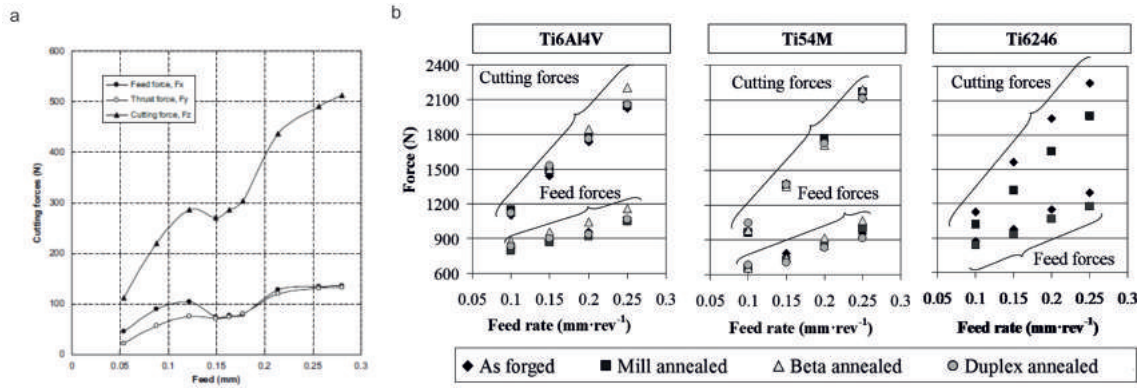

Figure 2.44: The effect of increased f on the average feed, thrust and cutting forces for a. dry turning of Ti-64 and [96] and cutting and feed forces for b. turning of Ti-64, Ti-54M and Ti-6246 [21].

A more distinct behaviour is observed when studying the effect of increased f on cutting forces, as shown in Fig.2.44. Several studies [20, 21, 96] have shown that cutting forces, especially the dominant (F_c) increase within increased f within moderate V_c during machining of titanium alloys. It has been discussed that the gradients represented in Fig.2.44b. for each alloy is indicative of the required shear stress to overcome yield and form chips [20]. A strong relationship exists between increased f and the increased (F_c), resulting from increased localised temperatures along with exacerbated tool wear rates [20]. This results in high susceptibility to deformation with increased f for titanium alloys.

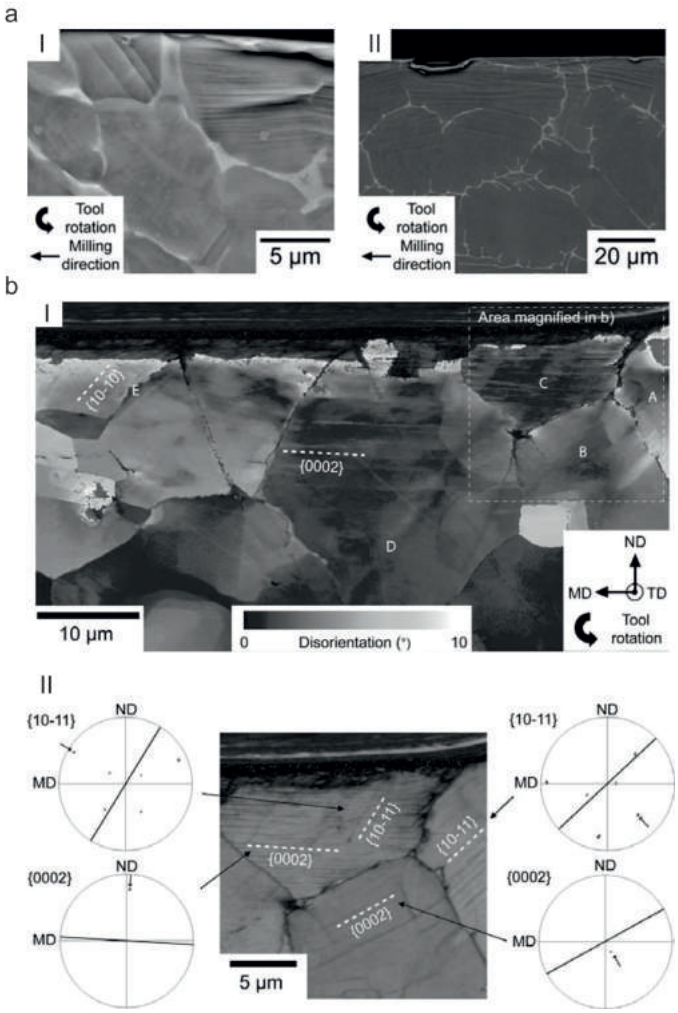

Figure 2.45: a. BSEI of dislocation slip bands formed from milling of i. Ti-64 and ii. Ti-834 and b. EBSD analysis of SPD in milled Ti-834 with i. a disorientation map and ii. slip trace analysis [14].

The aforementioned plastic deformation in some cases for high speed milling has been shown to be accommodated by titanium alloys as dislocation slip within the hard HCP α phase. Intense slip bands were formed during milling of both Ti-64 and Ti-834, as can be seen in Fig.2.45a [14]. Slip bands were identified to depths of 30 and 50 μm for Ti-834 and Ti-64 respectively, suggesting Ti-834 is less susceptible to plastic deformation for identical milling conditions [14]. Fig.2.45b.i. presents a disorientation band contrast map and ii. a slip trace analysis for a region of intense dislocation slip from milling of Ti-64 [14]. This result offers further evidence for the principle loading direction being 45°to the direction of cut. For milling of Ti-834, multiple slip systems were activated including {0002} basal and $\{10\bar{1}1\}$ pyramidal slip with associated Schmid factors of 0.5 and 0.46 respectively [14]. Activation of these slip systems is associated with the adiabatic heat generation during chip formation [14].

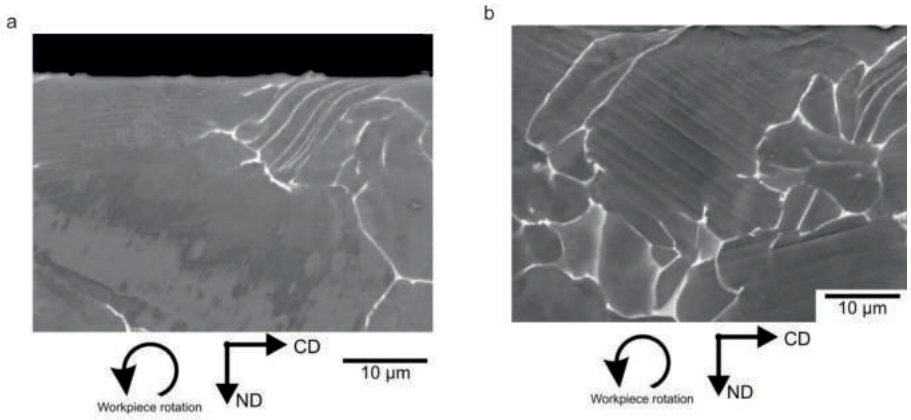

Figure 2.46: BSEI of dislocation slip bands formed from turning of Ti-834 at a. 80 m/min and b. 105 m/min [22].

Cutting parameters have been shown to influence the severity of these deformation modes. An investigation into turning of Ti-834 has shown how increased V_c can increase the propensity for dislocation slip activation [22]. At a V_c of 80 m/min, deformation was shown to be accommodated through lattice rotation, but at a V_c fo 105 m/min, the induced critically resolved shear stress (CRSS) has activated observed intense slip, Fig.2.46. It can be therefore inferred, in the same manner in which SPD and cutting forces can be increased at high V_c. The propensity for dislocation in titanium alloys can also increase with V_c.

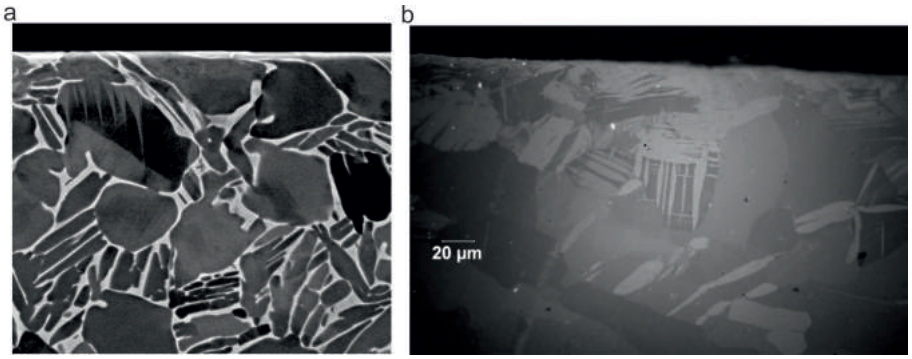

Figure 2.47: BSEI of deformation twins formed during a. turning of Ti-54M [22] and b. milling of CP-Ti [37].

From quick stop cutting trials, it has been shown that deformation twinning is induced during chip formation of CP titanium, parallel to the high shear strain direction within the deformation zone [74,93]. Deformation twins as a result of turning and milling of Ti-834 and CP titanium respectively, have been observed experimentally, see Fig.2.47 [22, 37]. For milling of CP titanium, increased V_c, increased the number and observable depth beneath the surface of deformation twins [37]. Above V_c of approximately 40 m/min, the depth of twins increased from 50 to 300 μm at which up to 40 x10^3 mm^3 twin density is present [37]. The increased imposed shear stress at higher V_c exacerbated the number and density of induced deformation twins for dry cutting conditions [37]. Again, supporting the influence of temperature on the activation of deformation mechanisms during machining of titanium alloys.

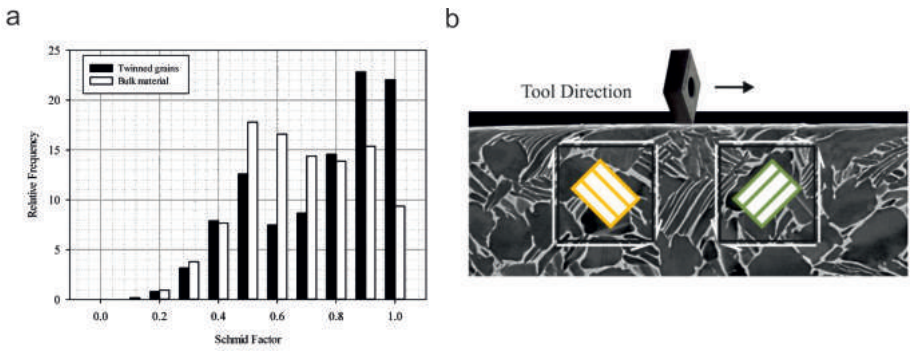

Figure 2.48: During turning of Ti-54M a. a schematic representation of the associated Schmid factors for bulk and twinned grains and b. a BSEI of deformation twins formed in the forward and backwards shear directions with respect to the cutting direction [22].

A detailed study into deformation twins formed during turning of Ti-54M determined the dominant observable twin mode to be of a tensile $\{10\bar{1}2\}$ type [22]. Fig.2.48a. is a representation of how the associated Schmid factors for twinned grains is greater than those within the bulk material, showing the high level of CRSS required to induce this type of deformation mode [22]. An interesting determination, which agrees with observed phenomena discussed previously, is represented in Fig.2.48b. It can be shown, for these tensile twins, those grains with their C-axes orientated at $\pm 45°$to the cutting direction, can have $\{10\bar{1}2\}$ twinning modes readily activated [22]. Mechanically induced twinning as a result of turning has also been observed in Ti-6242, Ti-54M ELA and Ti-575 [36].

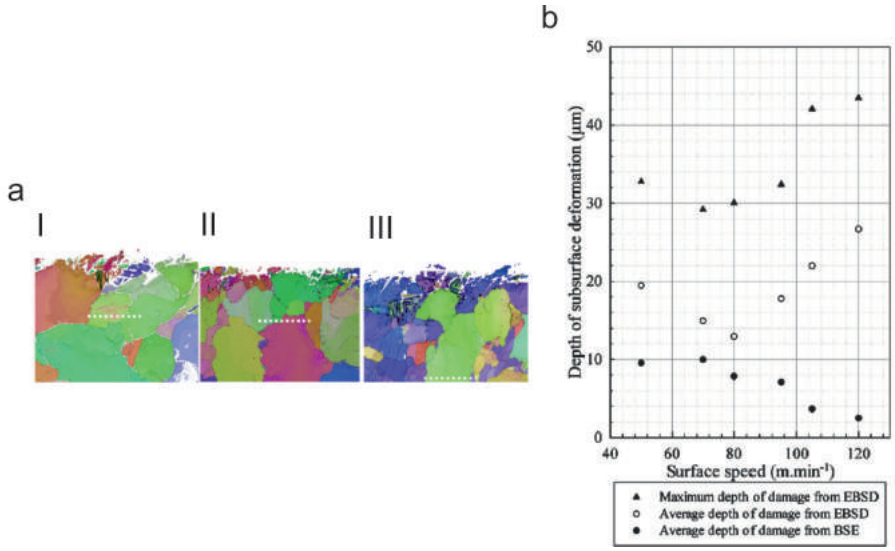

Figure 2.49: Observed maximum depth of deformation for turning of Ti-54M with a. an EBSD map at V_c of i. 50, ii. 85 and iii. 120 m/min when compared to b. observed deformation under BSEI [13].

Under BSEI, the observed depth of deformation decreases with respect to increased V_c, Fig.2.42 [13]. However, through the application of EBSD the true extent of machining induced deformation can be observed Fig.2.49a. It can be seen that the depth of deformation increases with V_c as demonstrated in Fig.2.49a)i-iii); 50, 85 and 120 m/min respectively, this result is summarised graphically in Fig.2.49b. [13]. Advanced materials characterisation techniques like EBSD, offer a greater level of

detail and insight into the true extent of deformation than those conventionally employed for analysis of machined material [12]. The results depicted in Fig.2.49b emphasise this fact and agree with the observations described in Fig.2.41 [89]. The measurements of region P2 in Fig.2.41 are as a result of accurate assessment of band contrast which is susceptible to the extent of deformation. SPD observed in zone P1 can also be identified as region unable to be indexed during EBSD analysis [89].

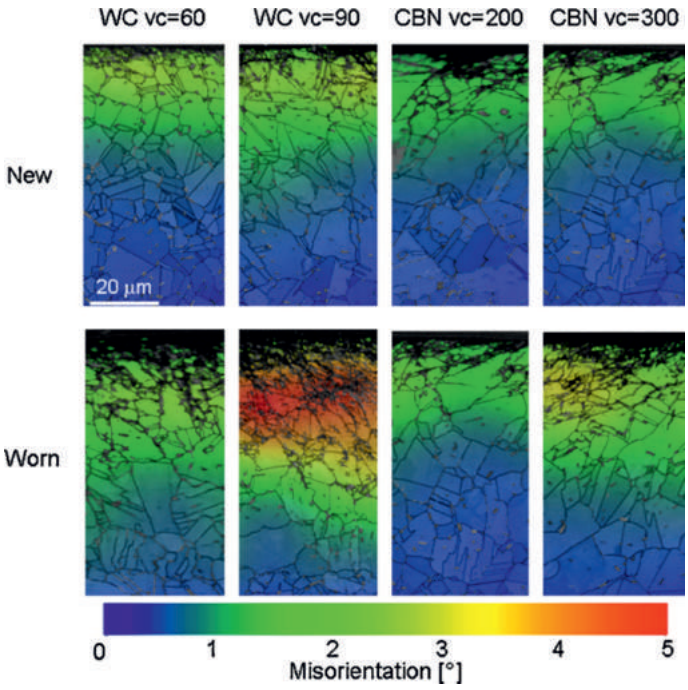

Figure 2.50: Strain misorientation contour plots for new and worn inserts at a range of V_c for turning of Inconel 718 [38].

EBSD techniques can also be used to visually represent and understand in detail, the imposed strain within the subsurface of a range of materials subject to changes in cutting parameters. Fig.2.50 shows the effect of increased V_c and tool wear on the deformation during turning of Inconel 718 [38]. These strain contour plots utilise the average intergrain misorientations (AIMS) that can be calculated for any array of points at a given resolution, over an analysed area. It can be seen that the induced strain is larger and to greater depths through the use of worn tools and at higher V_c. This SPD is localised to the near surface [38].

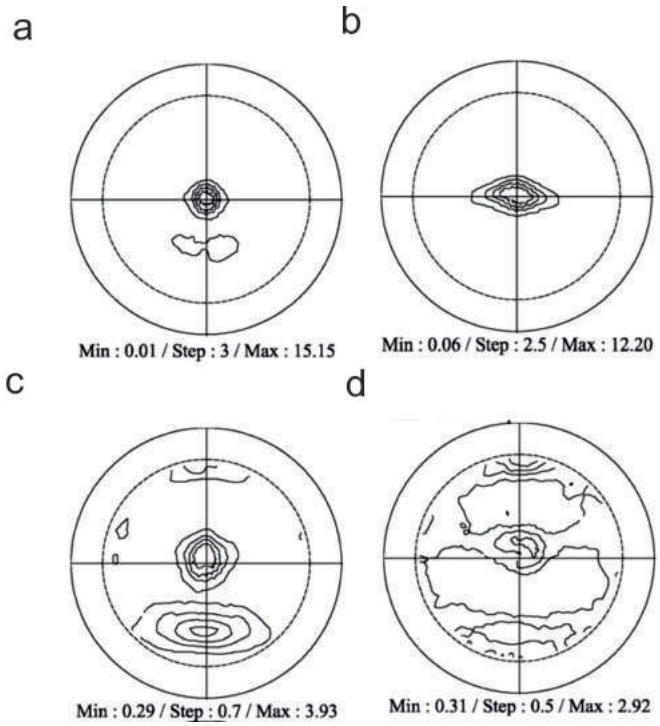

Figure 2.51: Pole figures of the $\{0002\}\alpha$ phase for turning of Ti-64 at V_c of a. 20, b. 100, c. 260 and d. 660 m/min [89].

The effect of increased V_c can be further interrogated through the use of pole figures as shown in Fig.2.51. As the V_c is increased, the disorientation increases and a tilt of the plane towards the direction of cut is observed, effecting the resultant texture of the subsurface [89].

2.3.3 Machinability

Detailed studies into the response to machining for Ti-5553 is limited to date. Some studies of machinability when compared to ubiquitous alloys such as Ti-64 have been conducted. The measure of machinability varies from source to source and is highly dependent on the principles of operation. Many use tool life, surface finish, chip morphology, power consumption and cost as measures of machinability, with no current standard dominating academia and industry [24, 27, 97]. The machinability of Ti-5553 has been reported to be lower than that of Ti-64 and another β alloy, Ti-10-2-3 [24, 98, 99]. When comparing the maximum cutting speed for a given tool life Ti-64 outperformed Ti-5553 [24]. It can be said that the machinability of Ti-5553 is 56% of that of Ti-64, with fellow beta alloy Ti-10-2-3 possessing an estimated 87% machinability when compared to Ti-64 [24, 99]. It was predicted this would be evident due to the thermal, mechanical and metallurgical properties of Ti-5553 [24]. The increased composition of β phase forming Mo present in Ti-5553, leads to an increase in hardness and strength when compared to Ti-64 [24]. Alloy chemistry has been shown to play, potentially, a significant role in machining performance of titanium alloys. The role of Mo-equivalence has been shown to influence the respective cutting and feed forces during turning trials and thus will affect the amount of observable deformation [36].

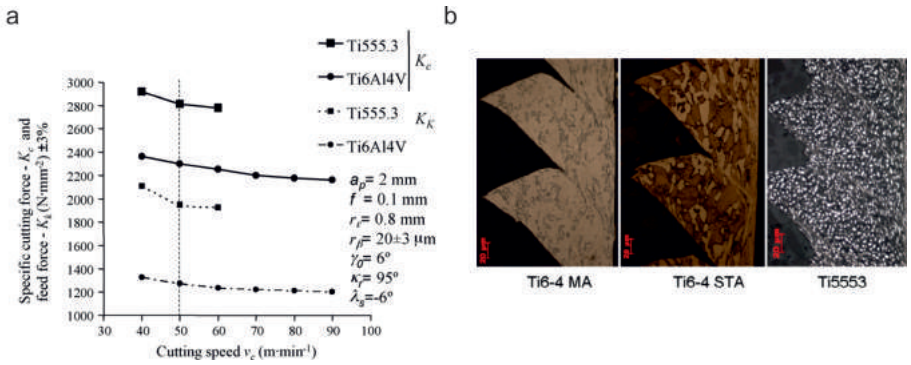

Figure 2.52: A comparison between the influence of Ti-64 and Ti-5553 on a. specific cutting forces [24] and b. chip segmentation [20] during turning.

Under identical cutting conditions during a turning trial, Ti-5553 exhibited significantly higher cutting forces when compared to Ti-64, see Fig.2.52a. [24]. The same behaviour was observed when comparing Ti-5553 to other alloys under identical turning trials [20,36]. Under identical conditions, Ti-5553 was found to produce the highest specific cutting forces over Ti-54M, Ti-10-2-3 and Ti-17 [20,36]. Another key factor in machinability is chip formation, be it the ease of chip formation and the strains associated with the process or the geometry of the chip itself. As can be seen in Fig.2.52a Ti-5553 readily forms serrated chips with a high density of shear bands. This phenomena is also more prevalent at lower V_c than Ti-64 [20, 24]. Infact, at 50 m/min the frequency of shear band formation was between 50-80 Hz for Ti-5553 compared to 30-40 Hz at 90 m/min for Ti-64 [20,24,99]. Formation of higher density shear bands within a chip is evidence of greater and higher fluctuations in cutting forces which leads to higher levels of tool wear and temperatures at the cutting edge, all of which are evidence of lower machinability [24,99]. Shear strain is present mostly in the shear bands within serrated chips [100]. Shear strain has been found to be proportional to material removal rate, therefore it is logical to assume that at higher V_c and f_z, shear strain and shear band formation would increase. Meaning metastable β alloys like Ti-5553, have reduced machinability at higher material removal rates [100]. This goes some way in explaining the effect of work hardening rates on the machinability of titanium alloys. It is clear that the metallurgical and microstructural differences between alloys with differing machinability is key to understanding and potentially improving performance under cutting. Limited proprietary data is available for the elastic, plastic and thermal properties of Ti-5553. The data that is available shows that the strain hardening exponent (n), thermal conductivity (at 20C, W/m-k) and heat capacity (J/g-C) are all higher when compared to that of Ti-64; 0.2, 4.78 and 0.628 respectively [18, 24, 98, 99, 101, 102].This also supplies supporting evidence to the explanation of why Ti-5553 shows lower machinability than Ti-64.

2.4 Tool wear analysis

2.4.1 An Introduction

Machinability is one of the key characteristics limited the widespread adoption of β titanium alloys throughout wider applications in many industries [16]. Machinability is a complex measure to qualify and define, an overarching metric across academia and industry is tool wear [27]. Tool wear is a limiting factor in machining as tool

wear degradation has a significant influence on component integrity and influences economic decisions for industrially machining processes. Tool wear can be broadly defined as the degradation of tool geometry through contact with the workpiece material during machining [97].

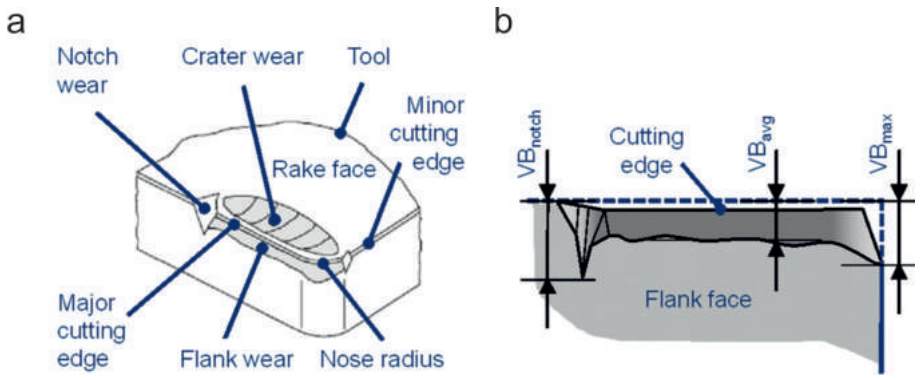

Figure 2.53: Schematic representation of a. typical tool wear regions of a turning insert and b. flank wear measurement principles [103].

Characterisation distinguishes typical regions of wear, some of which are identified in the schematic representation of a generic turning insert in Fig.2.53a. The most widely adopted metric of tool wear is Flank wear, the principle of which can be seen in Fig. 2.53b. Flank wear results from contact with the machined surface, the degradation of which can be easily characterised through basic light microscopy techniques. Existing ISO standards, for example, 3685, have been utilised for decades to quantify and monitor flank wear [97]. The flank wear land (VB) is measured against a predetermined maximum (VB_{max}), typically 0.4 mm, at which the tool is classified as worn. This is typically determined experimentally at the point at which surface roughness deteriorates [97]. This measure is used extensively in literature [26, 33, 95, 104–106].

Figure 2.54: 3D light micrograph of crater wear as a result of turning Ti-6Al-4V at 80 m/min [95].

Another widely adopted tool wear parameter is crater wear as the rake face wear region identified in Fig.2.53a and found experimentally from turning of Ti-6Al-4V in Fig.2.54. The extent of crater wear is measured through light microscopy (KT) as is a result of contact and evaluated temperatures between the rake face and chip formation [97]. This measure is used significantly in literature [26, 95, 104, 107, 108].

Under certain circumstances severe friction between the newly formed chip and tool rake face under high heat can cause welding and subsequent build-up of workpiece material along the cutting edge [97]. The material subsequently fractures

from the tool surface and can typically be redeposited onto the machined surface negatively influencing surface roughness [97].

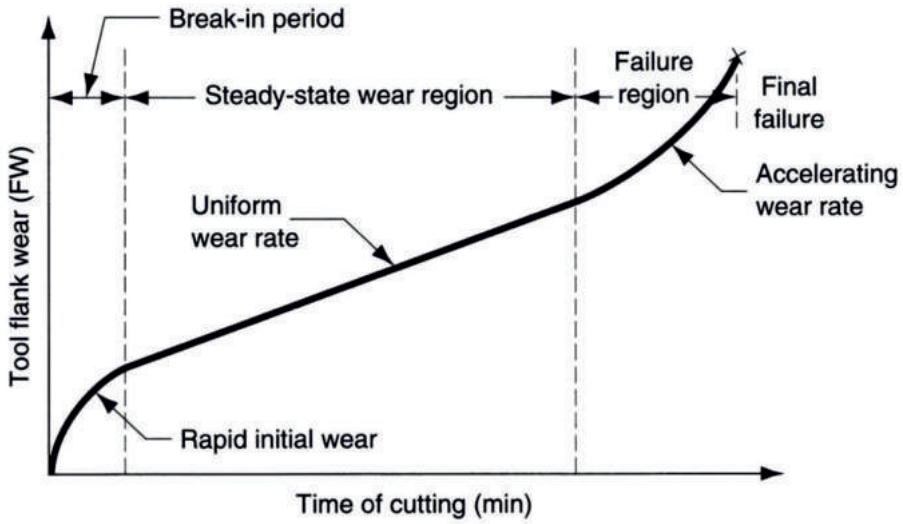

Figure 2.55: Conventional tool wear profile for flank wear against time [109].

The aforementioned tool wear metrics can be assessed over durations of cutting to produce tool wear or tool life profiles, a method employed for several decades since first defined in literature [109]. A typical tool wear profile is shown in Fig.2.55 in which after an initial rapid increase, wear rate becomes stable [97,109]. This steady state wear is utilised in manufacturing to determine safety factors in tool life. Comparable tool wear profiles have been produced experimentally in literature for a range of alloys, tools and cutting processes, [26, 27, 108, 110, 111]. The wear regions summarised in Fig.2.53 are driven by a number of wear mechanisms. Flank wear is produced through the mechanism of abrasive wear in which contact between the tool and machined surface gradually removes material from the tool [97]. Crater wear is typically driven through a diffusive mechanism as a result of elevated temperatures promoting the diffusion of atoms across the tool chip interface [97]. Detailed study into the response of diffusive wear mechanisms for a range of aerospace titanium alloys has been studied through static diffusion couples in literature [112, 113]. Diffusion of Cobolt to depths of 30 μm was found to form the embrilttling η phase [112] and subsequent subsurface deformation of the workpiece material [113]. Adhesive wear mechanisms in which fragments of workpiece material are adhered to the tool surface resulting in BUE are prevalent at low cutting speeds and high surface temperature [97]. In actual machining processes, multiple mechanisms typical occur resulting in various wear regions being produced.

2.4.2 Influence of Machining

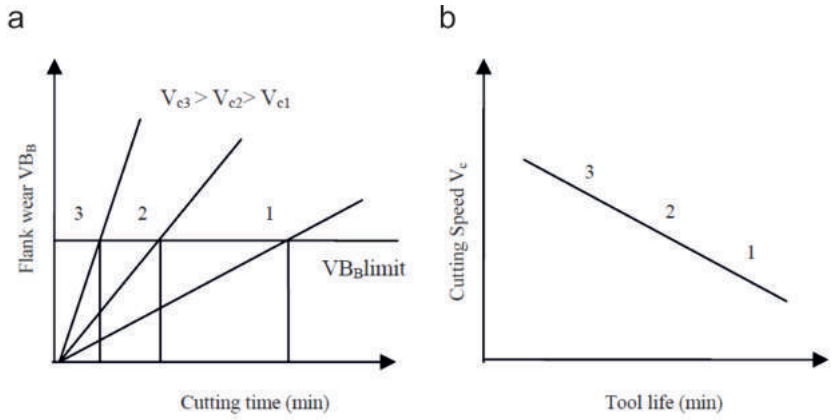

Figure 2.56: Schematic representations of the Taylor tool life model for increased V_c for a. flank wear limits and b. against tool life [68, 97, 109].

The drive for ever increasing machining rates has a subsequent and substantial effect on tool wear. It has been shown V_c has a linear relationship with tool life. The time dependency of this wear can be modelled through the Taylor's tool life formula, Eqn.2.13 and represented visually in Fig.2.56.

$$V_c T^n = C \tag{2.13}$$

Increasing V_c reduce stool life (T) for a range of materials and cutting processes with respective constants (n and C) for constant f_z and depth of cuts (a_p). Subject identical cutting processes, at constant f_z, this behaviour has been observed experimentally in literature for Ti-6246 [26, 31] and Ti-64 [105, 108]. Comparable reductions in tool life is observed for increased f_z at V_c, which has been studied experimentally in research but less considerably, [31]. The reduction in tool life for increased f_z is due to increases in localised temperatures and cutting forces.

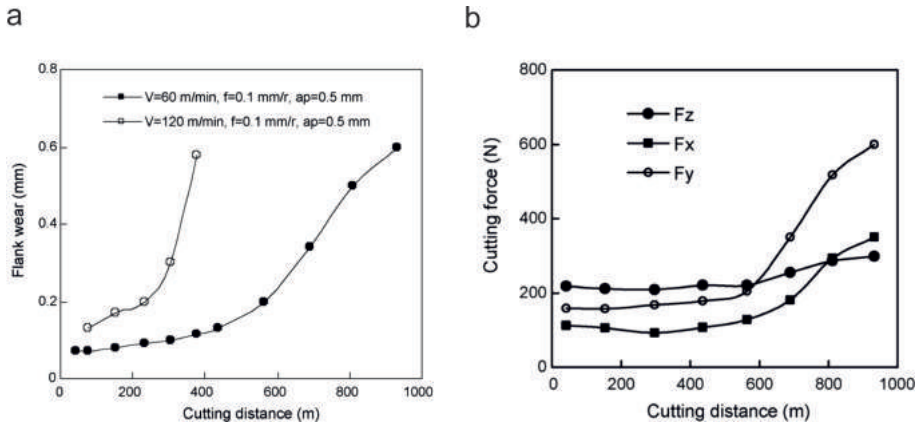

Figure 2.57: Schematic representations of a. tool wear for dry turning of Ti-64 for increased V_c and b. the effect of tool wear on cutting forces [108].

Increased tool degradation increases cutting forces during machining, as is depicted by Fig.2.57. As the volume of tool material removal increases, localised temperatures inducing diffusional wear and adhesion of workpiece material. This in turn increases localised friction and cutting forces [108]. This behaviour is accelerated once hardened coatings typically applied to tool substrate material is removed

via abrasion. One notable method for limiting tool wear is through the application of coolant or lubrication to the tool-workpiece interface. A range of coolant technologies including dry, flood, mist, oil and cryogenic have been investigated for a range of cutting conditions and aerospace materials [29, 108, 110, 114]. Flank and crater wear have been found to be reduced in many circumstances through increased coolant delivery and cryogenic cooling due to reduction in localised temperatures and diffusive mechanisms.

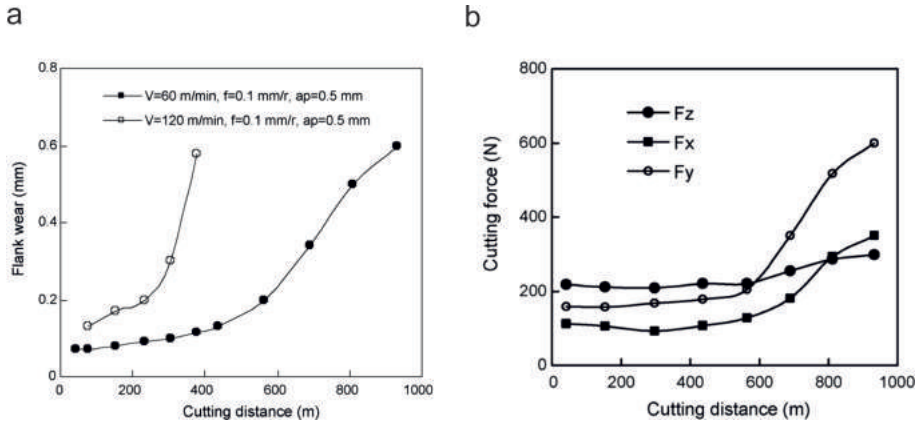

Figure 2.58: Schematic representation of flank wear over a range of V_c for Ti-5553 and Ti64 [24] and b. BSEI of worn inserts after milling of Ti-5553 [20].

Under identical cutting conditions, alloys possessing superior mechanical properties as a result of their respective chemical composition and thermomechanical processing produce increased tool wear. Flank wear for turning of Ti-6246 reached substantial values at lower V_c than that of Ti-64 and Ti-54M [21]. The same behaviour is observed for the alloy under investigation in this thesis, Ti-5553. For identical turning operations Ti-5553 presented crater, flank and notch wear at lower V_c than Ti-64 [24]. Face milling inserts characterised through BSEI in Fig. shows evidence of adhesive wear mechanisms for Ti-5553, more pronounced than comparable conditions for Ti-64, leading to eventual tool fracture [20]. Under chemical analysis, this was found to be Ti-C in nature, formed from contact with the PVD coating of the milling inserts [20]. Higher temperatures and friction recorded during cutting as a result of the chemical and mechanical composition of Ti-5553 is responsible for this behaviour [20].

2.4.3 Effect on surface integrity and subsurface microstructure

Increased cutting parameters have been shown to influence tool wear rates as a result of increased temperatures, cutting forces and friction. It is rational to infer from this, that increased tool wear will play a pivotal role on surface integrity and subsurface microstructures.

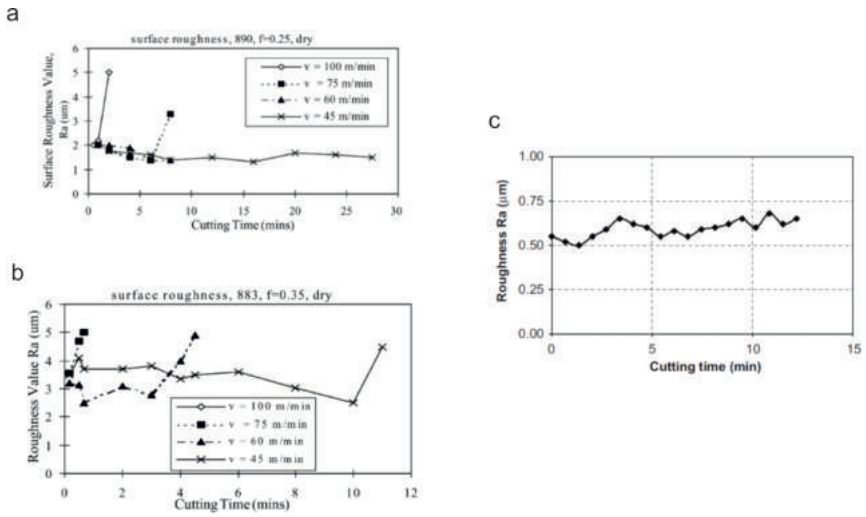

Figure 2.59: Schematic representations of the effect of a & b. V_c and f_z over time on surface roughness for turning of Ti-6Al-4V [31, 34] and c. tool wear on surface roughness for milling of Ti-6242S [29].

Research has been conducted into various cutting conditions and titanium alloys with subsequent surface condition inspected through 2D roughness profiling, Fig.2.59 [29, 31, 34]. A study into dry cutting of Ti-64 showed how increased V_c and f_z produced increased R_a values [31,34]. At low V_c a reduction in surface roughness was observed at long durations of cutting. This was determined to be due to deformation of tool flank faces which increased adhesion of material from the workpiece surface [29, 31, 34]. A study into dry milling of Ti-6242S showed how over the duration of cutting trials a gradual increase in R_a was observed [29]. In some cases, initial reductions of roughness was observed, after this point it was observed coatings were removed through abrasive mechanisms and increases in roughness correlated with increased tool wear [29].

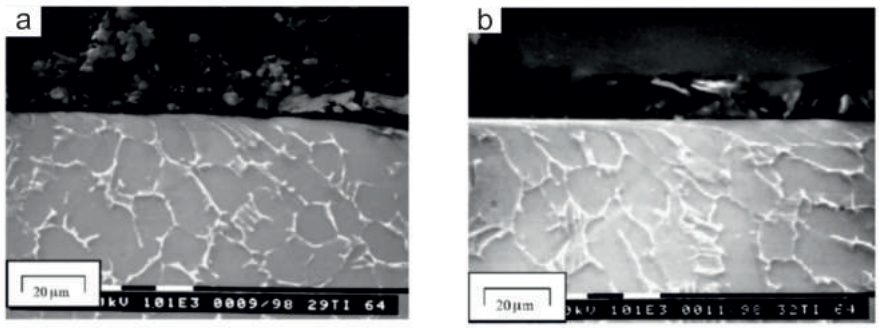

Figure 2.60: BSEI of Ti-6Al-4V subject to turning after a duration of a. 10 seconds and b. 12 minutes of cutting [34].

The same research showed how increased tool wear resulted in significant microstructural alteration to subsurface material. Prolonged use of worn tools induced severe plastic deformation, induced work hardening of near surface material and elongation of grain structure with respect to the tool motion direction, Fig2.60 [29, 31, 34].

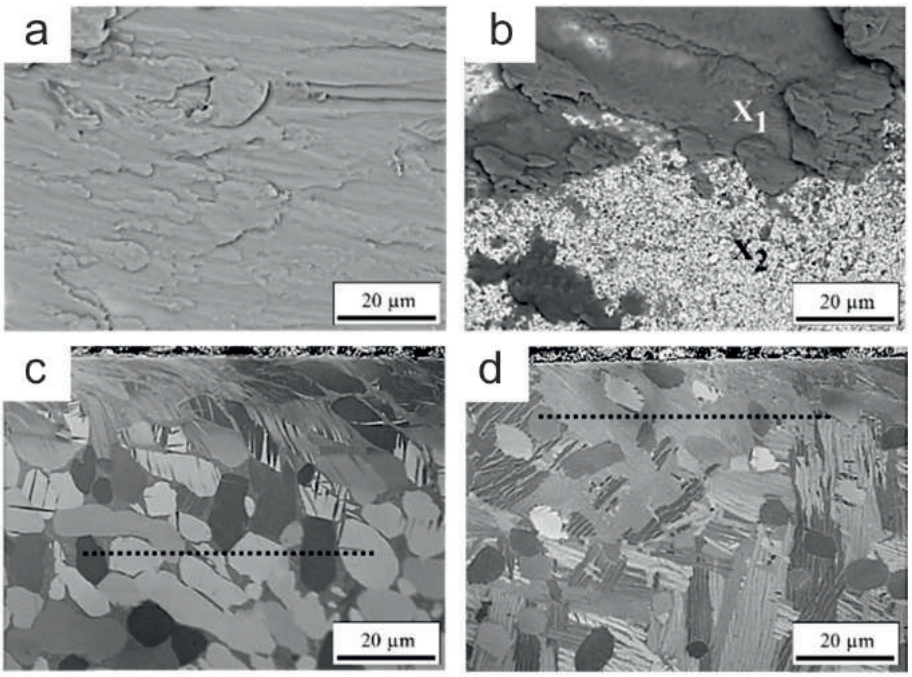

Figure 2.61: BSEI of a & c. Ti-54M tool rake faces and subsurface respectively and Ti-6246 tool rake face and subsurface, respectively [113].

Limited work exists in literature that investigates the influence of wear mechanisms and the response of machined materials. This behaviour is extremely difficult to characterise due to the great number of influential factors such as, chemistry, cutting parameter and temperature and in-depth array of techniques required to accurately characterise this behaviour. The complexity of this relationship can be seen in Fig.2.61 [113]. Tool wear is seen to be more pronounced for turning inserts used for machining of Ti-6246 (ref). When compared to that of Ti-54M, but transversely, less induced deformation is observable Fig.2.61 . A behaviour resulting from both the respective β phase fraction and subsequent mechanical properties but the rates of diffusion wear and eventual adherence of workpiece material [113].

2.5 Fatigue

2.5.1 An introduction

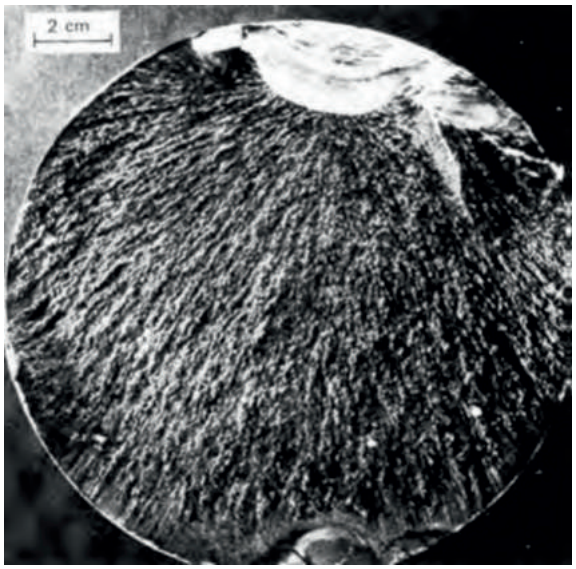

Figure 2.62: Photograph depicting a typical fracture face for fatigue failure [115].

Fatigue, the gradual deterioration of material structure through the application of cyclic stress, below that of the yield strength, is of significance for the design considerations and in-service performance of aero-structural components [115, 116]. Fatigue induced damage is often extremely difficult to detect in service, therefore, prediction is critical. A typical fracture face of metal failed through fatigue is presented in Fig.2.62 [115]. From this, striations can be clearly seen, distinguishing the path of fatigue crack propagation from the localised origin at the outer edge of the cross section. From this boundary, a fibrous texture respective to that of rapid failure presents itself across the majority of the sample, see Fig.2.62 [115]. Conventional fatigue failure initiates at features, both geometric and microstructural, that produce local stress concentration [41,115–119]. As dislocations pile up within these localised regions, coalescence leads micro-cracking, [51].

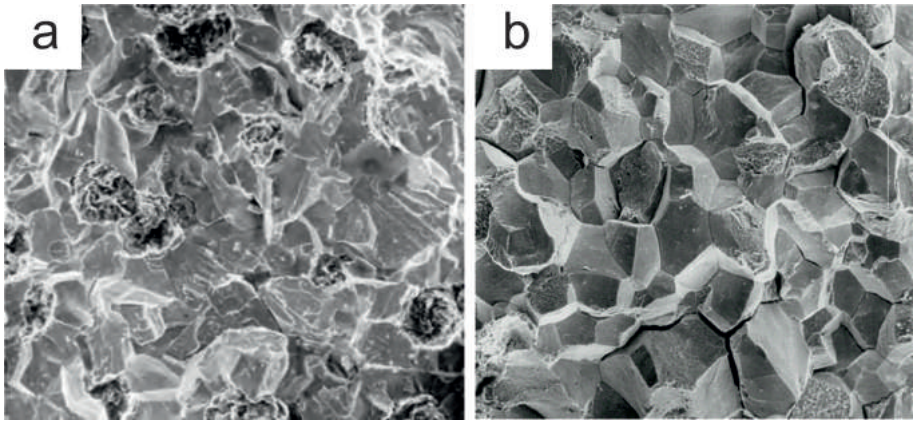

Figure 2.63: BSEI micrographs of a. transgranular and b. intergranular [115].

Fatigue cracking can be brittle or ductile in nature, dependant on the respective material's mechanical and chemical properties. Brittle cracking can propa-

gate through the subsurface of the material in either a transgraunlar or intergranular manner, being through the grains or along grain boundaries, as shown in Fig.2.63 [115].

$$\frac{da}{dN} = C\Delta K^m \tag{2.14}$$

Once these cracks grow to a size greater than that of a single grain, fatigue crack propagation commences [115]. This stage of fatigue failure, for many metals, produce a incremental crack growth rate than has been modelled through the Paris Law, as defined in Eqn.(2.14), [115, 116]. This stable crack growth region is dependant upon material constants c and m, determined experimentally [115]. Upon a given fatigue crack reaching a critical crack length, the size which a given material can no longer sustain, catastrophic fracture is produced. To design against this, it is imperative, for a given material, the cyclic fatigue behaviour can be modelled against applied stress. This is achieved through lengthy experimental programmes to produce SN, applied stress amplitude (S) against the natural logarithm of cycles to failure. Cyclic fatigue behaviour is often categorised by either low cycle or high cycle fatigue, distinguished by those materials statistically susceptible to failure above or below 10^4-10^5 cycles to failure [115, 116].

2.5.2 Fatigue in titanium alloys

Titanium alloys are often utilised in aerospace applications for their corrosion resistance and improved fatigue performance [18]. This is especially the case for β alloys, noted for their high strength and advantageous duplex microstructures resulting in improved fracture toughness [19].

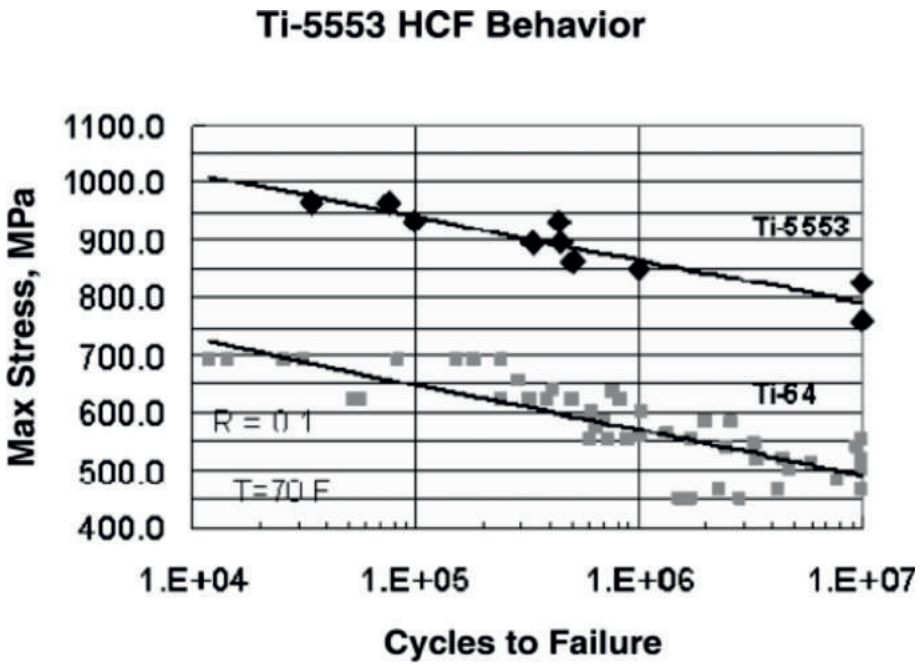

Figure 2.64: Schematic representations of the difference in HCF between Ti-5553 and Ti-64 in the hot isostatically pressed (HIP) and mill annealed condition [47].

The schematic representation in Fig.2.64 shows, for the hot isostatically pressed (HIP) mill annealed condition, the improved HCF performance of Ti-5553 over Ti-64 [47]. The combined influence of increased tensile strength, fracture toughness,

as a result of increased ageing and excellent ductility produced by the β matrix phase, are attributed to this improved performance [47, 120]. The presence of the fine, globular and evenly dispersed α_p acts as crack inhibitors limited the ability for crack propagation and eventually fatigue failure [18, 19, 47]. Therefore, chemistry and thermomechanical processing is seen to heavily influence fatigue mechanisms and subsequent fatigue life [121].

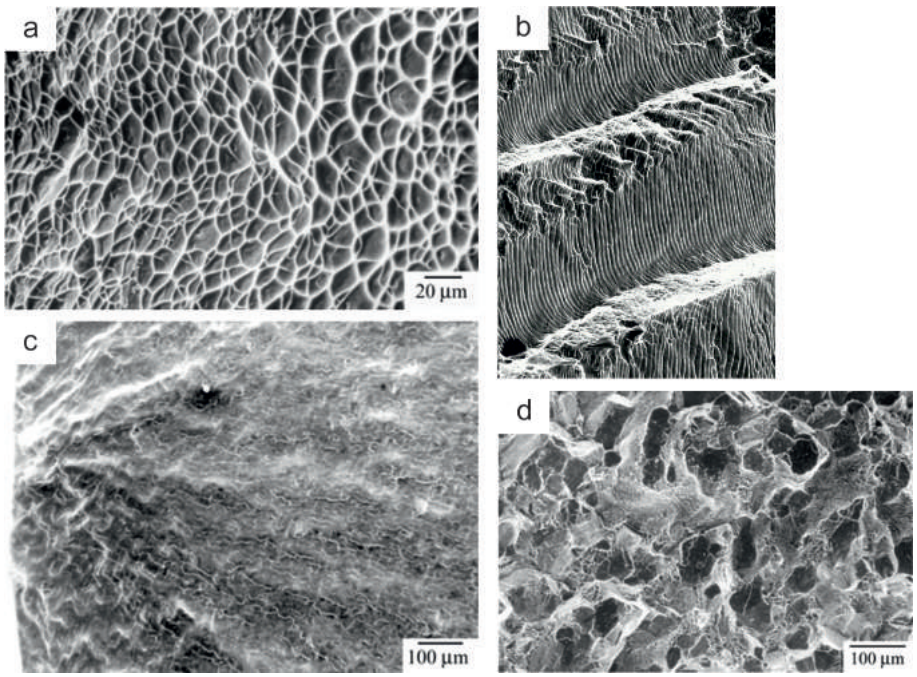

Figure 2.65: Light micrographs of a. equiaxed, ductile dimples, b. brittle fatigue striations, c. localised crack initiation and d. mixed mode failure presented from a range of titanium alloys [116].

The complex range of duplex microstructures, chemical distribution and variation in grain size will exhibit themselves in an array of fracture features as presented in Fig.2.65 [122]. The influence of ductility on fracture is present by the equiaxed dimples in Fig.2.65a. The size and orientation of such features goes some way to distinguish the local orientation of failure. The micrograph in Fig.2.65b, presents distinct striations typical of cyclic fatigue within a brittle α rich region, in which the number and spacing of these striations is manifested by the number of cycles experienced by the local material [122]. Mixed, ductile and brittle modes of fatigue failure are presented in Fig.2.65d, in which α precipitates present brittle cleavage within the fibrous ductile failure of the β phase [122]. The region in micrograph Fig.2.65c, is distinguished as the local crack initiation site, from which rivermarks identify the direction of initial crack propagation [122].

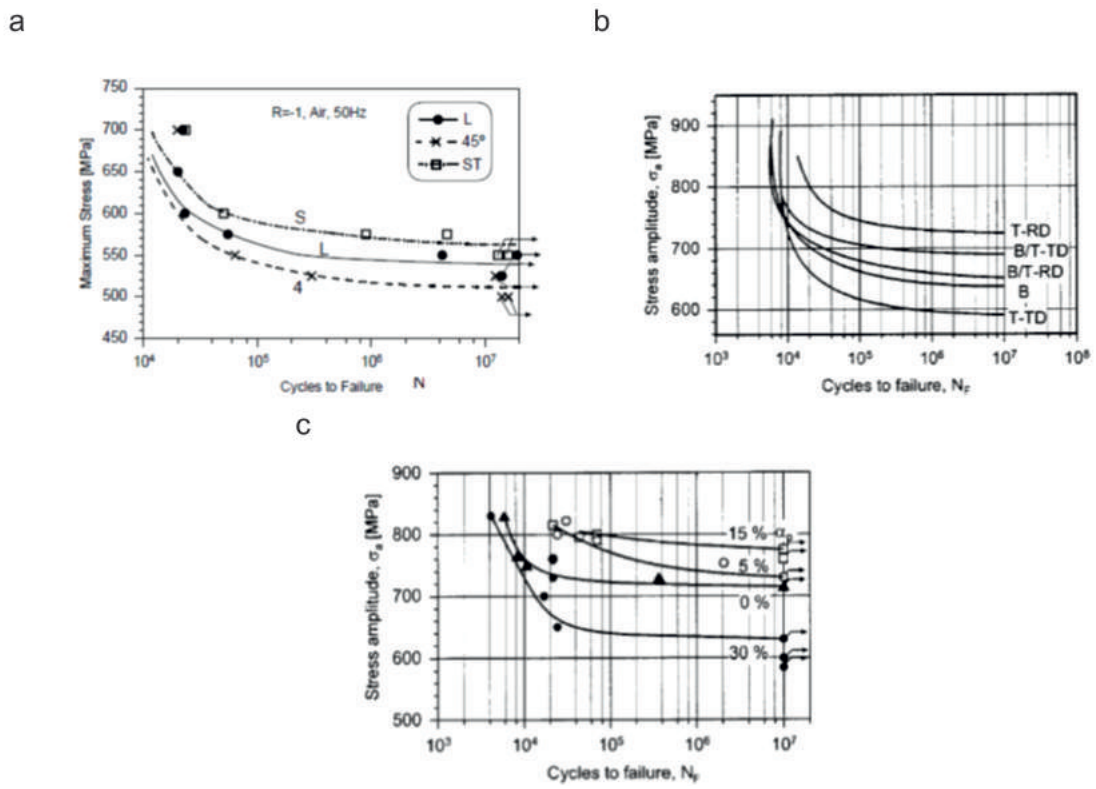

Figure 2.66: Schematic representations of the influence a. grain orientation, b. thermomechanical processing and c. microstructure on fatigue performance of titanium alloys [19].

The fatigue life of β titanium alloys, as presented in Fig.2.66 [19], as SN plots, are subject to numerous influential factors. The fatigue life of β-CEZ at R=-1 is presented in Fig.2.66a, is shown to be influenced by the respective orientation of the rolling direction and the applied stress. From this, the 45°exhibited to lowest fatigue life [19]. The driving force for this behaviour is believed to be the critical slip directions present in elongated β grains, respective to the applied stress direction [19]. Comparable behaviour is observed for the crystallographic orientations, as a result of thermomechanical processing, with respect to applied stress, for Ti-64 in Fig.2.66b [19]. Fig.2.66c, presents the influence of microstructure, namely, α_p volume fraction on fatigue life, in turn a result of chemistry and thermomechanical processing [19]. Improved fatigue life is achieved with reduced α_p volume fraction, which is believed to be due to the reduced presence of grain boundary α, resisting fatigue crack propagation [19].

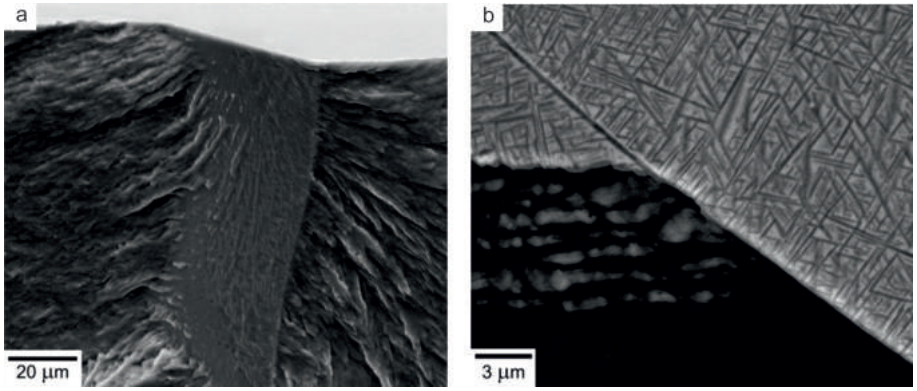

Figure 2.67: BSEI of the a. fracture face and b. surface of a fatigue failure initiated at the grain boundary of the β phase in titanium alloys [51].

Research has shown how the presence of α along β grain boundaries are detrimental to fatigue performance [19]. This has been attributed to the low energy path created over large distances allowing for ready crack propagation [19]. Such features have been shown to result in catastrophic fatigue failures as shown in Fig.2.67 [51].

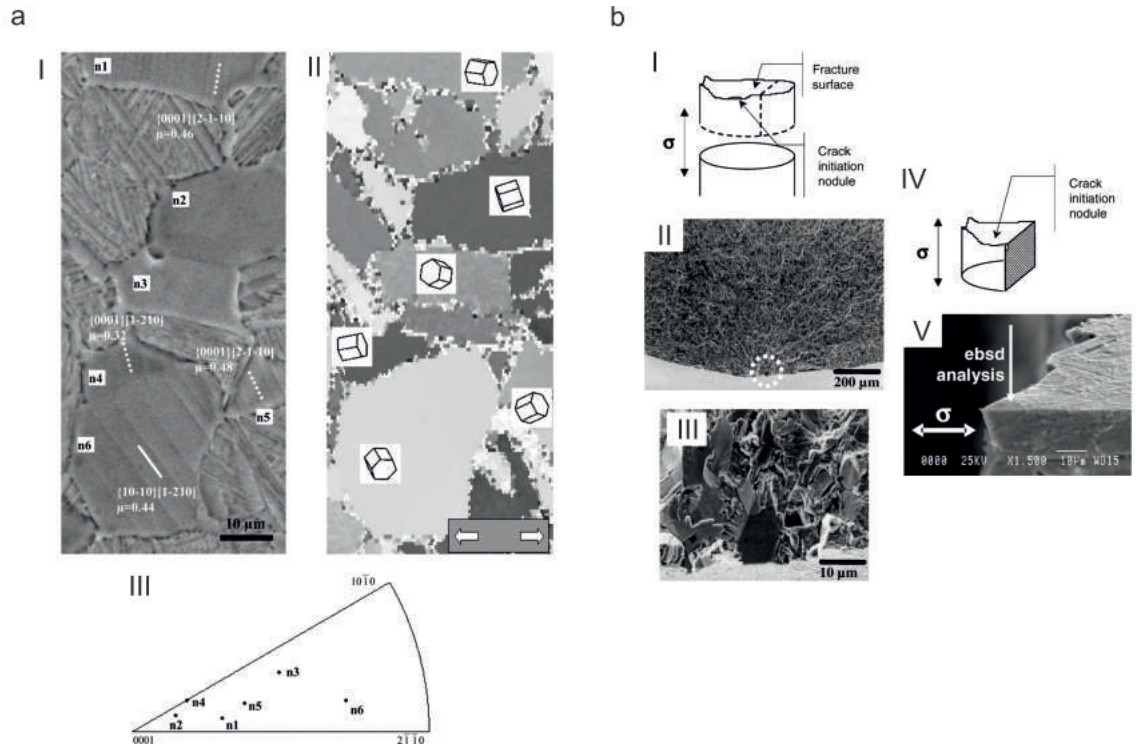

Figure 2.68: BSEI of a. I. dislocation slip as a result of fatigue loading with II. respective crystallographic orientations and III. pole figures and b. a method for identifying the crystallographic orientation of a grain resulting in fatigue crack initiation [123].

Conventional fatigue studies show how the crack initiation stage can dominate the fatigue life of titanium alloys [124]. Crack initiation, achieved through the activation of deformation modes, is accommodated via damage accumulation during cyclic stress application [59, 120, 123–127].For duplex phase titanium alloys, fatigue crack initiation is preferentially accommodated by the (HCP) α phase and can be observed as subsurface dislocation slip bands as shown in Fig.2.68. [59, 124].Fatigue facets and slip bands have been identified from fatigue failures in Ti-64, IMI-834

and Ti-10-2-3, see Fig.2.68, [59, 120, 128]. Prevalence for dislocation slip has been found parallel to the; Basal plane $\{11\bar{2}0\}$ (0001), C-axis in the (1010) direction and the $\{12\bar{1}0\}$ $(10\bar{1}0)$ prismatic plane within multiple α_p grains, see Fig.2.68, [59, 123, 127, 128]. Through the application of advanced characterisation techniques like SEM-EBSD and Transmission Electron Microscopy (TEM), studies have shown dislocation pile up and subsequent slip at the α/β

interface [59,126] as a result of the inherent precipitate free zone that exists [120]. The lower critically resolved shear stress (CRSS) required to activate Basal slip explains the dominance in fatigue initiation and rate of crack formation that occurs at Basal planes of α_p grains [123]. Due to microstructural and mechanical heterogeneities present for duplex titanium alloys, fatigue damage is inherently localised [120, 123, 124]. These in-homogeneities produce significant statistical variations in comparable studies on fatigue mechanisms [129, 130]. This substantiates the complexities and expense of the incremental performance improvements required for these components [16, 130]. For alloys with relatively low volume fractions ($<10\%Vol_f$) of α_p, as for Ti-5553 or Ti-10-2-3, competing microstructurally induced mechanisms both surface and subsurface, are found to contribute fatigue failure [124, 131]. Damage accumulation has been found to be promoted locally in macrozones, in which preferentially orientations of α_p, influenced through the Burgers relationship, by the preferential orientations local to the matrix phase, influence the susceptibility to deformation [123].

2.5.3 Influence of Machining on fatigue response

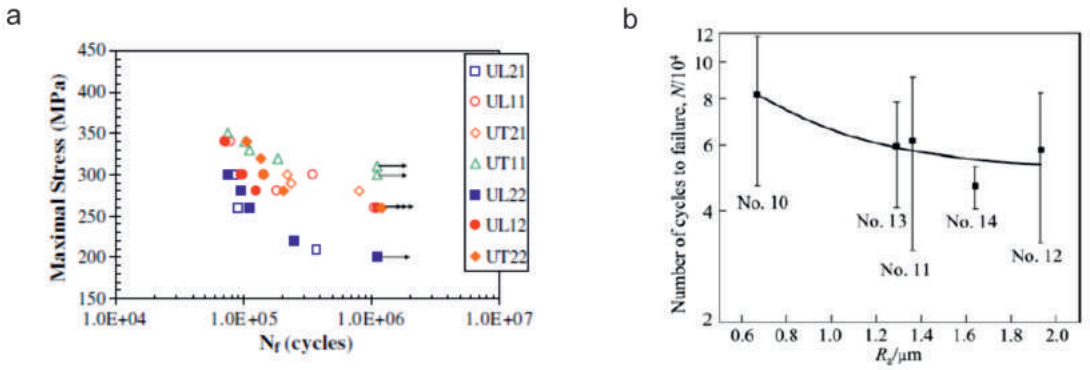

Figure 2.69: Schematic representations of the influence on surface roughness on the fatigue life of an a. aluminium [39] and b. a titanium alloy [132].

In existing literature, surface roughness or residual stress, as a result of machining, is the dominant subject regarding fatigue performance [**?**,39,41,42,97,132–136]. The focus of this research revolves around the influence of surface roughness and stress concentration factors on fatigue crack initiation. Evidence of the influence of machining induced surface roughness on fatigue life are presented in Fig.2.69a and b, in which increased surface roughness reduced fatigue life for an aluminium and titanium alloy, respectively [39, 132].The non-uniformity found in plastic deformation is not only evident in damage accumulation by fatigue loading but other deformational processes like machining. The intrinsic variations in the polycrystalline Ti-64 and Ti-845 alloys influences the intensity and depth of severe plastic deformation (SPD) and induced subsurface strain as a result of milling [14]. It has been postulated this

subsurface deformation can influence fatigue life, but limited correlations have been identified.

Chapter 3

Experimental Methods

3.1 Workpiece Material

For this study the material under investigation was the metastable beta titanium alloy Ti-5553, supplied by SLS as found on the Boeing 787 Dreamliner truck beam landing gear component. The chemical composition and fundamental mechanical properties for the solution heat treated and aged condition for this alloy can be seen in Tables 3.1 and 3.2 respectively.

Table 3.1: CHEMICAL COMPOSITION OF TI-5553 [24, 98].

Chemical composition (wt%)						
	Ti	Al	Mo	V	Cr	Fe
Nominal	Balance	5	5	5	5	0.4
Minimum	Balance	4.4	4	4	2.5	0.3
Maximum	Balance	5.7	5.5	5.5	3.5	0.5

Table 3.2: MECHANICAL PROPERTIES OF TI-5553 IN THE SOLUTION HEAT TREATED AND AGED CONTRIBUTION [24, 98].

Mechanical Properties	
Beta Transus (°C)	4.65
Density (g/cm^3)	4.65
Tensile yield strength (MPa)	1050
Ultimate tensile strength (MPa)	1200
Elongation (%)	13
Hardness (Vickers H_v)	370
Fracture toughness (MPa$\sqrt{m}$)	40

Ti-5553 is a high strength bimodal titanium alloy which possesses the combined effects of a lamellar and equiaxed structures producing well-balanced mechanical properties as shown in Table 3.2. Fig.3.1 shows the as-solution heat treated and aged microstructure of the Ti-5553 alloy under investigation in this thesis. The structure comprises of large β grains ranging up to approximately 1 mm in diameter as can be observed in Fig.3.1a. Primary alpha (α_p) is present as globular grains, approximately 3 μm in diameter at a volume fraction of approximately 10 $\pm$ 1 % within the retained β matrix. Fig.3.1b. displays the presence of (α_p) delineating the retained β grain boundaries, from here on referred to as grain boundary alpha

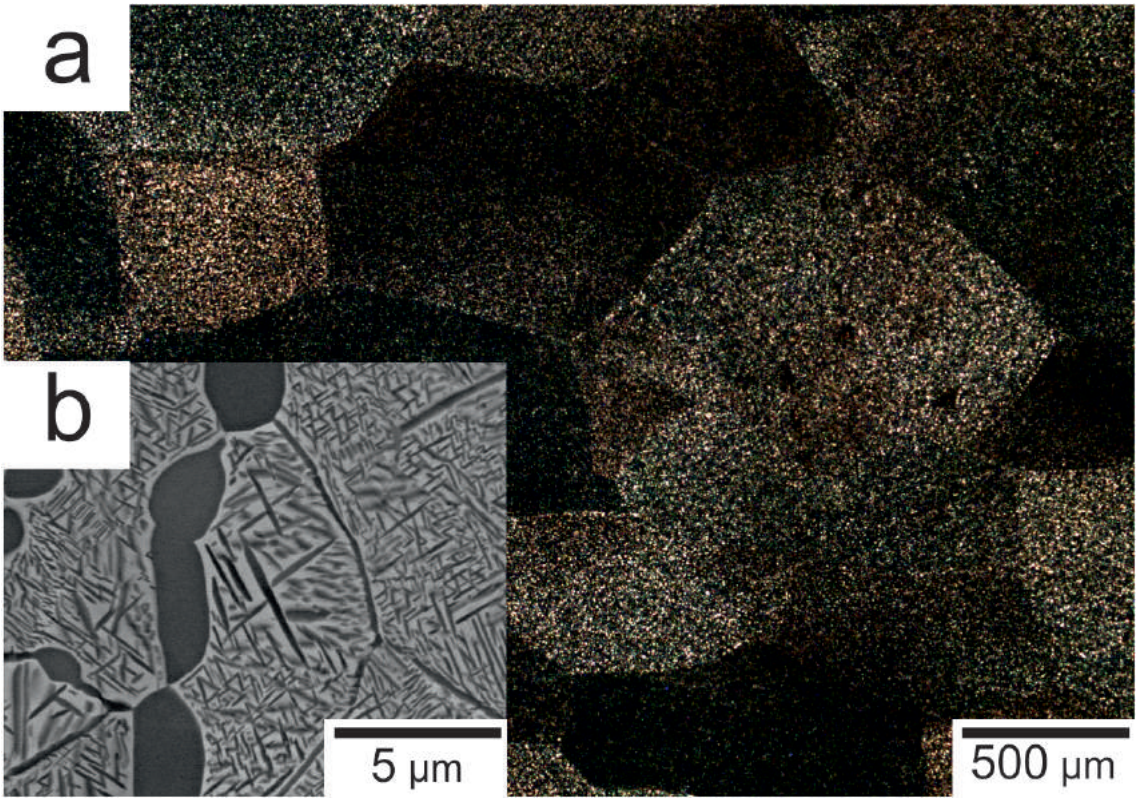

Figure 3.1: (a) Optical micrograph of the bulk beta (β) phase microstrucutre and (b) Electron Backscatter micrograph of the primary (α_p) and secondary (α_s) alpha microstrucutre.

(α_{GB}). As can be seen in Fig.3.1b. secondary alpha (α_s) is present within the β matrix in the form of high aspect ratio lathes on the submicron scale in a thatched or lattice array. Herein lies the crack retardation properties and thus the utilisation of Ti-5553 in fatigue dominant environments such as landing gear systems, further discussion of this can be found in Chapters 2 and 4.

Further details of titanium alloy processing and the resultant microstructures can be found in Chapter 2 and specific details relating to the processing of Ti-5553 truck beams can be found in Chapter 4.

3.2 Analytical Methodologies

3.2.1 Metallography

Metallographic preparation

Metallurgical samples were extracted from their respective source material through wire-electrical discharge machining (wire-EDM). Further size reduction of samples was achieved through sectioning using the Buehler Isomet 4000 and Struers Secotom-50 precision sectioning devices. Descriptions of the sample orientations with respect to machining and forging axes can be found in Chapter 4. Samples were mounted in Bakelite using the hot mounting press Buehler SimpliMet 1000 prior to surface preparation. For light microscopy samples were etched with a Krolls reagent composed of 6 vol % hydrofluoric acid and 12 vol % nitric acid for 5-8 seconds to expose grain boundaries. All samples were polished using a Buehler Automet progressively ground with silicon carbide grinding papers of P800 and P1200 grit then polished

with 9 μm diamond suspension and 0.06 μm colloidal silica suspension under 35 N load per sample.

Light Microscopy (LM)

Reflected light microscopy was conducted using a Nikon Eclipse LV150 and Reichert Jung Polyvar microscopes with a Zeiss Axio Cam ICc5 camera under varied magnification and lighting conditions. Grain boundary observation was subject to the act of etching detailed in the section above and the application of cross polarisation.

Microhardness

Micro-indentation was conducted using the Emco-Test Durascan-70 automated Vickers device under x10 objective lens with a x2 digital zoom. Tests were under standardised procedures in accordance with ASTM E384 with regards to hardenss calculations, indentation spacing and dwell times. Variations of loading conditions and indentation arrangement for individual testing requirements are described in their respective chapters later in this thesis. Data acquisition and initial hardness calculations were carried out on the software suite ecosWorklow. Post processing, statistical and quantitative data analysis was carried out on the commercial software suite MATLAB.

Scanning Electron Microscopy (SEM)

High magnification scanning electron microscopy (SEM) under secondary electron (SE) and back scattered electron (BSE) or Z contrast conditions were conducted on several systems; the FEI InspectF and InspectF-50 Field Emission Gun Scanning Electron Microscopes (FEG SEM) and Zeiss EVO60 SEM. The later was also used with an Oxford Instruments INCA X-sight EDX and SMART SEM software for chemical analysis or X-ray Energy Dispersive Spectroscopy (X-EDS). Quantitative metallography was conducted on images resolved from SEM using the free software suite ImageJ.

Electron Backscatter Diffraction (EBSD)

Electron Backscatter Diffraction (EBSD) analysis was conducted throughout this thesis to investigate quantitative crystallographic data as a result of machining operations or loading. The information gained from this technique enabled a greater level of understanding of deformational behaviour, the impact of crystallographic orientations on this deformation and subsequent failure mechanisms. For this work a FEI Sirion FEG SEM device was used with a Nordlys S detector for data acquisition and automated indexing using the Oxford Instruments HKL Channel 5 Flamenco software. Post processing and analysis of the data was carried out using the Oxford Instruments HKL Channel 5 post processing software suites; Tango, Mambo and Salsa. For all indexed maps, an accelerating voltage of 20 kV and spot size of 5 was used at a working distance of 14 mm from the sample surface which was tilted at 70° with respect to the electron beam. The detector was fixed at a distance of 166 mm from the sample surface and detected patterns were controlled and improved through a consistent time per frame of 6-10 seconds and a number of frames of 1-4. All other settings were adapted dependant on the specific requirements of

the individual maps under consideration. These settings are displayed in their respective chapters throughout this thesis. The fundamentals and applications of this technique is described further in Chapters 2 and 4 as well as in literature [22, 56].

3.2.2 Surface roughness analysis

Surface roughness profiling

The 2D surface roughness profiles were characterised through a mechanical stylus approach on a Mitutoyo SurfTest SV-600 profilometer. Measurements were taken in accordance with the international standard; BS EN ISO 4288:1998. Based on an assumption of an arithmetic mean roughness (R_a) of between 0.1 and 2 μm a sampling length of 0.8 mm was used over a 4 mm evaluation length. Typically, an average of 3 evaluation lengths were taken for each sample in at least 2 directions with respect to the cutting direction, perpendicular and parallel.

Surface light microscopy

The 3D surface roughness topography was characterised using light microscopy on the Nikon Eclipse LV150 and the Bruker Contour GT microscopes through a range of objectives and magnifications. The later allows for detailed 3D analysis of the surfaces through the commercial software suite (name). Typically, the average of at least 3 measurements were taken for each sample. The fundamentals and applications of this technique is described further in Chapters 2 and 5.

3.2.3 Cutting force analysis

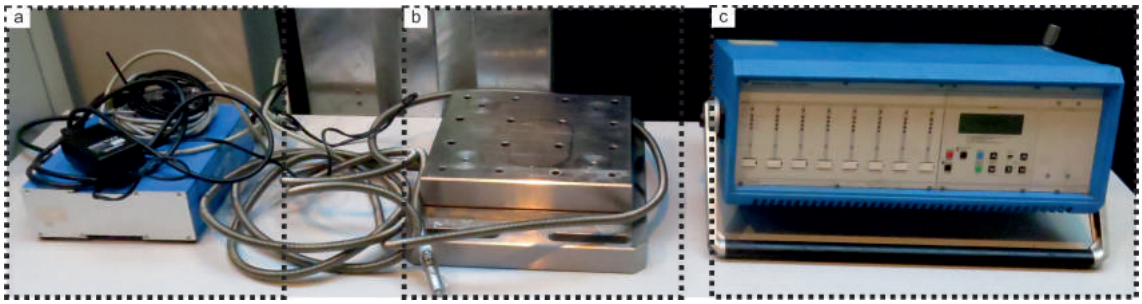

Figure 3.2: Photograph of cutting force equipment a. Kistler 5697A USB data acquisition (DAQ) interface, b. Kistler 9255B Dyno-table and c. Kistler 8 Channel charge amplifier.

The feed, thrust and cutting force feedback; x, y, and z respectively (further discussion of these orientations are given in Chapter 5 were acquired through the use of a Kistler 9255B Dyno-table and logged using a Kistler 5697A USB data acquisition (DAQ) interface at a 10 KHz frequency. Data analysis was conducted using the commercial software suite DynoWare. Force data was manipulated using a 2nd order high pass filter at 50 Hz, the 40 seconds of cutting was extracted and every 10th data point included to reduce total data size. The commercial software suite MATLAB was used for statistical and quantitative data analysis.

3.3 Small scale machining trial

Based on the conclusions from the industrial and the aims and objectives in Chapter 5.1.1, the independent and cumulative effects of increased V_c and f_z for finish end milling of Ti-5553 on the surface integrity and subsurface microstructure in a manner representative of industrial machining processes.

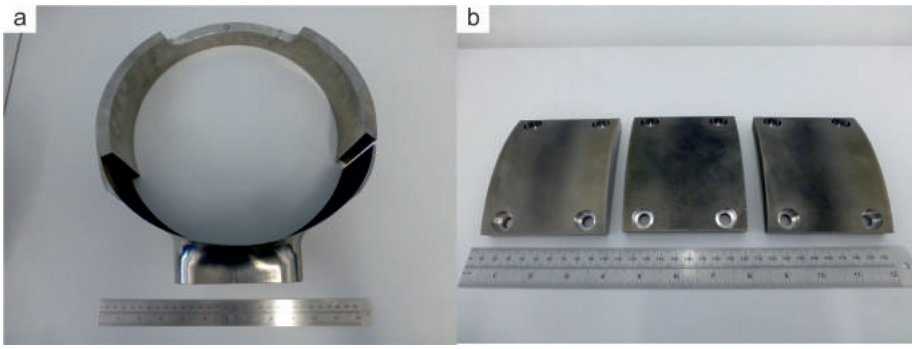

Figure 3.3: Photograph of a. B787 truck beam section with b. 3 wire-EDM curved coupons.

The source of material for this investigation were Ti-5553 B787 truck beam end cuts, Fig.3.3a, supplied by SLS and VSMPO. Using wire-EDM, the curved coupons, Fig.3.3b, were removed from each end cut and four counter-bored M8 holes were machined in place. The radius of curvature of these coupons was parallel to the external radius of a finished truck beam component, ensuring the geometry of the coupons were exactly representative of in service components.

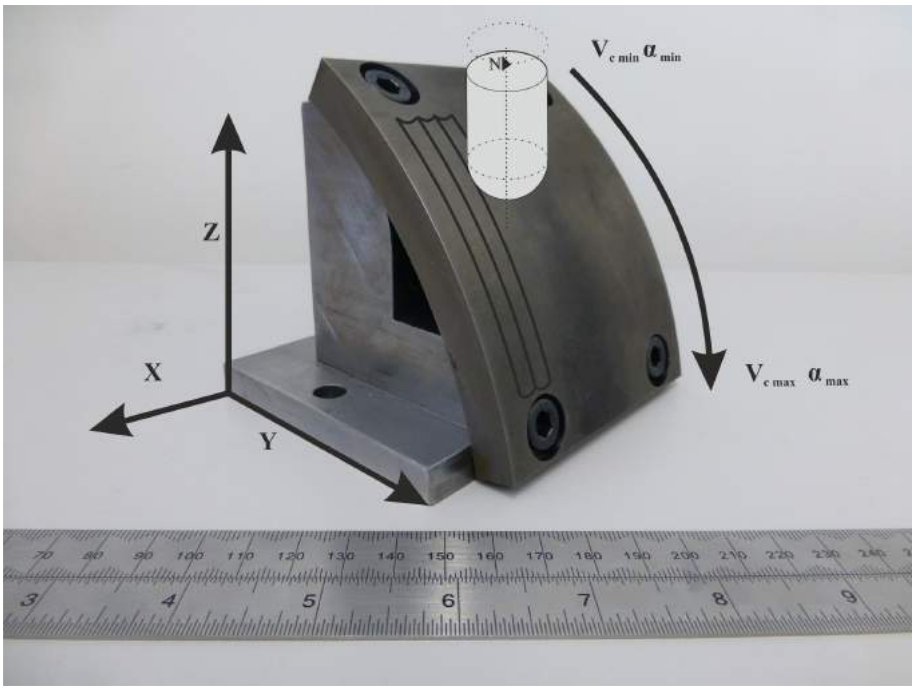

Figure 3.4: Photograph of a wire-EDM curved coupon and custom fixture with schematic superimposed tool path.

A custom fixture was manufactured to enable a representative manufacturing 5 axis cutting strategy to be achieved in a small scale 3 axis methodology, Fig.3.4. The length of the external face enables the full range of (ϕ_{eff}) to be engaged through a

3 axis strategy, as shown in Fig.4.8, which is representative of the finish end milling undertaken on the highlighted regions of Fig.4.6.

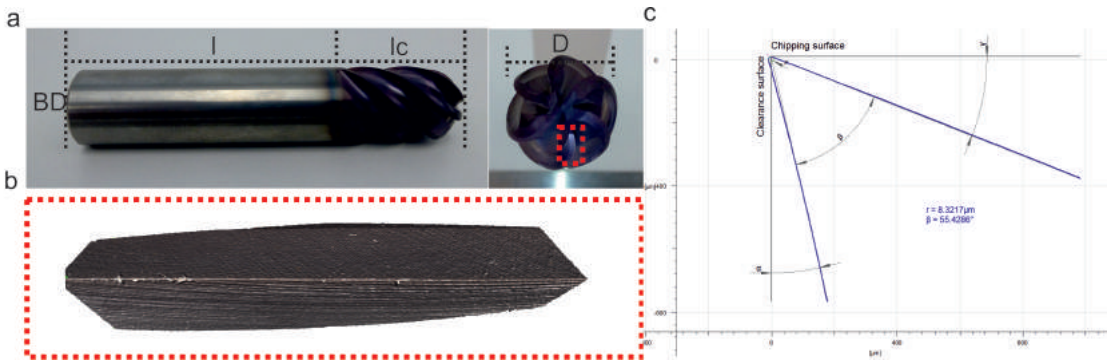

Figure 3.5: a. Photograph of the 20 mm ball nose end mill tool with b. a 3D image of a single cutting edge from Alicona SL analysis and c. the resultant average cross-sectional geometry of the given flute.

Based on total cutting time and area of operation in Fig.4.6, the tool of interest in this investigation is the 20 mm ball nose end mill cutter as shown in Fig.3.5a. This tool, supplied by Mitubishi tools is a 6 flute solid carbide coated tool of length (l) 110, flute length (l_c) and cutting diameter (D) and body diameter (BD) of 20 mm. Under inspection using an Alicona SL, in line with the methods described in Chapter 3.4, the cutting edge geometry of a new 20 mm ball nose end mill cutter were determined, as presented in Fig.3.5c. The mean cutting edge radius (r) and wedge angle β were found to be 8.775 μm and 57.067°(3sf), respectively.

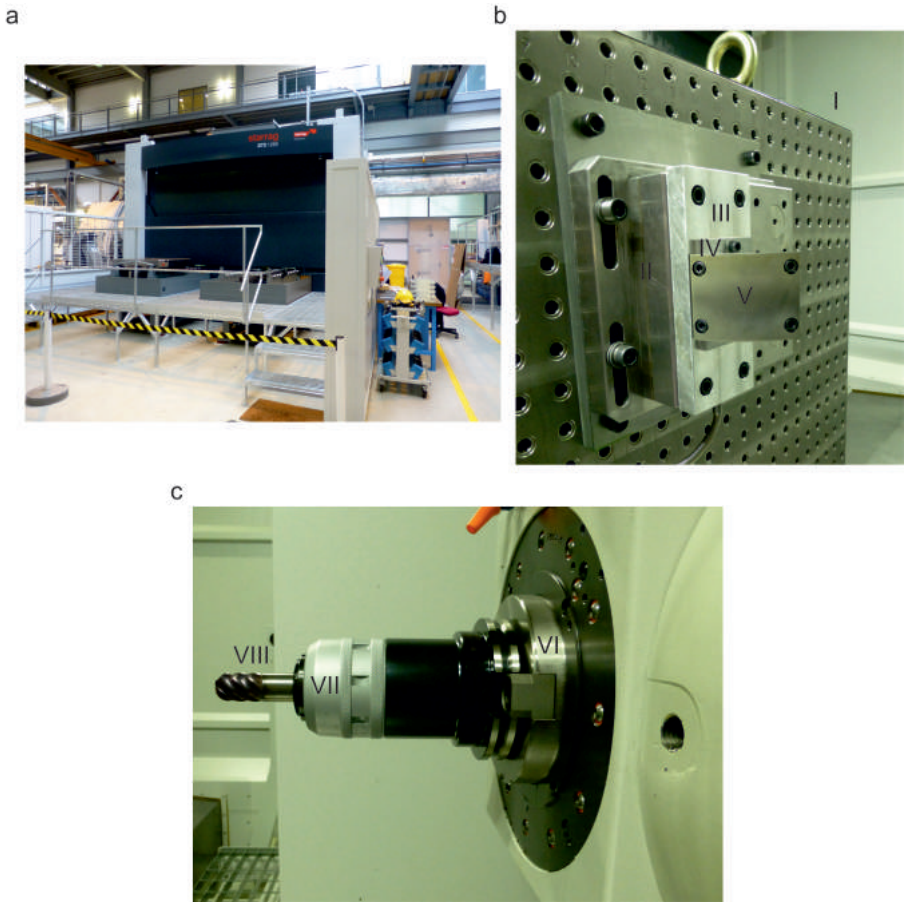

Figure 3.6: Photograph of a. the Starrag STC 1250 milling centre, b. wire-EDM coupon and fixture assembly and c. 20 mm ball nose end mill tool and holder assembly.

Milling trials were performed on a Starrag STC 1250 5 axis machining centre at the AMRC with Boeing Fig.3.6a. Wire-EDM curved coupons; Fig.3.6b.(V) and a custom fixture (IV) were secured to the dynamometer (II) via a aluminium fixture plate, placed on the tombstone of the machining centre. All 20 mm ball nose end mill cutters; Fig.3.6c were held by a Nikken multi-lock 32 mm chuck and a 20 mm collet. Hocut 795B coolant was delivered via flood and through tool holder supply at 100 bar and 70 l/min throughout all milling operations.

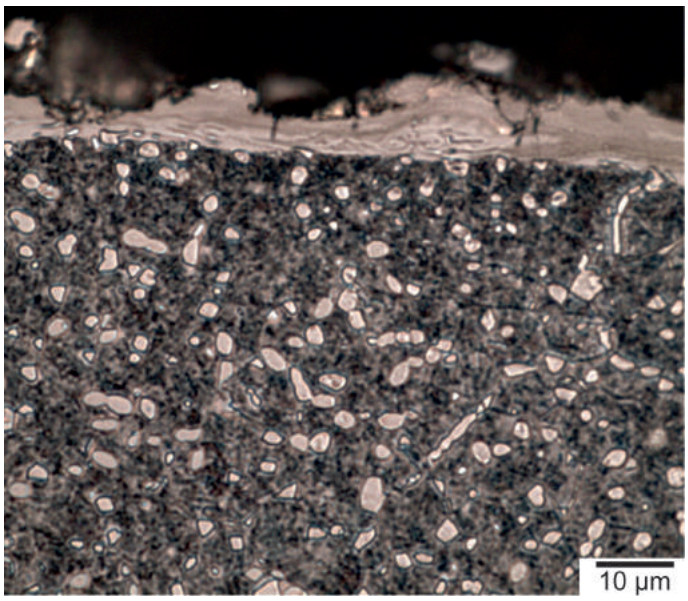

Figure 3.7: Light micrograph of a typical wire-EDM recast layer on the surface of Ti-5553.

Subsequent to wire-EDM extraction and prior to production of test cuts, the surface of the coupons is milled with a sacrificial ball nose end mill cutter to produce a geometrically tolerant and defect free surface. As can seen in Fig.3.7, a 10-20 μm recast layer is produced, possessing microstructurally heterogeneous subsurface structure when compared to the bulk material. This layer is inferior with regards to geometric tolerance and subsurface properties and is removed prior to investigative machining operations.

All test cuts were conducted at a_p and a_e of 0.3 and 0.7 mm, respectively. Based on the industrial operations discussed in Chapter 5, the Ψ_r required to engage the optimum Φ_{eff} are produced via the 3 axis operation, as a result of the arc length of the curved coupons and the custom fixture. The achieved -50 to -70°Ψ_r produced a range of Φ_{eff} of 11.74 to 18.79 mm from cutting engagement to cutting retraction. The spindle speed (RPM) and table feed (f) with respect to the Φ_{eff} are used to control the V_c and f_z as shown in Eqn.2.2 and 2.3.

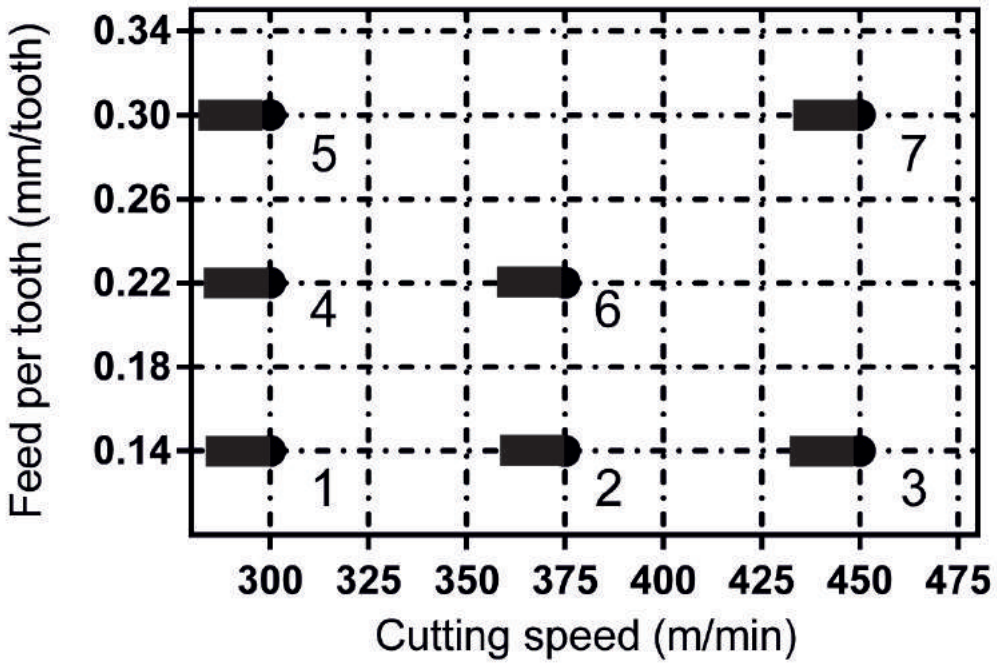

Figure 3.8: Schematic representation of the experimental cutting conditions with respect to V_c and f_z.

The commercial software MODDE by Umetrics was used to produce a suitable design of experiments (DOE) based on the available resources and objectives of the research. Cutting conditions chosen were targeted to maximise the potential increased processing window, utilising the capabilities and stability of the Starrag STC 1250, while operating within the industrial capabilities set by SLS. The nominal conditions of 300 m/min and 0.14 mm/tooth for V_c and f_z respectively were used in line with current industrial operations. Experimental machining conditions 1-7 used during the cutting trial are shown in Fig.3.8. Conditions at a fixed f_z of 0.14 mm/tooth at 3 V_c; 300, 375 and 450 m/min, a fixed V_c of 300 m/min at three different f_z 0.14, 0.22 and 0.3 mm/tooth were employed Fig.3.8. A final combination of the three f_z and V_c, were used to produce an increase in surface generation rates. Repeats of each condition were repeated once, with two repeats for the central condition, number 6.

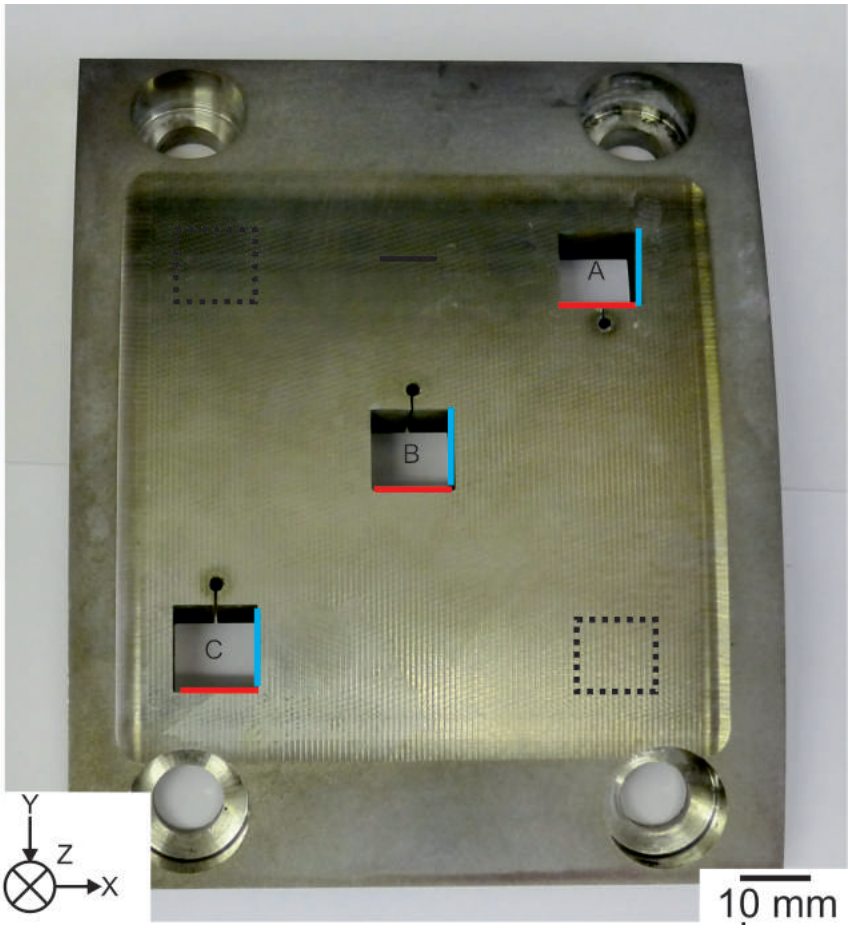

Figure 3.9: Photograph of a sectioned curved machining trial coupon with regions for surface and subsurface analytical techniques.

All coupons for each condition produced were subjected to analytical methodologies as described in section 3.2. The image presented in Fig.3.9 is a schematic illustration to describe the process of none destructive and destructive preparation required for analysis. Surface roughness for each coupon was recorded in 9 locations across each coupon. The solid black lines superimposed upon Fig.3.9 represents the evaluation length and position of 2D roughness profiles. Positions were taken to assess the roughness in the X direction at low, medium and high V_{ceff} across the outer circumference of the machined coupon. At each V_{ceff} position, measurements were taken in 3 different positions along the X direction so to normalise the response for any variation of r through tool wear. Each measurement was repeated 3 times and averaged. The same methodology was employed for 3D surface imaging as represented by the hashed black box in Fig.3.9. Within 3 of the positions , identified in Fig.3.9 as A, B and C also used for surface inspection, wire-EDM was employed to destructively extract equally sized cubic samples. From this, both planes in the X (red) and Y (blue) were imaged through light, SEM and EBSD microscopy.

3.4 Tool wear assessment

The analytical procedures described in both chapters 3, 4 and 5 were again employed during this tool wear trial. Additional experimental designs were used to induce tool wear over elongated durations of machining. Tool wear production was interrupted at predetermined intervals and resultant tools were then used during small scale

machining trials, in line with the procedures described in section 5.3.1. This enabled the surface integrity and subsurface microstructure to be interrogated and build on the results described in Chapter 5.

3.4.1 Tool wear production

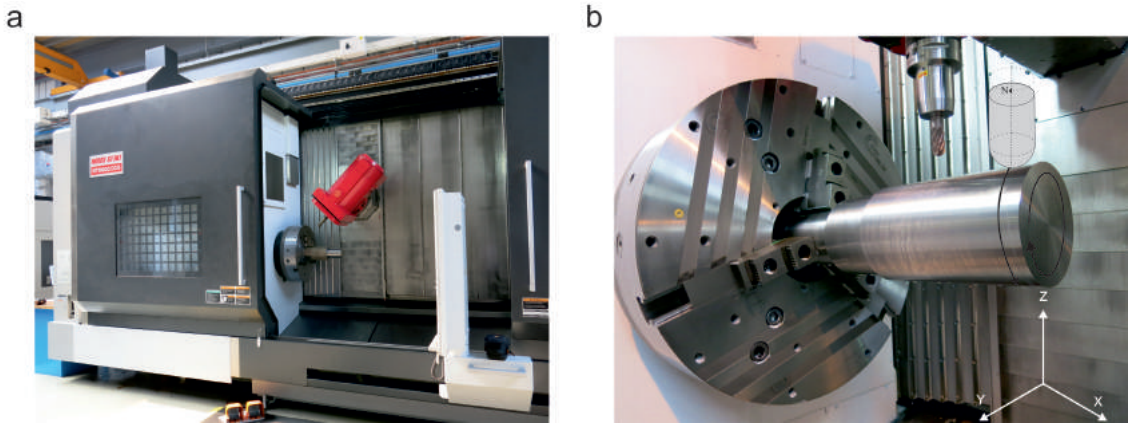

Figure 3.10: Photograph of a. the Mori Seiki NV 6600 mill-turn machining centre and b. 20 mm ball nose end mill tool, holder assembly and billet with superimposed schematic representation of fundamental orientations.

Tool wear production was performed using a Mori Seiki NV6600 mill turn machining centre at the AMRC with Boeing, as shown in Fig.3.10. A Ti-5553 billet supplied by SLS and VSPMO was used as the source material for this investigation, as described in section 3.1. The billet measured at a length and diameter of 750 and 250 mm respectively, see Fig.3.10. The outer diameter was machined utilising a standard turning operation, down to 100 and to a length of 250 mm, to produce a step in the outer geometry of the billet and improve stability of the billet within the jaws of the machining centre Fig.3.10. A complex 4 axis CADCAM programme was designed, developed and operated, in which the combined rotation of the billet about the c-axis and curved tool path in the Y and Z axis produced a specific f_z rate. This tool path also allowed for a single rotation of the billet to engage the full ϕ_{eff} of the milling tool, Fig.4.8. The tool path was sequentially transposed across the full length of the billet at a step of 0.7 mm (a_p) and at a repeated axial depth of cut of 0.3 mm (a_e) . This was repeated until the specified cutting duration was reached and the tool was removed for further testing. Hocut 795B coolant was delivered via flood and through tool holder supply at 100 bar and 70 l/min throughout all milling operations.

3.4.2 Small scale testing

Once removed from the tool wear trial, cutting tools were used to produce representative machined Ti-5553 curved coupons, as shown in Fig.3.3b and 3.4, in line with the procedure defined in section 3.4.2.

3.4.3 Tool wear characterisation

Tool geometries of new and used milling cutters were taken using an Alicona Infinite Focus SL with x5 and x10 objective lenses. Data acquisition was conducted

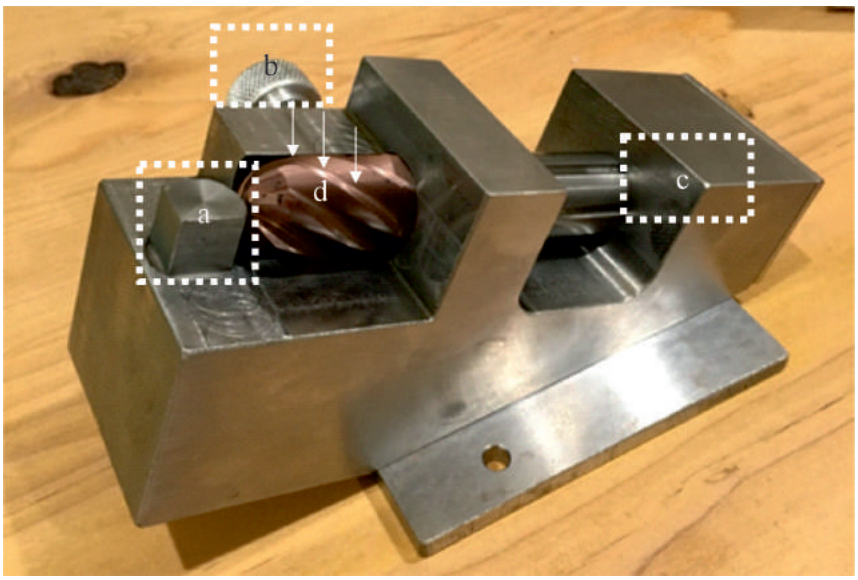

Figure 3.11: Photograph of the bespoke rig used for tool wear analysis of 20 mm ball nose milling tools with a. an orientation pin, b. locking pin, c. and spring which provided d. 3 imaging locations along each flute of the milling tool.

using the commercial software suite EdgeMaster and statistical and quantitative data analysis was carried out using MATLAB. A minimum of three measurements taken along every flute over the effective cutting diameter. To restrict the available degrees of freedom and improve the accuracy of measurements, a bespoke rig Fig.3.11 was designed and manufactured to secure a milling tool for analysis. A housed spring Fig.3.11c. allows for tool length normalisation (irrelevant of number of regrinds which shortens the total tool length). A grub screw Fig.3.11b. fixes the tool rotation around longitudinal axis. The angle between the light source and tool axis is constant as a result of the geometry of the rig. A pin at the tip of tool set measurement location along the flute Fig.3.11a. Tools can be rotated and locked in place allowing for the selection of the individual flute and location under consideration Fig.3.11d.

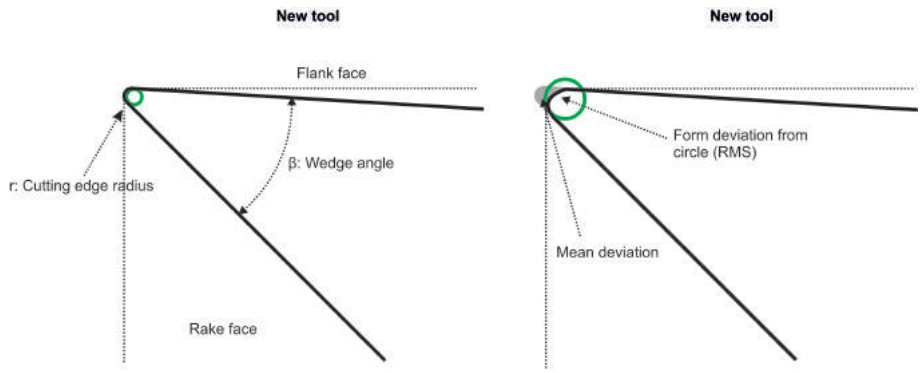

Figure 3.12: Schematic representations of new and worn tool geometries.

Tool cutting edge radius (r), rake(y) and relief (a) angles averaged over 50 geometric measurements from each scan. Within the EdgeMaster suite a geometric difference module allows for new tools to be compared to worn tools in a 3D environment for accurate wear volume calculations and deviations from idealised cutting edges Fig.3.12. The commercial software suite MATLAB was used for statistical and quantitative data analysis.

3.4.4 Tool system vibrational stability

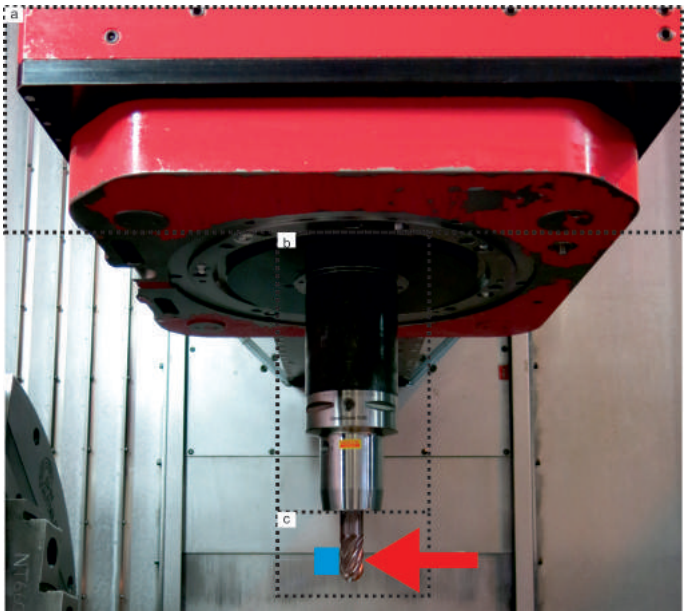

Figure 3.13: Photograph of tool system vibrational stability testing a. machine spindle, b. tool holder and c. tooling. The red arrow represents a hammer strike direction and the blue box represents the corresponding accelerometer placement.

The dynamic vibrational stability of the tool system (consisting of the cutting tool, tool holder and machine spindle) was assessed through the process of Tap Testing. This was carried out to support confidence that the individual tool systems and the cutting conditions under consideration were free from the effects of chatter, a topic introduced in Chapter 2. The tool tip is excited using a hammer (hammer sensitivity: (Sensor 086C04) 1.2 mV/N) with a Nylon tip. The motion or vibration is measured through an accelerometer (accelerometer sensitivity: (accelerometer 352C23) 5.15 mV/G) arranged in specific orientations on the tool with respect to the direction of impact from the hammer. These are recorded in the time domain and converted to the frequency domain using a Fourier transform. A minimum of 10 impacts for each direction is recorded and depending on the coherence or validity of the impacts, are then averaged. When the results from all directions are combined the stability plot can be produced for the tool system over a range of cutting parameters known as a lobe diagram. This is used to ensure all test conditions are carried out in stable regions and suggest no chatter should be observed. Data is assessed using the commercial software suit TXF MetalMax.

Prior to the small scale testing, all tools were characterised via the process described in section 3.4. Tool wear measurements were taken using an Alicona Infinite Focus SL light microscope utilising a bespoke rig, shown in section 3.4. Measurements were taken of all six flutes, at three identical positions along the cutting edge at equal positions between the (ϕ_{effmax}) and (ϕ_{effmin}), as depicted in Fig.4.8. Numerical averages were taken from all of these measurements and the 3D micrographs shown in this chapter were those that most closely represented the mean values. The images presented in Fig.4.51, 4.52 and 4.53 are 3D light micrographs showing the tools directly after use. The geometric differences between new and used tools were studied through 3D light microscopy. New tools were compared to used tools after cleaning, which was achieved through the application of an ultrasonic bath to remove redeposited chips due to BUE along the cutting edge. The cleaning procedure

was used to distinguish between redeposited and re-adhered chips along the cutting edge. Ti-5553 coupons were interrogated following procedures described in section 3.2.

3.5 4 point bend fatigue testing

3.5.1 Four point bend fatigue test coupon extraction

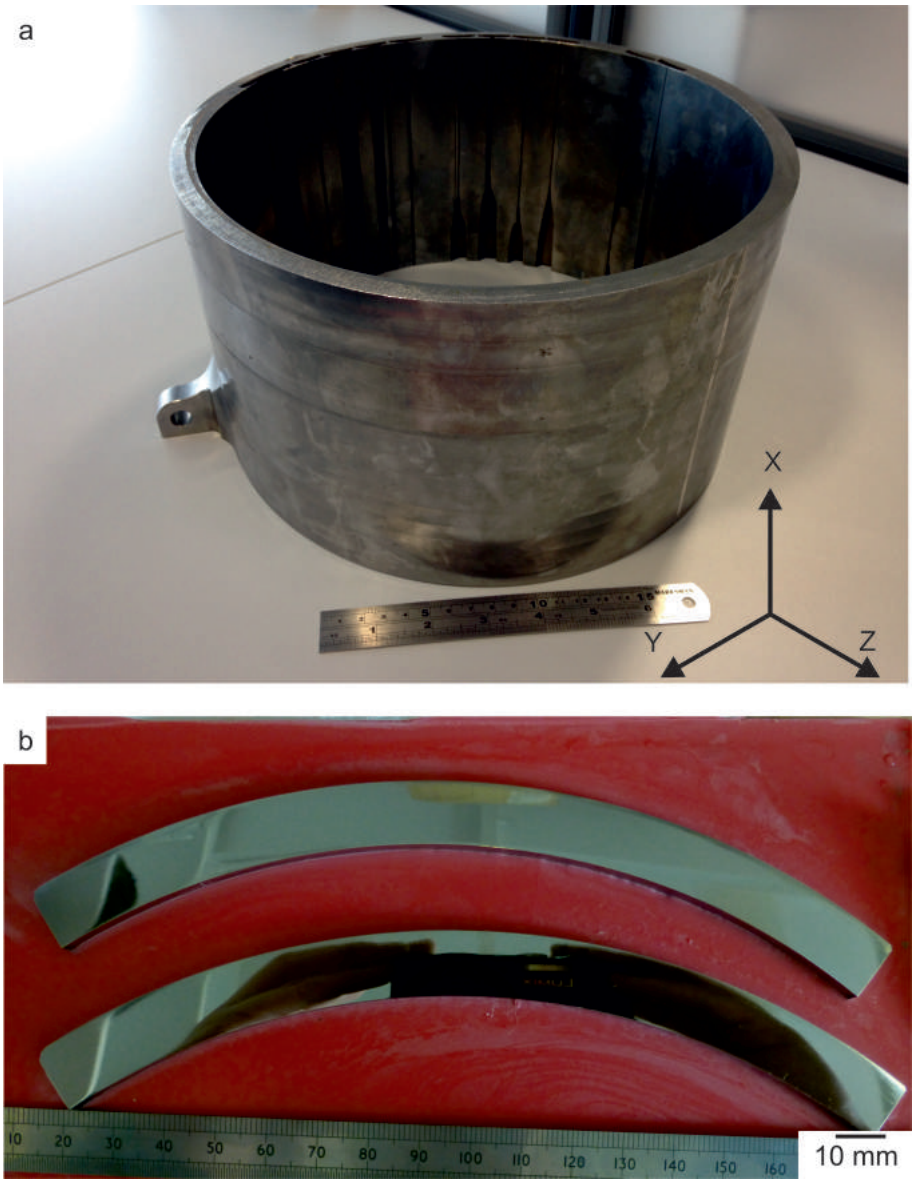

Figure 3.14: Photograph of a. Ti-5553 truck beam section used for the production of four point bend fatigue test coupons and b. sectioned, cold mounted and polished Ti-5553 truck beam specimens for material characterisation.

The source material for this investigation was Ti-5553, as defined in section 3.1, supplied by SLS and VSMPO. The section presented in Fig.3.14a was removed via machining, from a semi-finished B787 truck beam component, at an outer diameter, wall thickness and length of 300, 12 and 200 mm, respectively. From wire-EDM, a 10 mm thick, circumferential slice extracted from the truck beam. This was further sectioned into five arc shaped specimens, as shown in Fig.3.14b, at intervals of

70°, using a Buehler AbrasiMet 250 manual abrasive cutter. These sections were then cold mounted in resin and progressively ground and polished, as described in section 3.2. These specimens were used for material characterisation through light microscopy and micro-hardness Vickers indentation, as described in section 3.2. A high resolution indentation map comprising of 2160 individual indents was recorded and analysed across the entire surface of these five arcs, at an equal spacing radially by 2 mm and circumferentially by 1°. Coupons used during fatigue testing were extracted by wire-EDM from the remaining truck beam section, at a length of 180 mm along the X axis. Coupons were removed with surplus dimensions in all directions of at least 0.5 mm to allow for removal of the re-cast layer by machining as was defined in section 3.3 and Fig.3.7.

3.5.2 Four point bend fatigue test coupon production

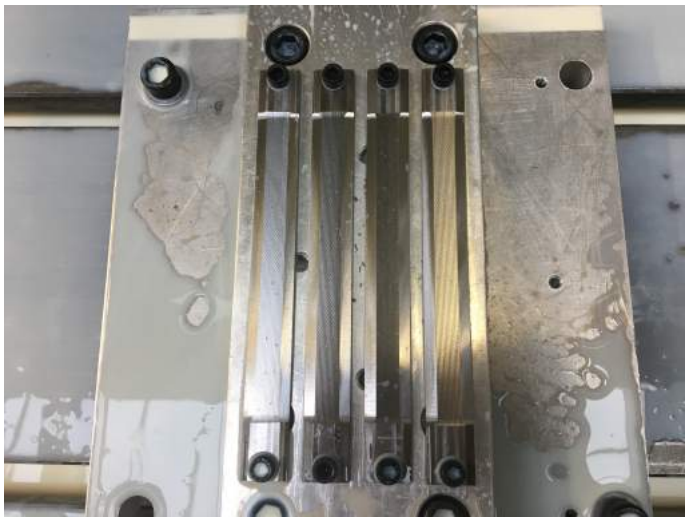

Figure 3.15: Machining set up for the production of Ti-5553 four point bend fatigue test coupons.

Four point bend fatigue test coupons were secured to a rectangular aluminium fixture, as shown in Fig.3.15. The surfaces were prepared by milling on a Haas TM-1P 3-axis CNC machining centre at the AMRC with Boeing. The upper and lower faces were machined with a 20 mm face milling tool and Sandvik milling inserts. The side faces were machined with 5 mm solid carbide end milling tools and chamfers with an 8 mm four flute solid carbide ball nose end milling tool. Machining trials were performed on a Starrag STC 1250 5 axis machining centre at the AMRC with Boeing producing coupons to the required geometry, as depicted in Fig.3.22, of 3.6, 19 and 120 mm in height (h), width (w) and length (2L), respectively. The chamfer angle (θ) of 100°produces an upper face of 10 mm in width. This upper face was milled with respect to industrial manufacturing processes of SLS, with a solid carbide end milling tool, see Fig.3.5, at identical cutting conditions as described in section 3.3. A lead angle (Ψ_r) of 67.5°was used in order to engage the Φ_{eff} and thus optimum SGR and tool life as in Fig.4.8. Hocut 795B coolant was delivered via flood and through tool holder supply at 100 bar and 70 l/min throughout milling. In order to study the effect of increased SGR two machining conditions were used. V_c of 300 and 375 m/min and f_z of 0.14 and 0.22 mm/tooth as with conditions 1 and 6, respectively. An additional condition-8 was produced via grinding progressively

with silicon carbide grinding papers of P800 and P1200 grit and polishing with 9 μm diamond suspension and 0.06 μmm colloidal silica using a Buehler Automet. This third condition was used as a benchmarking exercise to compare fatigue performance in a four point bend test design with that of conventional R=-1 testing. This condition also allowed for the isolation and consideration of the influence of machining on deformation and subsequent fatigue performance.

3.5.3 X-ray diffraction (XRD) residual stress analysis

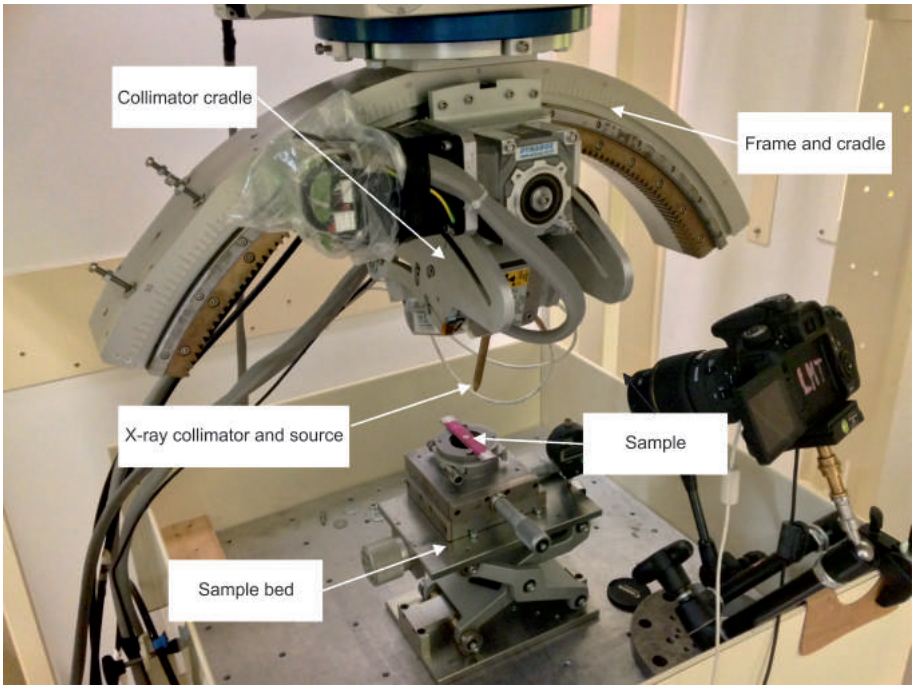

Figure 3.16: Photograph depicting the regions from a four point bend fatigue test coupon sectioned for subsurface characterisation.

The residual stress profiles, as a result of milling conditions, were obtained using the X-ray diffraction (XRD) method with a Cu source and Ni filter at 40 kV and 20 mA at Laboratoire de Mecanique et Technologie (LMT) Cachan, Paris. A Struers LectoPol-5 electropolishing device was used to expose subsurface material at 35 A and 0.43 V. This provided access to subsurface material to produce profiles of the subsurface stress state down to a depth of 200 μm, obtained in both the X and Y directions. Measurements are summarised for an interaction volume of $10^7 \mu m^3$ with a depth of penetration of 3 μm [137]. Results are presented as averages of 13 individual measurements, taken at angles over a range of between $\pm$90 degrees, with respect to the sample surface.

3.5.4 Fatigue testing

Stress calculations

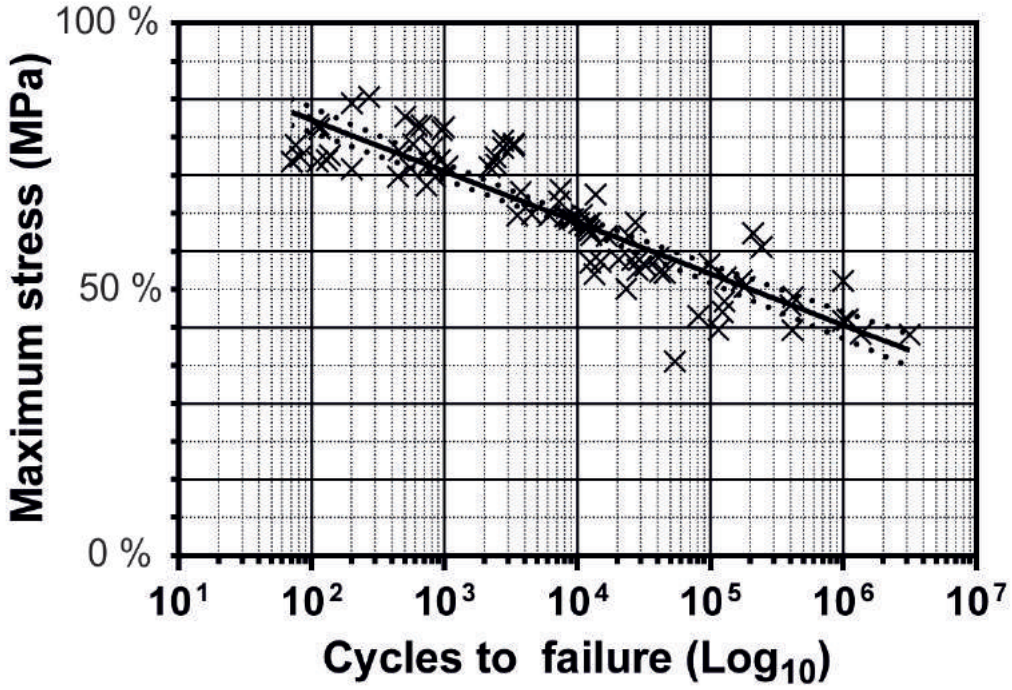

Figure 3.17: Ti-5553 cycles to failure fatigue data set (R=-1) with a 95% confidence interval (Courtesy of SLS).

The cycles to failure results for Ti-5553, with a 95% confidence level, in the heat treated condition, under ASTM standard, fully reversible (R=-1), room temperature tests are presented against σ_{max} in Fig.3.17 courtesy of SLS. Some of the detail in this figure, and the following calculations has been removed for confidentiality purposes.

$$y = -mln(x) + c \tag{3.1}$$

The equation that describes the linear regression fit for Fig.3.17 is shown in Eqn.3.1.

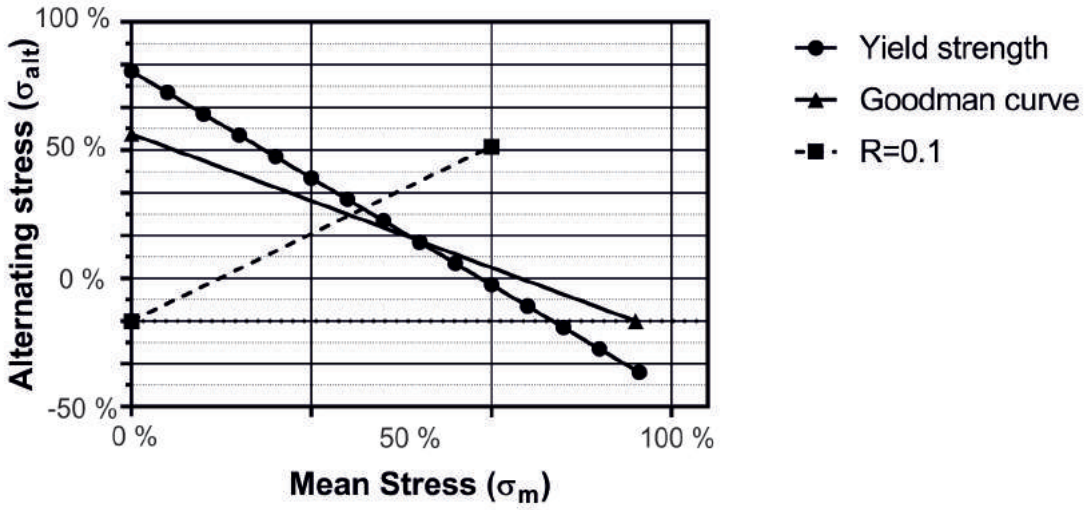

Figure 3.18: Schematic representation of a Goodman plot for LCF to failure for R=-1 fatigue testing of Ti-5553.

The maximum stress for fully reversed (R=-1) fatigue tests for the LCF cycles to failure under consideration, within the low cycle fatigue life regimen, Fig.3.17, as calculated by Eqn.3.1. Further calculations in this section are based on the mechanical properties listed in Table.3.2 and those obtained from fatigue testing presented in in Fig.3.17. The average UTS and 0.2% proof stress for the aforementioned coupons was 1290 and 1170 MPa (3sf), respectively. The results were used to construct the Goodman curve, presented in Fig.3.18, in which yield strength, for a variety of alternating and mean stresses are plotted. The point between the ultimate tensile strength and 0.2% proof stress intersects. For LCF cycles to failure the mean and alternating stress for the loading condition of R=0.1 can be calculated.

$$R = \frac{\sigma_{min}}{\sigma_{min}} \tag{3.2}$$

$$\sigma_{min} = 0.16\sigma_{max} \tag{3.3}$$

For any given value of mean stress (σ_m), the alternating stress (σ_{alt}), can then be found, for example, at any given stress (σ), the σ_m and σ_{alt} are calculated.

$$\sigma_{max} = \sigma_m = \sigma_{alt} \tag{3.4}$$

$$\sigma_{alt} = \frac{\sigma_{max} - \sigma_{min}}{2} \tag{3.5}$$

$$\sigma_{alt} = \frac{0.9\sigma_{max}}{2} \tag{3.6}$$

$$\sigma_{alt} = 0.45\sigma_{max} \tag{3.7}$$

Therefore the σ_{max} and σ_{alt} can be calculated.

$$\sigma_{max} = \sigma + 0.45\sigma_{max} \tag{3.8}$$

$$0.55\sigma_{max} = \sigma \tag{3.9}$$

$$\sigma_{alt} = \sigma_1 - \sigma \tag{3.10}$$

$$\sigma_{alt} = \sigma_2 MPa \tag{3.11}$$

The coordinates for the R = 0.1 line can be plotted from (0,0) to (σ_2,σ) on the Goodman plot in Fig.3.18. Any value of σ_{alt} can be used this way to calculate the σ_m. This is presented by the schematic plot in Fig.3.18, from which a linear equation can be determined and solved simultaneously.

$$y = 0.8175x \tag{3.12}$$

$$y = -0.6257x + 876 \tag{3.13}$$

$$X = \sigma_m = \sigma_4 MPa \tag{3.14}$$

$$Y = \sigma_{alt} = \sigma_5 MPa \tag{3.15}$$

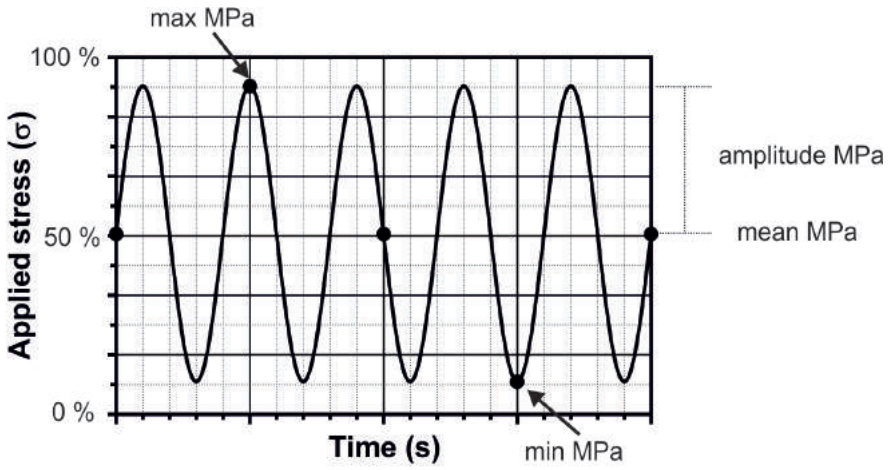

Figure 3.19: Schematic representation of cyclic stress applied during four point bend fatigue testing.

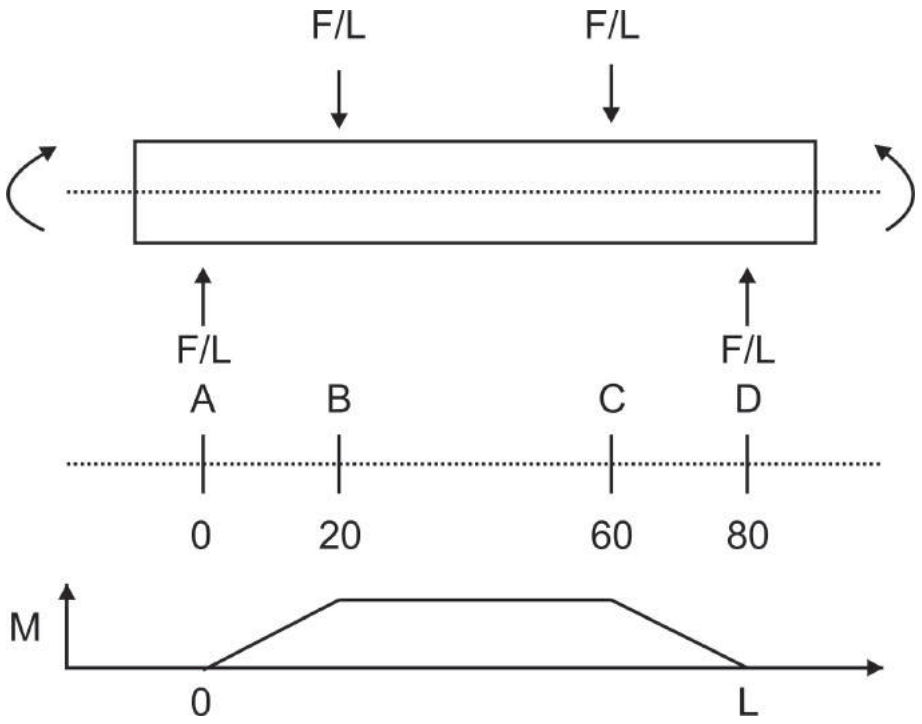

Figure 3.20: Schematic representation of the bending moment for the four point bend fatigue test set up.

A free body diagram and bending moment diagram are presented in Fig.3.20. These were used to calculate the applied load required to produce the determined stress profile shown in Fig.3.19. The bending moment equation was rationalised in Eqn.(3.16).

$$\sigma_{alt} = \frac{-My}{I_z} \tag{3.16}$$

From which the maximum bending moment for this four point bend scenario is determined.

$$M_{max} = \frac{1}{8}FL \tag{3.17}$$

With the maximum bending stress being found from Eqn.3.18;

$$\sigma_x = \frac{My}{I_z} \tag{3.18}$$

Based on the average geometry of the Ti-5553 coupons, the area and moment of inertia was calculated as 65.067 cm^2 and 0.663 x10^{-10} kgm^2 (3dp), respectively. From this and the values for the centroid of area and distances from the neutral axis, the maximum applied loads at the maximum and minimum applied stresses were found to be 4260 and 426 N (3sf), respectively. This therefore, satisfies the fatigue scenario of R=0.1 for an estimated life of the LCF cycles to failure under consideration.

Four point bend fatigue test

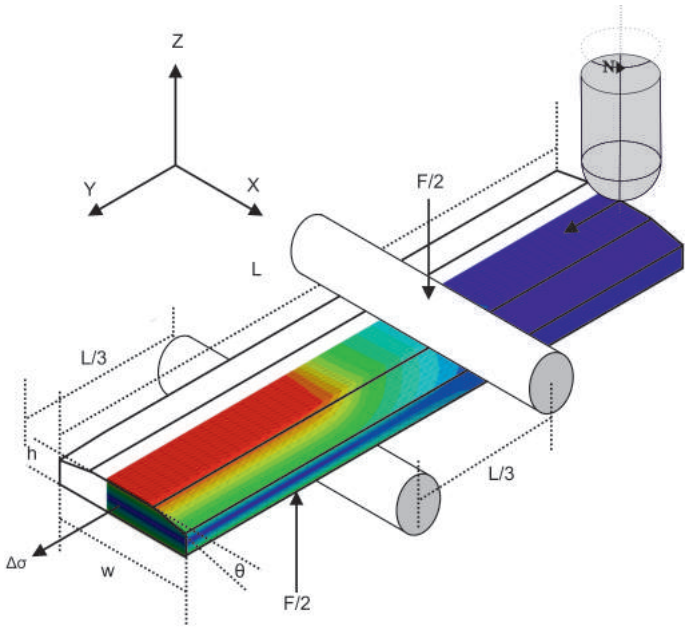

Figure 3.21: Schematic representation of four point bend fatigue testing with respect to machining conditions, microstructural direction and stress distribution as depicted from Ansys simulations.

The four point bend fatigue test offered numerous benefits when compared to conventional fully reversed or three point bend testing techniques. The nature of the four point bend technique produces a large area of maximum applied stress as is seen in both the bending moment diagram Fig.3.20 and the schematic stress distribution produced from simulations with Ansys in Fig.3.21. This in turn, allows for improved accuracy and simplicity for in-situ monitoring such as strain measurement, Fig.3.22b. This increased maximum stress distribution incorporates a greater number of the intrinsically large β grains, and thus, is a more representative sample of the available crystallographic orientations. The technique also permits a large area of the machined surface to be exposed to the potential for crack initiation. The direction of tool motion and rotation was kept consistent throughout testing, as shown in Fig.3.21.

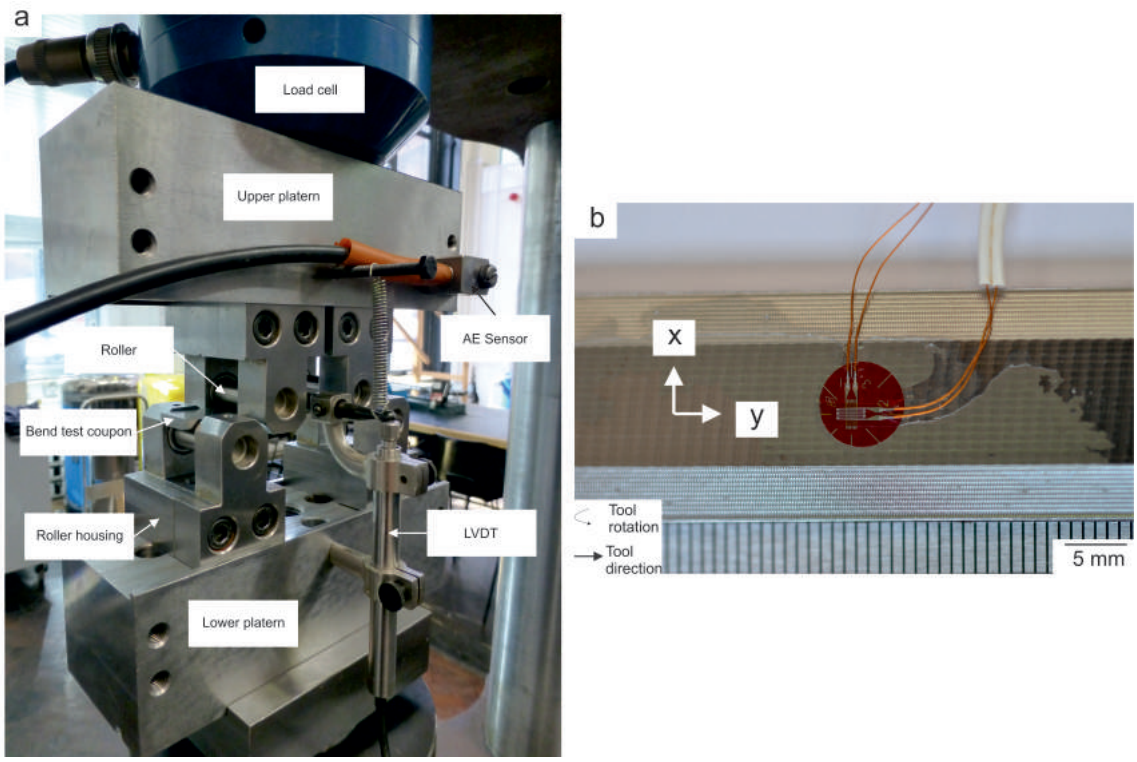

Figure 3.22: Annotated photographs of a. the four point bend fatigue test set up and b. the strain gauge assembly on a typical four point bend fatigue test coupon.

Fatigue tests were conducted at room temperature in air using a Nene 12 kN servo-hydraulic testing machine operated via a Moog SmarTEST One controller at the Lea Laboratory in The University of Sheffield. All tests were conducted to failure within the low cycle fatigue (LCF) range under controlled load at high stress, to induce local plasticity under a sinusoidal application at a frequency of 5 Hz and a stress ratio of R = 0.1. A custom four point bend fatigue test design was utilised for this study, as shown in Fig.3.22. The rig consisted of two large precision machined steel platens and four roller housings, each were constructed from two interlocking sections, secured with M8 bolts. Within these housings, two upper static and two lower dynamic, 10 mm diameter, BS8734/ISO 8734 hardened steel dowel pin rollers were secured within SKF BK1012 needle roller bearings. Force command, force feedback and displacement feedback data were recorded via the BNC data cables from the load cell and Moog SmarTEST controller of the Nene testing machine through National Instruments compactDAQ 9174 using the National Instrument DAQ cards, NI9234 and NI9201. Data was recorded via NIMax and post processed through MATLAB. Localised deflection was monitored via a Linear Variable Differential Transformer (LVDT), secured to the lower platen with a custom steel arm. The LVDT has a linear relationship between the change in voltage and distance, thus it was calibrated by compressing it over a set length and converting the voltage (mV) variation to a change in deflection (mm). External power was supplied to the LVDT and data was recorded through the compactDAQ 9174 and a NI9234 DAQ card. A set of 2 mm rosette mild steel compensation strain gauges supplied by TechniMeasure were secured to the machined surface at the centre of the coupon with Cynaoacrylate quick setting adhesive, see Fig.3.22b. Strain was recorded via the compactDAQ 9174 and a NI 9237 DAQ card and NIMax in the X and Y directions as shown in Fig.3.22a and b.

3.5.5 Fractography

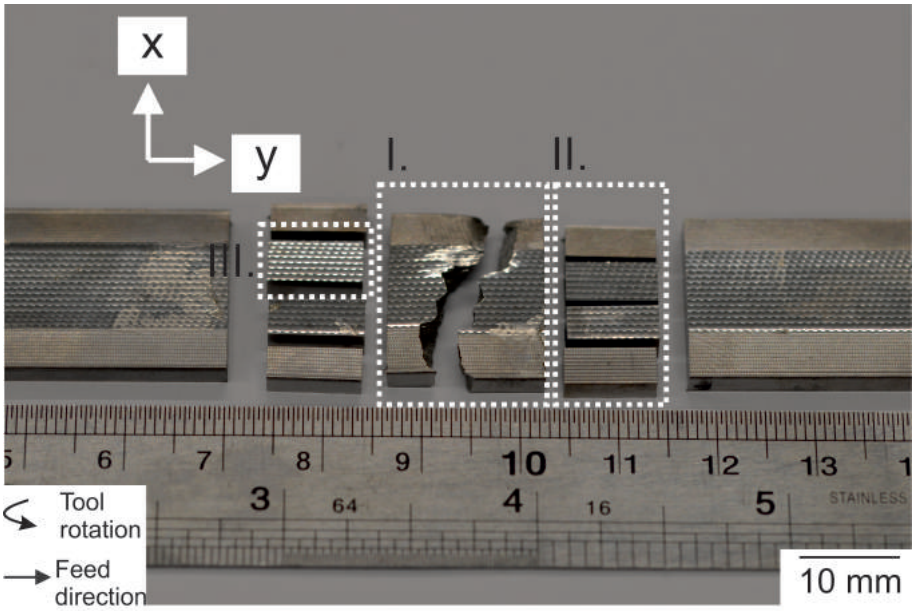

Figure 3.23: Photograph depicting the regions from a four point bend fatigue test coupon sectioned for subsurface characterisation.

Post fatigue failure, coupons were sectioned using a Struers Secotom-50 precision sectioning device, along the orientations depicted in Fig.3.23. Fracture faces were sectioned in the RD direction for BSEI. Subsurface samples for BSEI and EBSD analysis were used to study deformation within the high stress region of the fatigue test,see Fig.3.23ii. and iii. in which samples were orientated in the RD and CD direction.

Chapter 4

Results and discussion

4.1 Preliminary research

This chapter presents the preliminary activities carried to determine the which part of the fabrication process that offered the greatest opportunity for processing gains. This work is an amalgamation of literature reviews, industrial projects and first hand practical research activities. A description of the microstructural development from forging to assembly for Ti-5553 B787 truck beams is presented. An economic comparison of machining operations undertaken by SLS and down selection of the final machining operation chosen for this thesis are explored. The focus of this work was to refine the aims and objectives proposed in section 1.3 and to clarify the complexities and subtleties of this industrial thesis. By identifying the machining operation that possess the greatest opportunity for economic, operational and performance gains, the direction of this research was defined.

4.1.1 Machine strategy selection

Post heat treatment SLS is responsible for final rough, semi-finish and finish machining, post processing and assembly activities Fig.2.6. Post processing includes vibratory finishing, to remove mismatches in machined surfaces, removal of surface defects and improvement of the surface roughness. A combination of acid etching and visual, tactile and die penetrant non-destructive testing (NDT) techniques. Prior to assembly, structural titanium components are then shot peened to improve final in-service fatigue performance. These activities are out of scope for this research but it is important to consider the implications of any variations in prior machining operations. Any practical exercise involving the alteration of a machining operation with the goal of reducing production times have three fundamental parameters that must be considered.

- **Quality, Q** dependant on the operation and defines the level that the component must achieve to meet customer and application requirements
- **Prodtion time, P** the time taken for a given operation during a batch or continuous production process in order to achieve delivery or lead times
- **Cost, C** financial cost for manufacturing a given component on time to a given quality standard

For each of these parameters, there are a broad range of influential factors. The major factors to consider are listed, but not exhaustively, below.

- **Tooling systems** Tooling geometry, vibrational stability, wear rates and mechanisms.
- **Workpiece** Mechanical, microstructural and thermal properties and machinability.
- **Processing** Procedure and equipment factors and limitations, external factors such as the application and chemistry of coolant.
- **Personnel** Operating procedures, organisational structure and skill or experience of staff
- **Maintenance** Operational repair and system degradation rates and mechanisms

Based on the aims outlined in section 1.3, the objective of this work was to reduce the production time (P) while maintaining or improving the quality (Q) and cost (C). To do this the most important factors must be selected and investigated. An important consideration in this decisions was that in order to ensure the effectiveness and applicability of the results, the conventional manufacturing environment and resources used by SLS must be maintained. The solution was not to introduce disruptive technologies or to recommend fundamental changes in the tooling, workpiece, personnel or maintenance factors but to exploit variables within the conventional processing route for the greatest gains in Q, P and C parameters. The key variables that influence processing factors are listed below.

- **Cutting variables** Cutting speed, feed rate, radial and axial depth of cut and lead angle
- **Tooling variables** Rake angle, cutting edge radius, clearance angle, tool material, coating
- **Processing variables** Coolant pressure, composition and flow rate and workpiece clamping
- **Material variables** Composition, microsctructure, mechanical properties and geometry

Developments in tooling and material properties are restricted by the customer's requirements (Boeing), material selection and condition of supply (VSMPO-AVISMA) and industrial contracts with tooling suppliers (Kennametal and Mitsubishi). Within the capabilities of existing machining centres, processing variables and the response of the material and tooling can be exploited. For an existing operation, assuming that the tooling, processing and material variables must remain constant, these leaves the opportunity to exploit cutting variables.

There are over 30 individual machining operations carried out on Ti-5553 B787 truck beam components at SLS prior to post processing activities. Machining activities at SLS accounts for the removal of approximately 48% of the total as received Ti-5553 truck beam weight. An internal investigation utilising CADCAM information from the commercial software suite Catia V5 was carried in partnership with a SLS placement engineer (Theo Dorlin) to determine which tool paths offered the greatest potential for production rate (P) improvement. The total cutting duration and area covered all machining operations were considered. Those operations with

the longest cutting duration and largest area covered by either semi-finishing or finishing tool paths were deemed to be the most important.

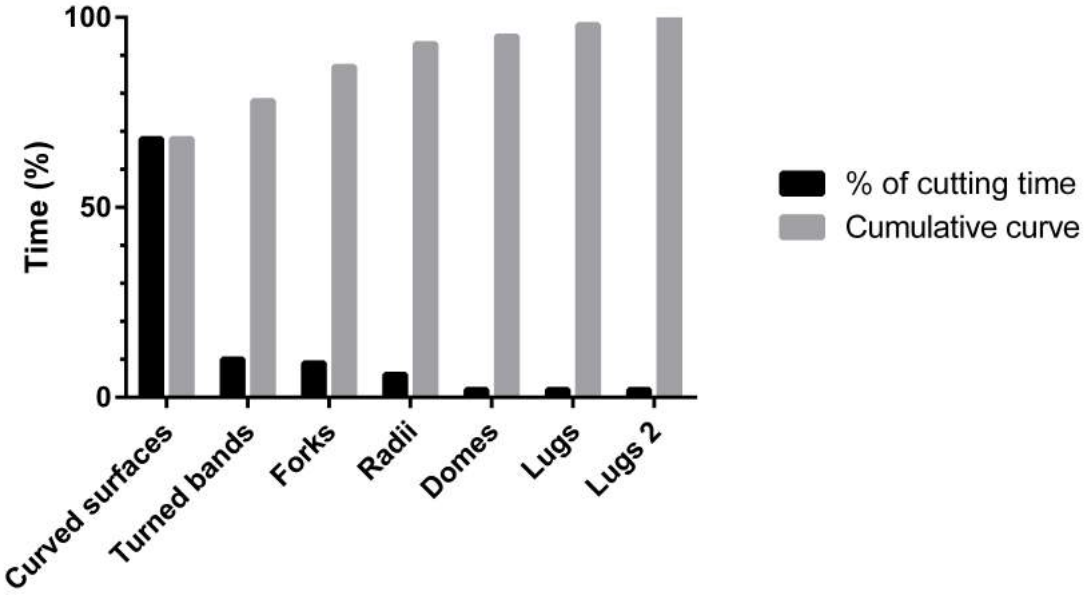

Figure 4.1: Schematic representation of the machining operations by surface area covered of the Ti-5553 B787 truck beam.

When considering the surfaces covered by all of the machining operations, it can be seen in Fig.4.1 that 68% of the total machining time is occupied by the machining of curved surfaces. Internal investigations identified that these curved surfaces are critical regions of the truck beam when considering in service fatigue performance. These regions are subjected to the highest static and dynamic loads during service. It was therefore critical to consider the impact that alterations to these machining processes would have on the quality Q of these surfaces. To that end it was determined that finish machining operations on curved surfaces would be considered. Not only due finish machining operations account for 40% of all machining time for theses components, but they are also the final source of deformation and have the greatest impact on geometric tolerances and other Q factors.

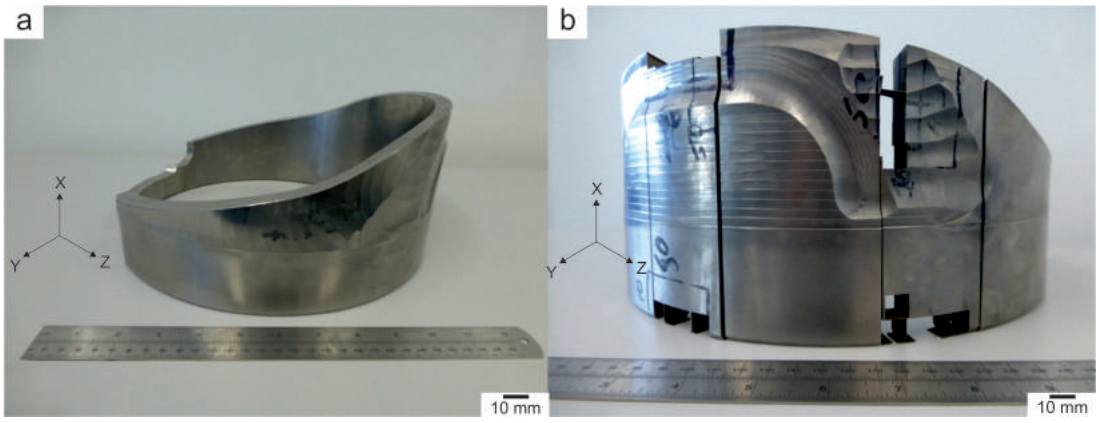

Figure 4.2: Photographs of a. a B787 truck beam end cut with b. annotations showing regions subject to i. semi-finish milling, ii. rough milling and iii. semi-finish turning operations.

Prior to studying finishing operations, it is important to understand the prerequisite material condition as a result of roughing and semi-finishing operations. This is to determine if finishing operations can be studied in isolation or if representative tests must also include the roughing and semi-finishing operations. Manufacturing quality material was exploited for this investigation, sections removed from the ends of the truck beam component prior to finishing operations previously utilised for locating during production were destructively examined. Theses end cuts can be seen in Fig.4.2 where different machining operations; i. semi-finish milling, ii. rough milling and iii. semi-finish turning. Samples were extracted through wire-EDM and prepared for metallographic analysis as described in section 3.2.

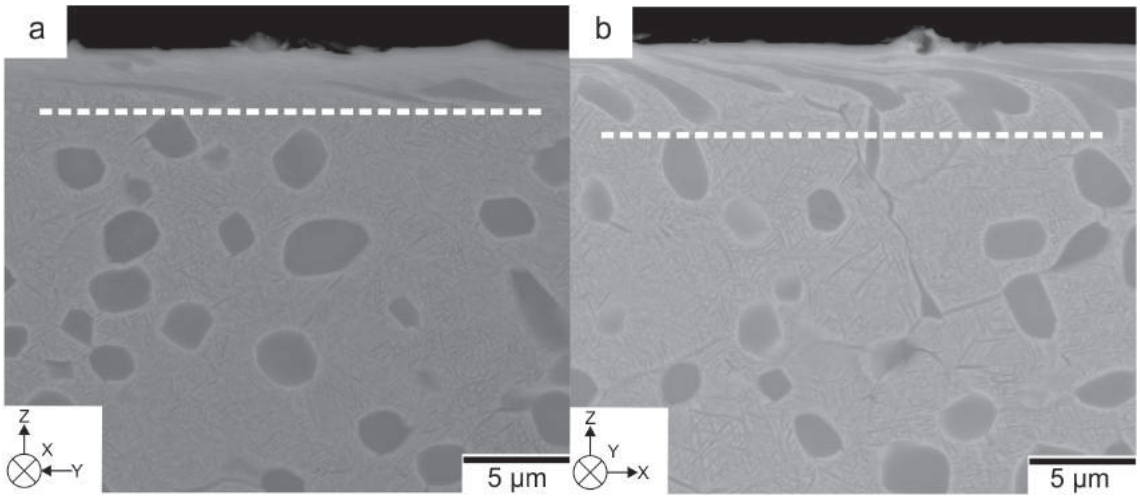

Figure 4.3: BSEI x16,000 magnification of B787 truck beam end cuts from a. region i. semi-finish milling and b. region ii. rough milling.

Fig.4.3 are electron micrographs displaying the subsurface deformation as a result of a. semi-finish milling and b. rough milling operations. The respective tool rotation and directions are labelled along with a dashed white line indicating the observable depth of severe plastic deformation (SPD). Typical SPD layers are observed in many metallic alloys subject to deformational processes such as machining and can be considered to be a regions where permanent deformation of the microstructure characterised as grain distortion, elongation or the presence of intense slip bands, mechanic twinning and other deformational features. In the case of rough and semi-finish milling operations of curved surfaces the observable SPD region is to an average measured depth of approximately 5-10 μm. Significant strain has been imparted in this region resulting in severe distortion to the α_p and α_s phases.

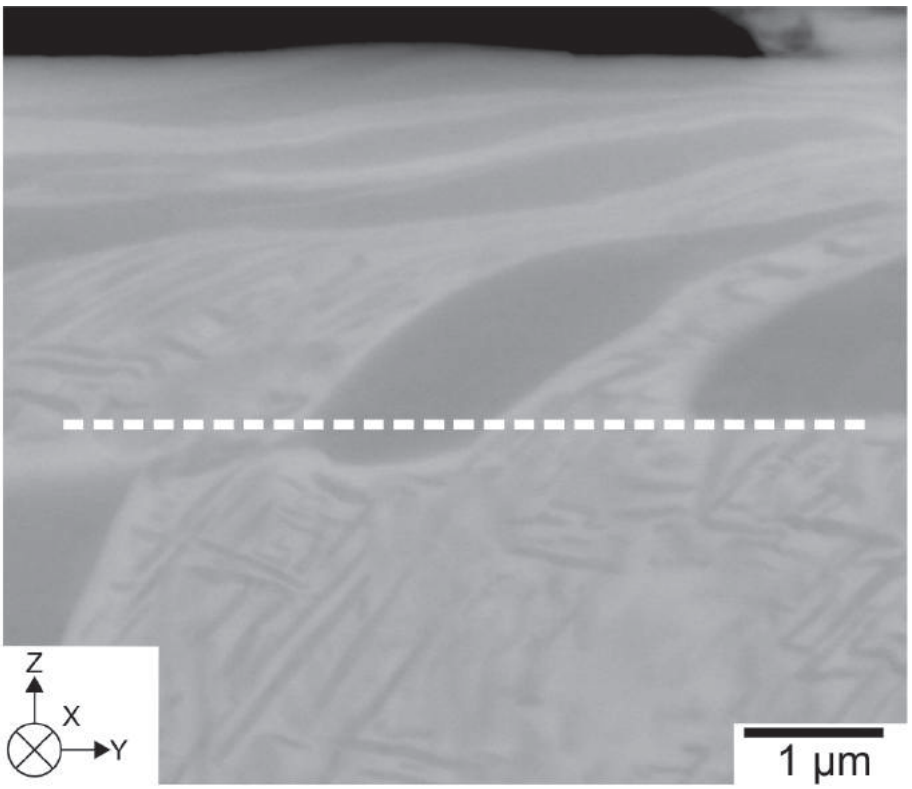

Figure 4.4: BSEI x40,000 magnification of B787 truck beam end cuts from region region ii. rough milling.

Under high magnification the severity of the plastic deformation can be clearly seen. A region of multiple nano-scale layers of α_p and β is produced as a result of the machining operation within the upper 1-2 μm of the subsurface. Though the observable deformation is not fully illustrative of the complete deformational response to machining it is assumed from this observation that the most significant deformation from roughing and semi-finishing operations would be removed by the act of finish machining. Therefore, it is concluded that any practical research activities can study finish milling in isolation.

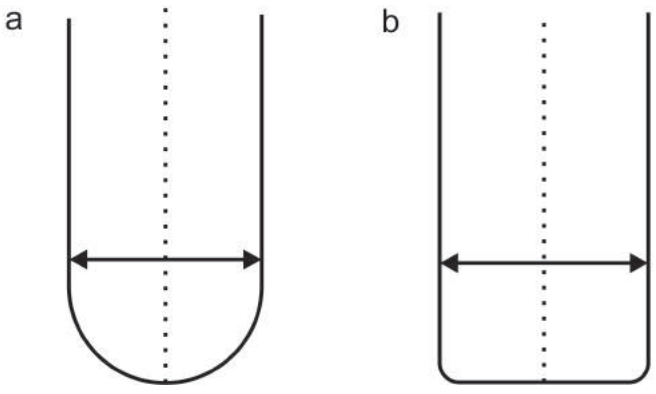

Figure 4.5: Schematic representation of tools used for finish machining of curved surfaces of the Ti-5553 B787 truck beam a. 20 mm solid ball nose and b. 25 mm solid end mill.

The two dominant tools responsible for finish milling operations of the curved surfaces are represented in Fig.4.5. Internal investigations identified that the major-

ity of cutting time (95%) for such operations are carried out using the 20 mm solid ball nose milling tool.

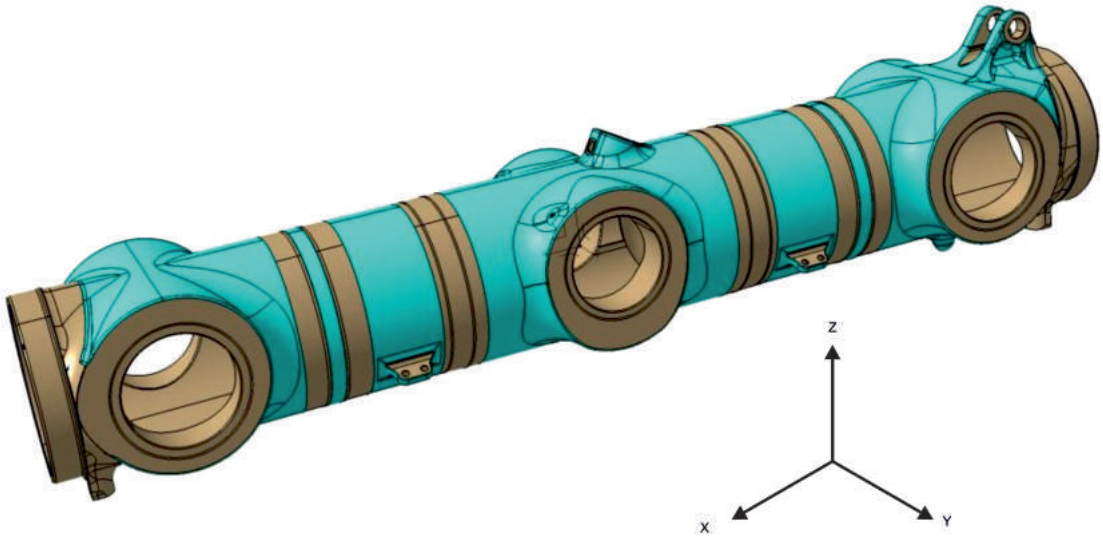

Figure 4.6: Schematic representation of surfaces covered of a B787 truck beam in finish milling by the 20 mm ball nose milling tool.

The schematic representation of the B787 truck beam in Fig. 4.6 shows the regions (highlighted in green) finish milled using the 20 mm ball nose tool. Other regions are finished using the 25 mm solid end mill or turning operations. It is clear to conclude that to maximise the impact of increased machining rates the best opportunity arises from the investigation of 20 mm ball nose finish end milling of curved surfaces.

4.1.2 Finish end milling

Ball nose finish end milling of curved surfaces is a critical operation in the production of B787 truck beams. This operation if the final source of imparted deformation prior to shot peening and assembly. The complexity of the operation is exacerbated by the long duration of machining time required to cover the surfaces identified in Fig.4.6, the relative low machineability of Ti-5553 and the expensive tooling required to produced the necessary surface quality.

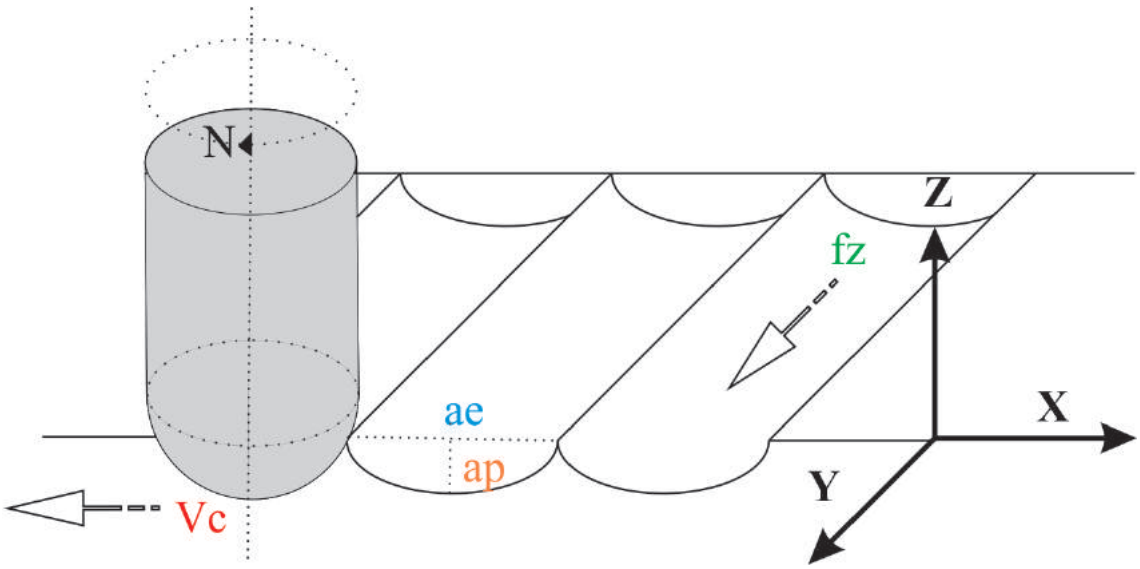

Figure 4.7: Schematic representation of the fundamental machining parameters for ball nose finish end milling.

Fig.4.7 is a schematic description of the fundamental machining parameters for a ball nose finish end milling operation with respect to a 3D Cartesian axis system in a conventional milling direction (up milling). The illustration displays a tool (highlighted in grey) rotating around the Z axis in a clockwise direction on a flat surface with the newly generated surface present.

- **Tool rotation, *N*** RPM, as a result of the spindle speed
- **Radial depth of cut,** a_p mm, depth of new generated surface along the Z axis
- **Axial depth of cut (step over),** a_e mm, width of the tool step over along the X axis
- **Cutting speed,** V_c m/min, if the surface speed of the cutter subject to the tool rotation, lead angle and number of flutes
- **Feed per tooth,** f_z mm/tooth, is the distance moved by the tool while a single flute is engages and is subject to the table feed rate and number of teeth

Ball nose end milling is a desirable machining technique as it enables the production of high quality surface finishes for complex non-linear tool paths and profiles. With alteration of the lead and tilt angles, varying locations along a tooth of the tool can be engaged, allowing for maximisation of tool life through distribution of wear over the length of the tooth.

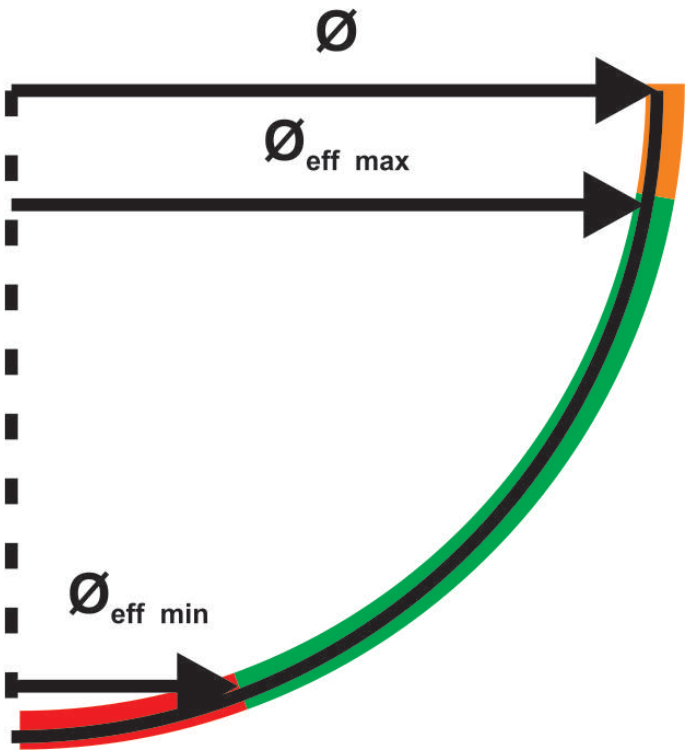

Figure 4.8: Schematic representation of the effective cutting zones with respect to lead angle of a ball nose cutting edge.

Through varying the lead and tilt angles at a constant RPM, a varied effective cutting speed is achieved which can affect the process performance parameters such as surface roughness and cutting forces. As can be seen in Fig.4.8 along a given tooth of a ball nose milling tool three regions exist. At large cutting diameters (highlighted orange region), achieved through tooth engagement at acute lead angles, near the actual tool diameter (ϕ) difficulties with tool wear and dimensional accuracies can occur. Below the minimum recommended effective cutting diameter (ϕ_{effmin}) (highlighted red region) only two of the six available teeth are engaged which accelerates wear rates and chip thickness loading and therefore power consumption during cutting. Between (ϕ_{effmin}) and the maximum recommended effective cutting diameter (ϕ_{effmax}) lies the optimum cutting region (highlighted green region). Within this optimum region all 6 teeth are engaged equally distributing chip loading and therefore wear.

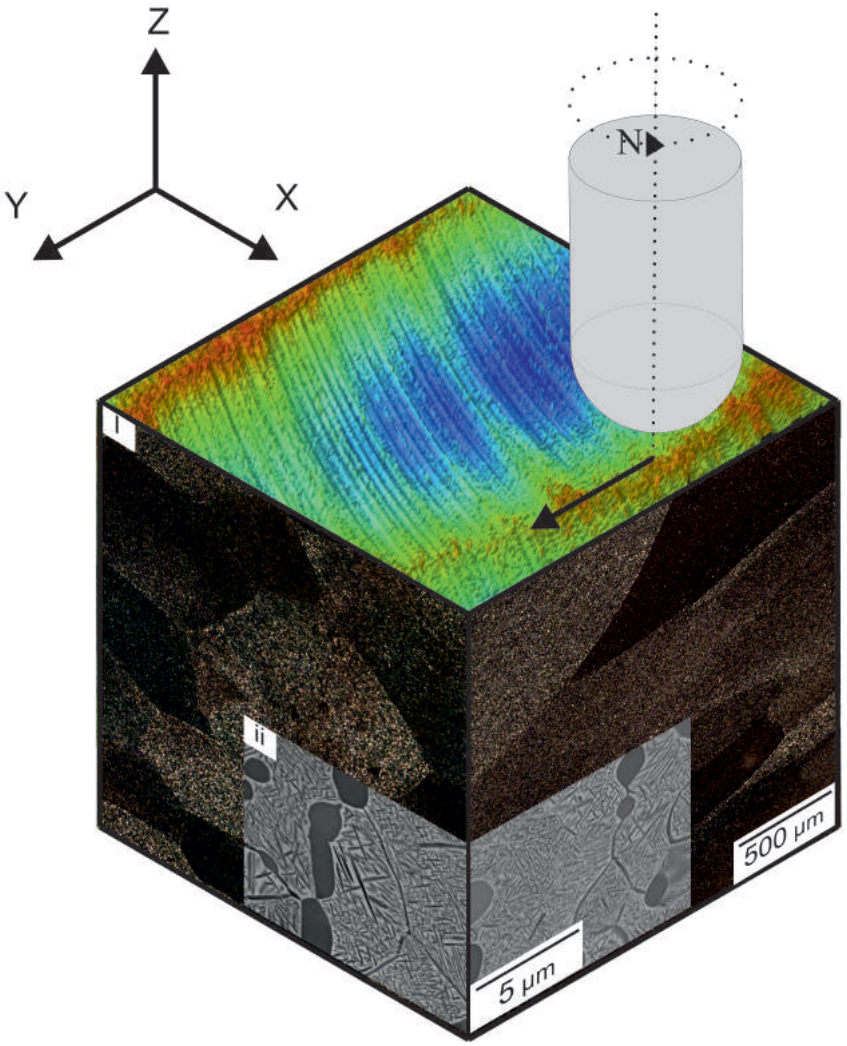

Figure 4.9: Schematic representation for ball nose finish end milling, main planes with respect to microstructure a. OM and b. BSEI in the feed (Y), cutting (X) and tool axis (Z) directions.

It is important to clearly identify, due to the complex 3D nature of ball nose end milling operations, the directions and planes of the surface and subsurface of the component with respect to the tool system. Throughout this thesis the Z axis will be referred to as the normal direction (ND) from which the tool lead angle is positioned. The Y axis will be referred to as the direction for which the tool is fed, or the feed direction (FD), with the associated plane parallel to this referred to as the Y plane. The X axis will be referred to as the direction of the axial depth of cut (a_e), or the cutting direction (CD), with the associated plane parallel to this referred to as the X plane. A visual representation of this axis system can be seen in Fig.4.9. The subsurface planes X and Y, as represented in Fig. 4.9, for individual samples these planes are independent of the forging axis.

4.1.3 Summary

Through this preliminary some fundamental aspects have been defined and will be considered throughout this thesis.

- **Condition of supply** The influence of the condition of supply (COS) from VSMPO AVISMA and the prerequisite machining operations must considered

during cutting trials. The closer test coupons are with regards to microstructure and mechanical properties to manufacturing quality material, the more accurate and applicable the results will be.

- **Microstructural distribution and orientation** Test coupons but be in the STA heat treated condition to avoid localised microstructural variations and the relationship between cutting directions and β elongation direction must be understood. Material used for test coupons must be within the outer circumference from forged and heat treated material.
- **Ball nose end milling** This operation has been deemed to be the most important with regards to cost and quality measures and will be investigated in isolation through the alteration of process variables like feed per tooth and cutting speed.

4.2 The effect of cutting parameters on the surface integrity and subsurface microstructure for finish milling of Ti-5Al-5Mo-5V-3Cr

Prior to machining, cross-sectional subsurface EBSD analysis was conducted on the as-received Ti-5553 material, described in section 3.1. Low magnification inverse pole figure (IPF) orientation image maps (OIM) are presented in the X and Y directions, see Fig.4.10a and b respectively. These maps are noise reduced in order to improve the visual representation of global grain orientations.

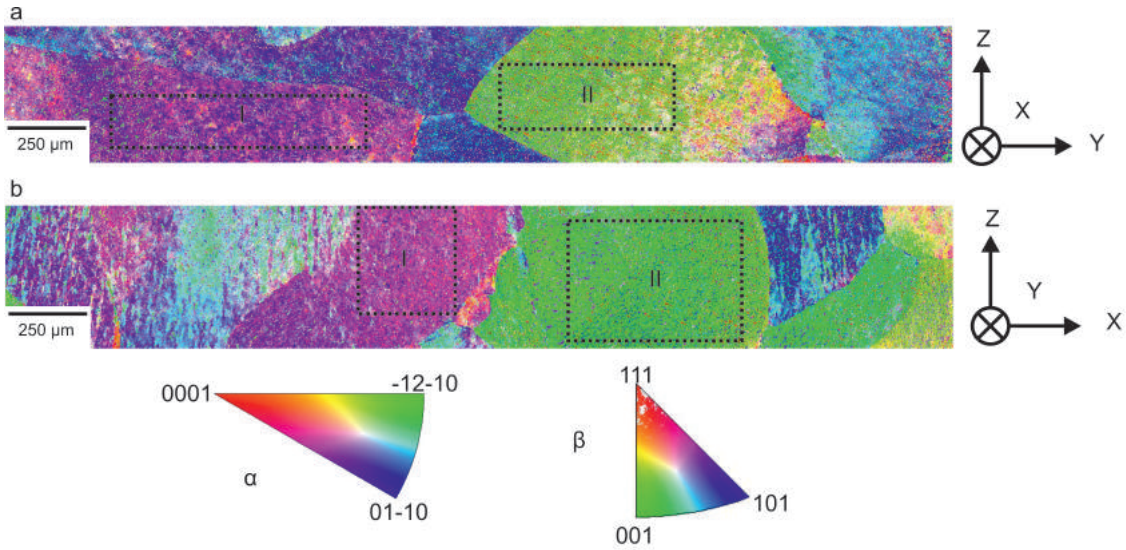

Figure 4.10: Low magnification EBSD noise reduced IPF OIM for the a. X and b. Y orientations of the bulk microstructure.

When considering the mesoscopic scale, strong orientational preferences are shown for individual β grains. Local texture orientations are present in the form of subgrain β, believed to be a result of parent β grain refinement and dynamic recovery during forging and heat treatment operations. Elongation in β grains is clearly visible, as discussed in section 4.1, but shows no clear preferential orientation for either the X or Y directions. This texture, is solely a response of thermomechanical processing. The process of dynamic recovery is impeded at subgrain β boundaries by α_p

pinning. Over the regions examined in Fig.4.10, orientation distribution functions (ODF) of the α phase show results in $f_a(g)_{max}$ of 6.98 and 8.12 (3sf) in the X and Y directions respectively. These results shows a relatively strong texture relationship between the α and β phases. Texture relationships within individual β grains show an ODF $f_a(g)_{max}$ value in the X direction of 42.8 and 13.9 (3sf) for grains i and ii respectively in Fig.4.10a. In the Y direction; grains i and ii, Fig.4.10b, show ODF $f_a(g)_{max}$ values of 32.2 and 21.6 (3sf), respectively. This shows a strong texture, influencing several hundred μm in area within individual β grains and due to the Burgers relationship explored in Fig.4.11, a corresponding strong texture preference by subsequent α_p grains.

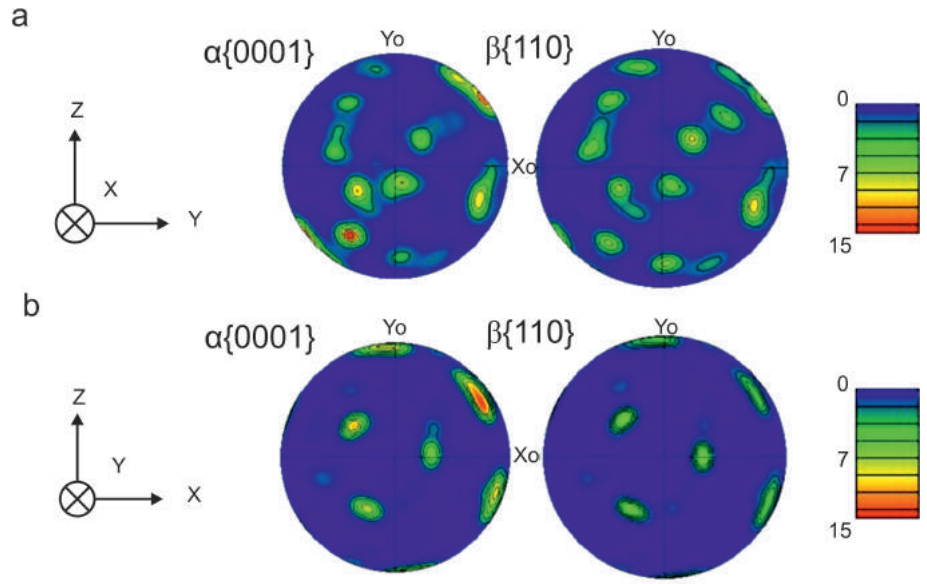

Figure 4.11: Equal area, upper hemisphere pole figures for the hexagonal {0001} and cubic {100} planes with colour contours in multiples of uniform density (MUD) as a result of low magnification EBSD analysis of the a. X and b. Y directions of the bulk microstructure.

Equal area upper hemisphere pole figures for the hexagonal basal plane {0001} and cubic {110} plane, for both directions, are shown for a range of multiples of uniform density (MUD) units in Fig.4.11. According to the Burger's orientation relationship, these planes should be parallel and therefore, the pole density contours should be representative of one another. Fig.4.11 confirms a good adherence to the Burger's orientation relationship, showing strong influence between α_p and parent β grains orientations in both directions.

All conditions depicted in Fig.3.8 were successfully achieved and multiple coupons were produced, as described in section 3.3. Fig.4.12 shows the results of tool system vibrational stability assessment. The results of 10 high coherence strikes in two directions, with respect to tool direction are presented over a range of spindle speed (RPM) and depths of cut (mm). It can be seen in Fig.3.8, for this tool system, the stability lobe diagram predicts all cutting conditions are achievable in a stable manner and no significant instability and chatter was to be expected. There is also evidence, outside the scope of this research, that further increases in cutting parameters such as depth of cut can be achieved with this tool system within a stable condition. Further accuracy to these results could be achieved through the assessment of the workpiece frequency response function; no standard method was

developed for this approach so the results were not taken. It can be concluded that, within the test conditions applied, any noticeable changes to surface roughness are as a result of the cutting parameters and not due to any induced self-excited vibration or chatter.

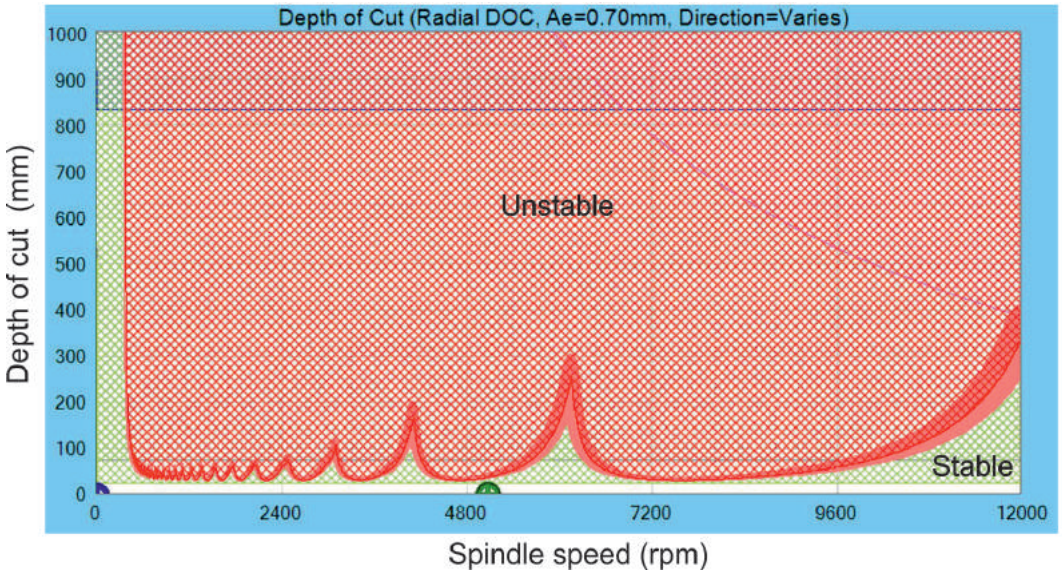

Figure 4.12: Schematic representation of the tool system stability over a range of cutting speeds and depths of cut for finish end milling on the Starrag STC 1250 machining centre.

Prior to the completion of experimental cutting trials, all coupons were photographed in their as cut state then lightly cleaned with isopropanol and compressed air, in order to remove excess coolant. Each coupon was subject to die penetrant and photographed at different magnifications in order to identify the presence of any major defects, such as surface cavities or tearing. Examples of this investigation for condition 1 and 2 are presented in Fig.4.13a and b respectively. No milled surface produced major observable surface defects using this technique.

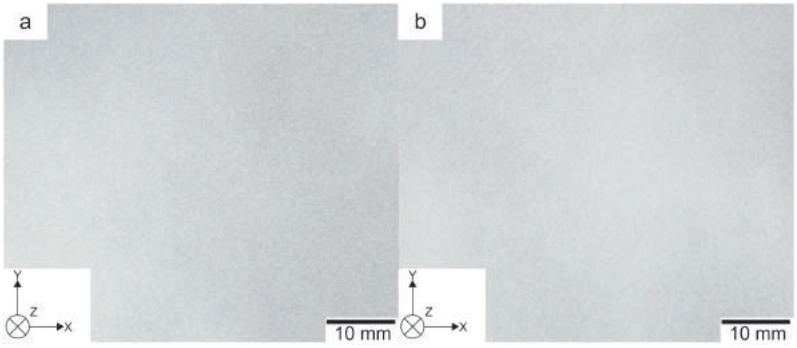

Figure 4.13: Photographs of the resultant surfaces for die penetrant testing of finish milled coupons subject to cutting parameters a. 1 and b. 2.

4.2.1 The effect of cutting speed

Conditions 1, 2 and 3 determine the isolated effect of increased V_c, from 300 to 375 and 450 m/min, respectively. No surface defects can be observed, Fig.4.14. These cutting conditions would successfully pass initial observational qualification for production by SLS.

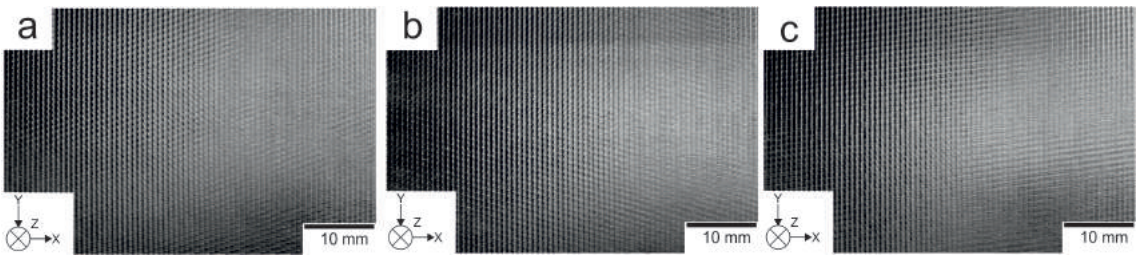

Figure 4.14: Photographs of the finish end milled surfaces for conditions a. 1, b. 2 and c. 3, coupons subjected to increased V_c of 300, 375 and 450 m/min respectively.

Under light microscopy, the influence of increased V_c is readily observed, Fig.4.15. At 300 m/min, a conventional end milled surface profile is produced, typical of SLS components. This result gives further confidence that through this trial design, production machining processes have been accurately replicated. A variation in cusp width is witnessed along the feed direction (Y), of between 647 and 798 μm (3 sf). This results in the average cusp width of 0.7 mm, equal to the radial depth of cut, a_p. As the V_c is increased, a noticeable transition in surface profile is produced with respect to cusp width and form. The cusp form becomes more linear in appearance, yet, the average cusp width is maintained. This consistency of surface profile and quality is in agreement with results in the literature, discussed in Chapter 2. Due to the short duration of cutting and the use of new cutting tools, limited tool wear was experienced and the minimal increased SGR across these three conditions, results in a limited effect on surface quality. The observed change in cusp form is due to the change in tooth frequency as spindle speed (RPM) increases at a constant feed rate (f).

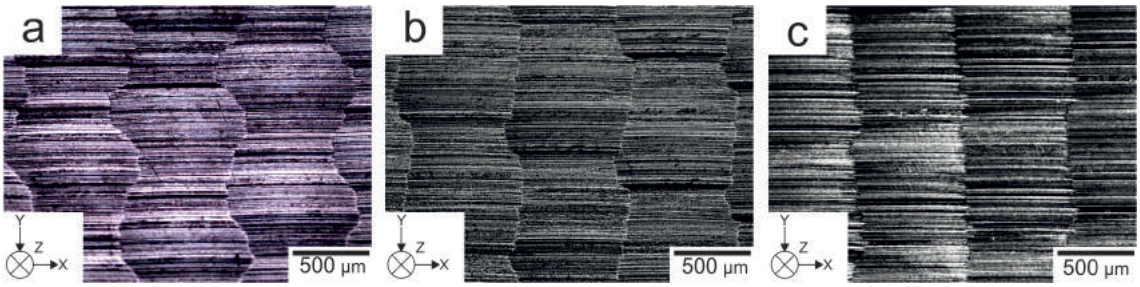

Figure 4.15: Light micrographs at x10 magnification of the finish end milled surfaces for conditions a. 1, b. 2 and c. 3, coupons subjected to increased V_c of 300, 375 and 450 m/min respectively.

Images taken using a 3D light microscopy as in section 3.2, show in superior detail, the localised surface topography with 3D contour plots at x5 magnification. The change in tooth frequency with spindle speed can be identified as variations of major feed marks, which are perpendicular to the tool direction (Y), see Fig.4.16. At high V_c, major feed marks become less frequent producing a more distinct and linear surface topography. Images taken at this magnification, provide evidence for their being no presence of surface defects with increased V_c.

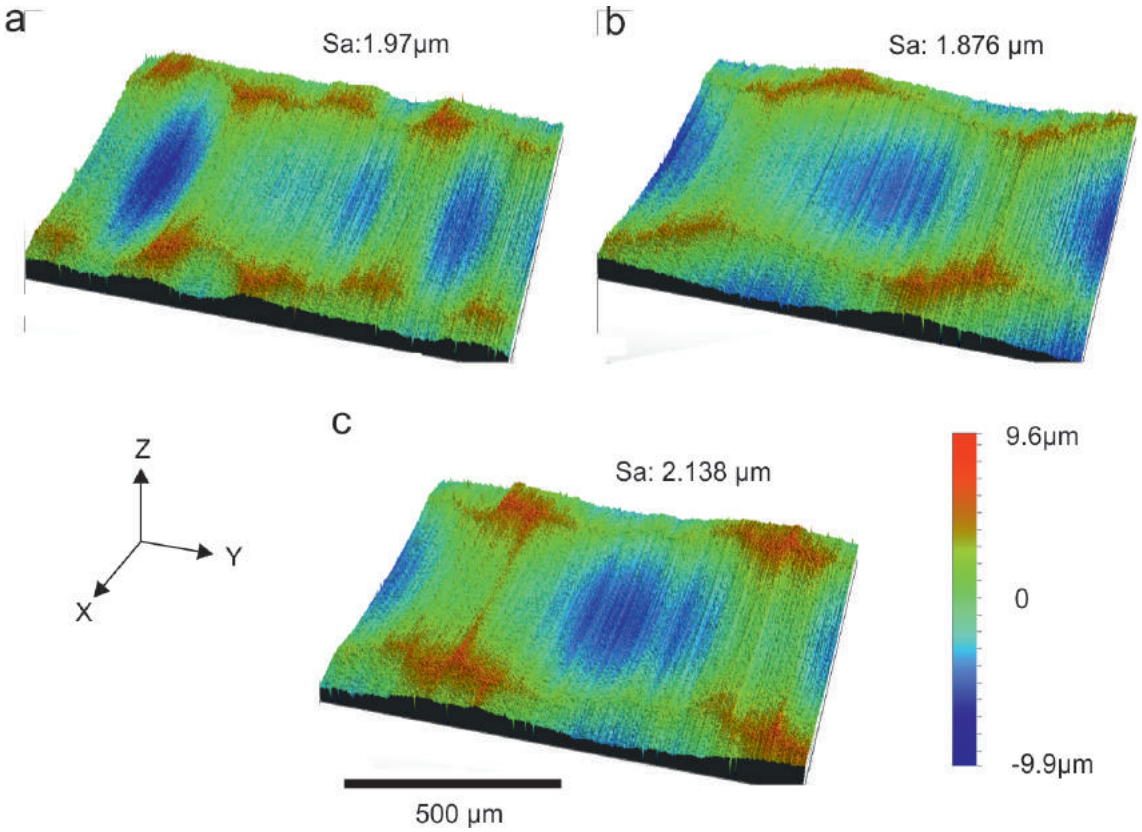

Figure 4.16: 3D Light images at x5 objective of the finish end milled surfaces for conditions a. 1, b. 2 and c. 3, coupons subjected to increased V_c of 300, 375 and 450 m/min respectively.

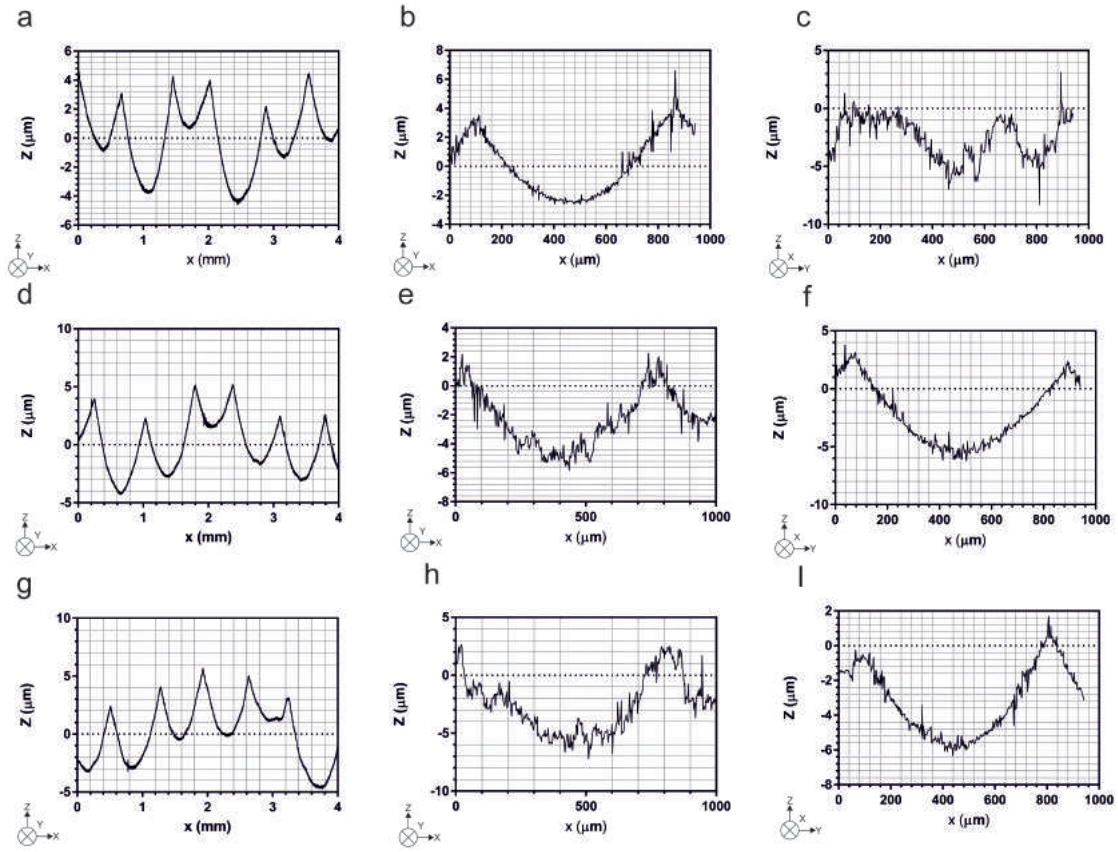

Figure 4.17: Roughness profiles for condition 1, 2 and 3 in a, d and g. 2D in the X direction and 3D in the b, e and h. X and c, f and i. Y directions.

Fig.4.17 presents 2D and 3D roughness profiles for all three conditions. Results in Fig.4.17 b, c, e, f, h and i correspond to averages of 50 line scans of those regions shown in Fig.4.16 in two orientations X and Y, perpendicular and parallel to the tool direction respectively. Results in Fig.4.17 a, d and g correspond to the average of three line scans in the X orientation, perpendicular to the tool direction. As can be seen from the 2D roughness profiles, Fig.4.17a, d and g, for increased V_c; conditions 1, 2 and 3, correspond to minimal effect to the secondary waviness profile, as described in the literature [42]. This increase in V_c also has a negligible affect on the primary profile, which is reflected in the consistency of average cusp height (R_t) of approximately 9 μm. Across all conditions, observable in both the 2D and 3D measurements in the both orientations, a minimal effect on the tertiary roughness profile is observable. The inherent improved resolution of the 3D measurements shows how increasing V_c, above 300 m/min, has induced roughness, especially within the valleys of the waviness profile, Fig.4.17 b, e, and h. The behaviour in which the frequency of the feedmarks is decreased can also be observed in Fig.4.17 c, f and i. This results in the major cusp and feedmark frequency becoming analogous to one another, creating the square like topography, shown in Fig.4.16. Variations in the 2D amplitude roughness parameter R_a are negligible with average values in the X orientation of 1.226, 1.323 and 1.239 μm (3dp) for conditions 1, 2 and 3, respectively. The more sensitive root mean squared (R_q) parameter shows a similar negligible increase at intermediate V_c in the X orientation of 1.42, 1.551 and 1.421 μm (3dp), for conditions 1, 2 and 3, respectively. All cutting parameters show a small positive skew (Sk), suggesting a tendency towards an increased number of high peaks above the mean. Conditions 1, 2 and 3, have values of 0.489, 0.681 and 0.383 respectively. Kurtosis (Ku) results of 2.044, 2.304 and 1.923 for conditions 1, 2 and 3, respectively, reveal a weak platykurtoic distribution with few high peaks and low valleys. Results from 3D spatial roughness parameters S_a and S_q, show greater increases in roughness when compared to 2D roughness parameters for the same conditions. In agreement with 2D metrics, minimal influence can be observed with increased V_c which correlates well with the 3D topographical images,Fig.4.16. Results show a slight increase at the highest V_c, with conditions 1, 2 and 3 possessing S_a values of 1.97, 1.876 and 2.138 μm (3sf) and S_q of 2.44, 2.286 and 2.626 μm (3sf), respectively. These results show good agreement with existing literature, in which V_c presents limited influence on conventional 2D roughness parameters for cutting of titanium alloys [31, 34, 35].

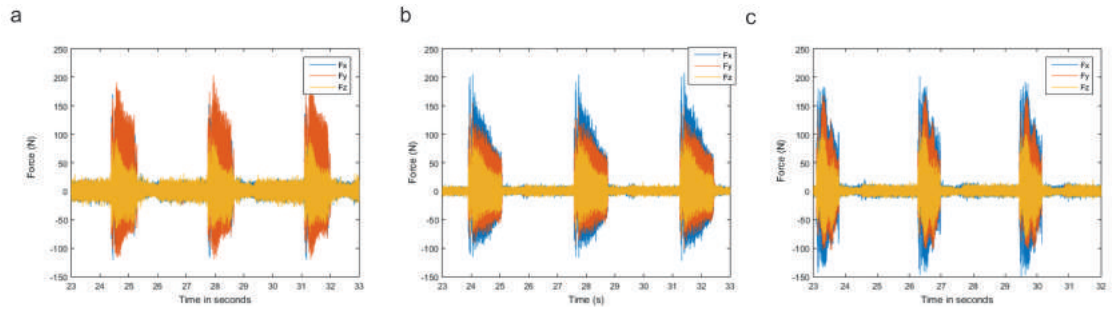

Figure 4.18: Cutting force profiles for conditions a. 1, b. 2 and c. 3, coupons subjected to increased V_c of 300, 375 and 450 m/min respectively, in the X, Y and Z; normal, thrust and cutting force directions respectively.

Cutting forces were recorded for the duration of cutting trials, as defined in section 3.2. Fig.4.18 shows cutting forces in the three fundamental directions; feed,

thrust and cutting force with respect to the tool axis for 3 cutting passes for each condition. The average maximum feed, thrust and cutting force for condition 1 are 176.46, 203.333 and 95.452 N (3sf), respectively. As V_c increases, both the thrust and cutting forces are seen to fall to 155.735 and 109.173 N (3sf), for condition 2 and 168.876 and 116.714 N (3sf), for condition 3. However, it was seen that the feed force increased to 207.901 N (3sf) and 202.157 N (3sf) for conditions 2 and 3 respectively. This behaviour is schematically visible in the data plotted in Fig.4.18 as the time progresses the tool proceeds further down the cutting path of the coupon. The ϕ_{effmax} decreases, as does the $V_{c_{eff}}$, corresponding to a reduction in cutting forces. This result corresponds with findings in literature as depicted in Fig.2.43 [22, 94].

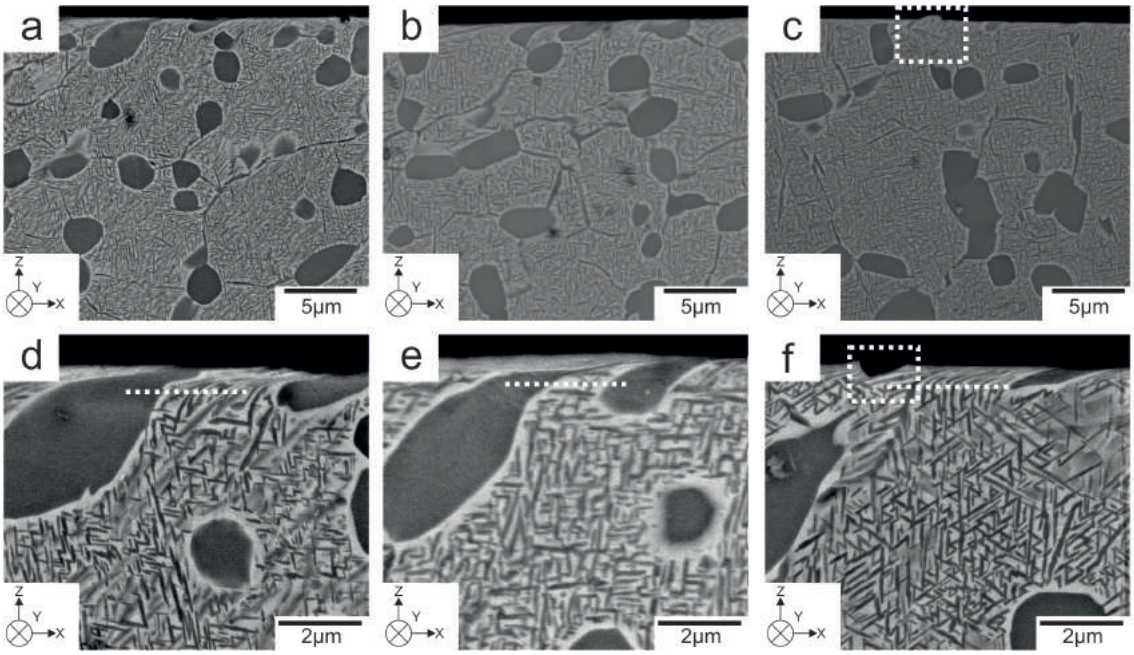

Figure 4.19: BSEI at a-c. x10,000 and d-f. x30,000 magnification of the finish end milled subsurface for conditions a & d. 1, b & e. 2 and c & f. 3, coupons subjected to increased V_c of 300, 375 and 450 m/min respectively in the X orientation.

This limited variation in cutting forces corresponds with the negligible effect on subsurface deformation as shown in Fig.2.42 and agrees with literature [22]. Deformation that can be inferred from light microscopy is limited by magnification and the localised nature of the SPD layer in Ti-5553. Fig.4.19 summarises, at two magnifications in the X orientation, the effect of V_c on subsurface deformation. Typical microstructural responses to deformation as a result of finish end milling include elongation and plastic deformation to α_p and α_s grains and surface tearing which can not be confirmed with BSEI alone. The observed depth of SPD changes in no observable manner at high V_c and becomes more localised to the near surface. No plastic deformation is observed below the surface at a depth of 2 μm, in any condition in the X orientation. Elongation to α_p above this depth is identified in Fig.2.42 by the white dashed line. Above this, α_p and α_s grains are elongated and distorted in the direction of the tool rotation, a behaviour which is exacerbated at increased V_c. At the highest V_c of 450 m/min, i.e. condition 3, examples of surface cavitation and deformation are observable and are highlighted by the white dashed box in Fig.2.42 c and f. Similar microstructural features have been observed in an array of titanium alloys subject to turning and milling operations [14, 22, 34, 53, 89, 91, 92].

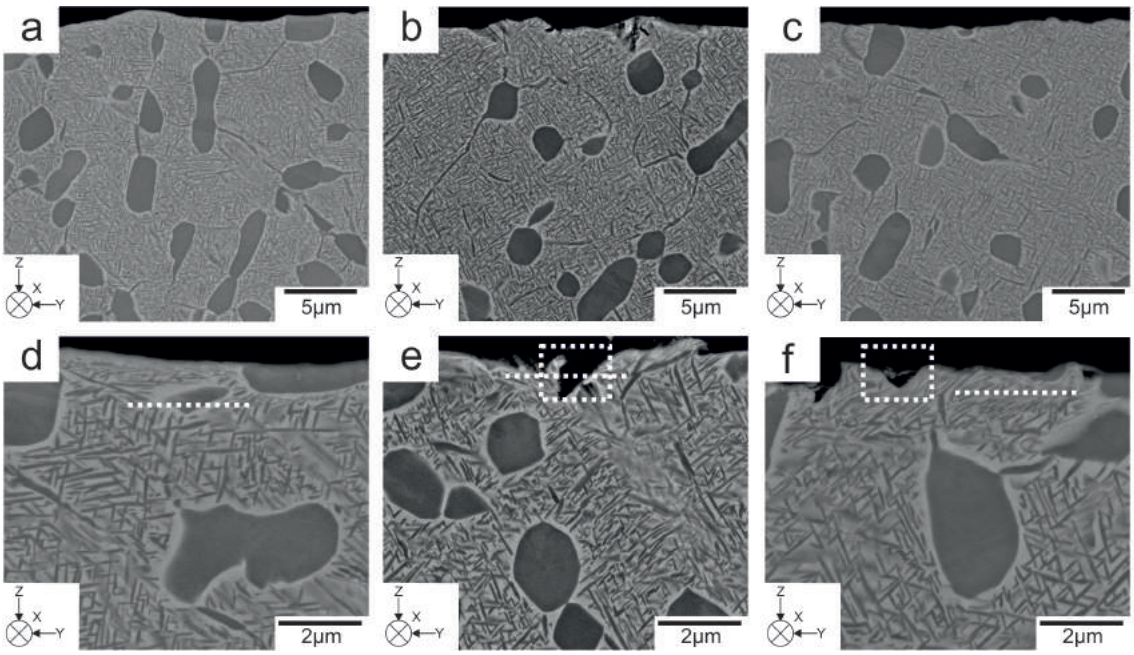

Figure 4.20: BSEI at a-c. x10,000 and d-f. x30,000 magnification of the finish end milled subsurface for conditions a & d. 1, b & e. 2 and c & f. 3, coupons subjected to increased V_c of 300, 375 and 450 m/min respectively in the Y orientation.

Fig.4.20 presents the cross-sectional subsurface deformation perpendicular to the tool direction and those regions presented in Fig4.19. In comparison, the elongation and distortion to α_p in the Y orientation is less pronounced. The influence of the feed marks, as previously discussed and observable in Fig.4.16 and 4.17, present themselves as surface cracks and cavitation in a much more pronounced way, when compared to the X orientation. These microstructural and surface features are seen more readily in conditions 2 and 3, as V_c is increased. Despite the limited presence of α_p elongation distortion of α_s is evident in the upper 2 μm of each condition. Again, as V_c increases, this observable SPD layer becomes more localised to the surface. Regions within certain α_p grains below the observed SPD region indicate plastic deformation. As no clear evidence of slip or twinning is present, it is determined that the contrast variation present in these α_p grains; for example in in Fig.4.20e, arise from imparted stress which is accommodated through lattice rotation as discussed by [22]. These microstructural features are evident to depths of 25-30 μm in condition 2, the V_c which corresponds to the highest feed force, as shown in Fig.4.18. However, this behaviour is not present in all neighbouring grains, suggesting a crystallographic dependency in the nature of imparted deformation.

4.2.2 The effect of feed per tooth

As with V_c, the isolated effect of increased f_z from 0.14 to 0.22 and 0.3 mm/tooth respectively, can be investigated with conditions 1, 4 and 5. As with conditions 2 and 3, at increased f_z, no significant surface defects can be observed at low magnification and no chatter or instability was observed during cutting. These results, again, show that these conditions would successfully pass initial observational qualification for production at SLS.

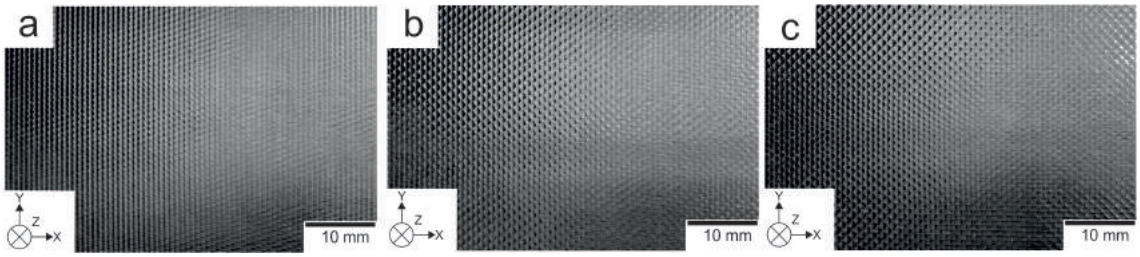

Figure 4.21: Photographs of the finish end milled surfaces for conditions a. 1, b. 4 and c. 5, coupons subjected to increased f_z of 0.14, 0.22 and 0.3 mm/tooth respectively.

Photographs of conditions 1, 4 and 5, can be seen in Fig.4.21, in which no discernible differences can be seen, nor surface defects.

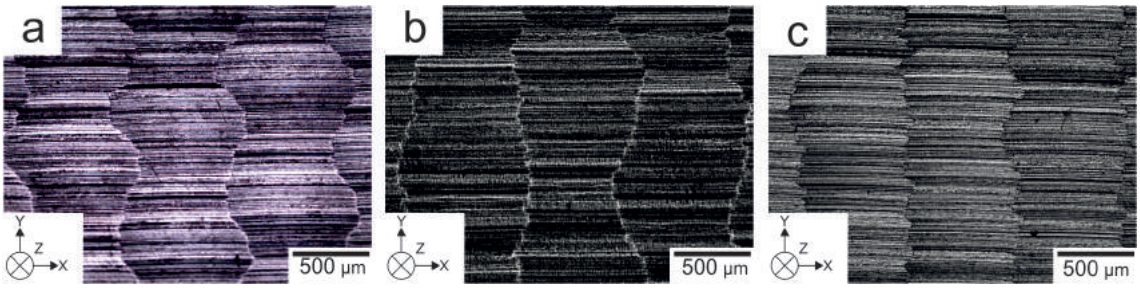

Figure 4.22: Light micrographs at x10 magnification of the finish end milled surfaces for conditions a. 1, b. 4 and c. 5, coupons subjected to increased f_z of 0.14, 0.22 and 0.3 mm/tooth respectively.

Under light microscopy at higher magnifications, the influence on increased f_z is readily observable as in Fig.4.22. Fig.4.22a is identical to the condition shown in Fig.4.15a and when compared to condition 4 and 5, the effect of increased f_z on surface profile can be seen. A variation in cusp width is observable parallel to the tool direction (Y), see Fig.4.22b. The average cusp width of 0.7 mm is maintained across all conditions, but at 0.22 mm/tooth, the measurable maximum and minimum cusp widths reach 797.887 and 646.714 μm (3dp) respectively. When the f_z reaches 0.3 mm/tooth, the cusp form becomes straighter. Again, this observed change in surface profile is due to the change in tooth frequency as the feed rate increases at a constant V_c. As f_z is increased to 0.3 mm/tooth, the feed marks become much more pronounced.

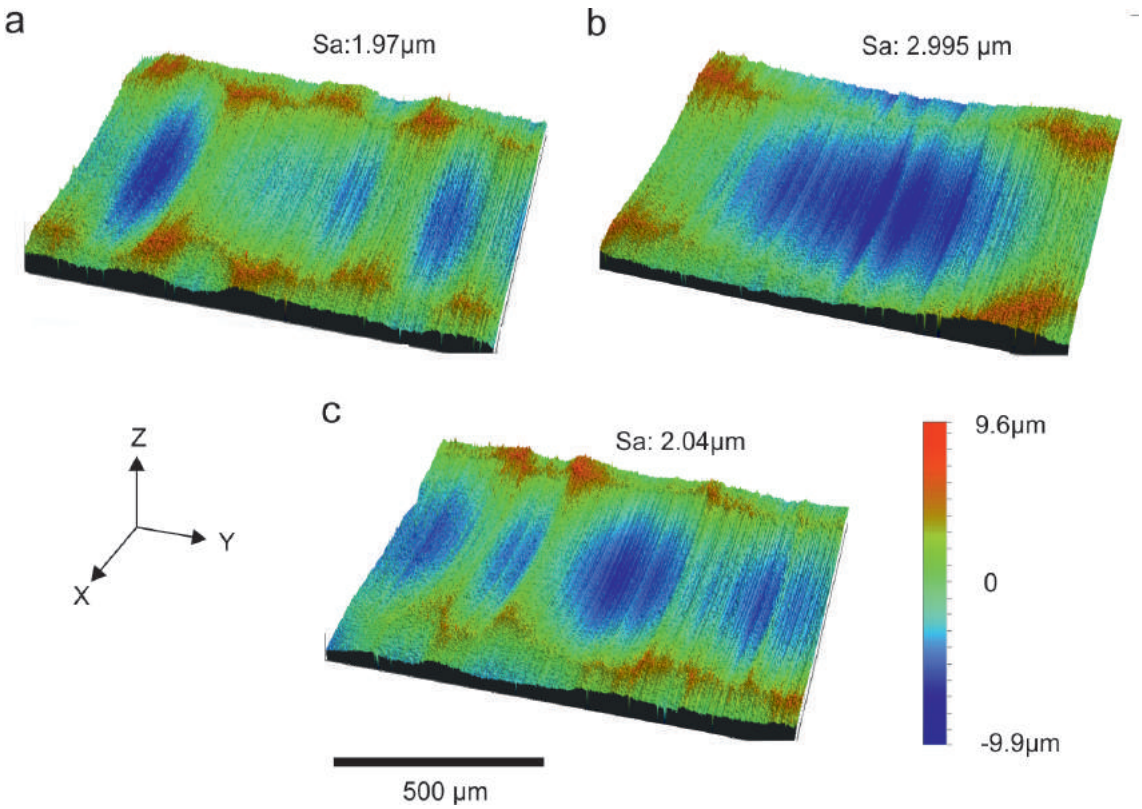

Figure 4.23: 3D Light images at x5 objective of the finish end milled surfaces for conditions a. 1, b. 4 and c. 5, coupons subjected to increased $f_z$of 0.14, 0.22 and 0.3 mm/tooth respectively.

The influence of increasing f_z becomes more distinct, as seen in Fig.4.23; images taken using 3D light microscopy. As with V_c, coupons subject to increased f_z produce anisotropic surface topographies in which the changing tooth frequency and tool eccentricity influences the feed marks and cusp forms, a phenomena discussed in the literature [87].

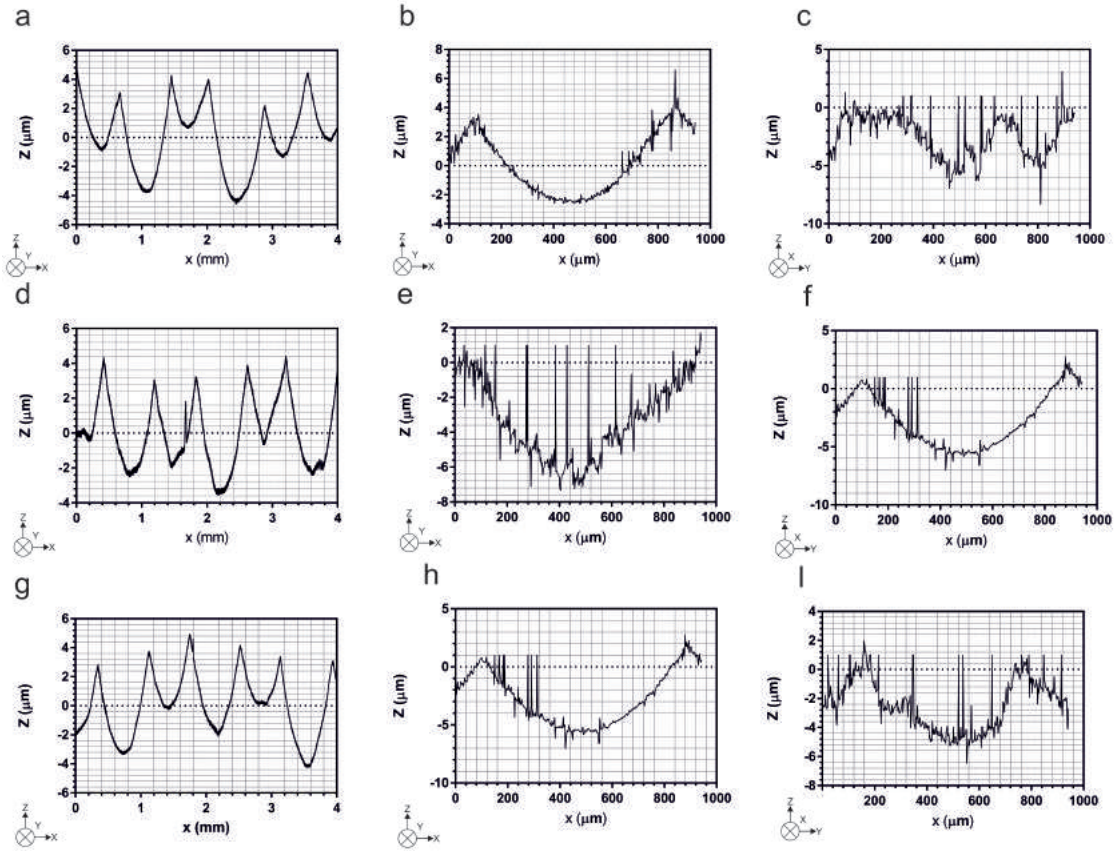

Figure 4.24: Roughness profiles for condition 1, 4 and 5 in a, d and g. 2D in the X direction and 3D in the b, e and h. X and c, f and i. Y directions.

Fig.4.24 presents 2D and 3D roughness profiles for all three conditions, with 3D profiles exhibited in Fig.4.24 in two orientations X and Y, perpendicular and parallel to the tool direction. Increased f_z; conditions 1, 4 and 5, see Fig.4.24a, d and g, respectively, influence the secondary waviness profile. Condition 4 produces a waviness profile with much sharper cusp peaks than the other conditions f_z utilised. A noticeable increase in third order roughness within the valleys as produced by the f_z increases from condition 1 to 5 Fig.4.24 a, d and g respectively with distinct increases in valley roughness for condition 4. Much like the cusp width, the average cusp height (R_t) across all three conditions, of approximately 9 μm is maintained to results of increased V_c. Variations in the 2D amplitude roughness parameter R_a are negligible between conditions 1 and 4, in which the average values in the X orientation are 1.226, 1.287 microns (3dp), respectively. For the high f_z condition 5, the R_a value reaches 1.368 μm (3dp). The increase in tertiary roughness profiles within cusps is distinguished through high resolution 3D measurements, shown in Fig.4.24 b, c, e, f, h and i. This is most noticeable in the X orientation. It can be postulated that this increase in roughness may influence both subsurface deformation and fatigue life by increased density of stress raising crack initiation sites. Results from 3D spatial roughness parameter S_a show identical behaviours with results for conditions 1, 4 and 5 being 1.97, 2.995 and 2.04 μm (3dp) respectively. The root mean squared R_q parameter and the 3D equivalent S_q show opposing behaviours. For conditions 1, 4 and 5 the R_q values are 1.42, 1.489 and 1.634 μm (3dp), respectively where the increase in f_z corresponds to a marginal increase in roughness. Whereas, the S_q values are 2.44, 3.575 and 2.443 μm (3dp) for conditions 1, 4 and 5, respectively, where a significant increase for 0.22 mm/tooth is noticeable. The positive skew ob-

served in all conditions shows increases with f_z with conditions 1, 4 and 5 resulting in skews of 0.489, 0.524 and 0.618 (3dp) respectively. This positive skew is reduced when 3D spatial parameters are considered, with conditions 1, 4 and 5 resulting in skews of -0.192, 0.117 and 0.178 (3dp) respectively. The increase of skew with f_z suggests the tendency for f_z to increase the severity of roughness peaks. Spatial kurtosis parameters suggest that with increased f_z, the surface roughness becomes more platykurtoic in its distribution, with relatively few high peaks and low valleys. Kurtosis (Ku) in 2D for conditions 1, 4 and 5 are 2.044, 2.078 and 2.447 (3dp) respectively. A trend that disagrees with 3D SKu measures of 2.709, 2.193 and 2.352 (3dp) respectively. It is clear, in comparison to V_c, the isolated increase in f_z has a more noticeable influence on surface topography and roughness measures. These results are in agreement with existing literature, in which f_z shows a positive effect on conventional 2D roughness parameters for titanium alloys [31, 34, 35].

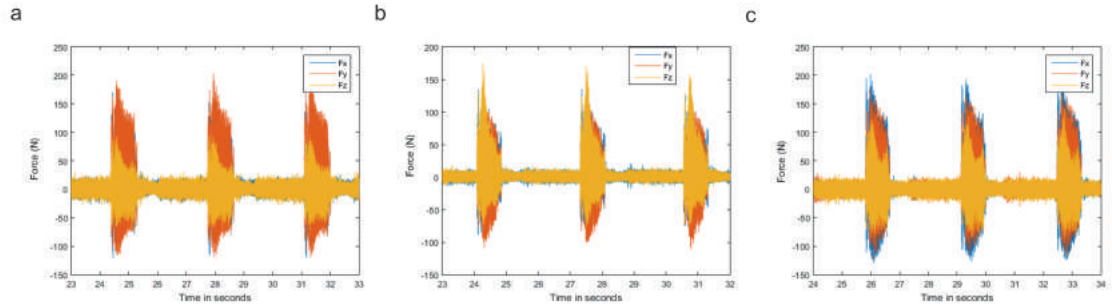

Figure 4.25: Cutting force profiles for conditions a. 1, b. 4 and c. 5, coupons subjected to increased f_z of 0.14, 0.22 and 0.3 mm/tooth respectively, in the X, Y and Z; normal, thrust and cutting force directions respectively.

Fig.4.25 presents examples of cutting forces in three directions; feed, thrust and cutting force with respect to the tool axis for each condition. The average maximum feed, thrust and cutting force for condition 1 are 176.46, 203.333 and 95.452 N (3dp), respectively. As the f_z increases, both the feed and thrust forces decrease to 144.328 and 116.276 N (3dp) respectively for condition 4. However, the major cutting force increases significantly to 174.762 N (3dp). When the f_z is increased to 0.3 mm/tooth, as in condition 5, feed and thrust forces increase to 205.745 and 176.057 N (3dp), respectively, but the major cutting force decreases to 140.797 N (3dp), Fig.4.25. Though the relationship is not linear, f_z has been shown to increase cutting forces in differing directions in a significant manner than increased V_c. This result satisfies the findings determined in literature as depicted in Fig.2.43 [22, 94].

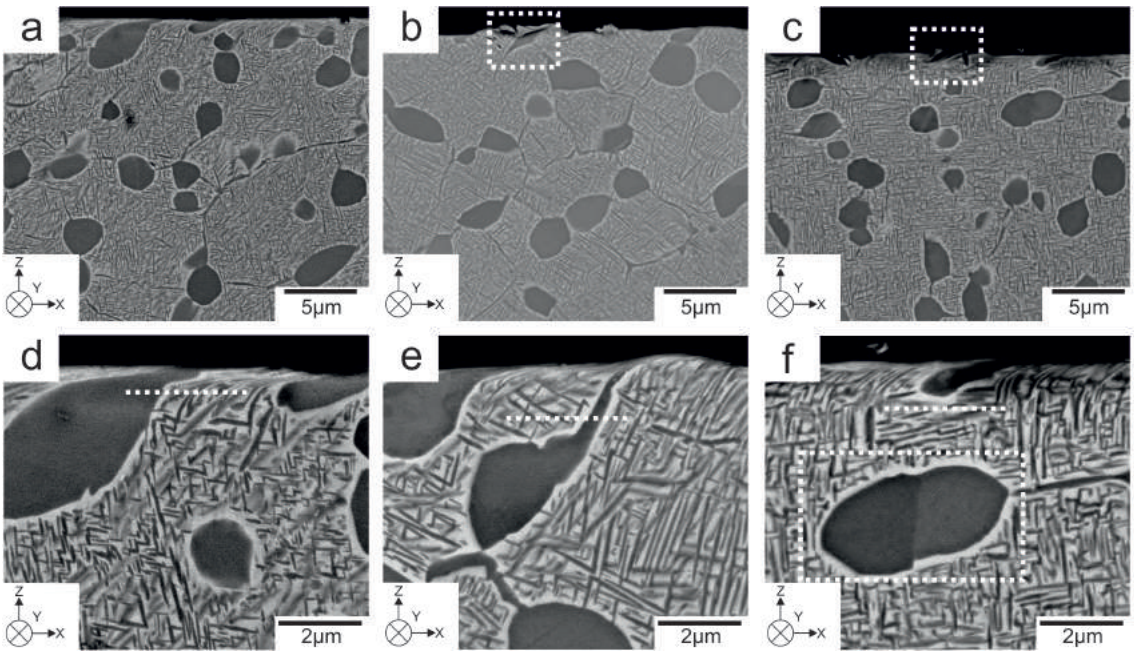

Figure 4.26: BSEI at a-c. x10,000 and d-f. x30,000 magnification of the finish end milled subsurface for conditions a & d. 1, b & e. 4 and c & f. 5, coupons subjected to increased f_z of 0.14, 0.22 and 0.3 mm/tooth respectively in the X orientation.

This variation in cutting forces goes some way to explain the effect on subsurface deformation as the imparted stress in conditions 1, 4 and 5 with vary. This has been discussed in literature, Fig.2.44 [21, 96]. The observed depth of SPD increases gradually with f_z from <2 to >3 μm but is therefore still much localised to the near surface, Fig.4.26. The most significant influence of increased f_z however, is not from the effect on α_p distortion, but induced strain within α_p grains distinguished as contrast variations in Fig.4.26. Surface cavitation and the associated subsurface distortion is produced with increased f_z when compared to increased V_c. These deformation induced features were only induced in the highest V_c and observable only in the Y orientation.

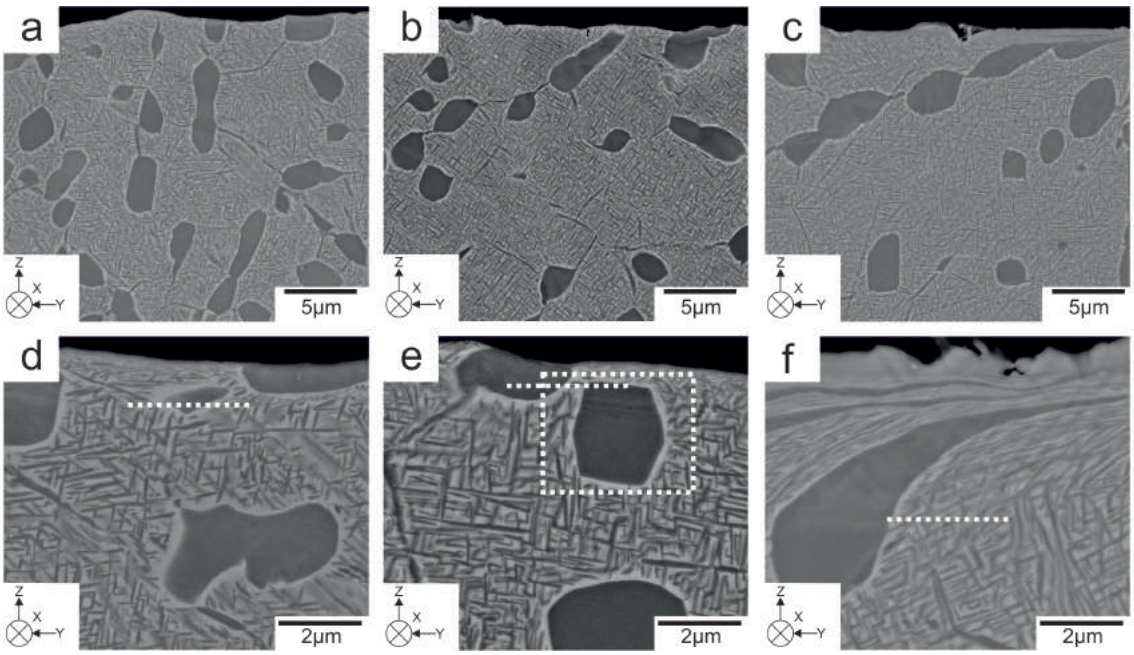

Figure 4.27: BSEI at a-c. x10,000 and d-f. x30,000 magnification of the finish end milled subsurface for conditions a & d. 1, b & e. 4 and c & f. 5, coupons subjected to increased f_z of 0.14, 0.22 and 0.3 mm/tooth respectively in the Y orientation.

As with increased V_c, f_z induced deformation is far more noticeable in the Y than the X orientation, see Fig.4.27. As f_z is increased to 0.22 mm/tooth as in Fig.4.27b and e, the depth of SPD remains consistent, although clear regions of induced strain and evidence of dislocation slip is present. When f_z is increased further to 0.3 mm/tooth, an increase in SPD and elongation to α_p and α_s occurs. The induced deformation is severe enough in the upper 3 μm of the subsurface, that the contrast between α and β phases is indistinguishable. This cutting condition has induced deformed nano-composite layers of α and β phases that resembles a white layer. The higher levels of deformation found in the Y orientation suggest that the direction of tool motion has a significant influence on damage.

4.2.3 The effect of surface generation rate

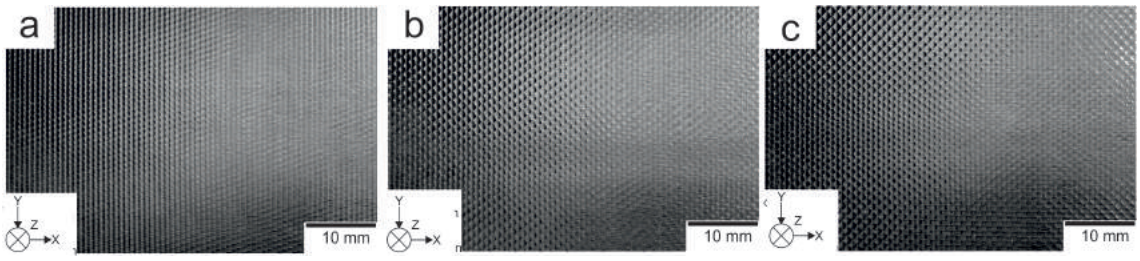

Figure 4.28: Photographs of the finish end milled surfaces for conditions a. 1, b. 6 and c. 7, coupons subjected to increased SGR 0.14, 0.22 and 0.3 mm/tooth and 300, 375 and 450 m/min respectively.

Conditions 1, 6 and 7 represent the combined effect of increased V_c and f_z, as shown in Fig.3.8. The influence of increased SGR, can be seen from low magnification photography. Fig.4.28b and c show that a repeated square surface profile pattern is produced and maintained.

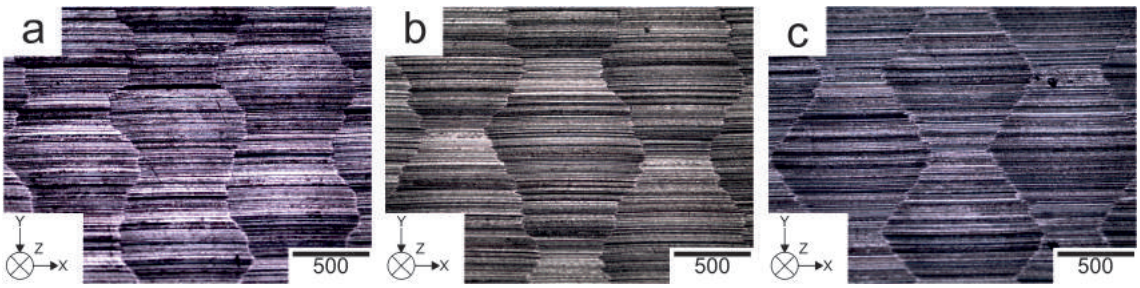

Figure 4.29: Light micrographs at x10 magnification of the finish end milled surfaces for conditions a. 1, b. 6 and c. 7, coupons subjected to increased SGR 0.14, 0.22 and 0.3 mm/tooth and 300, 375 and 450 m/min respectively.

Under light microscopy at higher magnifications, Fig.4.29 increased SGR influences the surface profile, in a significant manner, different to the that of isolated increases in V_c or f_z. Though the average cusp width is maintained at 0.7 mm, the maximum and minimum cusp widths for increased SGR range considerably. Condition 6 and 7 possess maximum and minimum cusp widths of 997.934 and 395.07 μm (3dp) and 868.692 and 537.15 μm (3dp), respectively.

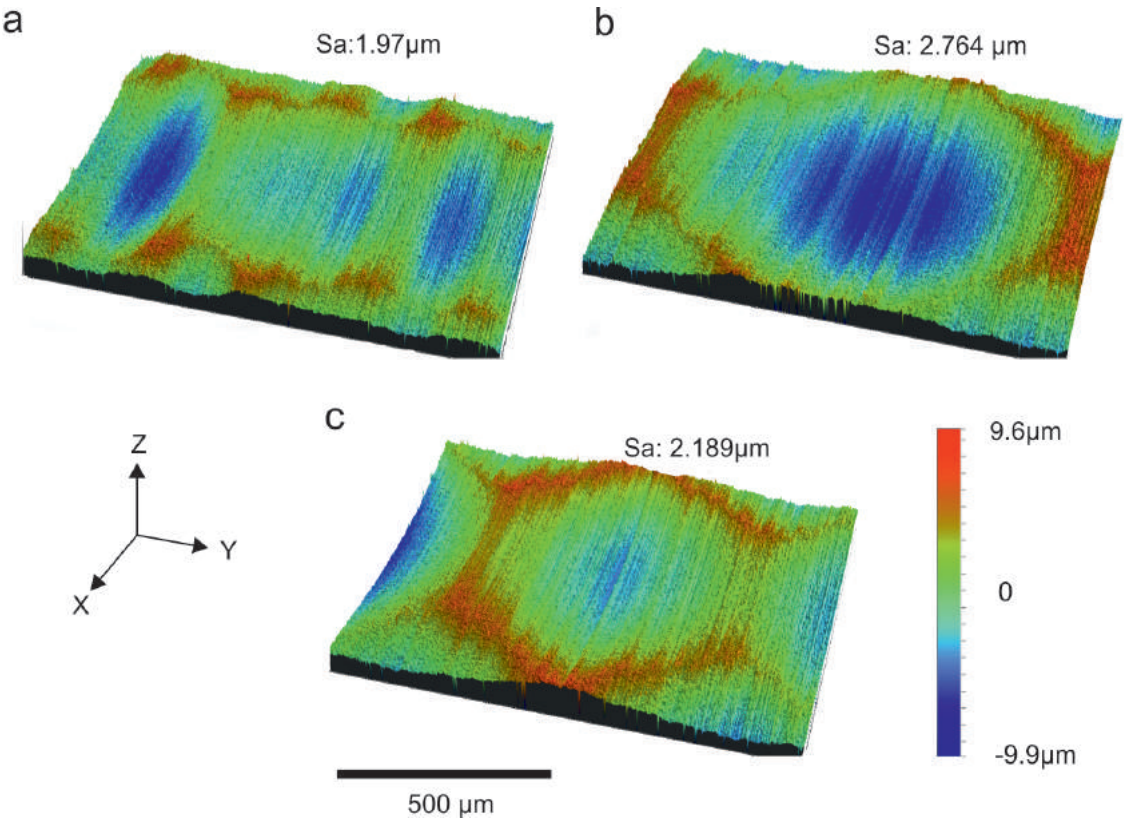

Figure 4.30: 3D Light images at x5 objective of the finish end milled surfaces for conditions a. 1, b. 6 and c. 7, coupons subjected to increased SGR 0.14, 0.22 and 0.3 mm/tooth and 300, 375 and 450 m/min respectively.

The distinct variation in cusp width is observable along the tool direction, Fig.4.30. Fig.4.30b and c shows a clear transition from the profiles produced by condition 1. The combined increase in V_c and f_z has a different influence on surface topography. Feed marks do not become any more distinct than those found by isolated increases in f_z. The complimentary increase in V_c influences the tooth frequency to produce an angular surface topography.

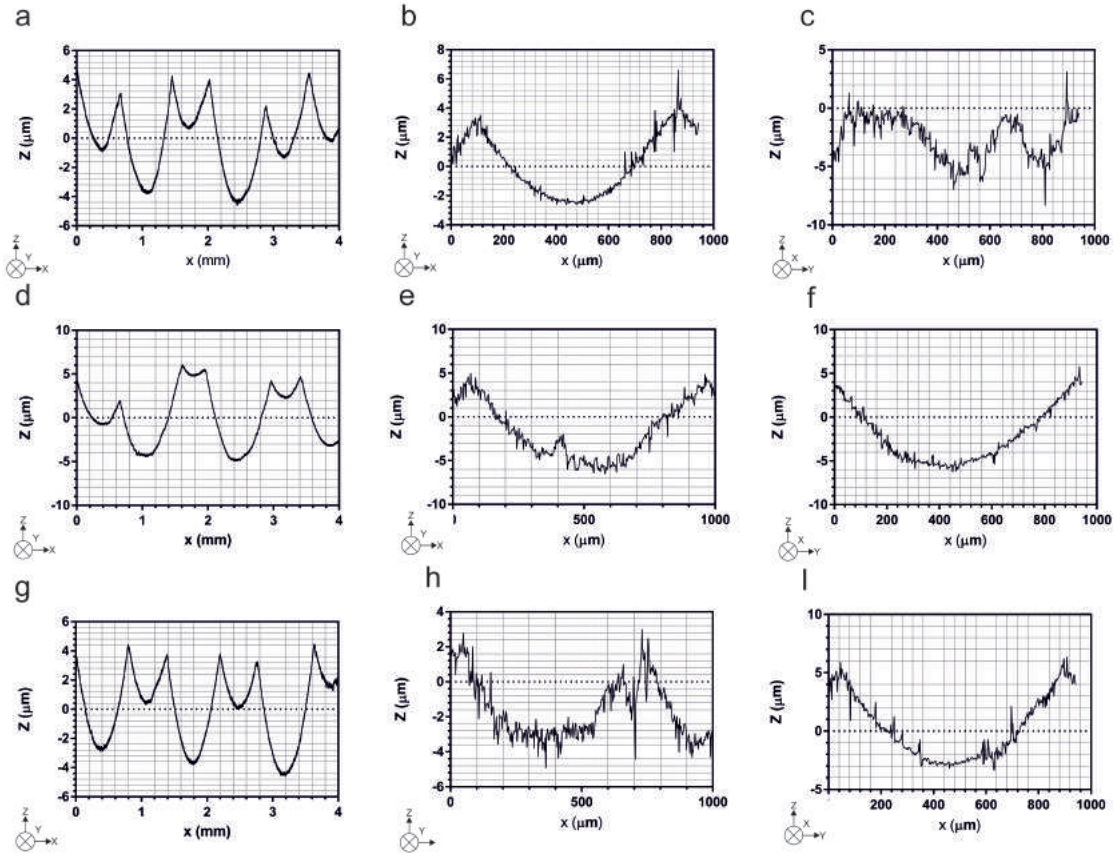

Figure 4.31: Roughness profiles for condition 1, 6 and 7 in a,d and g. 2D in the X direction and 3D in the b, e and h. X and c, f and i. Y directions.

Fig.4.31 presents 2D and 3D roughness profiles for all three conditions. From the 2D roughness profiles, Fig.4.31 a, d and g, the increased SGR corresponds to changes to the secondary waviness profiles. In this orientation, a repeated sequence of deep and then shallow valleys is produced. Within these valleys the tertiary roughness profile remains consistent. Unlike previous conditions, the average cusp height of 9 μm is not maintained across all conditions. For conditions 6 and 7, cutting produced R_t values of 8.312 and 7.611 μm (3dp) respectively. Values in R_a in the X direction for conditions 1, 6 and 7 were measured at 1.226, 1.074 and 1.24 μm (3dp) respectively, showing that the increase in SGR has had a negligible effect on 2D roughness. The slight decrease in roughness at moderate SGR is consistent when considering R_q values over these three conditions. For conditions 1, 6 and 7, R_q was recorded as 1.41, 1.268 and 1.441 μm (3dp), respectively. Results for 2D skew show a consistent positive skew, suggesting a tendency towards an increased number of high peaks above the mean, with conditions 1, 6 and 7 being 0.489, 0.59 and 0.473 (3dp) respectively. Kurtosis results of 2.044, 2.294 and 2.211 (3dp) for conditions 1, 6 and 7, respectively, reveals a weak platykurtoic distribution from which few high peaks and low valleys, similar to all other conditions tested. When compared to the independent increases in V_c and f_z, the effect of increased SGR on secondary roughness profiles, can be seen to be minimal in both the X and Y orientation. The trend in 2D roughness is reversed when studied in 3D, in which the increase in SGR produces increases in roughness metrics. For S_a, measurements conditions 1, 6 and 7 produced results of 1.97, 2.764 and 2.189 μm (3dp) respectively and S_q results of 2.44, 3.33 and 2.681 μm (3dp), respectively. In 3D, the positive skew is reduced to a small negative skew with -0.192, -0.018 and -0.264 (3dp) for conditions 1, 6 and 7

showing a tendency for low valleys below the mean. Kurtosis results in 3D of 2.709, 2.254 and 2.731 (3dp), respectively show increased platykurtoic distribution from which few high peaks and low valleys.

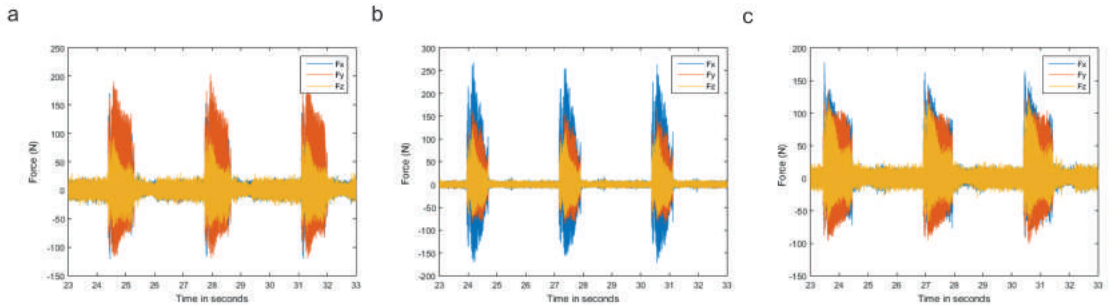

Figure 4.32: Cutting force profiles for conditions a. 1, b. 6 and c. 7, coupons subjected to increased SGR 0.14, 0.22 and 0.3 mm/tooth and 300, 375 and 450 m/min respectively, in the X, Y and Z; normal, thrust and cutting force directions respectively.

Fig.4.32 shows typical cutting forces in three directions; feed, thrust and major cutting force, with respect to the tool axis for each condition. The average maximum feed, thrust and cutting force for condition 1 are 176.46, 203.333 and 95.452 N (3sf), respectively. As SGR increases, feed and cutting forces increase to 268.464 and 124.915 N (3dp), respectively, for condition 6 with a reduction in thrust force to 167.209 N (3dp). At the maximum SGR feed and thrust forces are further reduced to 177.575 and 136.637 N (3dp), respectively, minimal increases with the cutting force show to 128.119 N (3dp). The major cutting force in the Z direction, shows an increase with SGR with feed and thrust forces showing increases at intermediate SGR. An increase in the major cutting force and reductions with thrust and feed forces. When comparing high SGR, condition 7, with high f_z condition, reductions in all three force components are observed. This illustrates the influence of f_z on cutting forces and how increases in SGR can be achieved by complimentary increases of V_c, to reduce the influence of increased cutting forced and imparted stress

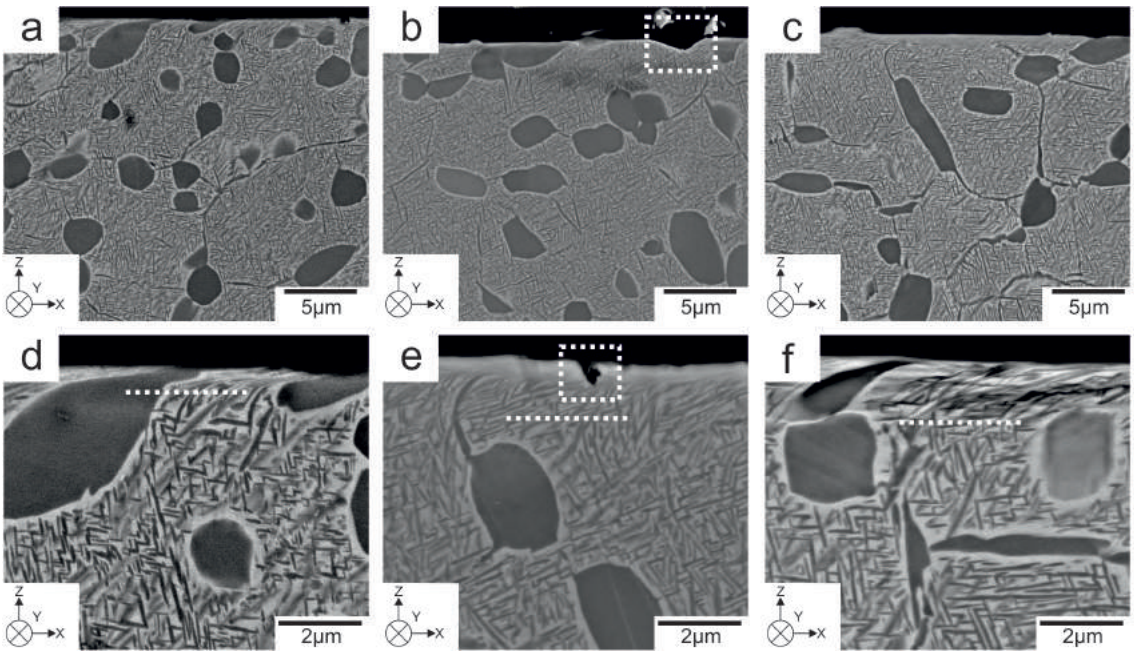

Figure 4.33: BSEI at a-c. x10,000 and d-f. x30,000 magnification of the finish end milled subsurface for conditions a & d. 1, b & e. 6 and c & f. 7, coupons subjected to increased SGR 0.14, 0.22 and 0.3 mm/tooth and 300, 375 and 450 m/min respectively in the X orientation.

The response to isolated increases in f_z and SGR, with respect to subsurface deformation is comparable in Fig.4.33. Significant cavitation and subsurface tearing is present in condition 6, as depicted in Fig.4.33 b and e. Comparable depth of SPD and distortion of α_p and α_s is observed at the highest SGR condition Fig.4.33 c and f. Both conditions, 6 and 7 show SPD in the upper 3 μm. Condition 7 shows evidence of dislocation slip planes within α_p grains. The slip lines appear isolated to shallower depths, when compared to condition 5. In Fig.4.33 f, severe distortion is present and evidence of subsurface crack propagation is noticeable along α/β grain boundaries.

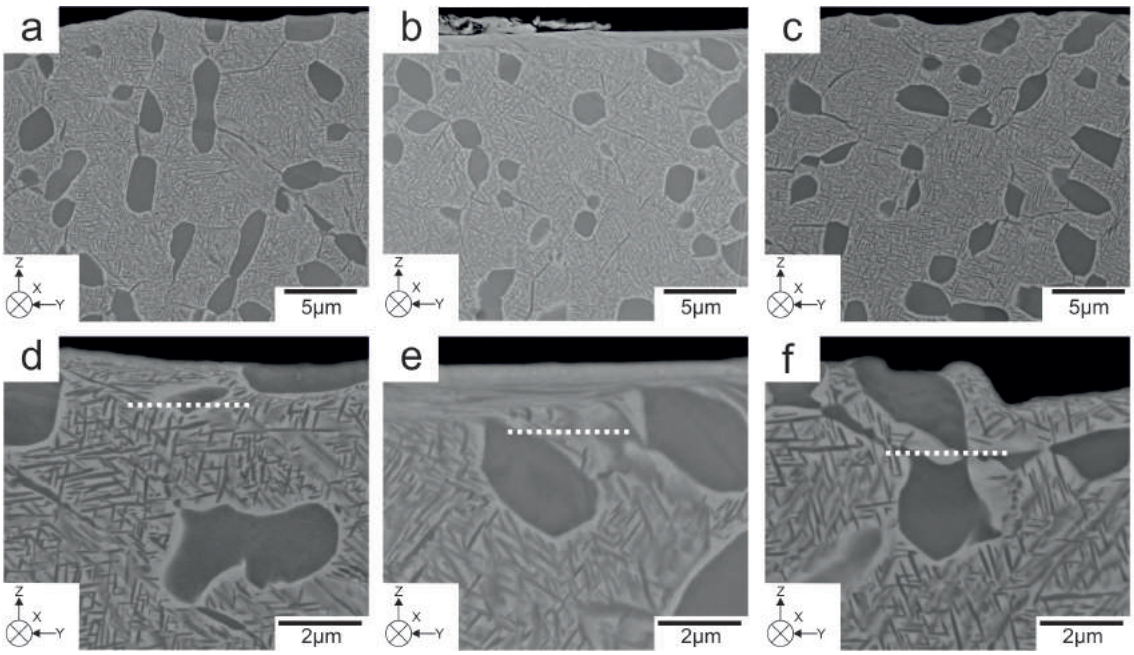

Figure 4.34: BSEI at a-c. x10,000 and d-f. x30,000 magnification of the finish end milled subsurface for conditions a & d. 1, b & e. 6 and c & f. 7, coupons subjected to increased SGR 0.14, 0.22 and 0.3 mm/tooth and 300, 375 and 450 m/min respectively in the Y orientation.

In the Y orientation, increases in SGR shown in condition 6, Fig.4.34 b and e, have a marked effect on SPD. A difference between an undeformed and deformed region is clearly distinguishable in the upper 2 μm. This behaviour may be in response to the peak in feed forces observed during this condition. At the maximum SGR, less distortion to α_p and α_s is present. But in response to an increase in cutting force, induced SPD and slip is observable in α_p grains down to 3 μm from the surface.

4.2.4 Discussion

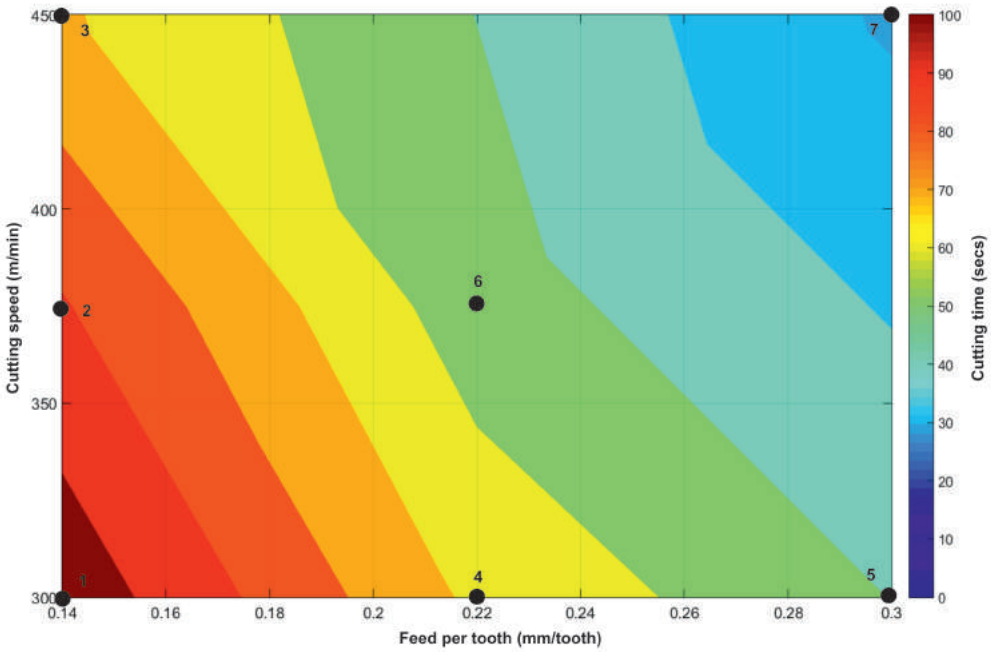

Figure 4.35: Interpolated contour plots for all cutting conditions for cutting time in seconds with test conditions identified as points.

The cutting conditions investigated are superimposed on to a contour plot, Fig.4.35 which visually depicts the influence of each cutting parameter on the cutting time (secs) for milling of test coupons, Fig.3.3b and Fig.3.4. This visually emphasises the significant reductions in operation time, that increases in V_c and f_z can facilitate. Increases in f_z have the greatest impact in reducing cutting time, due to an increased MRR. Several surface roughness metrics have been used to characterise the effect of increased cutting parameters on surface integrity. Conventionally a field for mechanical engineering, 2D arithmetic mean measures R_a dominate manufacturing industries. Much existing academic research also focusses on these basic metrics. The results shown in section 4.2, show V_c has no discernible effect on 2D roughness parameters. f_z however, when increased to 0.3 mm/tooth, increases 2D roughness metrics. The individual changes in roughness with parameters are subtle, a more complete way of studying these results is to consider the change in MRR across all conditions. Current cutting conditions of 300 m/min and 0.14 mm/tooth equates to 0.84 cm^3/sec MRR, with the greatest MRR of 2.71 cm^3/sec resulting from condition 7; 450 m/min and 0.3 mm/tooth. Therefore, over the spectrum of tests carried out, an increase of over 222% in MRR has been achieved, a fact depicted schematically in Fig.4.36 with a vast reduction in cutting times.

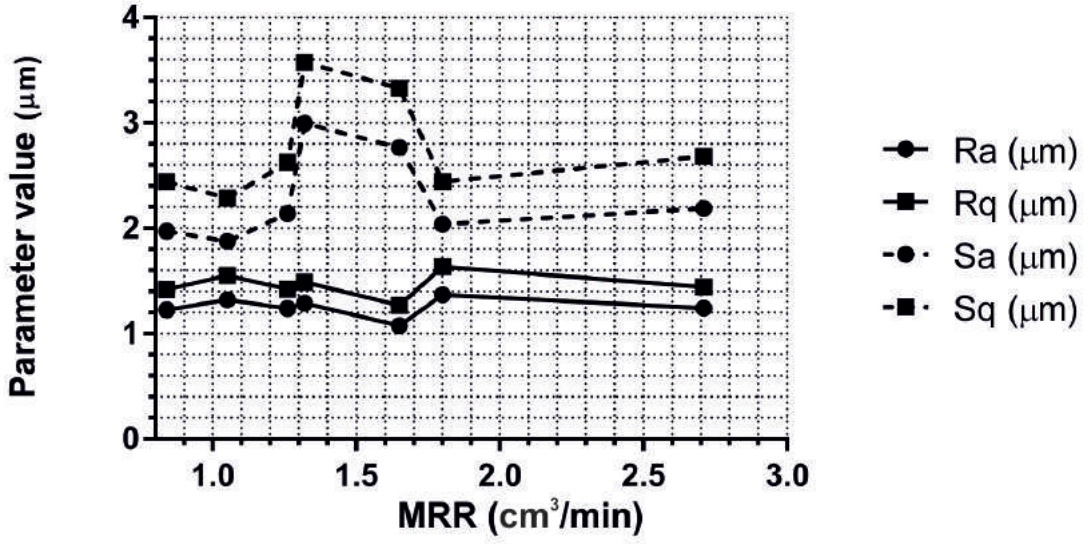

Figure 4.36: Graphical representation, for all cutting conditions, the 2D roughness parameters a. R_a and b. R_q and 3D roughness parameters c. S_a and d. S_q.

The variations in roughness metrics across all 7 conditions, with respect to MRR are shown in Fig.4.36. It can be seen visually that over a 222% increase in MRR, minimal increases in R_a and R_q are observed. Both metrics vary to similar extents. A slight reduction is observed in condition 4, at intermediate f_z of 0.22 mm/tooth. The behaviour of 2D roughness metrics R_a and R_q are presented as a contour plot, in Fig.4.37 a and b, similar to that of Fig.4.35. It is clear from Fig.4.37 a and b, that over the range of tests, no discernible variation in roughness is observed. Finish milling operations such as this are dynamic and complex cutting process and produces complex 3D surfaces. Due to the curved geometry and tool path, Fig.3.4 it is vital to consider the 3D surface and the roughness metrics associated with that. Increasingly, academic research is utilising these roughness measurements (refs). As can be seen in both the schematic profile in Fig.4.36 and the contour plots of Fig.4.37 c and d, a much more distinct behaviour is verified. The first observation is that from a quantifiable perspective, 3D roughness metrics are greater in value (μm) than their equivalent 2D metrics. These metrics are not directly comparable to one another, as the 3D parameters are averages of over 50 line measurements in 2 orientations over a more localised area of interest. Over the full range of MRR, a slight increase in 3D roughness parameters is produced. Notably, a sharp increase of both S_a and S_q is seen at intermediate MRR for conditions 3 and 4, at 450 m/min and 0.22 mm/tooth respectively. This behaviour is directly opposed to the behaviour seen in the 2D roughness parameters. It is determined that this is due to the influence of cutting parameters on the Y orientation roughness. As shown in Fig.4.17, 4.24 and 4.31, cutting parameters, especially increased f_z, show a greater influence on feed marks and thus the Y orientation roughness, than that of the X orientation. The same behaviour is seen in the subsurface BSEI in Fig.4.20, 4.27 and 4.34, in which the incidences of cavitation and surface tearing are much more frequent.

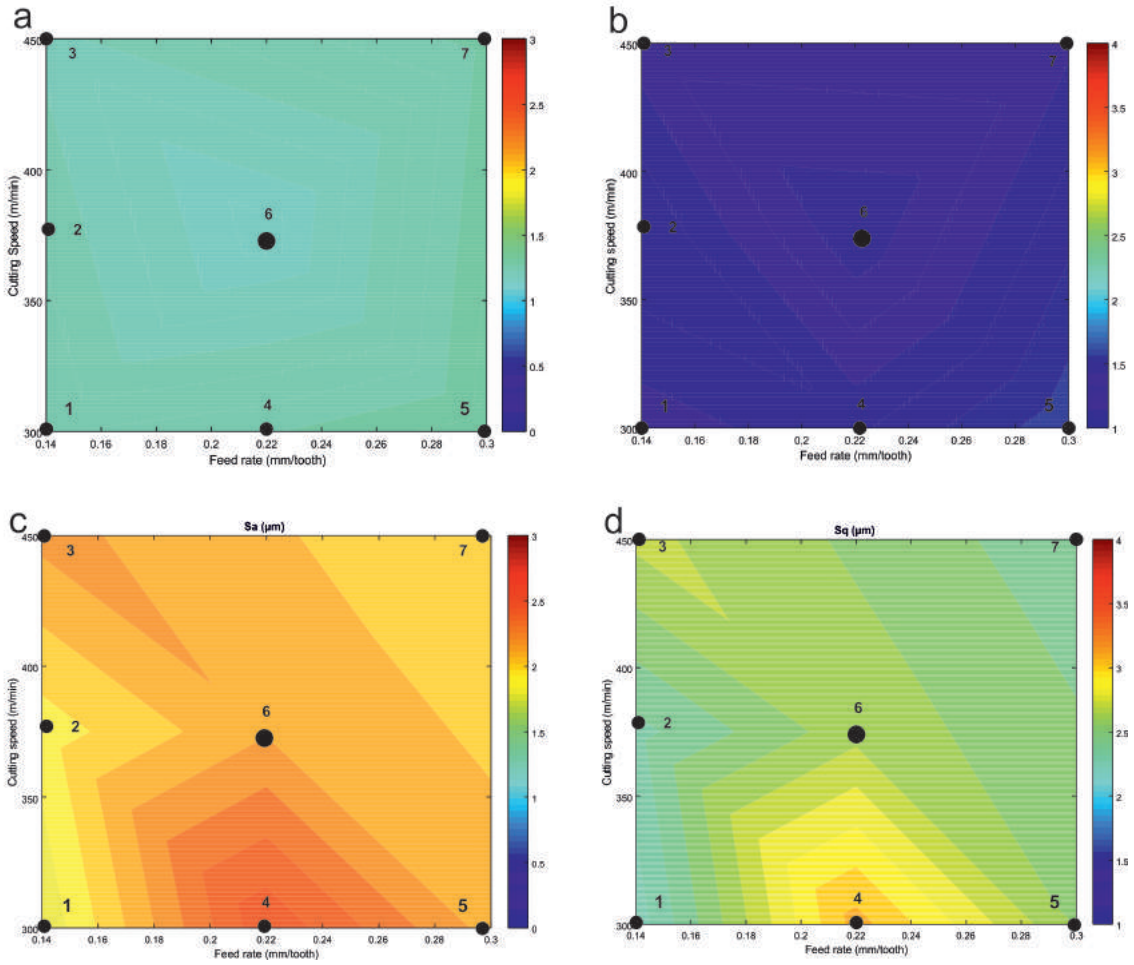

Figure 4.37: Interpolated contour plots for all cutting conditions for 2D roughness parameters a. R_a and b. R_q and 3D roughness parameters c. S_a and d. S_q.

When comparing the contour plots in Fig.4.37 for 2D and 3D roughness metrics, it can be said that the sensitivity of S_a and S_q allow for a more detailed understanding of the susceptibility to finish milled surface integrity with changing cutting parameters. Increases of surface roughness as a result of increased f_z can be to some extent offset by complementary increases of V_c.

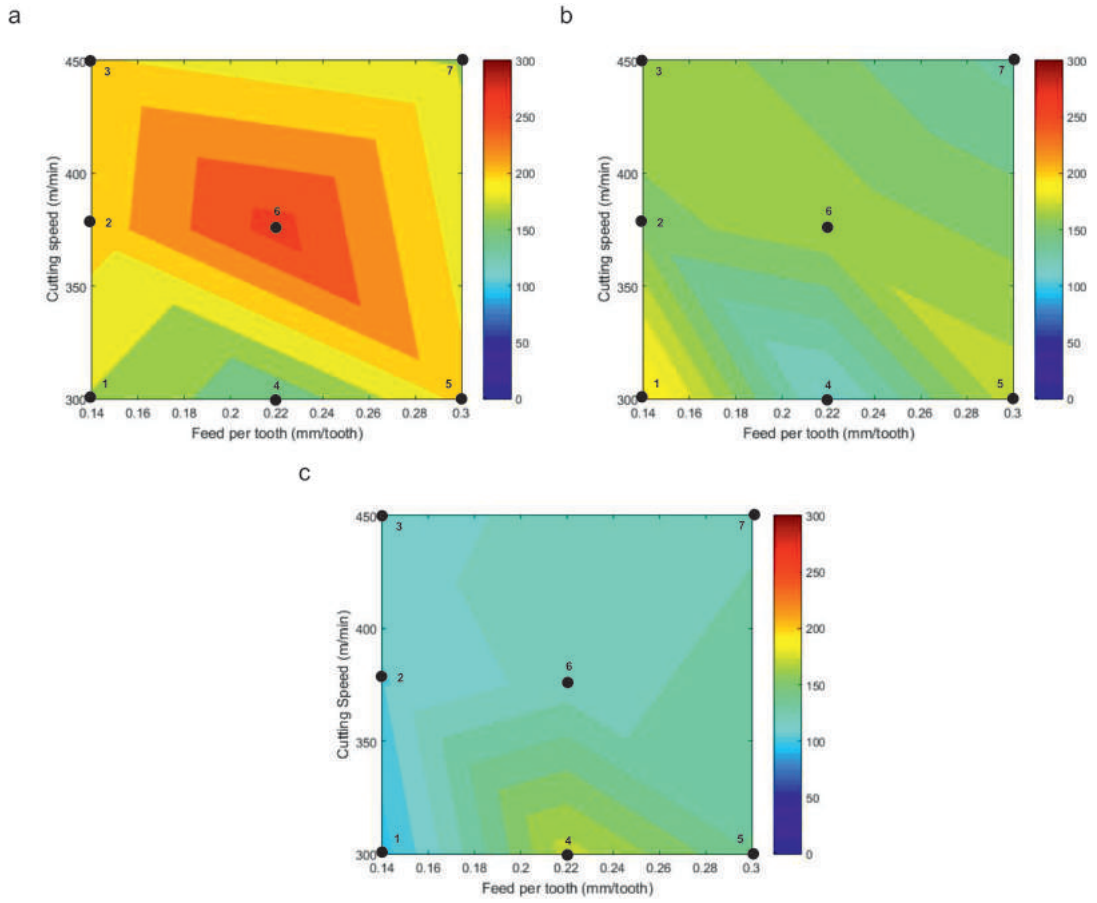

Figure 4.38: Interpolated contour plots for all cutting conditions for cutting forces in the a. X, b. Y and c. Z; normal, thrust and cutting force directions respectively.

The maximums of the three fundamental cutting forces form an interesting picture when schematically represented as contour plots over the range of cutting parameters, shown in Fig.4.38. Over the entire spectrum of cutting parameters, minimal variation of the thrust force is produced. However, for both the normal and cutting forces, some clear trends are observed. At intermediate SGR and increased V_c, an increase in normal force is produced. This coincides with the observed behaviour of α_p grain distortion, as seen in Fig.4.19, at intermediate SGR in Fig.4.33e and Fig.4.34e and high f_z in Fig.4.27f. As for the Z orientation cutting force, a nominal increase is seen with V_c, but a significant increase is seen with increased f_z. These conditions exposed to this, show a reduced tendency for increased normal cutting force and the α_p sweeping associated with this force. However, these conditions show a greater tendency for dislocation slip within α_p grains. It is postulated that this is due to the effective increase in imparted stress. A behaviour observed in a similar manner to shot peening of titanium alloys, which too induces dislocation slip [53]. Similar relationships can be hypothesised between cutting forces and roughness metrics. Increases in S_a and S_q coincide with intermediate f_z and high cutting forces. The same conditions subject to high normal cutting forces, have high instances of microstructural distortion or swept α_p grains. A positive relationship can also be identified for the 3D measurement of skewness and tendency for increased skew at high Z orientation cutting forces.

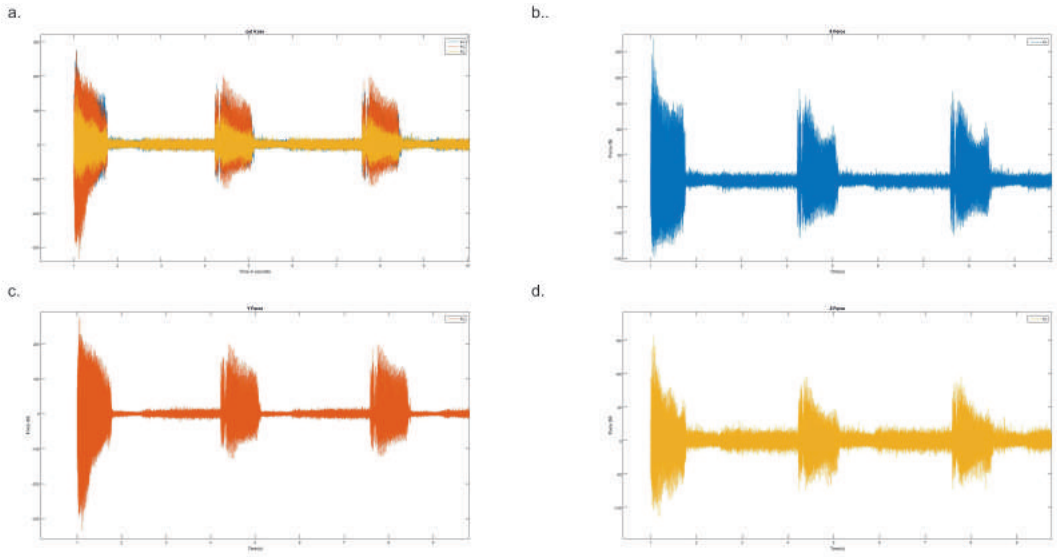

Figure 4.39: Graphical representation, for cutting condition 1, a. all three fundamental cutting forces, b the X orientated, c Y orientation and d. Z orientated cutting force over the first 10 seconds or 3 tool passes.

The results presented in Fig.4.18, 4.25 and 4.32 are explored further in 4.39 in which the first three passes for cutting condition 1 are examined. It can be seen how the maximum cutting forces, in all three directions, are experienced in the first pass in which the full width of the cutting tool is engaged, as shown in Fig.4.39a. This force is reduced for subsequent tool passes as due to the imposed a_e reduces the overal contact area between the workpiece and cutting tool. This behaviour is consistent across all three fundamental cutting force directions, just experienced to different extents, as seen in Fig.4.39.

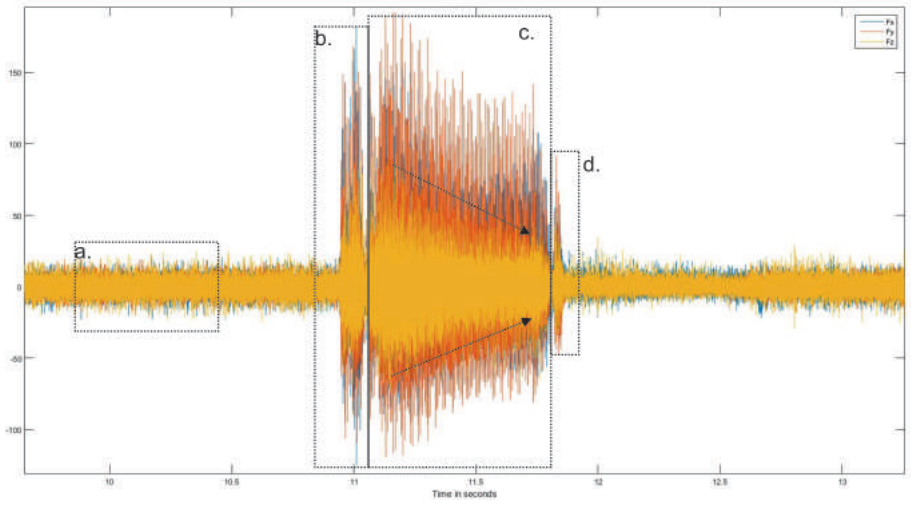

Figure 4.40: Graphical representation, for cutting condition 1, all three fundamental cutting forces for a single tool pass showing a. the cutting forces in air, b the cutting tool engagement, c the influence of effective cutting speed and d. the cutting tool retraction.

Under increased resolution some significant behaviours are observed and shown in Fig.4.40. Between cutting passes, the tool is rotating in air and no longer in

contact with the workpiece, a remenant low level force is present in all three directions as shown in Fig.4.40a. The influence of the increased contact area present during cutting tool engagement is shown by rapid increase in cutting forces shown in Fig.4.40b. A subsequent immediate reduction in cutting forces are observed after the initial tool engagement is achieved. This is as a result of the NC programme in which an engagement radius to the tool motion is used to protect the cutting edge radius from high surface stresses. After the engagement the tool then progresses along the cutting path in which, as described in sections 3.3 and 4.1.2, the effective cutting diameter is reduced along with the V_{ceff}, which is accompanied with a reduction of cutting forces as shown in Fig.4.40c. A small increase of cutting forces is shown to be experienced as a result of the radius employed during tool retraction as shown in Fig.4.40d.

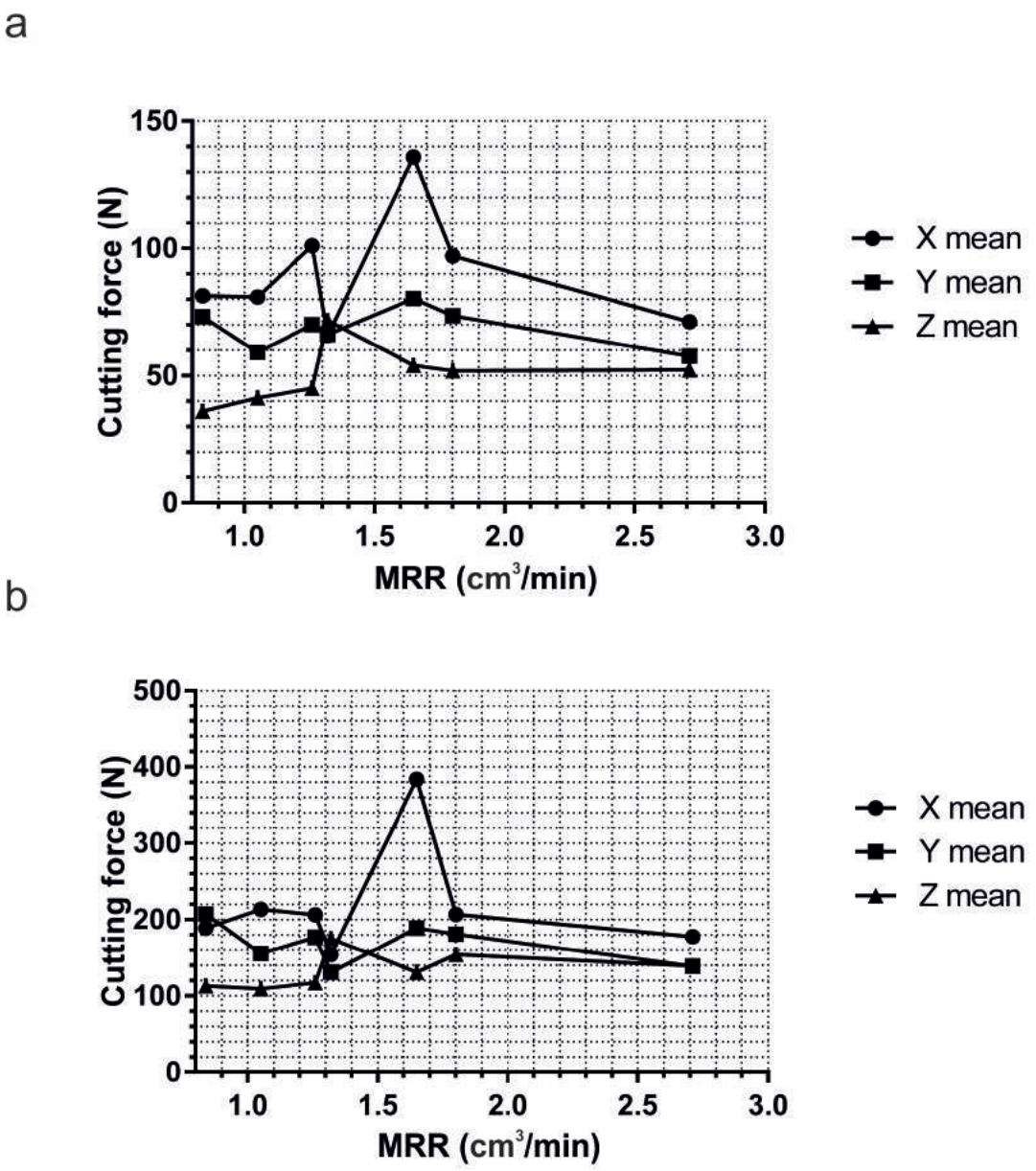

Figure 4.41: Graphical representation, for all cutting conditions, the cutting forces parameters in the a. X, b. Y and c. Z; normal, thrust and cutting force directions respectively.

As can be seen from Fig.4.41, a sharp increase is present, induced by the cutting parameters at condition 6, particularly in X normal orientation for both mean and maximum measures. The mean measure presented in Fig.4.41b allows for the compensation of the variation observed in cutting force measurements, as identifiable in Fig.4.18, 4.25 and 4.32. An initial spike in cutting force is produced by the large cutting diameter induced from the first tool pass. Each subsequent tool pass has a reduced cutting diameter engagement. This effect is exacerbated by the variation in effective cutting diameter as the tool progresses along the circumference of the coupon as described in section 4.1.

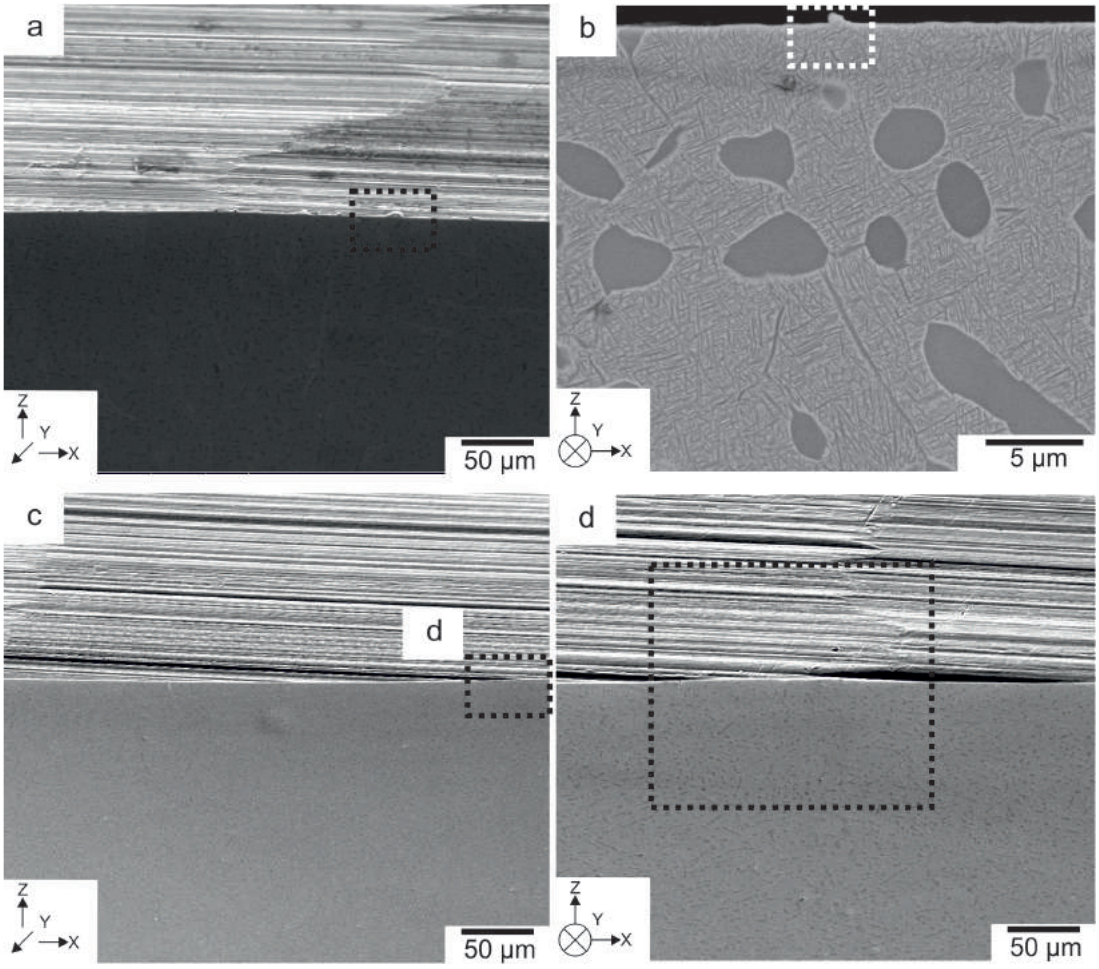

Figure 4.42: Tilted BSEI showing the effect of surface roughness on surface deformation with a focus on a & ,b. surface defects and c & d. feed marks.

The interaction between surface roughness and subsurface microstructure is most evident at regions where surface defects and cavitation is present Fig.4.42a and b and where the major feed marks Fig.4.42c and d. Subsurface regions in close proximity to these defects, are more prone to incidences of both SPD and dislocation slip in α_p and α_s grains. As variation in cutting parameters influence the tooth path frequency and subsequent surface topographical profiles and cutting forces, increased f_z and Z orientated cutting forces increase the possibility of these localised defects.

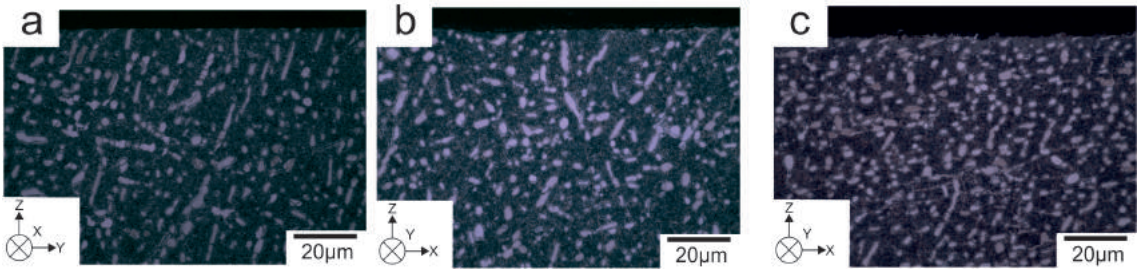

Figure 4.43: Subsurface light micrographs at x100 magnification of conditions a. 1 and b&c. 3, coupons subjected to increased V_c of 300 and 450 m/min respectively, in the a. X and b &c. directions respectively.

Light micrographs were used as initial inspection for subsurface micrsotrucral deformation and is frequently employed in industry and a standard characterisation technique. However, as has been identified by this study the deformation is typically localised to the SPD layers in the upper 5 μm and dislocation slip dominated region in the upper 25 μm . Due to the limited magnification and resolution of these light microscopy techniques it is determined that this conventional approach is unsatisfactory to confidentially identify the extent of deformation. Fig.4.43 shows how only the most extreme examples of α_p grain elongation with respect to the tool rotation direction can be identified Fig.4.43c.

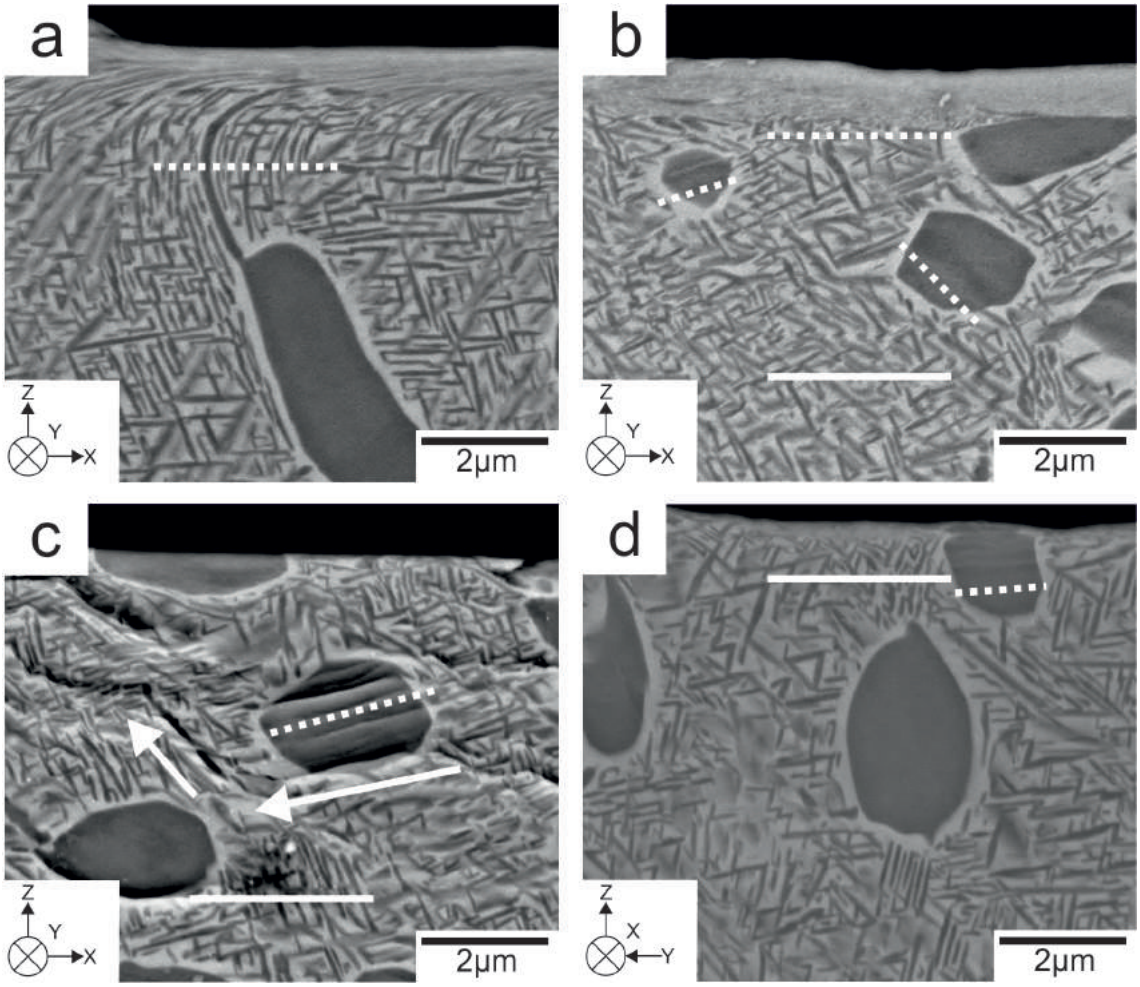

Figure 4.44: BSEI x30,000 magnification of the finish end milled subsurface for conditions a. 1, b. 6, c. 7 and d. coupons showing SPD, induced strain, intense slip bands and subsurface micro-cracking.

The principal deformation modes attained from varied cutting parameters for finish end milling of Ti-5553 are summarised in Fig.4.44. Fig.4.44a shows the influence of high normal cutting force and tool rotation direction with SPD layer and high instances of swept α_p grains and compression of α_s platelets in the upper 3 μm, forming a white layer of severely deformed material. Fig.4.44 shows the influence of both increased V_c and moderate normal cutting forces in forming SPD layers, along with increased Z cutting forces and imparted stress inducing dislocation slip in the upper 10 μm. With isolated increases in f_z, increased Z cutting force are imposed along with low levels of normal cutting force. This produces dislocation slip in α_p without inducing significant presence of swept grains. The micrograph, Fig.4.44c and d demonstrates the most severe instance of deformation found in a localised region within machined valleys in the Y orientation of condition 5, the high f_z condition. Within the upper 10 μm , α_p grains were found to have propagated subsurface micro-cracks as a result of dislocation slip. These deformation induced micro-cracks are formed via a strain localisation process [138] and propagate intragranularly into the β matrix via the α/β boundaries, around the periphery of α_p and α_s grain boundaries. An observation can be made that these cracks propagate until impeded by a crystallographically orientated "hard" α_p grain, in which no dislocation slip is identifiable. It is proposed these deformation modes will pay a significant role in the fatigue performance of truck beam components and is an area of investigation in Chapter 7.

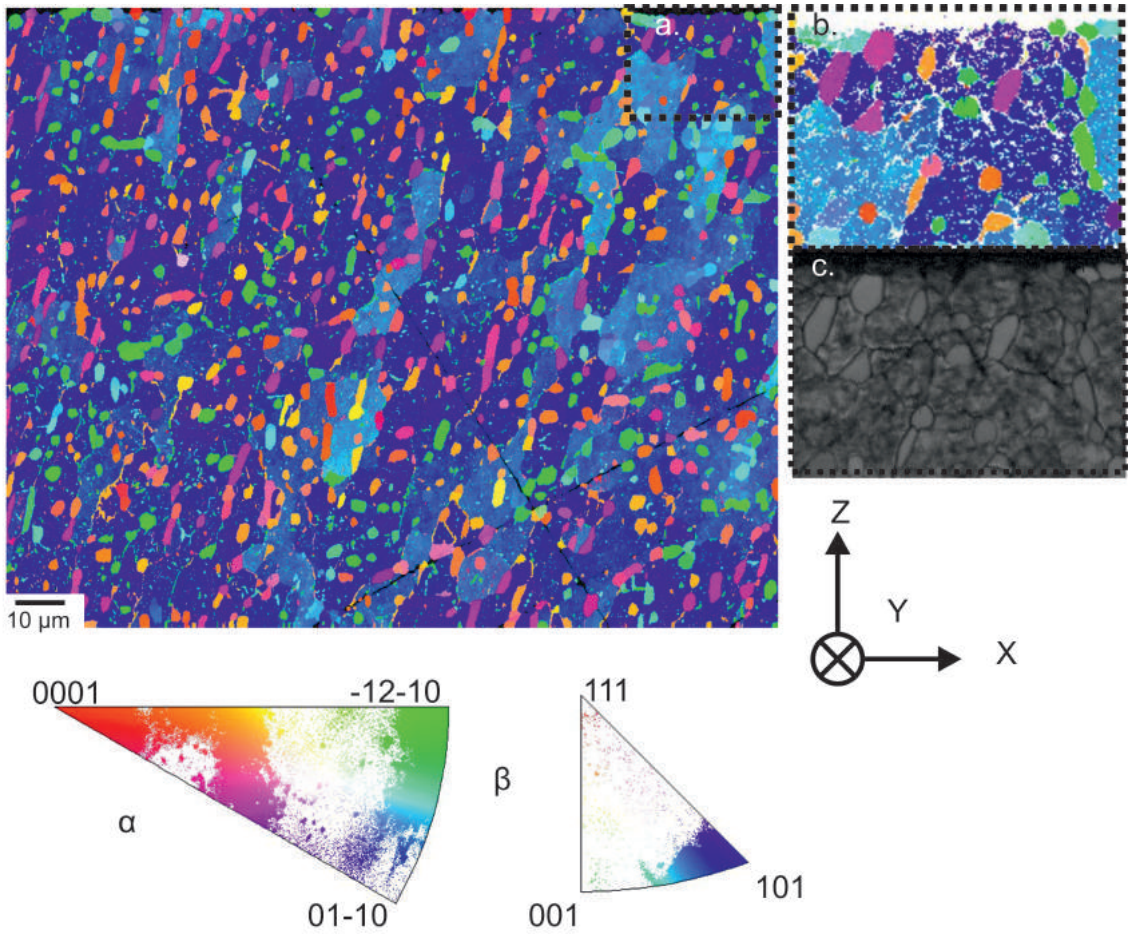

Figure 4.45: a. Noise reduced inverse pole figure (IPF) orientation image map (OIM) for cutting condition 1 in the Y orientation with regions identified in b. magnified with c. raw inverse pole orientation and d. band contrast map showing severe plastic deformation (SPD).

Under BSEI, observable deformation is localised to the upper 2-5 μm for each condition. Detailed EBSD analysis was performed and compared to previously attained microscopy results. A noise reduced inverse pole figure (IPF) orientation image map (OIM) for condition 1 is presented in Fig.4.45. The upper 100 μm of the subsurface was studied in order to ensure the required magnification and resolution of indexed coordinates were obtained and deformation modes of both the α and β phases could be characterised. The IPF OIM in Fig.4.45a shows the crystallographic orientation for a single β grain, predominantly orientated, relative to the viewing plane, in the (101) orientation. However, as can be seen in both the IPF OIM and the pole orientations, that a distribution of β grain orientations are present. This is due to the presence of a subgrain β structure, delineated by α_p grains. This agrees with the results presented in Fig.4.10. A range of α_p grain orientations are evident in this analysed region. Through a process of grain boundary delineation, no evidence of twinning was observed at this cutting condition. The highlighted region in Fig.4.45b is presented in Fig.4.45c as a raw IPF OIM with the corresponding band contrast map Fig.4.45d. These OIM show a region of non-indexed positions at the near surface as result of SPD region. These regions possess heavily deformed structures of α_p and α_s, on a scale finer than that of the EBSD interaction volume, resulting in high levels of noise and un-characterised material. This SPD region is on the order of magnitude observable by BSEI and agrees with the findings of an array of literature, localised to the upper 2 μm of the subsurface [13, 14, 63]. The band contrast map presented in Fig.4.45d represents material below this SPD region, showing no evidence of dislocation slip or mechanical twinning. When compared to the bulk measurements presented in Fig.4.11, upper hemisphere equal area projection pole figures result show that MUD values for the α and β phases have increased to 35.26 and 37.77, respectively. However, this result is limited as only a single large β grain has been characterised.

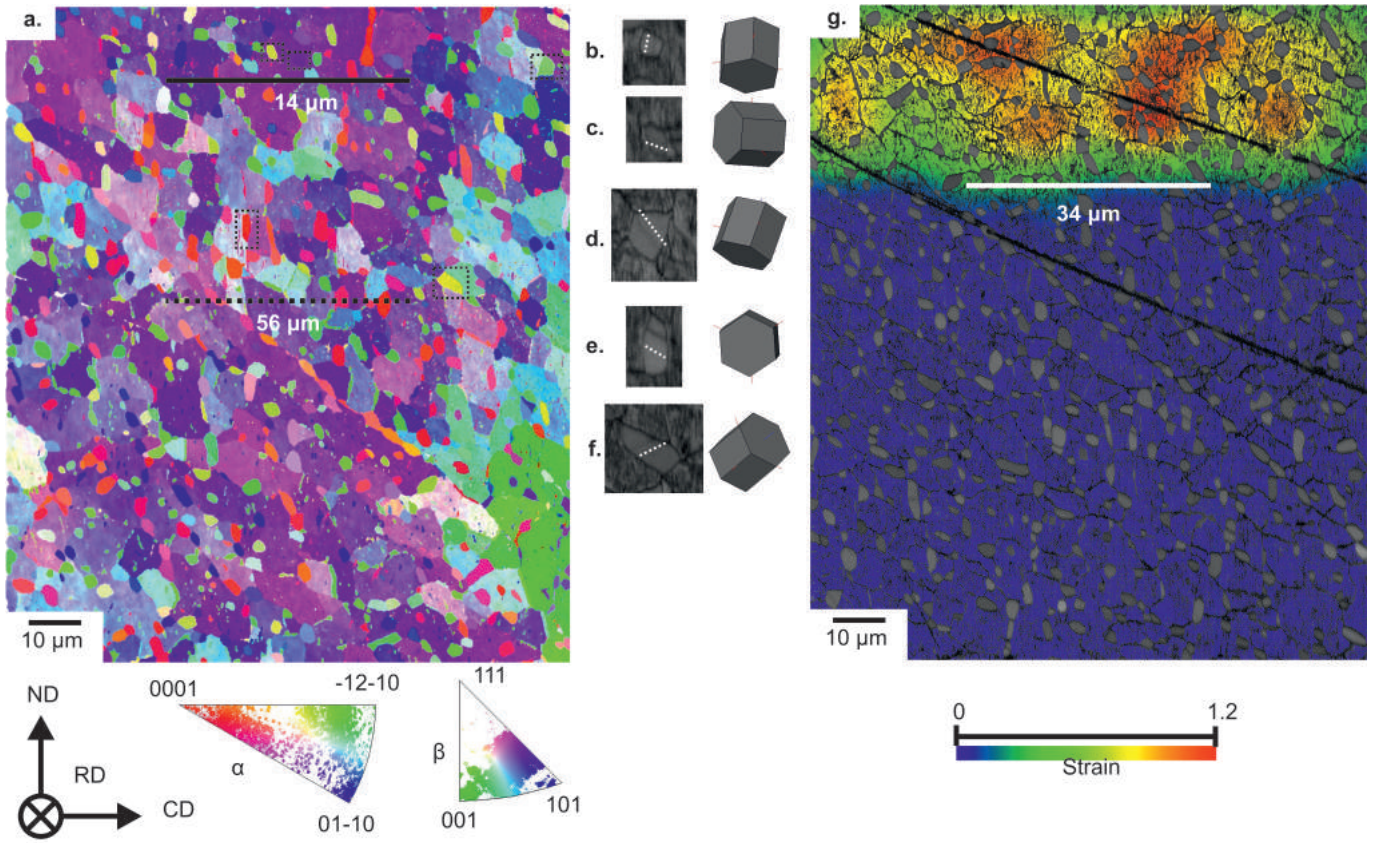

Figure 4.46: a. Noise reduced IPF OIM for cutting condition 6 in the Y orientation with the average and maximum depths of machining induced deformation identified by the solid and dashed black lines respectively. b-f. Band contrast (BC) images and corresponding 3D crystal orientation representations of α_p grains with strain induced dislocation slip directions presented as dashed white lines. g. A BC map with superimposed strain contour with SPD delineated by a solid white line.

A comparable noise reduced IPF OIM for increased SGR at condition 6 is presented in Fig.4.46a. Noise reductions were conducted to an extent to interpolate and therefore, complete the full data set and remove the 2 μm SPD layer, to allow for accurate measurements of the depth of deformation. The effect of increased SGR, from condition 1 to 6, has a notable effect on subsurface deformation. Through studying the BC map at high magnification dislocation slip lines can be identified presiding within α_p grains throughout the subsurface. Due to the grain size, relatively low slip band intensity and limited resolution of the BC maps, slip lines are faint and required detailed consideration prior to analysis. Grain boundary delineation and crystallographic orientations of individual grains, suspected of possessing dislocation slip were studied to ensure the evidence was not misconstrued. Individual α_p grains presenting slip lines are presented as BC images, with their equivalent 3D hexagonal crystallographic orientation schematically represented in Fig.4.46b-f. Through slip trace analysis it is determined that multiple slip systems are activated through this milling process. Dislocation slip was identified in pyramidal planes $1\bar{2}1\bar{3}(01\bar{1}\bar{1})$ and prismatic planes $\bar{2}11\bar{3}(01\bar{1}0)$. The IPF OIM image in Fig.4.46a is delineated by two lines. The first signifies the depth to which the average deformation is observable. This was analysed qualitatively, based upon the severity and numbers of α_p grains displaying dislocation slip lines. The second dashed line delineates the boundary between the maximum observable deformation and un-deformed material. The upper un-indexed SPD region, for condition 6, was deemed to be 2 μm, in agreement with BSEI studies presented in Fig.4.33 and 4.34. The average and maximum depths of deformation were calculated to be 14 and 56 μm, respectively. In agreement with the literature, this shows the true extent of machining induced deformation can not be examined solely by BSEI. In manufacturing industries, typical subsurface inspection is conducted by light microscopy. It is worth noting at this point, that the combination of fine microstructure and limited MRR throughout this investigation has limited the severity of induced deformation. Alloys with lower machinability subject increased MRR operations such as roughing, would inevitably be susceptible to deformation features significantly more exaggerated than those presented in this thesis. It is however of interest the stark difference in resolution achieved by EBSD when compared to BSEI. This fact is exacerbated when studying the imposed strain contour profile on the BC presented in Fig.4.46g. This contour translates the strain induced within the β phase. A distinct boundary between deformed and undeformed material at 34 μm is delineated by a solid white line. This contrast lies within the maximum and average depths of deformation reinforcing our understanding that the SPD region observable by BSEI shows an incomplete description of the deformation behaviour. The average depth of deformation shown in Fig.4.46a, determined from observable deformation in α_p grains, coincides with the depth observed by the larger strain induced within the softer β phase. This suggests, as has been previously postulated, two observations: First of which, deformation is induced in the ductile β matrix phase as a result of end milling machining, a fact that has been undistinguishable through previously employed characterisation techniques. Secondly, this induced β phase deformation has a direct relationship with the severity of α phase deformation. When comparing to the average depth of α phase deformation at 14 μm, the β phase deformation can be seen to be to a greater depth, 34 μm.

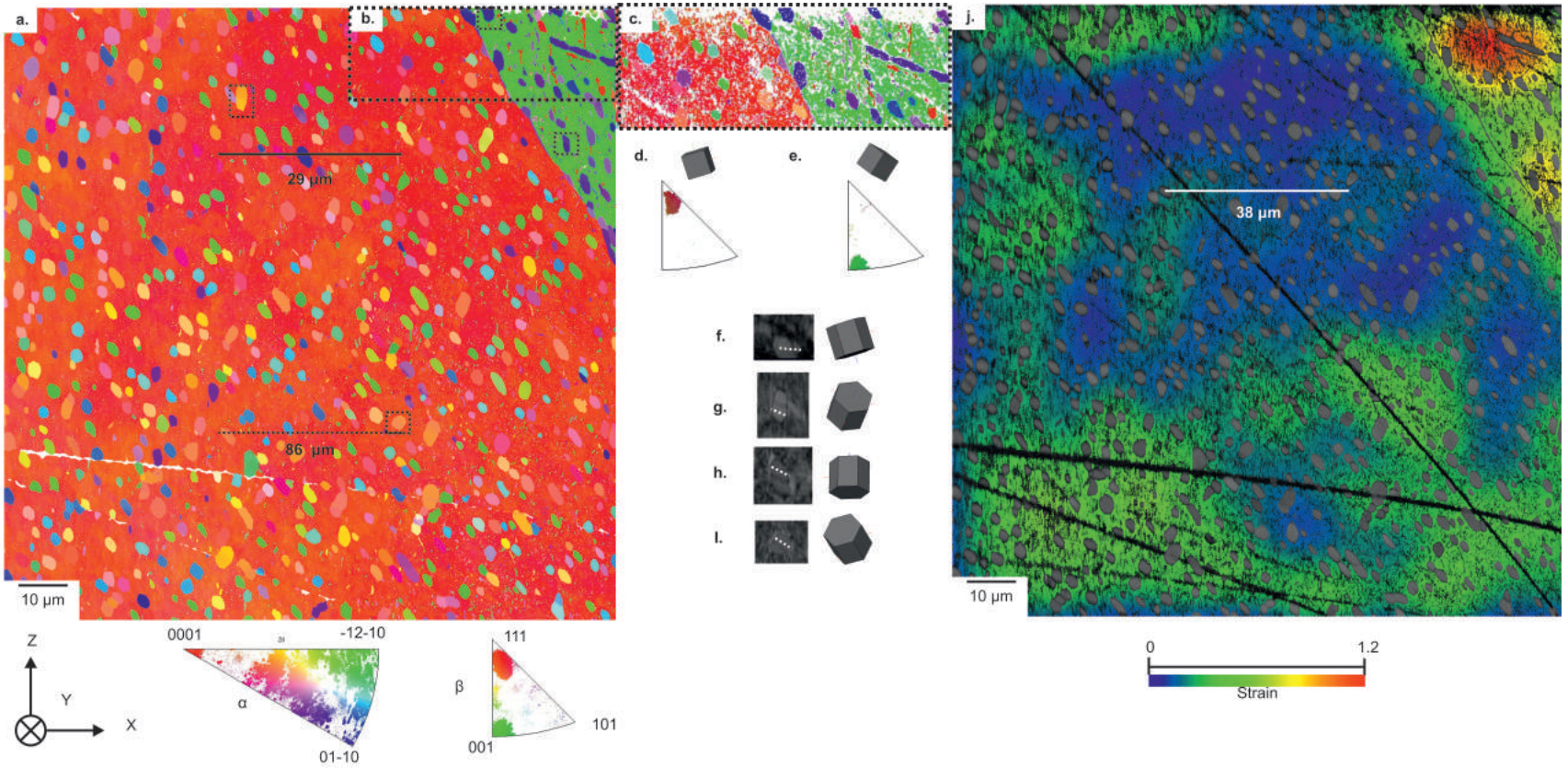

Figure 4.47: a. Noise reduced IPF OIM for cutting condition 6 in the Y orientation with the average and maximum depths of machining induced deformation are identified by the solid and dashed black lines respectively. Magnified region b. is presented as c. a raw IPF OIM with d&e crystallographic orientations of the respective β grains. d-g. BC images and corresponding 3D crystal orientation representations of α_p grains with strain induced dislocation slip directions presented as dashed white lines. i. A BC map with superimposed strain contour with SPD delineated by a solid white line.

At the maximum imposed SGR, in condition 7, EBSD analyses shows an increase in both the average and maximum depths of induced deformation, as shown in the noise reduced IPF OIM in Fig.4.47a. BC images with corresponding 3D hexagonal crystallographic orientations of α_p grains, subject to dislocation slip are presented in Fig.4.47f-i. Milling at condition 7 has activated multiple slip systems including basal $\bar{2}110(000\bar{1})$ and pyramidal planes $\bar{1}2\bar{1}\bar{3}(\bar{1}101)$. Unlike previous IPF OIM, this figure shows orientation information over multiple β grains. A comparison of the magnified area Fig.4.47b is presented in the raw IPF OIM in Fig.4.47c. This presents some interesting observations. A greater depth of SPD can be inferred from the increased un-indexed region observed in the green coloured β grain. The 3D cubic crystallographic orientation and pole figure distribution for the two β grains are presented in Fig.4.47d and e. This shows two grains with strong orientations relative to the analysed plane of the 111 and 001 orientation, for Fig.4.47d and e respectively. Accompanied by the increased depth of SPD present in the 001 β grain, this orientation shows a clear increased susceptibility to induced strain, as is shown in the BC map with superimposed β strain contour in Fig.4.47j. It can be postulated here, that if the 001 plane of the β phase is orientated parallel to the tool direction, greater deformation is induced than that found in those grains orientated by the 111 plane. As with previous results, increased severity of deformation to the β phase also presents greater levels of deformation to the α phase and modes of dislocation slip. With SGR, the depth of deformation observable in both phases increases. The average and maximum depth of deformation for the α phase for condition 7 has increased to 29 and 86 μm, respectively. With the average deformation in the β increasing to 38 μm. It can be stated, that strain is present at low levels within the β phase through the entirety of the analysed area.

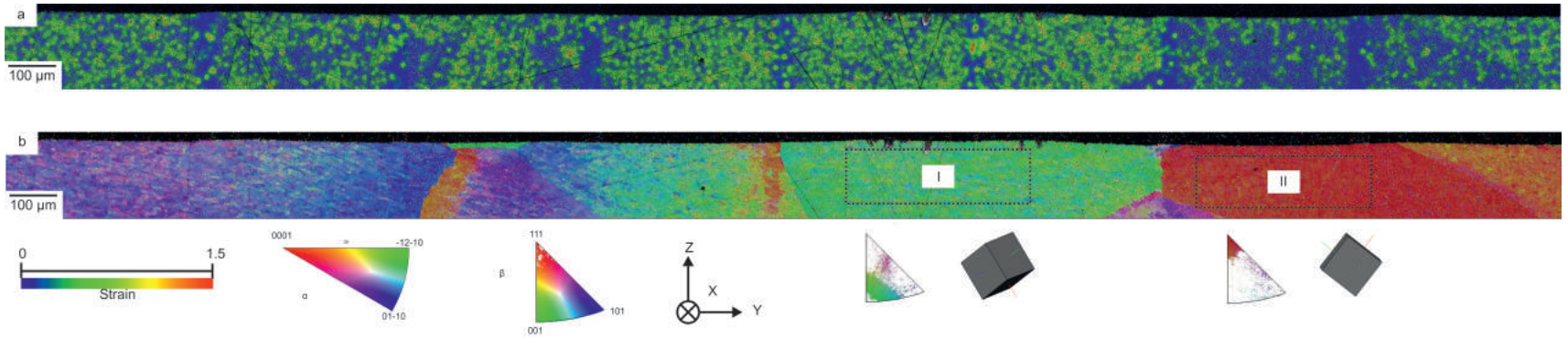

Figure 4.48: a. Band contrast map with a superimposed strain contour and corresponding b. Noise reduced IPF OIM for cutting condition 6 in the Y orientation. Two regions I and II highlighted with dashed black boxes with corresponding 3D crystal orientation representations of respective β grains.

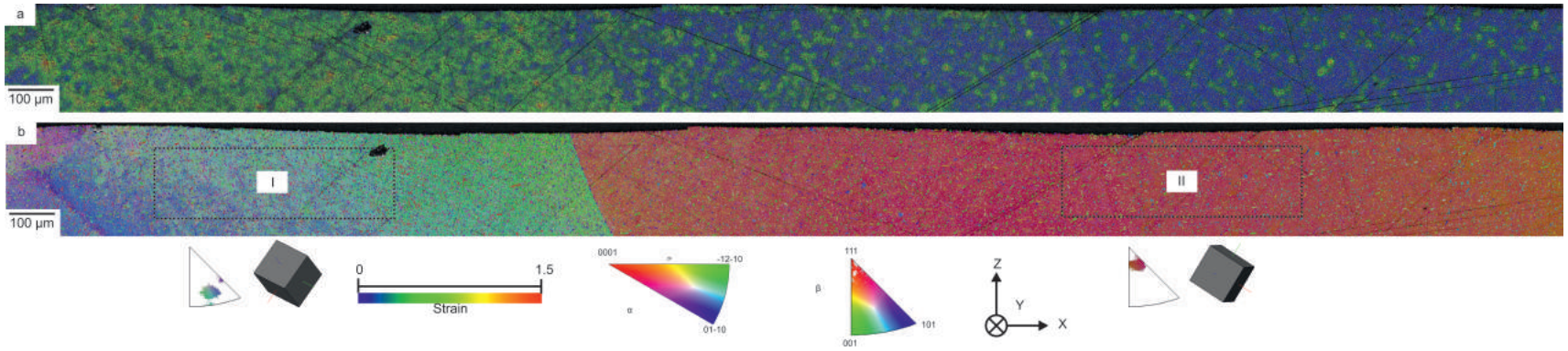

Figure 4.49: a. Band contrast map with a superimposed strain contour and corresponding b. Noise reduced IPF OIM for cutting condition 7 in the Y orientation. Two regions I and II highlighted with dashed black boxes with corresponding 3D crystal orientation representations of respective β grains.

The influence of β grain orientation with respect to the tool direction shows influence in the Y orientation. As was determined from BSEI, the X and Y orientations are both influenced by the tool motion and rotation directions. Increased deformation was observed in the Y orientation. The same has been seen through EBSD analysis. Large area low magnification EBSD analysis was conducted in the X orientation to determine the effect of deformation in the β phase across multiple grains. Noise reduced IPF OIM are presented for conditions 1 and 6, in Fig.4.48a and 4.49a, respectively. Corresponding BC maps with superimposed β phase strain contours for conditions 1 and 6 can be seen in Fig.4.48b and 4.49b, respectively. In both cases low levels of strain are present to the full depth of the regions presented with variations evident across each individual β grain. This variation is believed to be due to the subgrain β structure present and the presence of α_p grain colonies. For both conditions, differences in strain can again be seen between β grains orientated in the 001 and 111 planes. When a β grain is orientated with the 001 plane parallel to the tool rotation direction increased levels of strain are observed. Due to the strong texture and adherence to the Burgers orientation relationship significant levels of deformation is accommodated in the α_p grains in this orientation also.

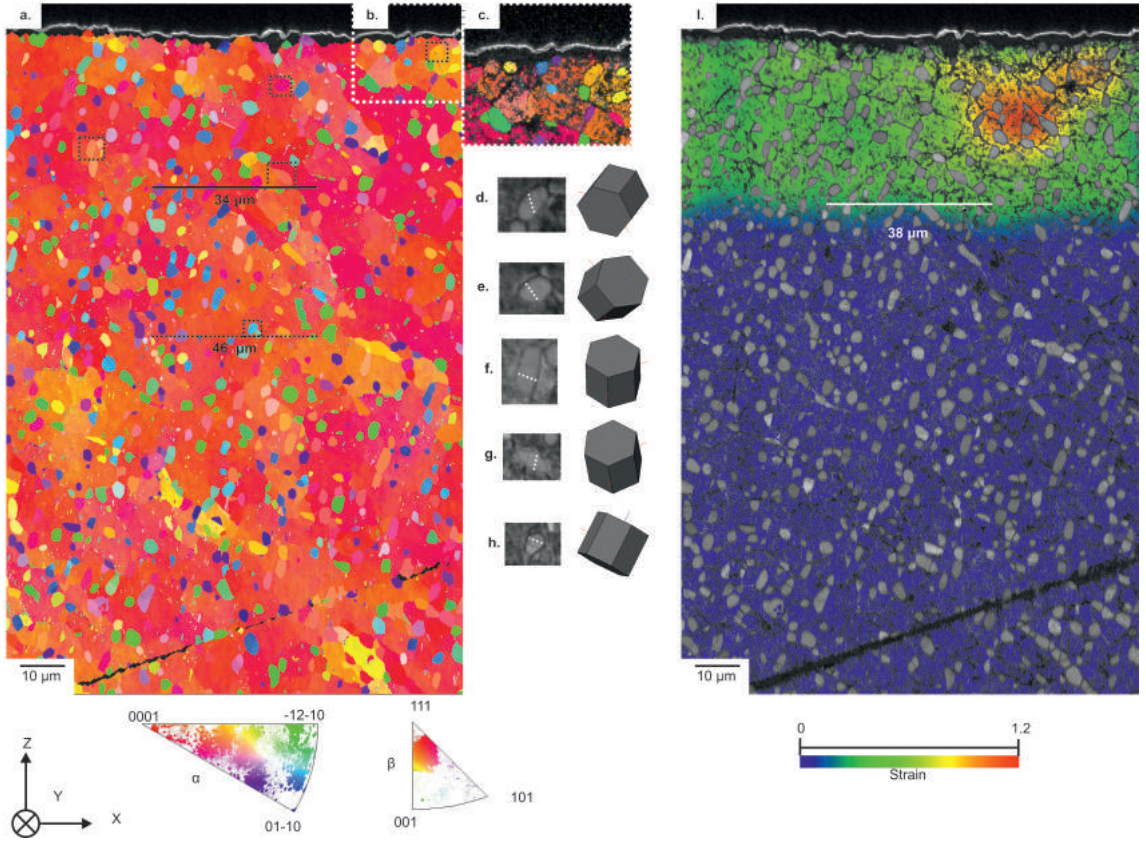

Figure 4.50: a. Noise reduced IPF OIM for cutting condition 5 in the Y orientation with the average and maximum depths of machining induced deformation are identified by the solid and dashed black lines respectively. Magnified region b. is presented as c. a raw IPF OIM with d-h. band contrast (BC) images and corresponding 3D crystal orientation representations of α_p grains with strain induced dislocation slip directions presented as dashed white lines. i. A BC map with superimposed strain contour with SPD delineated by a solid white line.

Despite the dominate orientation of the β grain analysed in the noise reduced IPF OIM in Fig.4.50a being in the hard 111 orientation, the high f_z of condition 5, is shown to induce significant deformation. An increased depth of SPD has not been mitigated through noise reduction, due to the high major cutting force as a result of increase f_z. The regions delineated in Fig.4.50b is magnified and presented in the raw IPF OIM form in Fig.4.50c, showing the extent of SPD on indexed positions. Multiple slip systems have been activated including basal $\bar{2}110(000\bar{1})$ and prismatic $11\bar{2}\bar{3}(\bar{1}100)$ summarised in the BC images, with corresponding 3D hexagonal crystallographic orientation representations in Fig.4.50d-h. The average and maximum depth of deformation was shown to be 34 and 46 μm respectively. Isolated increases in f_z, have therefore shown, increases in average depth of deformation. Conditions 6 and 7 show that comparable increases in deformation can be offset marginally with complimentary increases in V_c. This finding is in agreement with previous results from BSEI analysis. The strain contour superimposed on the BC map, presented in Fig.4.50g shows the deformation is localised to the upper 38 μm. A behaviour typical of β grains orientated with the 111 plane relative to the analysed area.

4.3 The effect of cutting parameters on tool wear for finish milling of Ti-5Al-5Mo-5V-3Cr

4.3.1 Tool wear

Fig.4.51 shows the effect of V_c on tool wear for conditions 1, 2 and 3 at V_c of 300, 375 and 450 m/min, respectively. The effect on surface integrity and subsurface can be seen in section 5.4.1. It can be seen that as V_c increases to 375 m/min there is an increase in the presence of both re-adhered and re-deposited chips. This is reduced as V_c is increased to 450 m/min. The highest instances of re-deposited chips on all tools are evident at moderate ϕ_{eff}. In all three conditions, no significant tool wear is observable and the effect on surface integrity and cutting forces, from section 5.4.1, supports this observation.

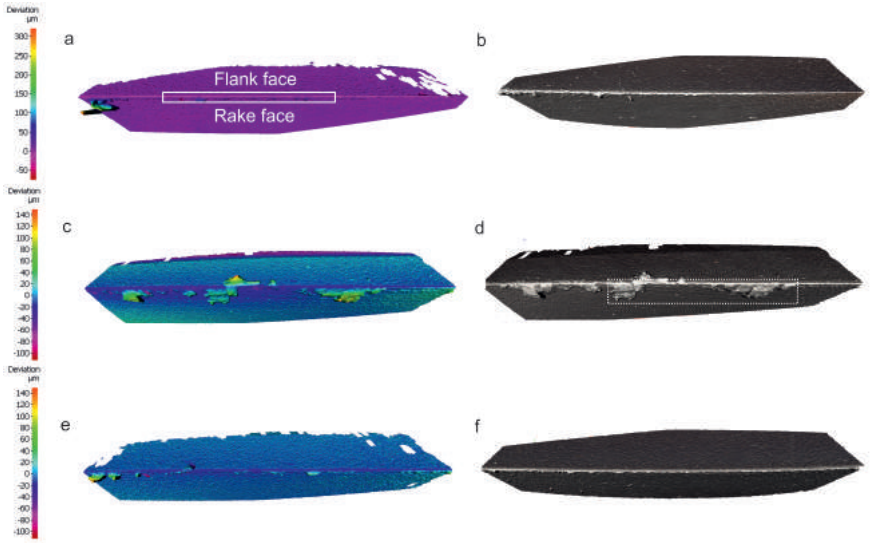

Figure 4.51: 3D contour light images of the the geometric differences for cutting edges between new and used before cleaning of deposited chips a-c. and after cleaning d-f. conditions a and d. 1, b and e. 2 and c and f. 3, coupons subjected to increased V_c of 300, 375 and 450 m/min respectively.

The effect of increased f_z has a more distinct influence on the cutting tool. As f_z increases, it can be seen in Fig.4.52, that the instances of re-deposited and re-adhered chips increases. Ultrasonic cleaning has minimal effect on the chips present along the cutting edge, suggesting adhesion between chips and the cutting edge is significant.

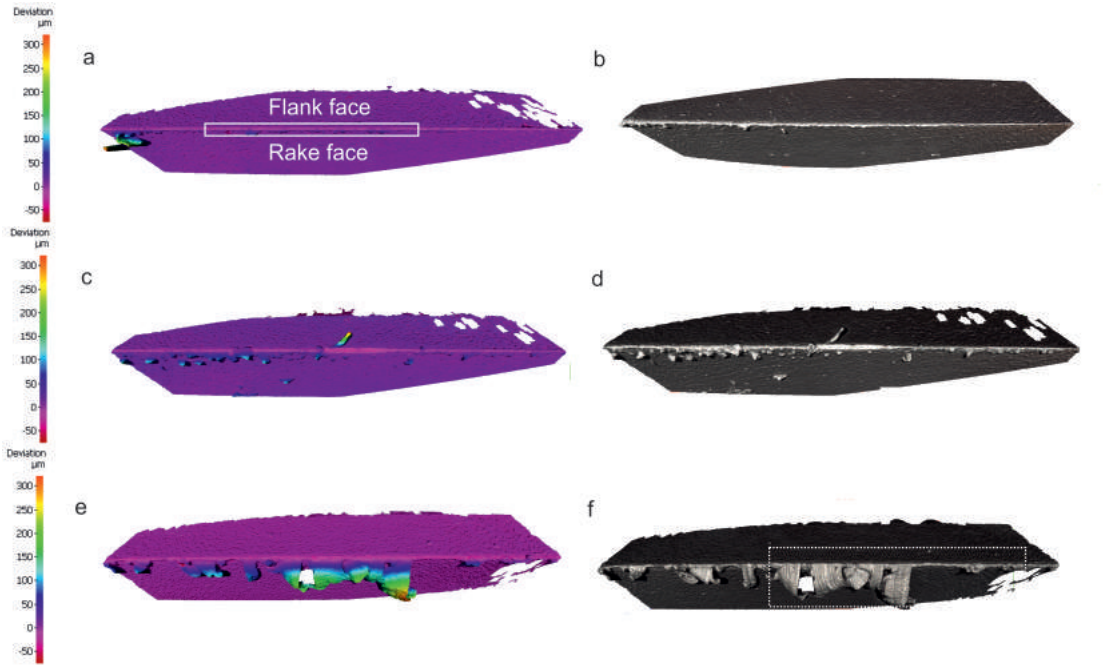

Figure 4.52: 3D contour light images of the the geometric differences for cutting edges between new and used before cleaning of deposited chips a-c. and after cleaning d-f. conditions a and d. 1, b and e. 4 and c and f. 5, coupons subjected to increased f_z of 0.14, 0.22 and 0.3 mm/tooth respectively.

Minimal flank wear is noticeable in all conditions. This is accounted for by the short duration of cutting time for all conditions. With increased f_z the presence of built up edge (BUE) on the rake face increases. This is evidence of a comparably low V_c for the specific f_z applied resulting in limited coolant delivery and chip evacuation. This allows for increased temperatures and adhesion of the chip material on the rake face. This result suggests that over increased cutting durations, high f_z at relatively low V_c will result in reduced surface finish. If this BUE becomes severe enough, a degradation of the cutting edge geometry and poor tolerances of the machined surface is to be expected.

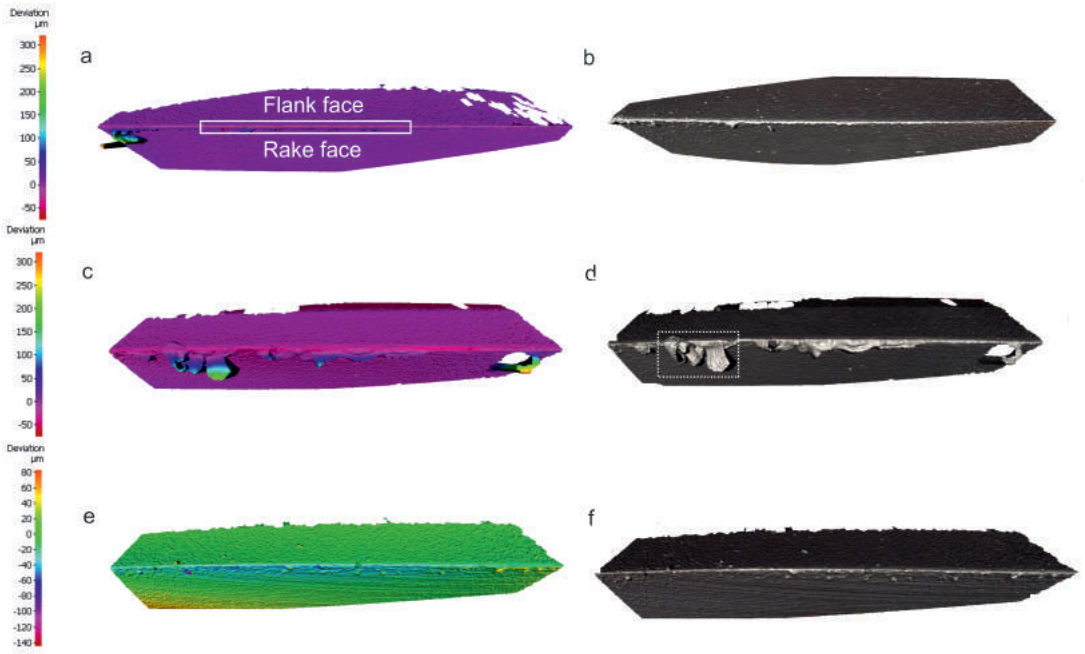

Figure 4.53: 3D contour light images of the the geometric differences for cutting edges between new and used before cleaning of deposited chips a-c. and after cleaning d-f. conditions a and d. 1, b and e. 6 and c and f. 7, coupons subjected to increased SGR 0.14, 0.22 and 0.3 mm/tooth and 300, 375 and 450 m/min respectively.

At the high SGR of condition 7, as seen in Fig.4.53; which is subject to the same increased f_z of 0.3 mm/tooth, as condition 5, in Fig.4.52, the presence of BUE is significantly reduced. This is due to the corresponding increase in V_c, allowing for improved coolant delivery and chip evacuation. The same can not be said for the moderate SGR of condition 6 as seen in Fig.4.53b and e. Significant re-adhered chips and BUE are observed. As with all conditions no flank wear is observed due to the limited cutting duration. For the first investigation, with limited cutting durations, the dominant tool wear mechanism is adhesive wear or BUE.

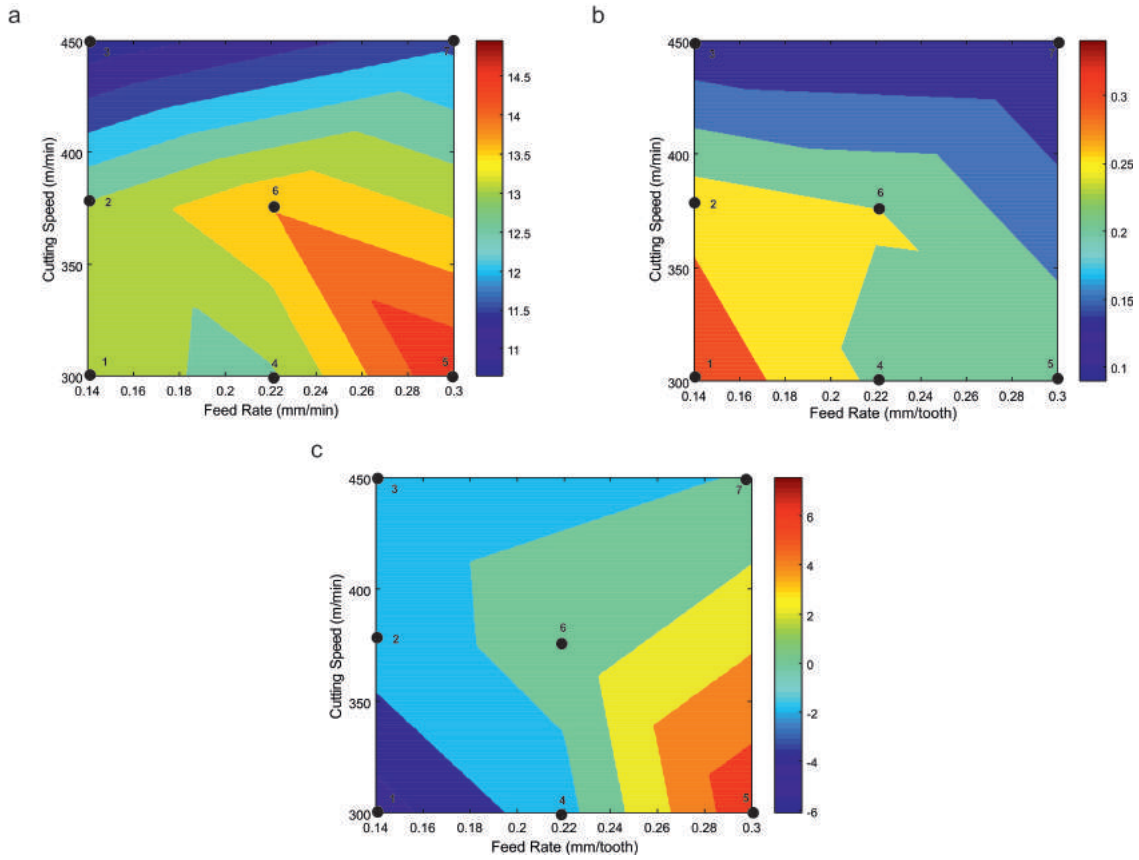

Figure 4.54: Interpolated contour plot for all cutting conditions for average a. cutting edge radii and b. mean deviation (RMS) of all 6 flutes.

The averages of three measurements per each flute of all tools used are summarised for three fundamental tool wear parameters over the spectrum of cutting conditions employed, see Fig.4.54. Fig.4.54a shows the average cutting edge radius *(r)* has a clear relationship between V_c and f_z. Increased V_c has the ability to reduce r at high f_z. This correlates with the 3D light micrographs presented in Fig.4.51, 4.52 and 4.53. At current cutting conditions, the r is increased from 8.775 to 13.09 μm (3dp). At the greatest isolated increase in f_z the r reaches its maximum of 14.95 μm (3dp). At the same f_z, with a corresponding increase in V_c for condition 7, the r is reduced to 11.864 μm (3dp). For all measurements, increased V_c has the effect of reducing tool wear when compared to f_z. This observed behaviour agrees with the dominant findings of existing literature. The mean deviation for current cutting conditions was recorded as 0.246 (3dp). A result of 1 would represent a perfect cutting radii. Therefore the greater the numeric value, the lower the level of tool wear. Mean deviation is reduced from condition 1, 0.339 (3dp) by all parameters to different extents. At high V_c, condition 3; 0.109 (3dp) and high SGR, condition 7; 0.0962 (3dp), the greatest deviation from a perfect cutting edge found. The final parameter, *deviation*, Fig.4.54c, measures the volumetric deviation when compared to a new tool. A negative deviation depicts removal of material from the cutting edge, where as a positive deviation shows the presence of re-adhered material and BUE. For condition 1, removal of material at the cutting edge is evident through a negative deviation of -0.00546 mm^3 (3sf). Increases in f_z, which increases the evidence of BUE shows the greatest increase in positive deviation at 0.00524 mm^3 (3sf). The influence of increasing V_c is clear, the reduction of BUE as a result of improved chip evacuation reduces the deviation over the cutting edge.

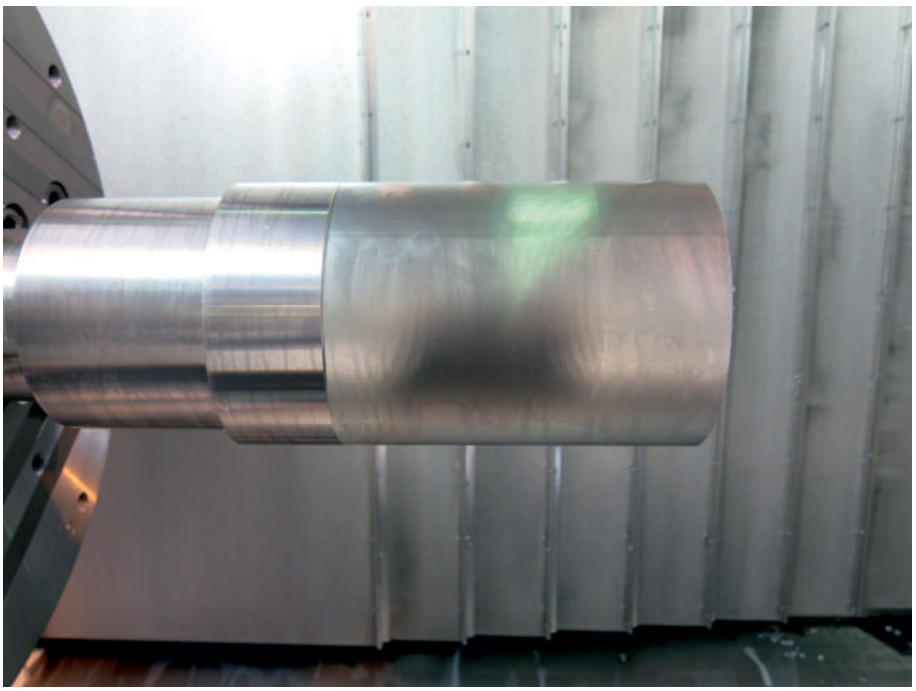

Figure 4.55: Photograph of the Ti-5553 billet at the conclusion of a tool wear trial.

To fully comprehend the influence of tool wear on surface integrity and sub-surface microstructure, and determine the dominant tool wear mechanisms during elongated cutting trials have to be understood. The methodology employed for this testing is described in section 3.4 and an example of the Ti-5553 billet condition during the trial is shown in Fig.4.55. Based on the results from Chapter 4.1 and those presented in this section, the conditions of 1, 2, 4 and 6 were downselected. This limitation was due to the expense of conducting elongated tool wear trials and the quantity of analytical activities required to fully characterise the tools and workpieces. The conditions investigated were selected as they produced a study that isolated and combined the influence of each cutting parameter, while working within the developing operating window.

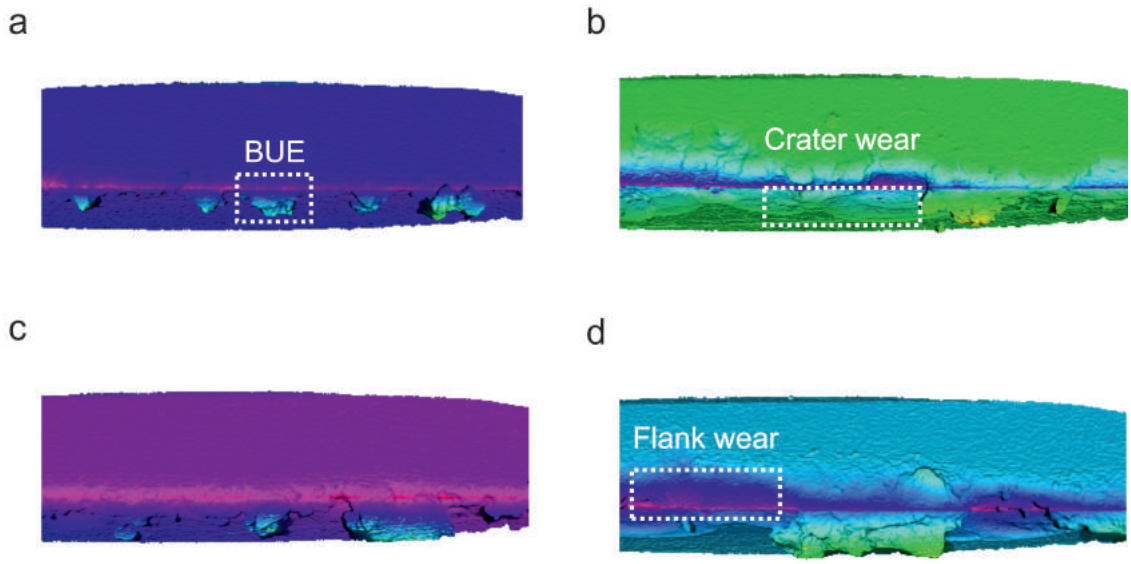

Figure 4.56: 3D contour light images of the geometric differences between new and used tools for cutting edges used for finish end milling of coupons at conditions 1 (a & b) and 6 (c & d) at tool uses of a. 2, b. 3, c. 0.5 and d. 2 hours.

Fig.4.56 presents 3D light micrographs of cutting edges for conditions 1 and 6 at different time intervals. Identical wear mechanisms were identified for both conditions but significantly accelerated for condition 6. From Fig.4.56a and b typical flutes for condition 1 at 2 and 3 hours of cutting time. For durations of cutting under 2 hours, wear progression is stable and focussed predominately at the cutting edge radius showing evidence of abrasive wear and minimal flank wear. BUE on the rake face is present, showing evidence of readhered material. The amount of flank wear and progressive cutting edge wear increases dramatically after 2 hours up until the final 3 hours of use as shown by Fig.4.56b. After 2 hours, the incidences of BUE are reduced and crater wear on the rake face becomes a dominant wear mechanism. It is proposed that as the cutting edge wear becomes severe, the contact area between tool and workpiece changes dramatically producing a ploughing mechanism. Increasing contact between the formed chip and rake face resulting in differential wear rates between the tool and workpiece, leading to crater production. The crater wear is evidence of a transition from abrasive and adhesive wear mechanisms to diffusion driven wear. This behaviour is replicated by condition 6, but significantly accelerated and the transition between adhesive and abrasive to diffusive wear mechanisms is achieved after only 1 hour of cutting time, as shown by Fig.4.56c and d.

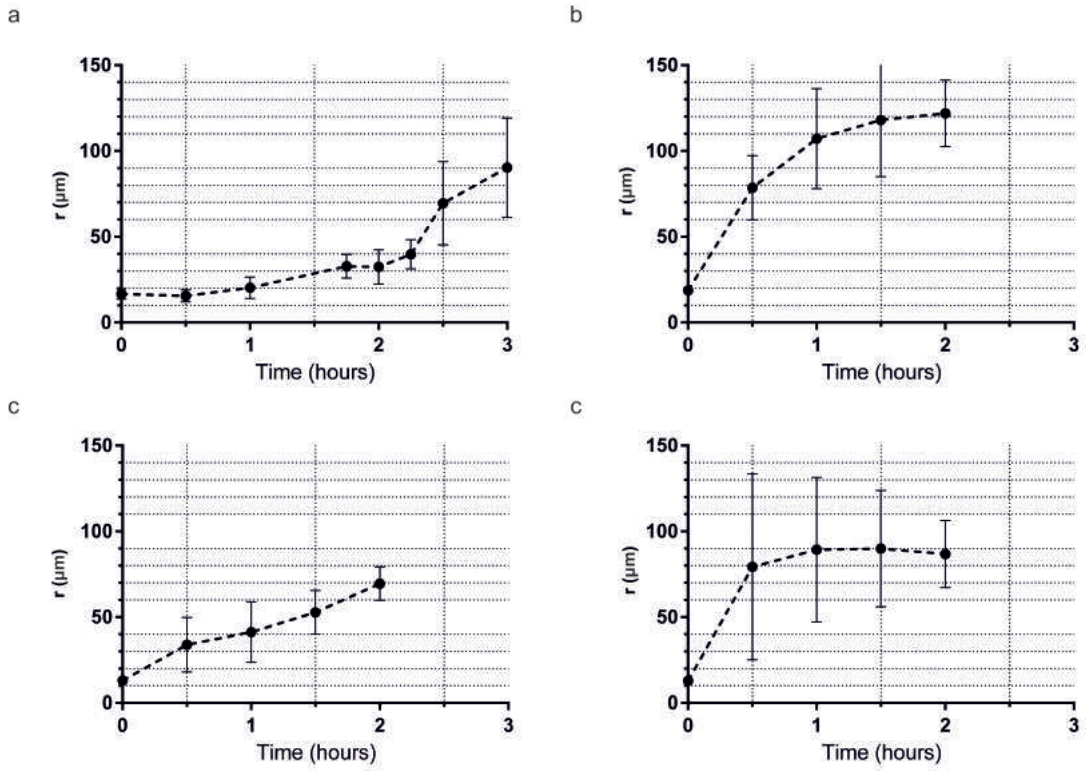

Figure 4.57: Schematic representations of the average cutting edge radius profiles for conditions a. 1, b. 6, c. 4 and d. 2; coupons subjected to increased V_c and f_z against time (hours).

Average cutting edge radii (r) over all six flutes in three positions for each cutting condition over the duration of the tool wear trial are presented in Fig.4.57. The abrasive and adhesive wear mechanisms driving tool wear for condition 1, as seen from the 3D light micrographs in Fig.4.56, show stable degradation of the average r. After initial rapid tool wear, from the starting geometries of a new tool to an initial r of 16.683 μm (3dp), the wear progresses up to approximately 39.805 μm (3dp) at 2.25 hours. Wear then experiences a transition to a diffusion dominated mechanism in which crater wear is initiated and wear rapidly progresses to 90.252 μm. It is also observable that based on the increase in SD over the 6 flutes analysed, that the wear becomes more localised as time progresses. Increased SGR drastically transforms the wear progression from a conventional tool wear time function, see Fig.4.57a. Tool wear is near linear for the initial hour of the cutting trial. The average r for condition 6 reaches quantities found after 3 hours of cutting for condition 1, after only approximately 0.75 hours Fig.4.57b. Crater wear is evident in tools subjected to condition 6, after 1 hour of use, signalling the tool wear mechanism transition occurs earlier and wear is accelerated with increased SGR. Increased V_c, in isolation shows stable wear progression up to 2 hours of tool use to an average r of 69.533 μm (3dp). The SD remains stable over the duration of the cutting trial, wear progresses consistently over all flutes. For condition 2, the presence of a BUE is reduced but still experienced. Wear is predominantly abrasive in nature causing a progressive increase in the average r Fig.4.57a. Near the later stages of the cutting trial, an increase incidence of BUE and localised crater wear is apparent Fig.4.57b. Comparable wear behaviour and average r quantities are observed in 2 hours of cutting between conditions 1 and 2. The wear behaviour for condition 4, shown in Fig.4.57d is comparable to that of condition 6, but reduced in its severity. An initial

rapid wear rate is experienced up to 0.5 hours, followed by a plateau up until 2 hours. When compared to condition 6, the noticeable difference in increased SD for condition 4 can be seen in Fig.4.57d. Dramatic adhesion of chips and crater wear is produced after 1 hour of cutting time. In localised areas of the cutting edge, seizure is present, which provides evidence for the increase SD and variation of wear over each flute.

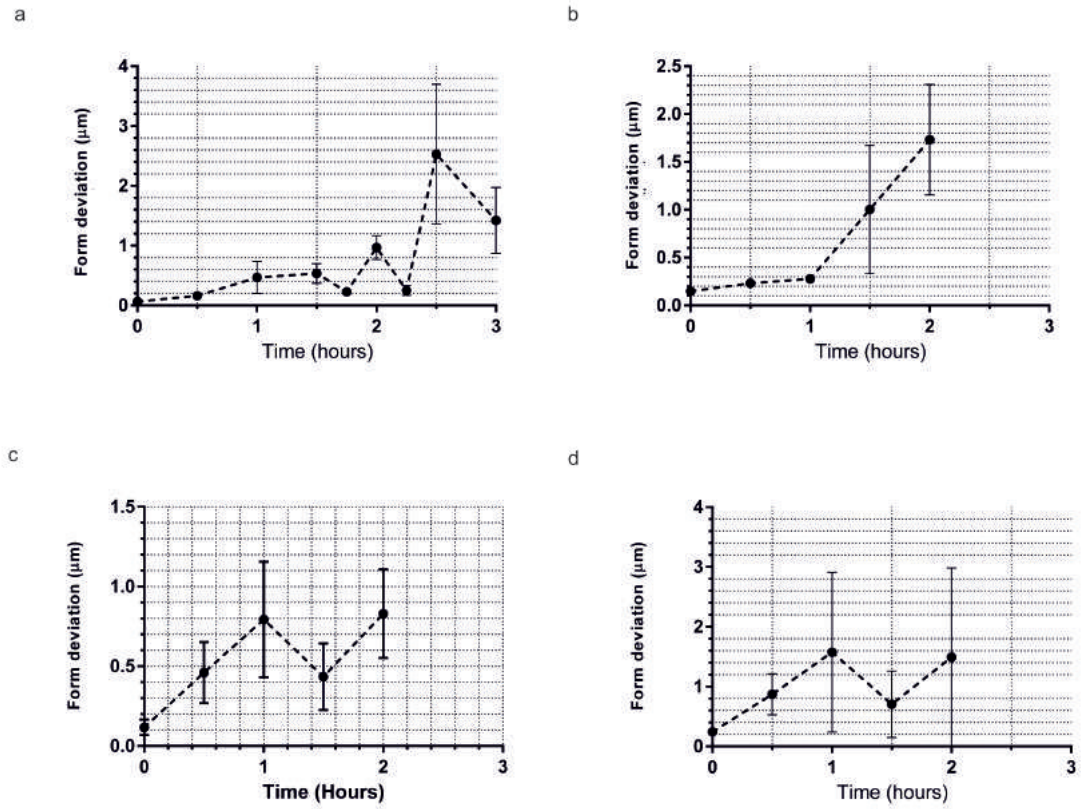

Figure 4.58: Schematic representations of the form deviation profiles for conditions a. 1, b. 6, c. 4 and d. 2; coupons subjected to increased V_c and f_z against time (hours).

An additional tool wear measurement has been proven to be of use in this investigation and demonstrates good agreement with the observed wear trends. The results of form deviation for each cutting condition are presented in Fig.4.58. Form deviation is shown to be a good measure for tool wear during stages of abrasive mechanisms, particularly in condition 1 Fig.4.58a. It can be said that once the wear mechanisms transitions from abrasive to diffusion dominated, the SD increases and the results become less coherent.

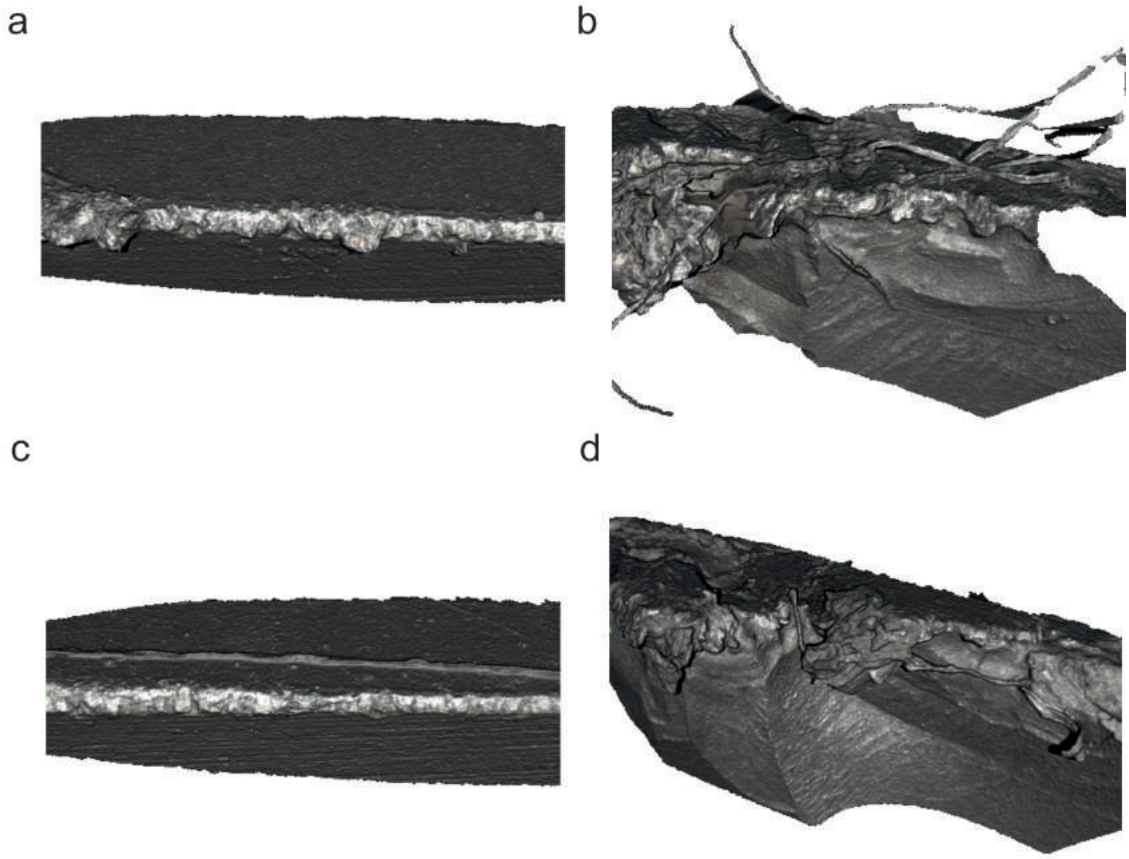

Figure 4.59: 3D contour light images of the geometric differences between new and used tools for cutting edges used for finish end milling of coupons at conditions 4 (a & b) and 2 (c & d) at tool uses of a & c. 0.5 and b. & d. 2 hours.

4.3.2 Surface integrity

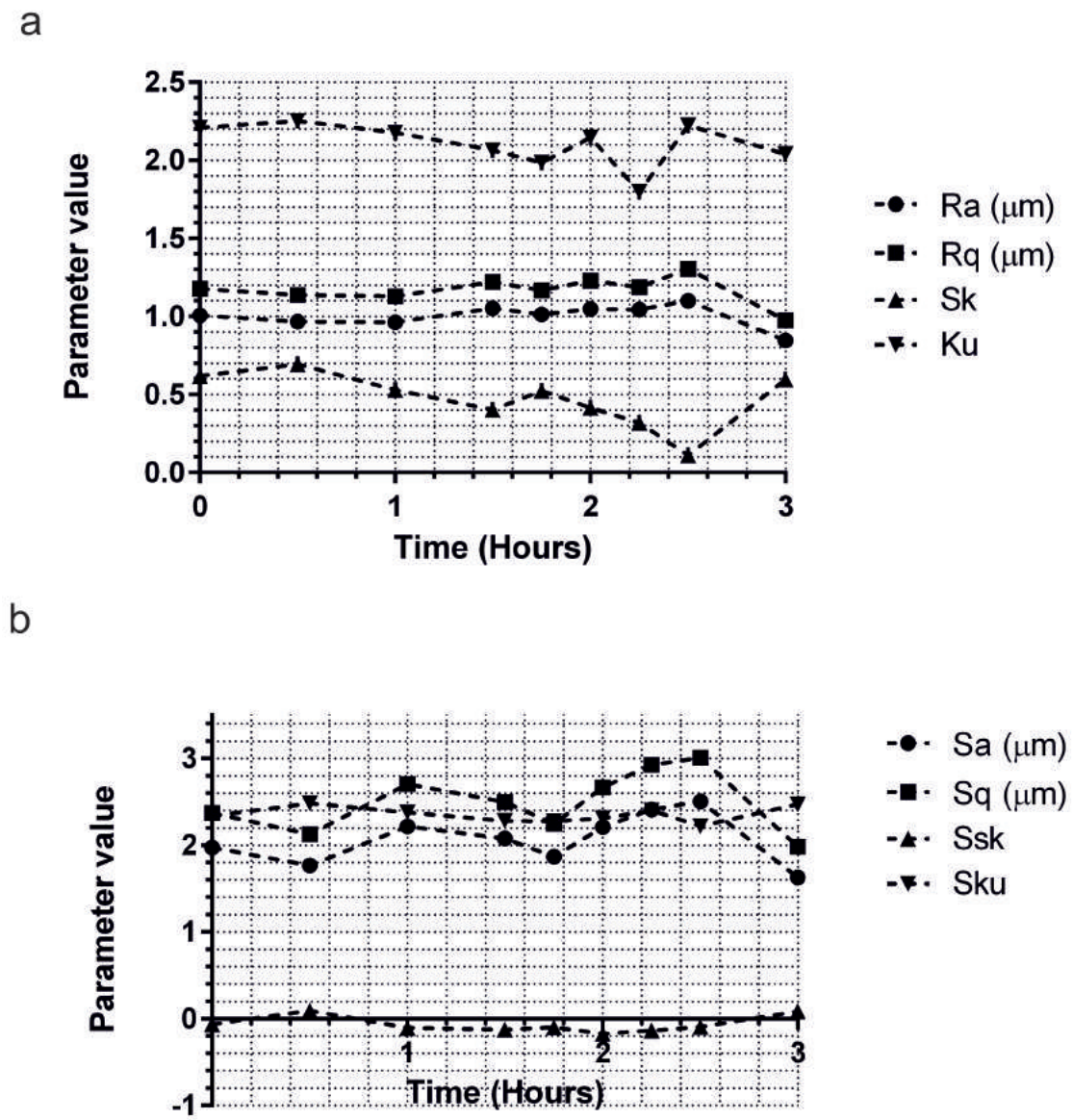

Figure 4.60: Schematic representations of roughness parameters for condition 1 against time in a) 2D and b) 3D.

Results in both 2D and 3D for condition 1, show stable behaviour up to 2 hours of tool use, see Fig.4.60. Minimal variation is observed in R_a and R_q metrics, until the final hour of use, in which a slight reduction is observed. All states of tool wear produce surface roughness with moderate positive skewness, which is reduced to approximately 0.1, until a final increase to approximately 0.6 after 3 hours. R_a and R_q values reach a maximum of approximately 1.3 and 1.1 μm, respectively. Comparative values for S_a and S_q also show their maxima at 2.5 hours of tool use, 2.411 and 3.005 μm (3dp), respectively. Again, a reduction in S_a and S_q is seen after 3 hours. In an identical way as discussed chapter 5, skewness is reduced to near 0, when considered in 3D.

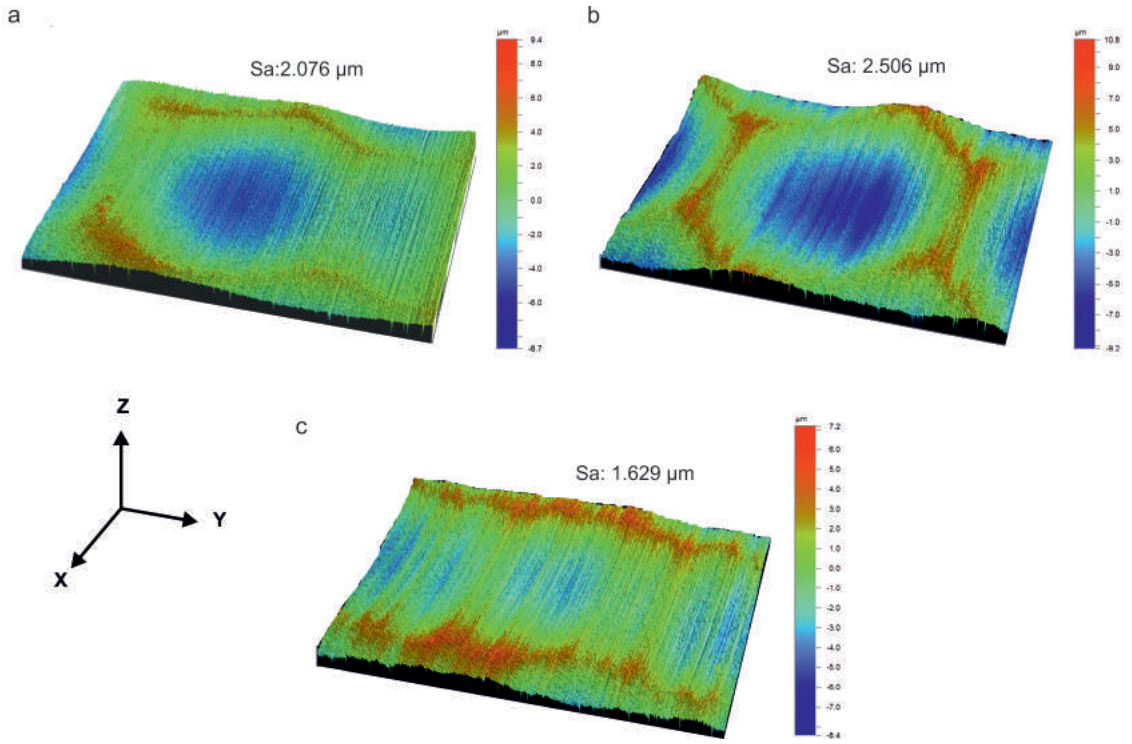

Figure 4.61: Light micrograph at x10 magnification for conditions 1 after a. 1.5, b. 2.5 and c. 3 hours of tool use.

Surfaces produced from cutting at condition 1 after a duration of 1.5, 2.5 and 3 hours of tool use are presented in Fig.4.61. The conventional surface topography is maintained and then exacerbated as time increases from 1.5 and up to 2.5 hours in Fig.4.61a and b. The transition in surface topography and roughness as seen in Fig.4.61c, coincides with the transition in tool wear mechanism discussed with Fig.4.56b.

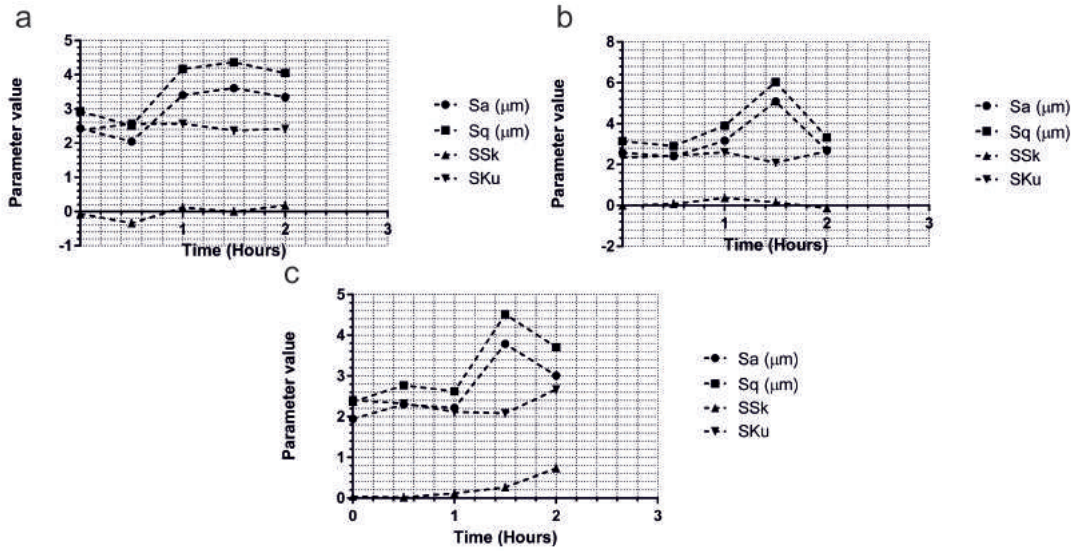

Figure 4.62: Schematic representations of 3D roughness parameters for condition a. 6, b. 4 and c. 2 against time.

Roughness parameters in 3D against time for conditions 2, 4 and 6 are all presented in Fig.4.62. The trends observed in 3D surface roughness parameters reflect

the behaviours portrayed in average *(r)* responses. The increase in SGR for condition 6 in Fig.4.62a, shows that after an initial reduction, parameters S_a, S_q and SSk all show increases, from 0.5 hours of use with S_a and S_q peaking at 3.61 and 4.362 μm (3dp) respectively. This is a significant increase achieved in shorter periods of time when compared to surfaces produced from condition 1. The effect of increased V_c expressed in condition 2, see Fig.4.62b, reflect the results shown in r measurements in Fig.4.57c. A dramatic increase in surface parameters can be seen at 1.5 hours with S_a and S_q peaking at 3.789 and 4.151 μm (3dp), respectively. These results show a slight increase in some parameters for condition 2, when compared to condition 6. When studying the information presented in Fig.4.56d and 4.59b, this increase in surface roughness parameters with V_c is believed to be due to the apparent increased flank wear and the abrasive mechanism which increases the average r. A similar trend in roughness parameters can be seen for increased f_z for condition 4, Fig.4.62c. Peaks in S_a and S_q are shown at 1.5 hours with values of 5.084 and 6.036 μm (3dp), respectively. These are the highest roughness values recorded as a result of tool wear, which corresponds to the dramatic crater wear and localised tool fracture, as a result of increased f_z as in Fig.4.59d.

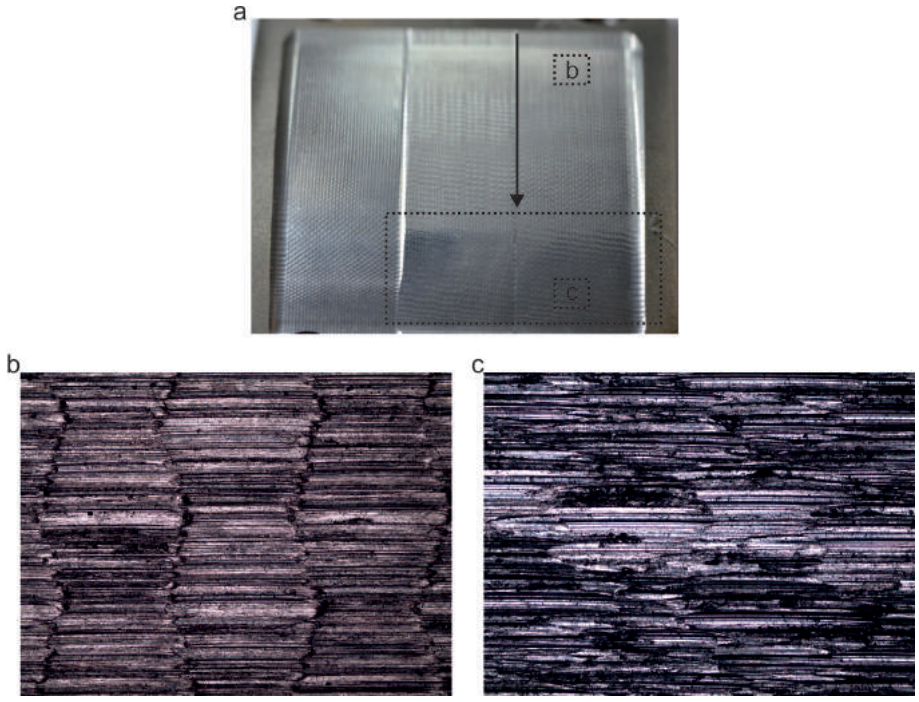

Figure 4.63: a. Photograph of a Ti-5553 coupon subject to condition 4 with light micrographs at x10 magnification presenting the affective of b. low and c. high effective V_c.

In all conditions, the final surface roughness measurement shows reductions in parameters. It is believed that this is a result of the onset of localised crater wear and cutting edge fracture. A coupon subjected to condition 4, increased f_z as seen in Fig.4.63a, in which the region identified as a dashed black box shows evidence of a decreased cutting depth. This region corresponds to the maximum $V_{c_{eff}}$, which is subsequently the region of the cutting edge subject to the greatest amount of crater wear. The result of this behaviour on the surface is shown in Fig.4.63b and c. The region of Fig.4.63b corresponds to the surface as a result of the ϕ_{effmin}, in which a more conventional surface profile is produced. The region identified by Fig.4.63c is the surface subject to the ϕ_{effmax} and the regions of crater wear.

This produced an intermittent cutting action and a reduction in the cutting depth. Though this produces a reduction in surface roughness, due to the lack of complete tool engagement, it also means that the primary surface profile and component geometry is not achieved.

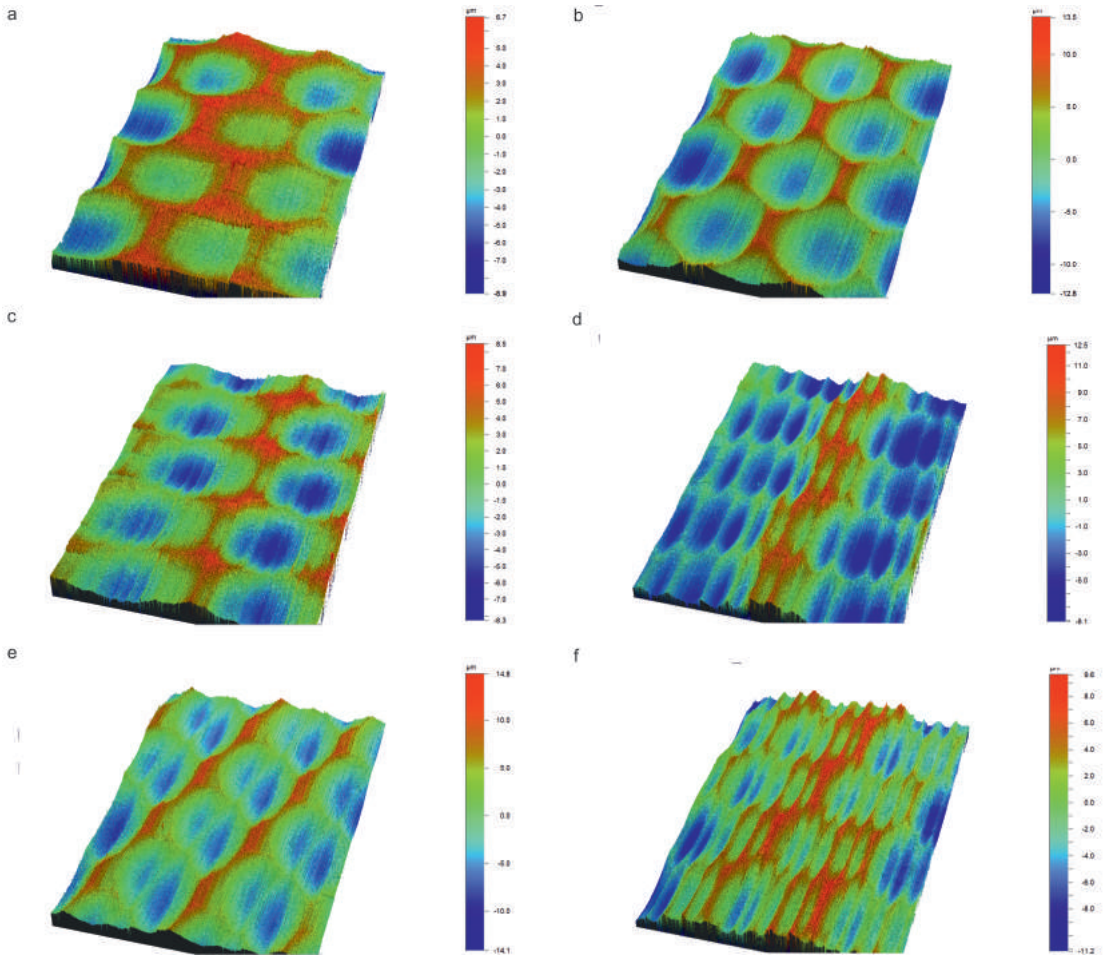

Figure 4.64: Light micrograph at x10 magnification for condition 2 for a-c. 2 hours of tool use compared to d-f. 0 hours of tool use. Light micrographs taken at the a & d. upper, b & e. middle and c & f. lower regions of the coupons.

Stitched 3D light contour micrographs for conditions 6, 2 and 4 are presented in Fig.4.64 at 0.5 and 2 hours of tool use. Stitched images are used to show the surface topography over a larger area to best describe the influence of localised crater wear. When studying Fig.4.64b, d and f, the localised diffusive wear mechanism that leads to cutting edge fracture can be seen. The intermittent cutting action is evident in Fig.4.64c,d and f. The increase in SGR expressed in condition 6, between Fig.4.64a and b shows consistent cutting and explains the maintenance in surface roughness parameters achieved in Fig.4.62a. However, for isolated increases in V_c or f_z, conditions 2 and 4 respectively, non-uniform surface topographies are produced, Fig.4.64d and f. Therefore, isolated increases in cutting parameters not only influence wear mechanisms but subsequently produce surface roughness magnitudes, greater than is required by industry and in a non-uniform manner. Surfaces produced in this way will have a significant influence on in-service performance.

4.3.3 Cutting forces

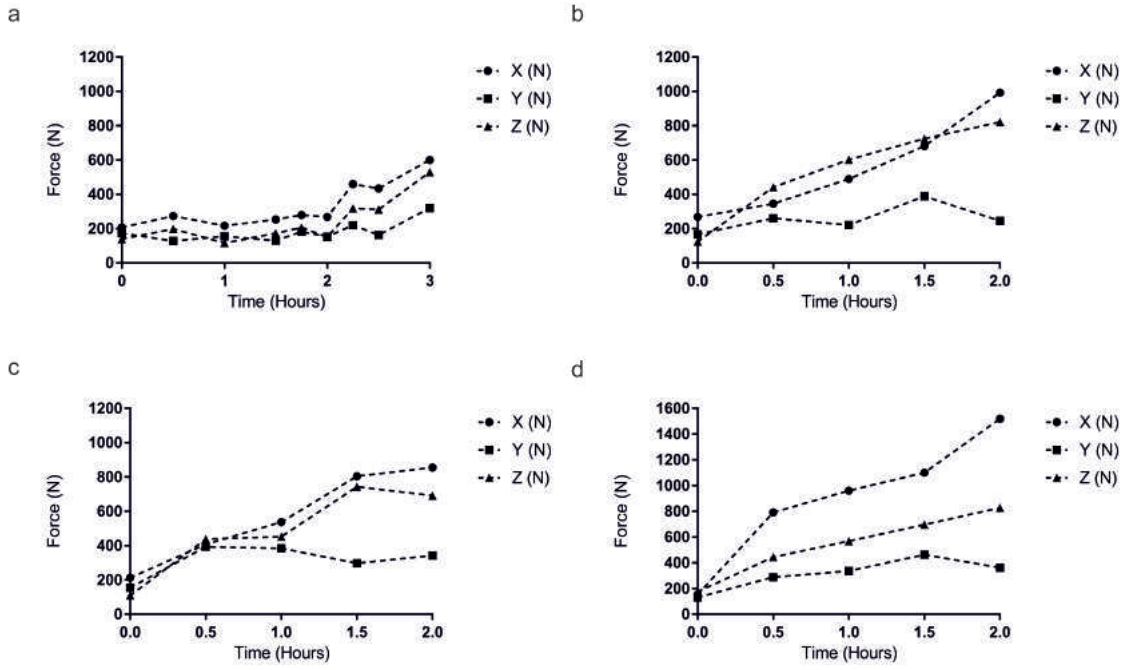

Figure 4.65: Cutting force profiles for conditions a. 1, b. 6, c. 4 and d. 3; coupons subjected to increased V_c and f_z against time (hours), in the X, Y and Z; normal, thrust and cutting force directions respectively.

When studying cutting forces over the duration of each condition, several conclusions can be drawn, as shown in Fig.4.65. Cutting forces increase with r, over the time of tool use with a clear increase in all cutting force directions. After 2 hours of tool use a noticeable increase in all cutting forces for condition 1 can be seen Fig.4.65a. This transition again coincides with the increase in flank wear and crater wear identified as a transition in wear mechanism. The same can be observed for condition 6, Fig.4.65b, for which all cutting forces, in each of the three directions are greater in magnitude than condition 1. Over the majority of the duration of testing, it can be seen that for condition 1, normal cutting forces, in the X orientation are the greatest in magnitude. For condition 6, between 0.5 and 1.5 hours the major cutting force in the Z orientation is the greatest in magnitude. For both conditions, as with the results in Chapter 4.1, the Y orientation cutting force is the lowest recorded cutting force. In both cases, the largest recorded cutting forces are at the last measured tool state in the X orientation, at 3 and 2 hours for conditions 1 and 6 respectively. For both isolated increases in V_c and f_z, see Fig.4.65c and d respectively, at all time intervals, the X orientation cutting force is the greatest in magnitude. Again, the Y orientated cutting forces are the least prevalent at all time intervals for both conditions 3 and 5. Conditions 3 and 4 show a steady increase in cutting forces over time, with the increased f_z condition presenting the greatest recorded force at 2 hours of use with 1519.05 N in the X orientation. This coincides with the greatest increases in both r, roughness parameters and subsurface deformation. The behaviour of r and transitions in tool wear mechanisms are reflected in many ways by the monitored cutting force.

4.3.4 Subsurface microstructure

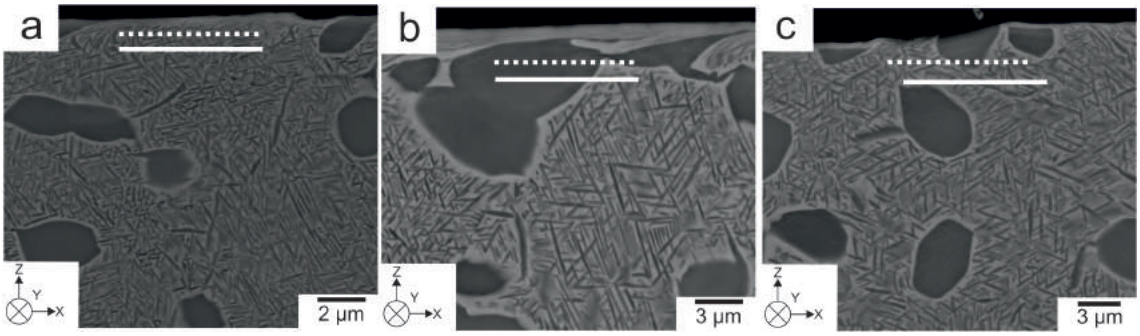

Figure 4.66: BSEI at x20,000 of the finish end milled subsurface for condition 1, coupons subjected to a V_c and f_z of 300 m/min and 0.22 mm/tooth at a. 0.5, b.1 and c. 2 hours of tool use in the X orientation.

Curved coupons subject to cutting at condition 1 after increasing tool use at 0.5, 1 and 2 hours in the X orientation are presented in Fig.4.66. For cutting under 2 hours of tool use the high X orientation cutting force results in SPD and sweeping of the α_p grains in the upper 2 μm of the subsurface. The intensity of the SPD layer increases with tool wear. Limited surface defects like cavitation and tearing are evident in all conditions. After 2 hours of tool use, when the wear mechanism transition occurs and increase in Z orientated cutting force coincides with a reduction in α_p grain deformation but increased instances of dislocation slip. The depth of SPD increases gradually with tool wear. The influence of tool wear is shown to have a moderate effect on deformation for current cutting conditions. In industry, these milling tools at these cutting conditions are typically utilised for up to 2 hours. The results of this investigation suggest an additional 0.25 hours of tool use could be safely utilised and the surface integrity and those is comparable to subsurface structures observable for less than 2 hours of tool use. With no incremental increase in cutting parameters, substantial economic gains are potentially available through elongated tool life. This opportunity has previously not been known as no substantial tool wear trial has been conducted for such complex industrial milling operations.

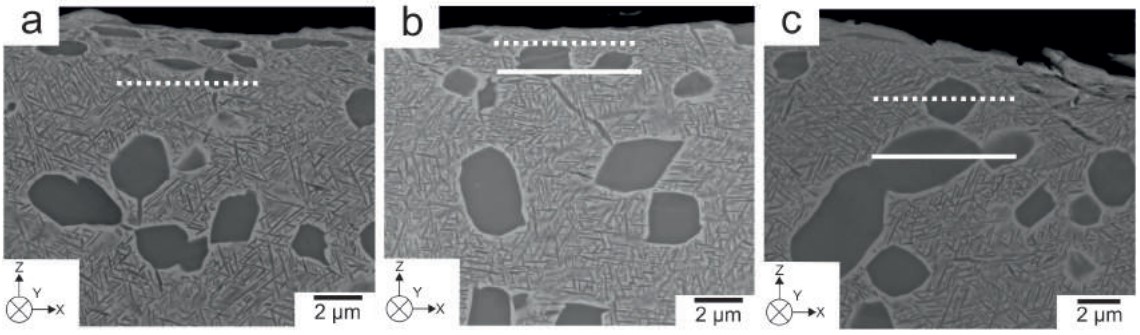

Figure 4.67: BSEI at x20,000 of the finish end milled subsurface for condition 2, coupons subjected to an increased of V_c of 375 m/min at a. 0.5, b.1 and c. 2 hours of tool use in the X orientation.

Subsurface microstructures of coupons subjected to the increased cutting speed of condition 2 at 0.5, 1 and 2 hours of tool use in the X orientation are presented in Fig.4.67. As tool use increases, the depth of SPD and instances of slip and

surface defects all increase. The substantial evidence of surface defects in Fig.4.67c, correlate with well with the findings of surface imaging in Fig.4.64d. The influence of high X orientated, normal cutting forces on the SPD are expressed during this tool wear trial.

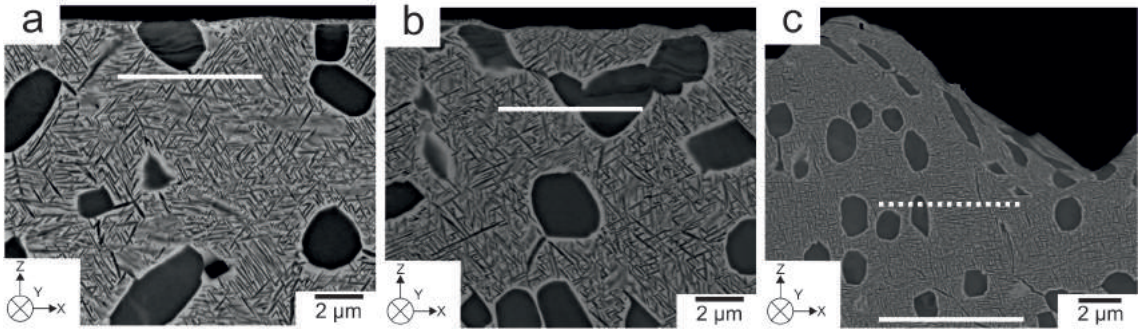

Figure 4.68: BSEI at x20,000 of the finish end milled subsurface for condition 4, coupons subjected to an increased of f_z of 0.22 mm/min at a. 0.5, b.1 and c. 1.5 hours of tool use in the X orientation.

The influence of substantial crater wear and the process of interrupted cutting, as shown in Fig.4.64f, present themselves to a greater extent in Fig.4.68c. With increased f_z at long durations of cutting, up to 2 hours, the surface becomes severely undulated, both globally as in Fig.4.64f and locally as in Fig.4.68c. SPD is produced to greater depths due to this surface behaviour. High Z orientated cutting forces influence deformation at earlier stages of tool use for this high f_z condition. Limited elongation to the α phase is observable, but the onset of dislocation slip within α_p grains is achieved after only 0.5 hours of cutting. Extensive and well defined intense slip bands are present in α_p within the upper 5 μm. After 1 hour of tool use, pronounced levels of dislocation slip are present in α_p grains. For neighbouring colonies of α_p grains, slip bands appear activated in planes that have the potential to produce unimpeded crack propagation paths, that could be achieved over lengths of multiple α_p grains. No EBSD analysis was conducted during this stage of the study, due to the quantity of samples produced. The presence of dislocation slip appears not to be influenced by grain size, but rather the proximity of the grain to the highly strained surface and the influence of the parent β grain orientations. The behaviour defined in the later is believed to be true due to the tendency for extensive slip being present in localised colonies of α_p grains. Previous work presented in this thesis shows the strong Burgers relationship present between the β and α phases throughout the material.

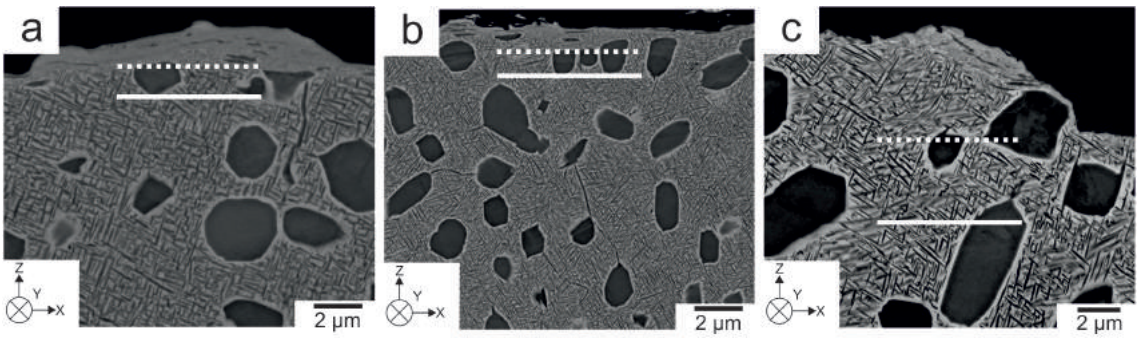

Figure 4.69: BSEI at x20,000 of the finish end milled subsurface for condition 6, coupons subjected to an increased of V_c and f_z of 375 m/min and 0.22 mm/min respectively, at a. 0.5, b.1 and c. 1.5 hours of tool use in the X orientation.

When considering the influence of increased SGR, as in condition 6 on subsurface microstructure, at wear durations of 0.5, 1 and 2 hours, the machining induced deformation behaviour can be studied in Fig.4.69. The high magnitudes of both X and Z cutting forces show their influence on subsurface deformation, in both Fig.4.69a and b. Localised and extensive SPD is seen after 0.5 in the upper 2 μm of the subsurface with faint induced strain observable in the nearest 3 μm of α_p grains. No distinct evidence of induced deformation modes such as slip are seen. As tool use progresses to 1 hour, the region of SPD in the upper 2 μm persists and now induced deformation is present in the form of slip bands, within α_p grains down to 5 μm below the surface. There is evidence of localised surface defects after 2 hours of tool use in Fig.4.69c. Evidence of SPD is reduced at this time and induced deformation within α_p grains is present, but it is not clear whether this has resulted in induced slip.

4.4 The effect of machining induced deformation on fatigue performance for finish milling of Ti-5Al-5Mo-5V-3Cr

The results presented in this chapter explore the influence of SGR on fatigue performance as an approach to defining the effect on in service performance. Due to limited access to suitable source material and the lengthy process of detailed fatigue performance characterisation, only two machining conditions were studied. Conditions 1 and 6 were chosen, due to the variation in subsurface deformation achieved and the substantial difference in SGR. Both conditions were achievable utilising the machining centres available at the AMRC with Boeing and SLS.

4.4.1 Mechanical property inspection

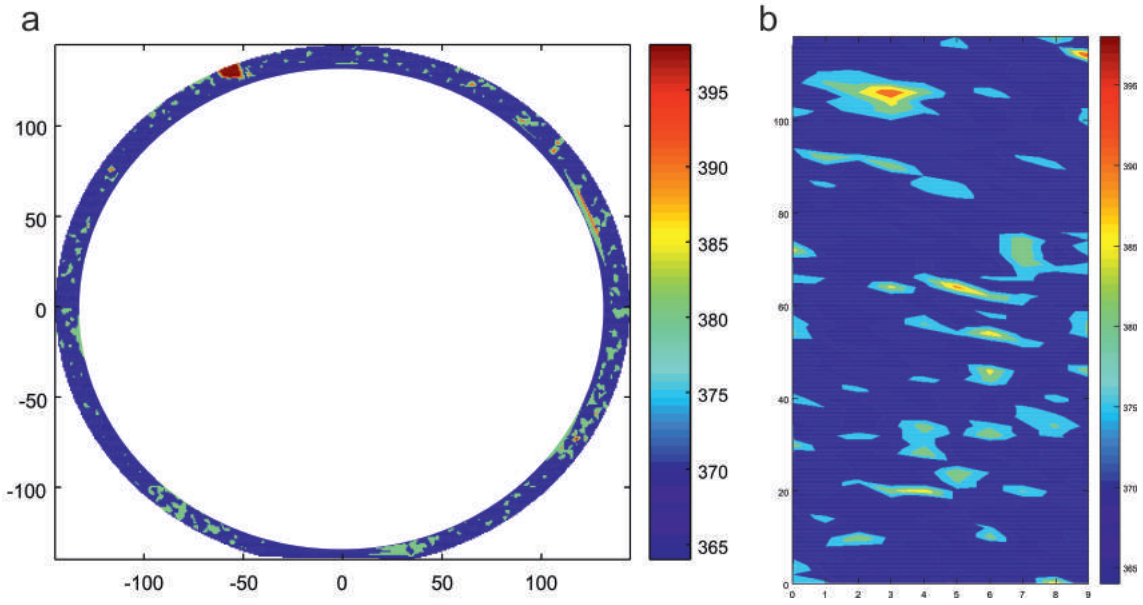

Figure 4.70: Schematic representation of Vickers micro-hardness indentation contour plots for the Ti-5553 truck beam section in the a. circumferential and b. longitudinal directions.

Due to the large β grain size and strong texture possessed by this alloy, there is the potential for microstructural variation that could have a significant influence on mechanical properties. Fatigue behaviour between the two machining conditions and different coupons can not be accurately assessed if the material has such a variation in mechanical properties. Results from a detailed Vickers micro-hardness indentation study are presented in both the circumferential (X) and longitudinal (Y) directions, in Fig.4.70a and b, respectively. The results in the X, see Fig.4.70a, show average and standard deviation results of 374.375 and 4.456 H_V (3dp), respectively. In the Y, see Fig.4.70b, show average and standard deviation results of 373.457 and 5.77 H_V (3dp), respectively. These results show consistency in mechanical properties throughout the source material, which is in good agreement with the work presented in section 4.1. It was concluded coupon extraction could occur from any location of the source material.

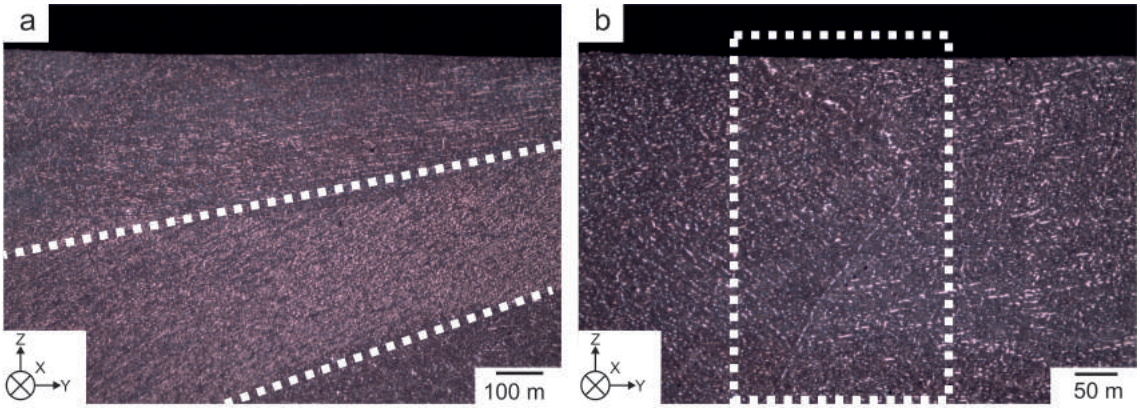

Figure 4.71: Light micrographs at x10 magnification, depicting a. the influence of β phase on microstructural characteristics and b. the presence of α_{GB}.

The source material, Fig.3.14a, was further characterised through light microscopy. A substantial area of the material was studied in both orientations to distinguish any significant microstructural features. It was concluded that this material is representative of the Ti-5553 utilised throughout this thesis with respect to grain size and distribution. The light micrographs presented in Fig.4.71, show examples of microstructural features of interest. Fig.4.71a shows the observable influence of the β phase on α_p grain orientation, with substantial numbers of α_p grain over several hundred μm presenting preferential c-axis grain orientations. This variation can be distinguished by the delineation of dashed white lines in Fig.4.71a. The presence of α_{GB} within the region is delineated by the dashed white box in Fig.4.71a. This shows the potential for hard α_{GB} to produce a distinct path from the surface to the subsurface, on the order of several hundred μm, from which fatigue cracks could propagate.

4.4.2 Surface integrity

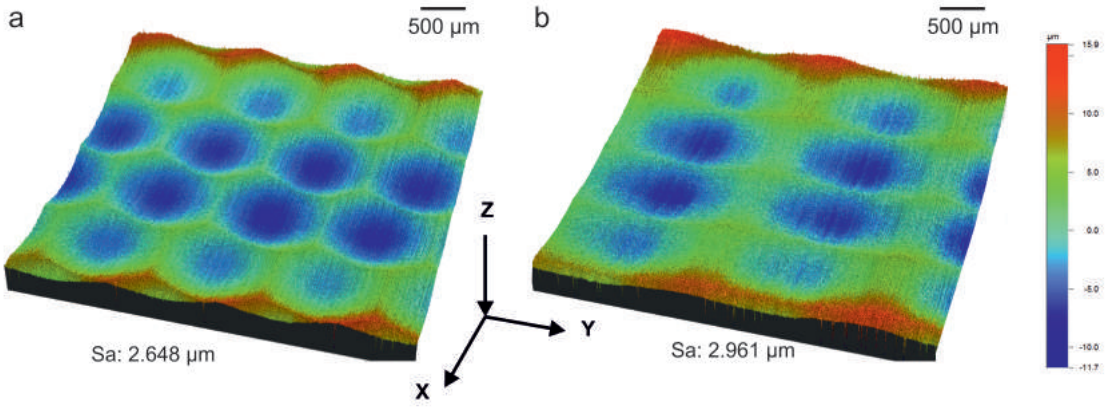

Figure 4.72: 3D light image at x2.5 magnification for conditions a. 1 and b. 6 prior to four point bend fatigue testing.

No significant surface defects were identified through surface light microscopy or dye penetrant testing. The 2D and 3D surface roughness was characterised, with examples of large area stitched 3D light micrographs presented in Fig.4.72. 2D roughness profiles were recorded across all coupons in three locations and two directions, X and Y, as shown in Fig.3.22. The results for all measurements were averaged and presented, showing good agreement with corresponding results for equivalent cutting conditions in Chapter 4.2 and 4.3. Values for R_a, R_q, Sk and Ku for condition 1, Fig.4.72a, were found to be; 1.353 μm, 1.576 μm, 0.244 and 2.081 (3dp), respectively. The corresponding values for condition 6, Fig.4.72b, were recorded as, 1.233 μm, 1.432 μm, 0.19 and 2.135 (3dp), respectively. Values in 3D for condition 1 for the metrics S_a, SR_q, SSk and SKu were 2.648 μm, 3.328 μm, 0.417 and 2.782 (3dp), respectively. The corresponding values for condition 6 were 2.961 μm, 3.708 μm, 0.455 and 2.084 (3dp), respectively.

4.4.3 Subsurface microstructure

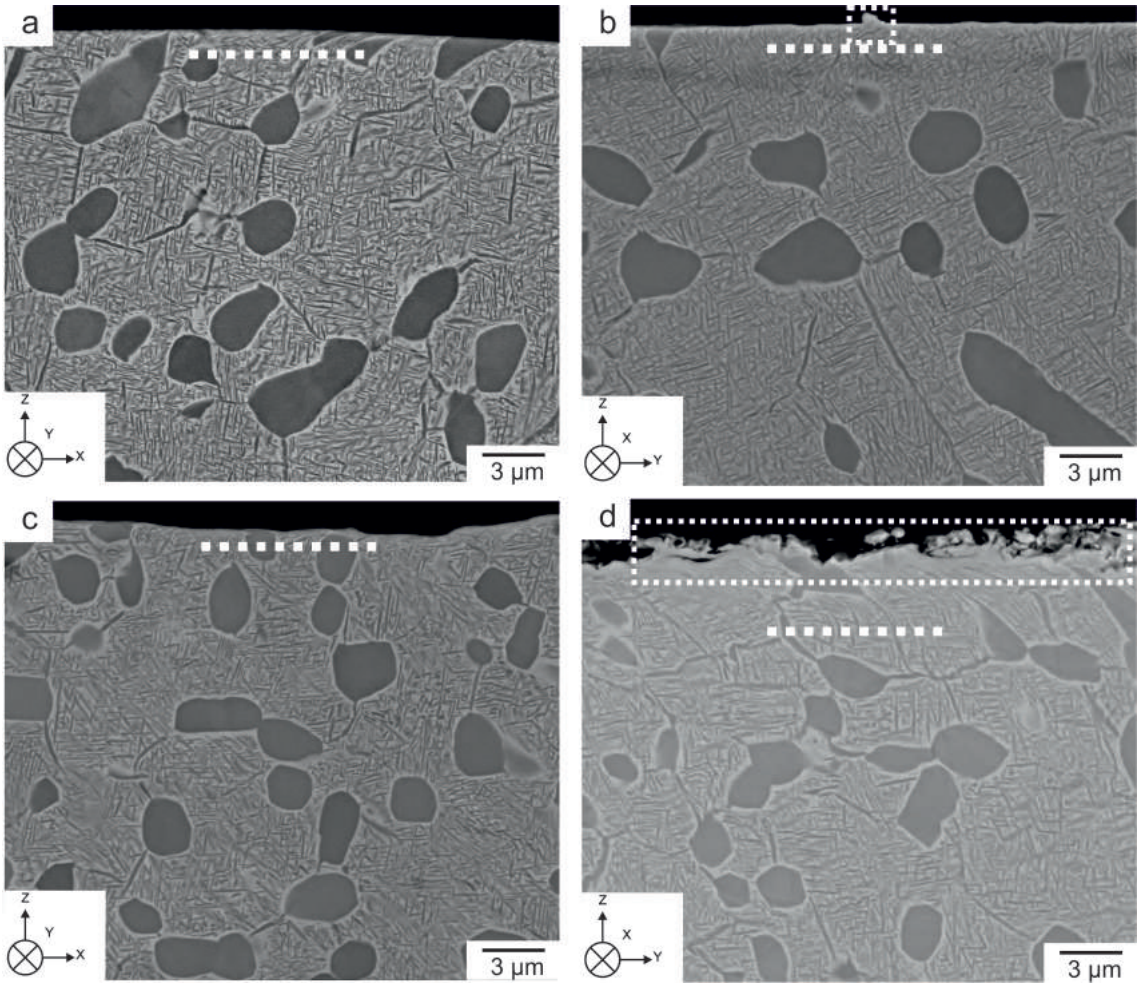

Figure 4.73: BSEI at x10,000 of the finish end milled subsurface for conditions a & c. 1 and b & d. 6 in the a & b. Y and c & d. X orientation prior to four point bend fatigue testing.

The as-machined subsurface microstructure, for both conditions, were characterised through BSEI, in both the X and Y direction and orientations, as presented in Fig.4.73. It was concluded that subsurface deformation was comparable to that presented in section 4.2.3 and 5.4.4. Condition 1 presents localised SPD in the upper 3 μm, seen as microstructural distortion and sweeping of the α_p grains. Limited dislocation slip is evident for this condition, with some low intensity, faint slip lines present in the upper 2 μm of α_p grains in the Y orientation, as shown in Fig.4.73c. Unlike condition 1, 6 does show the presence of surface defects such as cavitation and tearing, as seen in Fig.4.73b. This is exacerbated in the Y orientation, where the influence of increased f_z and cutting forces produce SPD and dislocation slip along prismatic and basal planes as determined in section 4.2.4. It can be concluded that the machining operations, described in section 3.5.2, have produced representative surface and subsurface conditions as with those in Chapters 4.2 and 4.3.

4.4.4 X-ray diffraction (XRD) residual stress analysis

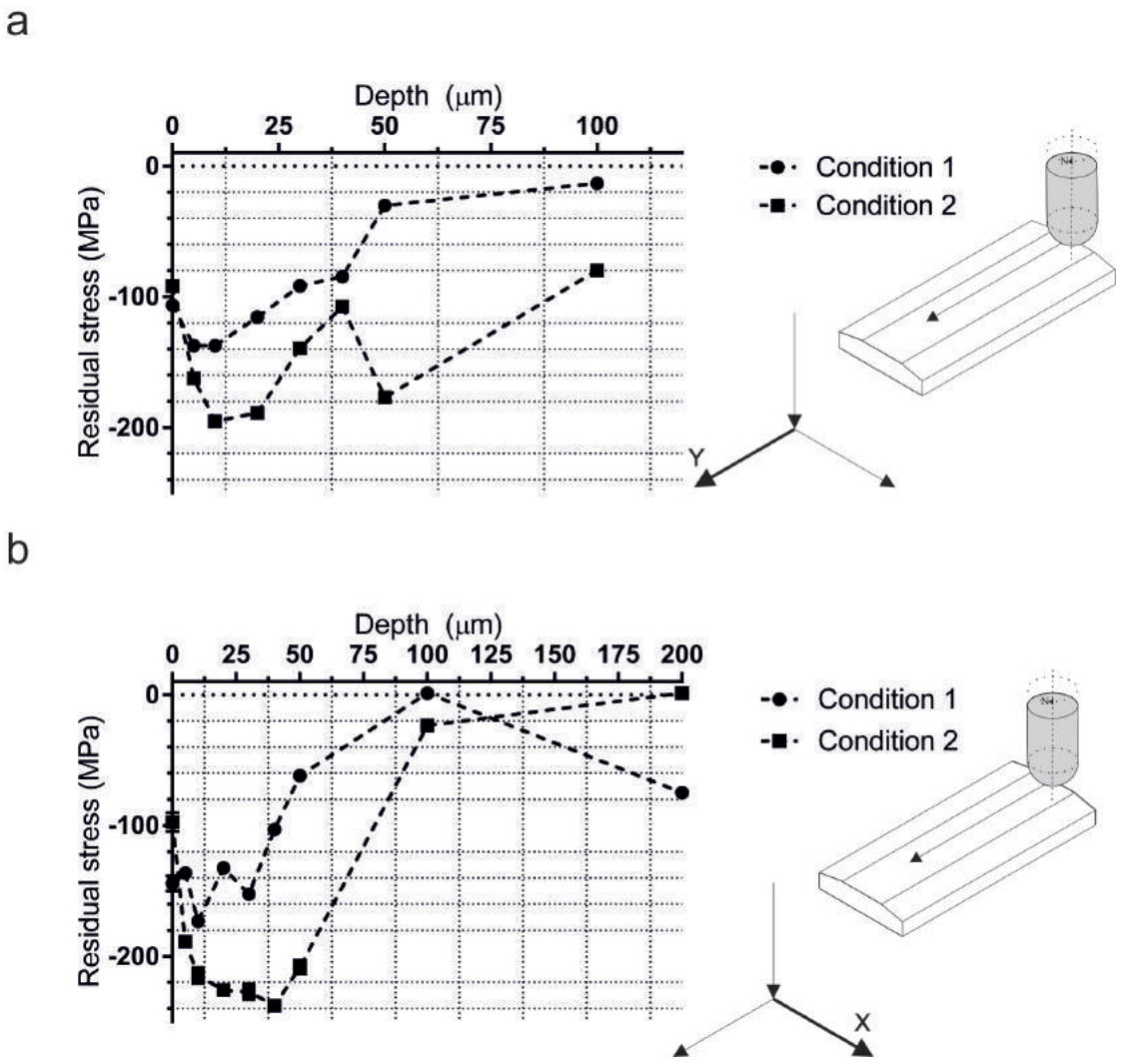

Figure 4.74: Schematic representation of the subsurface XRD residual stress profiles for conditions 1 and 6 in the a. Y and b. X direction.

A detailed procedure, as described in section 3.5.3, was undertaken to characterise the as-machined subsurface stress state for conditions 1 and 6. The results are summarised in Fig.4.74. Results for both conditions are presented in the Y orientation, Fig.4.74a and the X in Fig.4.74b. Through the XRD residual stress characterisation of commercially pure titanium HDH powder, as a stress free standard, the measurements of machined Ti-5553 four point bend test coupons could be calibrated. Due to the combination of a large grain size and a strong texture present in the β phase, only the α phase could be characterised. This was aided by the small interaction volume of measurements. Due to the strong Burger's relationship between the two phases, it was concluded this was satisfactory to characterise the induced stress in machined Ti-5553. Measurements of the bulk material below a depth of 200 to 500 μm, for machined and polished Ti-5553 samples, showed an average residual stress measurement of -8.099 MPa (3dp) with a standard deviation of 11.181 and a range of 36.441 MPa (3dp). It was concluded, machining operations induced no residual stress below this depth. In both directions, it was found residual stress was reduced to that of the bulk measurements by a depth of 200 μm. Results to depths of 100 μm are presented in Fig.4.74. In both the X and Y orientations at each depth the

residual stress was found to be compressive in nature and of greater magnitude for condition 6. Greater compressive residual stresses were found to be evident in the Y Orientation. This is in agreement with results from Chapter 4.2, in which cutting forces increased the propensity for subsurface deformation. In both directions, the upper 5 μm SPD region, presented compressive stresses of 106-144 MPa for condition 1 and 91-97 MPa for condition 6. In the Y orientation, the stress for both conditions peak at a depth of 10 μm with conditions 1 and 6 being 137.426 and 173.17 MPa (3dp), respectively. From this depth, residual stresses trend towards that found in the bulk, this behaviour occurs more rapidly for condition 1. This behaviour was observed to a greater extent in the Y orientation. For condition 1 in the Y orientation, compressive residual stress reaches a maximum of 173.167 at 10 μm and 237.73 MPa for condition 6 at a depth for 40 μm. This result shows that compressive stresses are increased in both magnitude and depth with increased SGR. When studying the error for each measurement, which is calculated from the standard deviation (SD), it can be seen error decreases with depth. Surface measurements in both directions possess errors of between 5.96 and 7.342 MPa (3dp), for conditions 1 and 6, respectively. This is reduced to 3.081 and 4.684 MPa (3dp) by 100 μm in depth. This shows the accuracy of residual stress measurements is reduced nearer the machined surface. This is due to the increased crystallographic distortion as a result of deformation through fatigue loading. As distortion is increased, diffraction of the incident X-ray is exacerbated and quality of the measurement is reduced. It is believed with some confidence that the remainder of the bulk material has negligible stress associated with it. It is also noteworthy that no significant tensile residual stresses were recorded throughout the subsurface. Due to the increased error of near surface measurements and the size relationship between penetration depth and grain size, it is hypothesised that there is a potential for localised tensile stresses to be present within the upper 5 μm of the subsurface. Such tensile residual at the surface could balance the compressive stresses present in the upper 200 μm and would lend support to the increased tendency for dislocation slip within α_p grains as a result of tensile loading.

4.4.5 Four point fatigue bend testing

Load confirmation

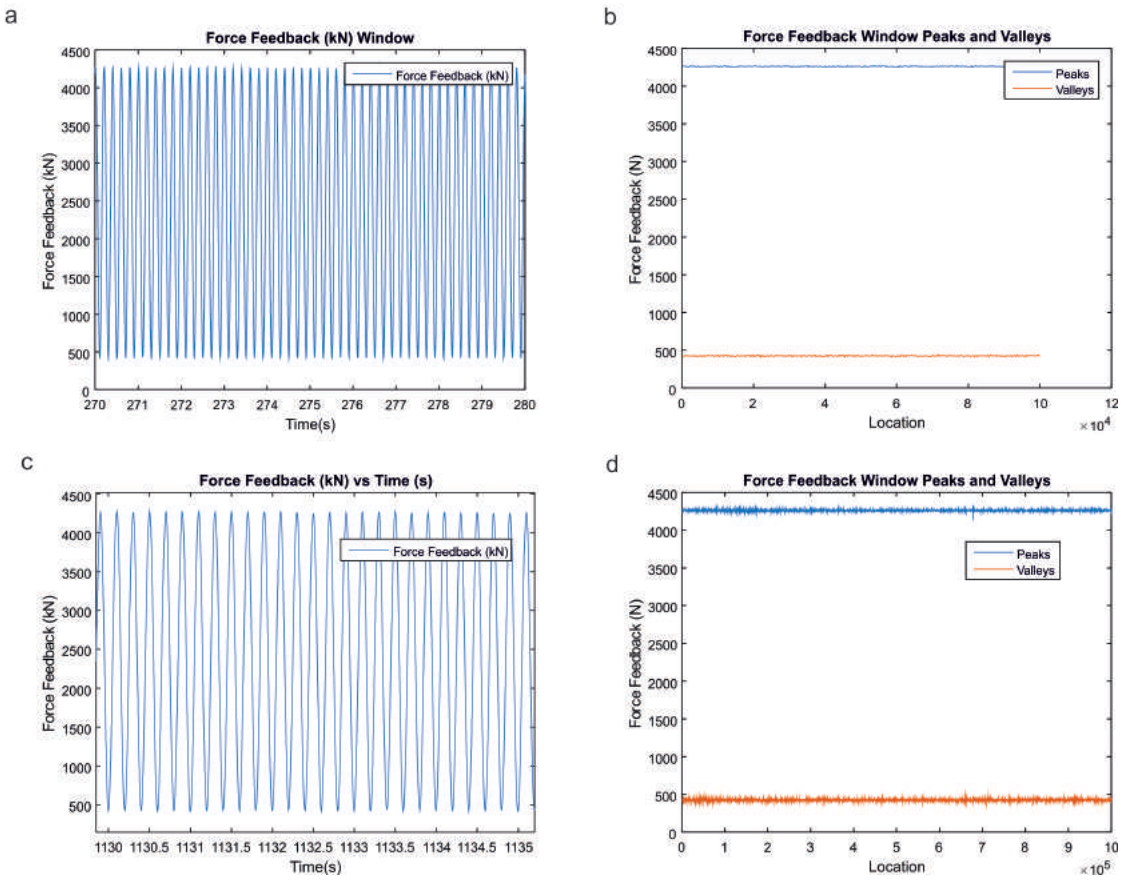

Figure 4.75: Schematic representation for conditions a & b. 1 and c & d. 6, depicting a & c. force feedback against time and b & d. maximum and minimum force feedback against time.

A minimum of 10 coupons were successfully tested to failure for both conditions 1 and 6. Condition monitoring techniques showed load control was achieved throughout the duration of each test, with typical examples for condition 1 and 6 presented in Fig.4.75a and b and Fig.4.75c and d, respectively. Fig.4.75a and c present time samples from the steady state fatigue life for both conditions, showing load control was successfully maintained the required 4260 and 426 N upper and lower limits, respectively. Fig.4.75b and d, show the upper and lower recorded loads throughout testing, in which a typical standard deviation of 5.183 and 4.945 N (3dp), respectively was observed. It is therefore confirmed, that throughout testing, for both conditions, a stable and accurate R = 0.1 is maintained.

Displacement observation

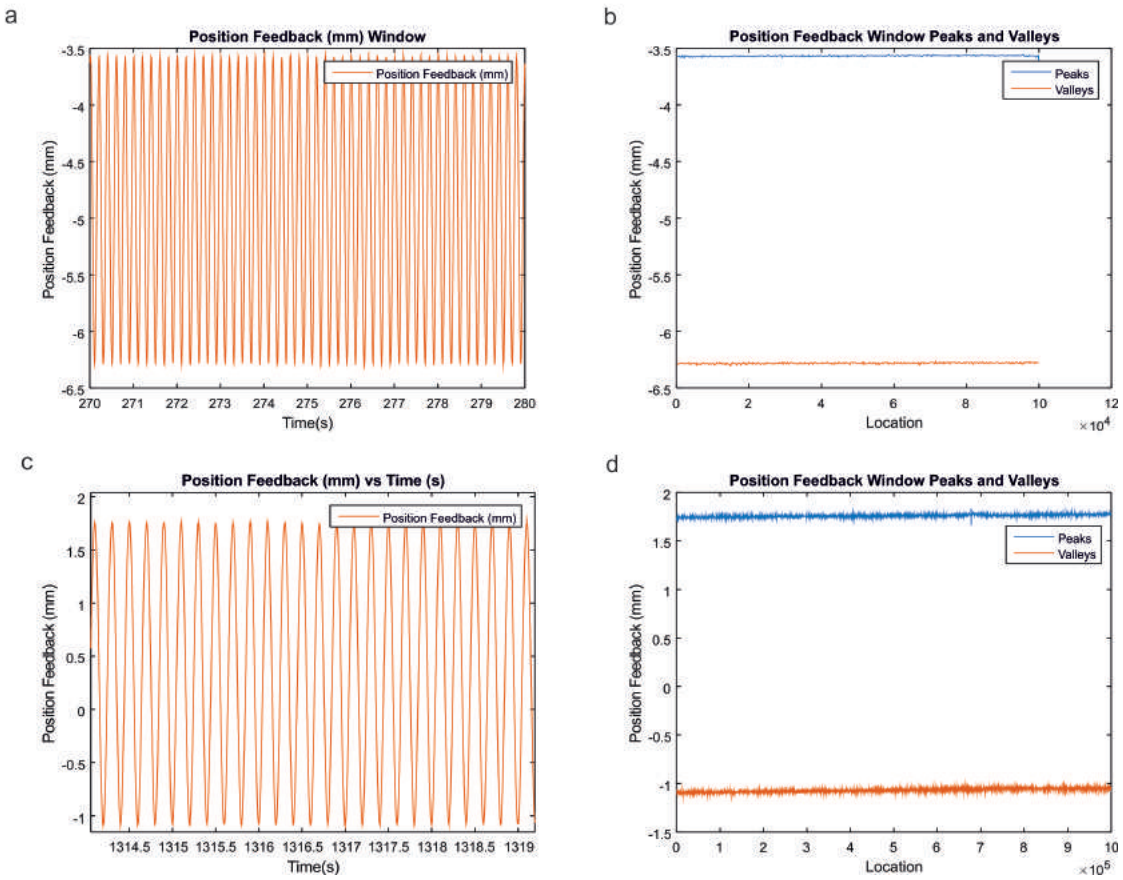

Figure 4.76: Schematic representation for conditions a & b. 1 and c & d. 6, depicting a & c. position feedback against time and b & d. maximum and minimum position feedback against time.

The position of the coupon during testing was recorded through two means, the first of which, presented in Fig.4.76 is monitored from the Moog SmartTest one controller and relates to the position of the dynamic lower platen in Fig.3.22a. The exact position recorded and presented in Fig.4.76, is relative to the starting position during that test, which varied throughout testing. However, the relative difference between upper and lower recorded position, is the value of interest and is presented clearly for condition 1 and 6 in Fig.4.76b and d, respectively. The data presented in Fig.4.76 are examples of typical coupon displacements during the steady state fatigue life. Condition 1 was typically displaced by 2.713 mm, Fig.4.76a and b, between applied loads, with condition 6, as shown in Fig.4.76c and d, showing displacement of 2.81 mm. During steady state fatigue life, both conditions showed negligible difference in displacement or variation in magnitude over all tests.

Strain observation

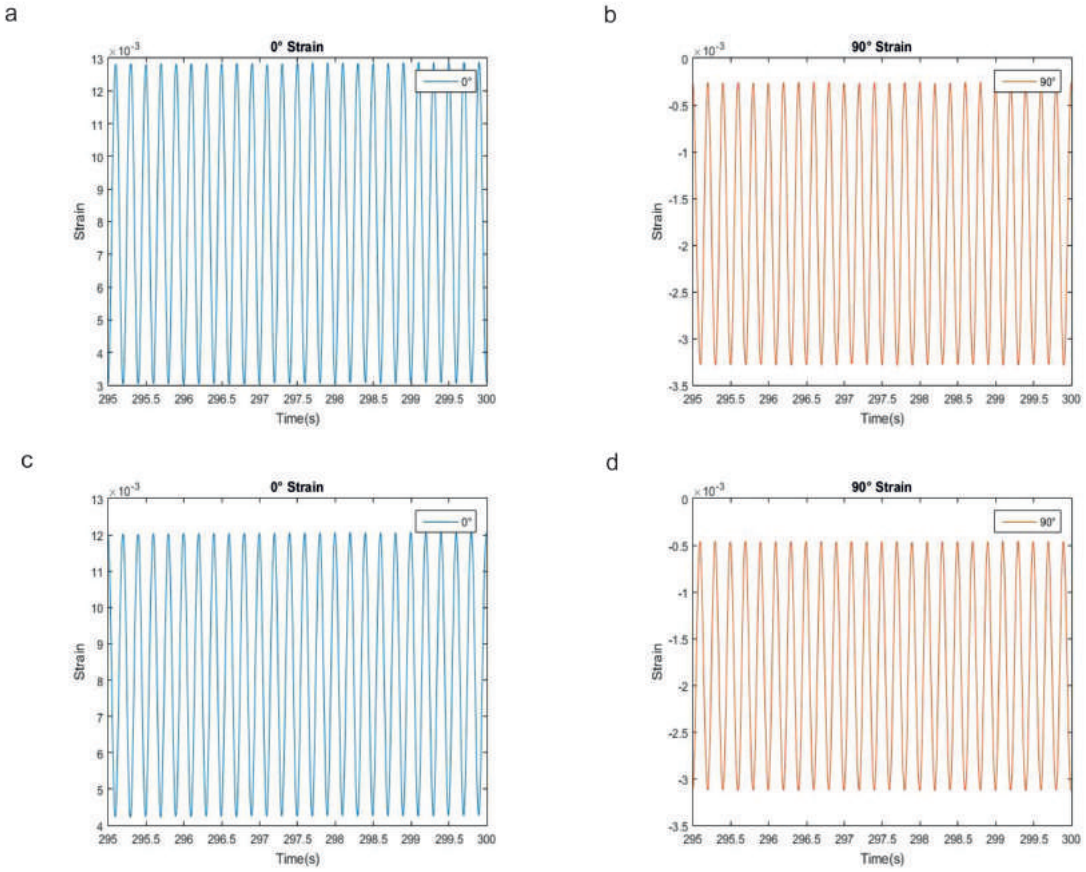

Figure 4.77: Schematic representation for conditions a & b. 1 and c & d. 6, depicting micro-strain against time for the a & c. 0°longitudinal direction and the b & d. 90°transverse direction.

Strain in both the 0°Y and 90°X directions were recorded thoughtout testing, on the upper high tensile stress surface, as shown in Fig.3.22b. Due to the magnitude of the bending moment, it was discovered that at various stages of fatigue life the 0°strain gauge frequently became damaged resulting in incomplete sets of data. However, substantial durations of data were attained for the majority of tests. During the steady state portion of fatigue tests, condition 1 presented an average micro-strain of 9.895 x10^{-3} and 2.64 x10^{-3} (3dp), for the 0 and 90 °directions, respectively. The comparable measures of micro-strain for condition 6 were 9.191 x10^{-3} and 3.194 x10^{-3}, respectively. Negligible variation in strain and therefore inferred stress is observed across both conditions in all tests.

4.4.6 Fractography

Over the entire testing programme, the average cycles to failure for condition 1 and 6 were 100% and 42.63%, respectively. The upper and lower fatigue life recorded, for condition 1 was 153.83% and 66.14% with the equivalent for condition 6 being 48.75 % and 41.27% cycles to failure, respectively. It can be seen from these results that fatigue life has been reduced significantly with increased SGR. Excluding the anomalous high life test for condition 1 at 153.83%, results showed good consistency with a standard deviation measured at 13.84 % and 40.77 % cycles (3dp) for conditions 1 and 6, respectively.

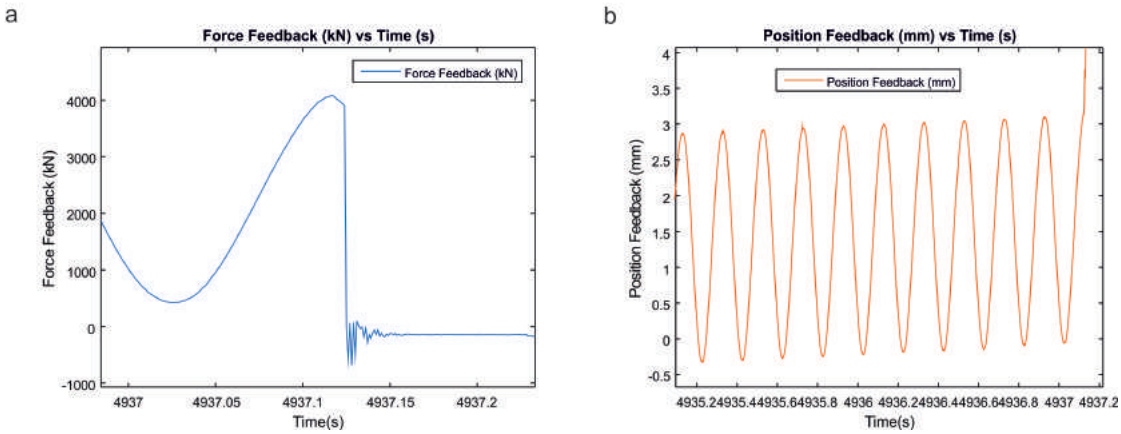

Figure 4.78: Schematic representation of a. force feedback and b. position feedback at the point of failure of a typical Ti-5553 four point bend fatigue test.

The typical response found from monitored data at the point of failure is shown in Fig.4.78. Failure occurred within the upper 5-10% of applied load and displacement concluding that final fracture occurs at the maximum applied stress. The controlled loading regimen induced gross plastic deformation, as is evident through the increases in total displacement within the final 5% of fatigue life, in which several hundred μm of increased total deflection was achieved. It can be seen that increased SGR has a substantial affect on fatigue life. Coupons subject to condition 6 presented average fatigue lives of almost 50% of that shown in condition 1.

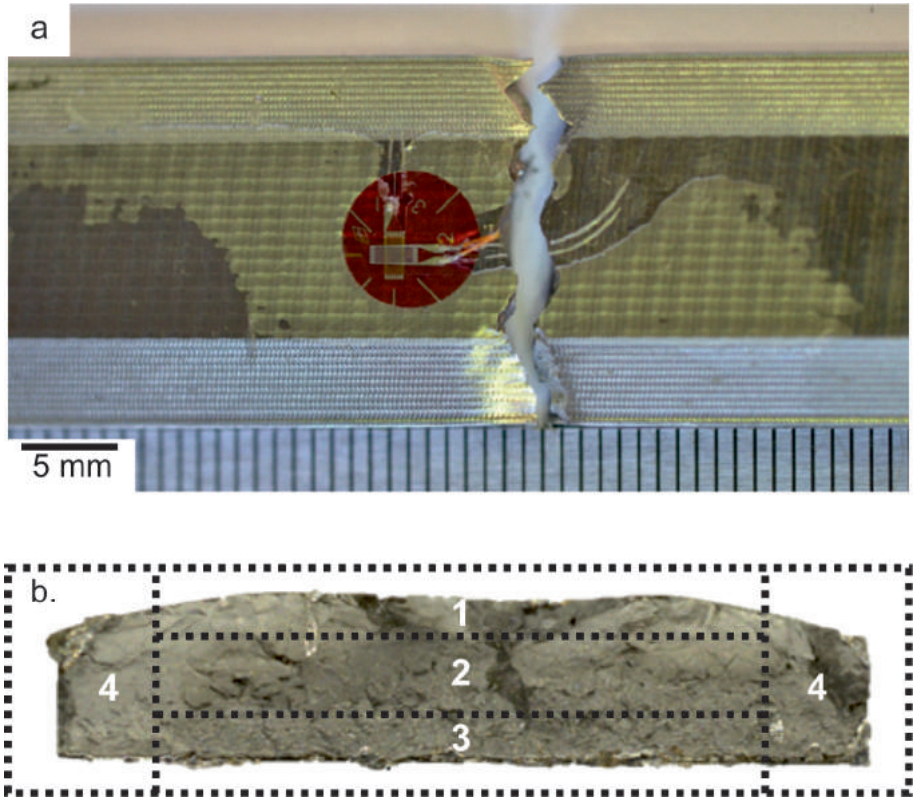

Figure 4.79: a. Photograph of a typical four point bend fatigue test failure and b. a schematic representation a typical Ti-5553 four point bend fatigue test fracture face with the four key zones highlighted; 1. upper edge, 2. bulk, 3. bottom edge and d. chamfers.

All failures occurred within the maximum surface stress region of the coupons, represented by the region BC in Fig.3.20 and shown in the red region of contour schematic in Fig.3.22. A typical fracture face is presented in Fig.4.79a. The fracture face can be subdivided into four fundamental zones, to describe the failure behaviour. Region 4, is defined as the chamfer region and are further interrogated in Fig.4.80. On the microscopic scale, as shown in Fig.4.79a, this region is characterised by large serrated features, with evidence of gross plastic deformation and necking. Region 3, defined as the bottom edge, shows evidence of an even face, burnished in appearance. The bulk region 2, is defined by a many faceted surface with a range of orientations present. Region 1 is characterised by the presence of crack initiation sites influenced by machining deformation and is explored in detail beginning with Fig.4.83. As shown in Fig.4.80d, evidence of micro void formation is present and based on the scale of which this occurs, it is believed this propagates along α/β grain interfaces. It was determined that, no crack initiated failure within this region. This is supported by the FEA investigation in which the material within the chamfers are subject to the lowest surface tensile stresses. From fractography, it is believed that final failure propagates through these regions in a ductile manner, with regions of shear lip formation and localised necking.

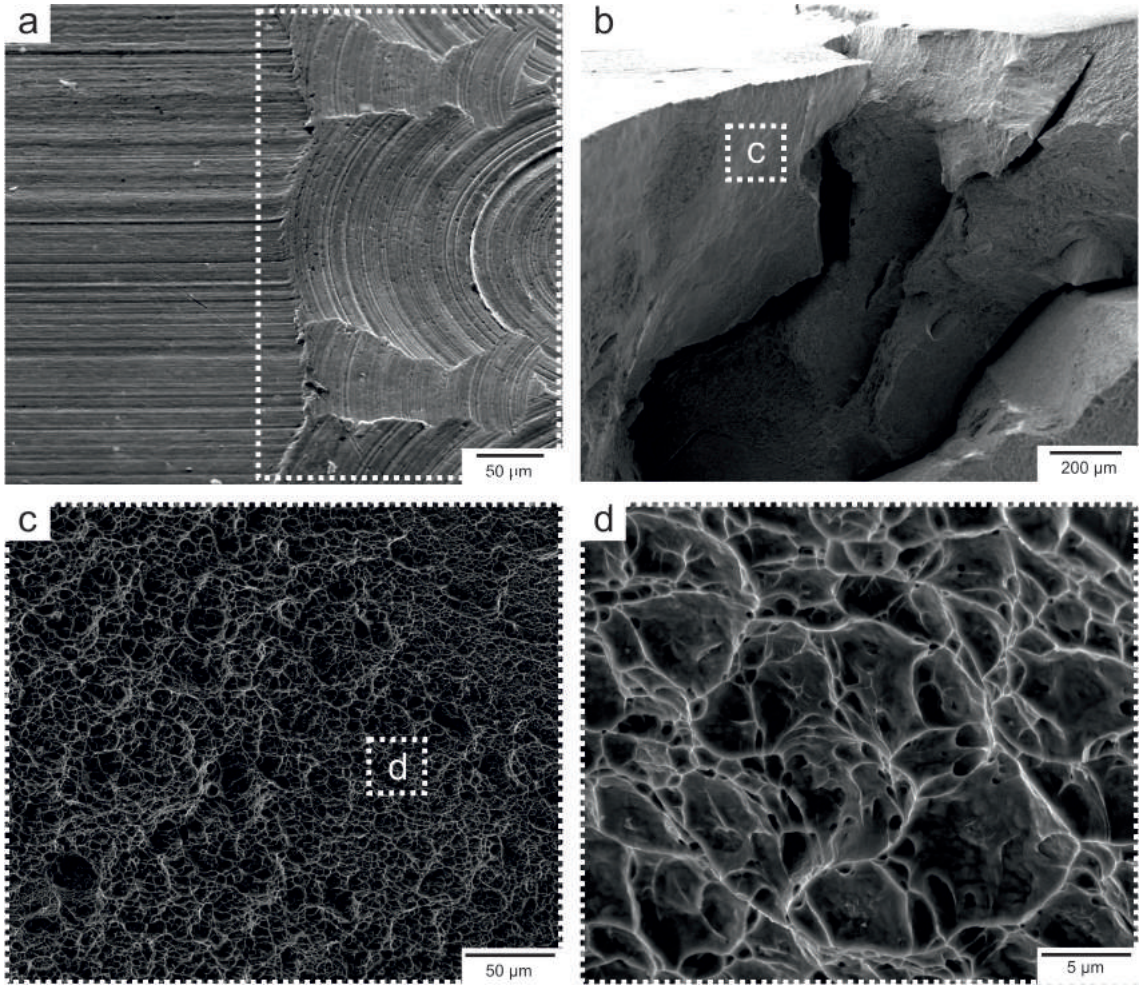

Figure 4.80: BSEI of a. the surface between finish end milling of the upper and chamfered surfaces (deliniated by the white dashed box) and b-d. BSEI at different magnifications presenting typical microscructural features for region 4; chamfer, of the four point bend fatigue test fracture face.

Typical fracture features witnessed in region 4, Fig.4.79, for both conditions are summarised in the BSEI presented in Fig.4.80. The influence of the ball nose milling utilised to produce the chamfers can be seen in the highlighted region of Fig.4.80a. As shown in the photograph in Fig.4.79a, the interface between this chamfered milling process and that used to produce the finish end milled test upper surface, influence final fatigue failure. The final crack propagation path was influenced by this interface and evidence of localised shear lips can be observed in Fig.4.80b. Under BSEI, the fracture face of this region can be discerned. Low magnification BSEI in Fig.4.80b, shows the presence of macroscale cracking and shear tearing within the chamfer region. Under increased magnification, the region identified by the white dashed box, Fig.4.80c, presents a microscopic equiaxed dimpled surface evidence of ductile failure as shown in the literature.

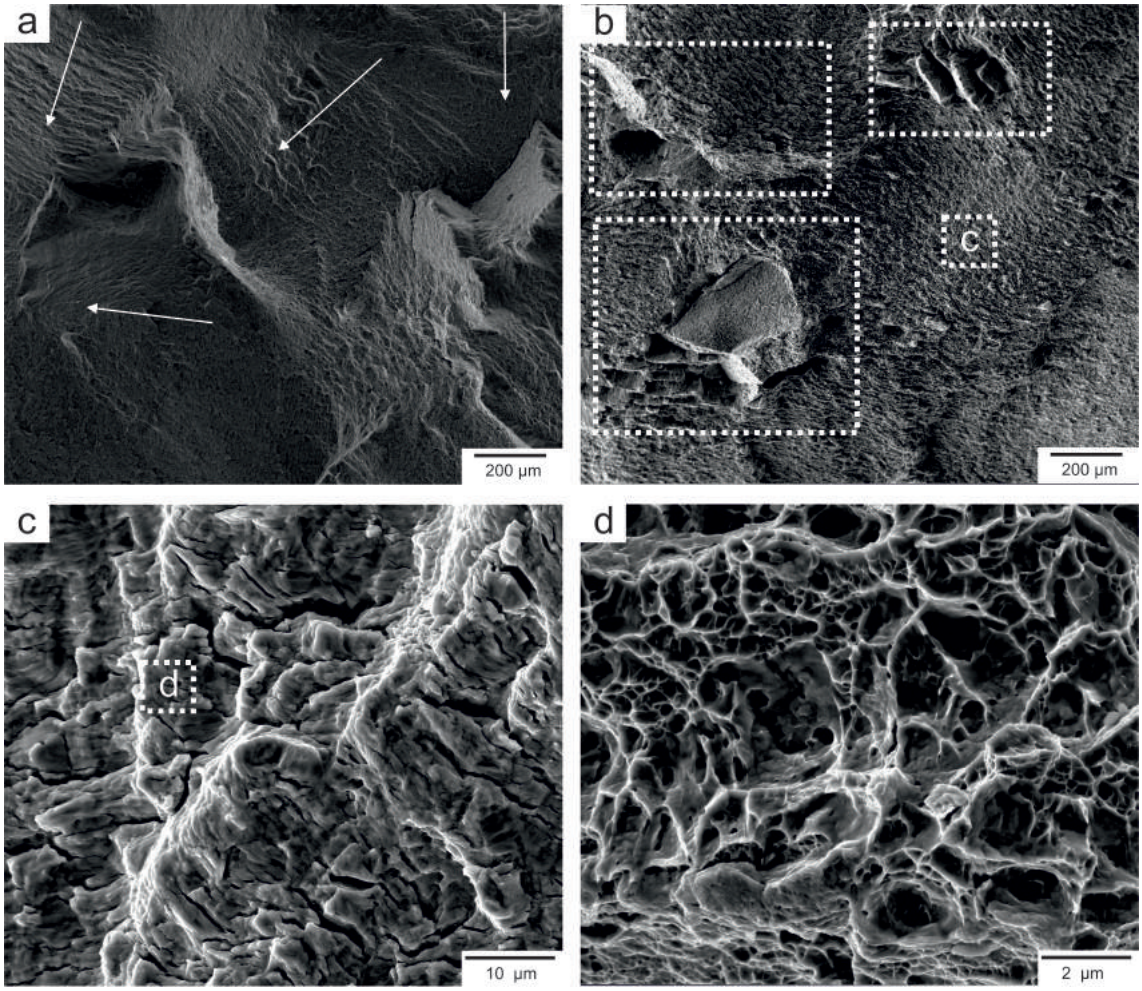

Figure 4.81: BSEI at different magnifications presenting typical microscructural features for region 2; bulk, of the four point bend fatigue test fracture face.

The bulk material presented in region 2 shows evidence of gross ductile failure, as is expected with a β alloy, but also localised brittle fracture. No crack initiation in this region was discovered, across both conditions and all coupons analysed. Under low magnification BSEI, as presented in Fig.4.81a and b, gross ductile failure can be clearly distinguished. The white arrows superimposed on Fig.4.81a, depict the orientations of crack growth. Individual β grain orientations influence the direction of crack propagation. These directional regions of fracture are on a comparable scale of that of β grains, like those shown in Fig.4.71a. The large faceted regions,

delineated with dashed white boxes in Fig.4.81b, are evidence of gross brittle fracture intergranular in nature along brittle α_{GB} at β grain boundaries, like that observed in Fig.4.71b. These regions show localised preferential orientations as a result of crystallographic texture of the large grained β phase. Under high magnification BSEI the bulk fracture texture can be perceived clearly, Fig.4.81c and d. Striations and secondary cracks propagating in the direction away from origin are present on a scale comparable to the sub-grain β structure. These present a mixed mode of ductile shallow dimples on brittle facets, at a scale comparable to α_p grains, Fig.4.81.

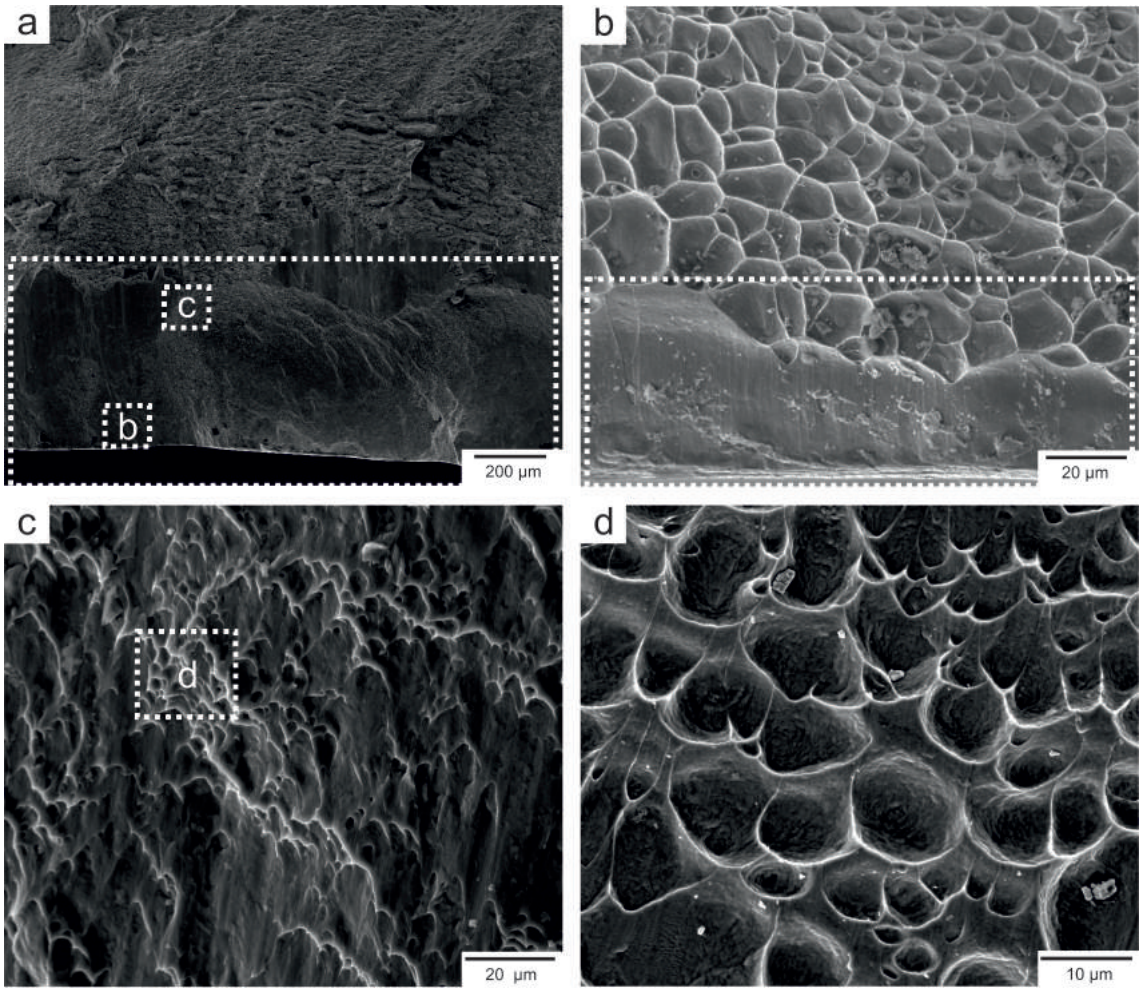

Figure 4.82: BSEI at different magnifications presenting typical microscructural features for region 3; bottom edge, of the four point bend fatigue test fracture face.

When studying region 3 under BSEI, Fig.4.82, a distinct transition in the fracture surface can be observed. At the bottom edge of the fracture face, a pronounced fast fracture zone is delineated by the dashed white box in Fig.4.82a. Fast fracture zones across both conditions were typically found to range from 200 to 600 μm in depth irrespective of fatigue life. Within this fast fracture zone, localised regions of mixed mode failure are observed, Fig.4.82b with ductile equixed dimples and smooth brittle fracture faces. Under high magnification BSEI, the majority of the fast facture zone is constructed of elongated dimples in the direction of final failure Fig.4.82c and d. The severe elongation and shallow depth of these dimples, Fig.4.82c and d represent a low number of cycles, typical of material subject to final fast fracture.

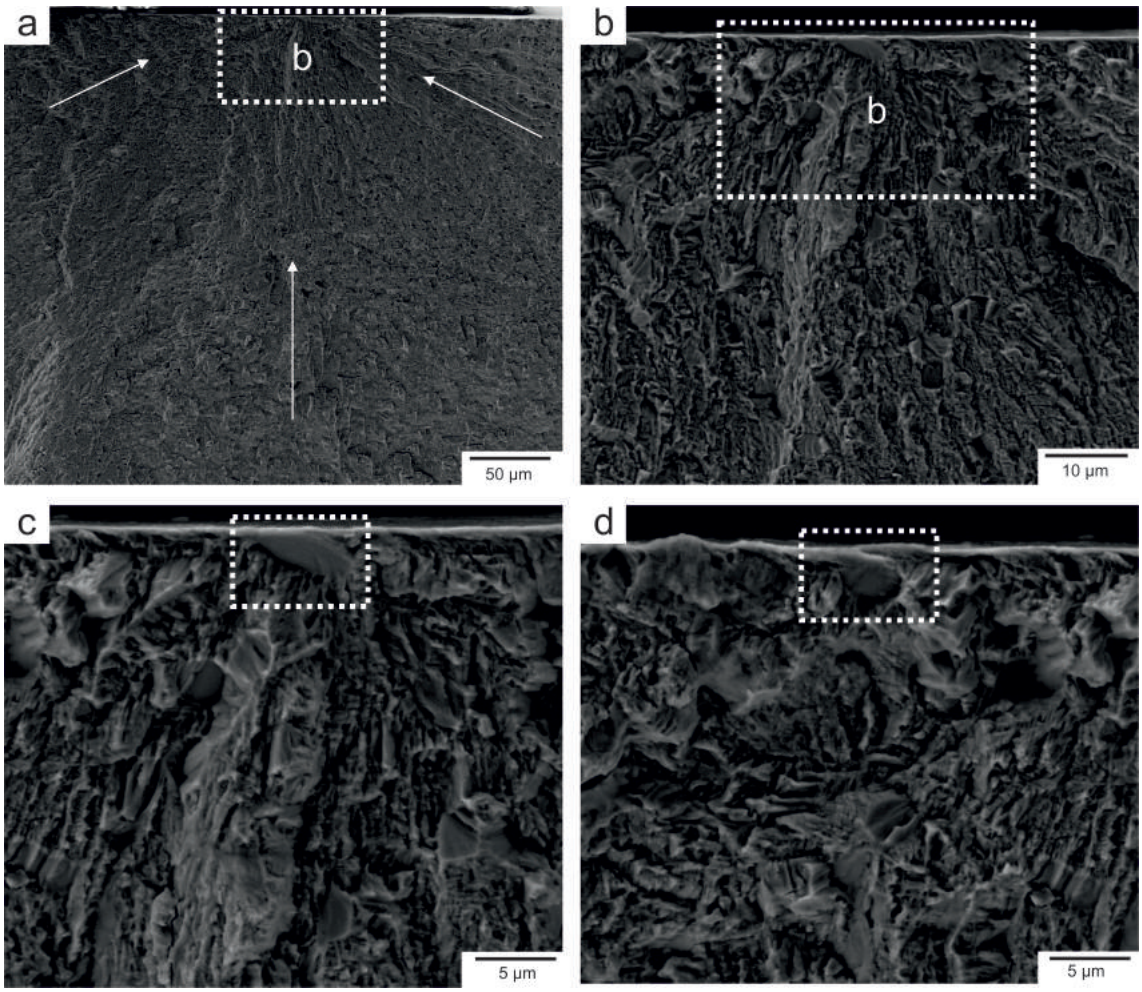

Figure 4.83: BSEI of a typical initiation site found in region 1; upper edge, of the four point bend fatigue test fracture face. Images show increasing magnification of typical fatigue crack initiation with cleavage and slip of severely plastically deformed α_p grains.

For both conditions across all tests conducted, fatigue cracks were determined, consistently, to initiate at the upper edge. This is the surface subjected to the ball nose finish end milling operation and the region subjected to the greatest imparted deformation. Initiation zones were identifiable during inspection, as large semi-circular regions of up to 250 μm in diameter. These regions possess macroscopic and microscopic striations propagating from a specific surface location. These striations, depicted in Fig.4.83a by the white arrows, suggest localisation within the region, which is further delineated by the dashed white box in Fig.4.83a, then magnified and presented in Fig.4.83b. Within this upper 50 μm initiation region, a defined mixed mode fracture surface of fibrous and dimpled ductile fracture within the β matrix face and faceted α grains are present. In many cases, initiation is localised and can be distinguished by a single deformed α_p grain. Two such examples are presented in Fig.4.83c and d, in which α_p grains directly located at the machined surface present quasi-cleavage facet fracture features. Such fatigue behaviour in duplex titanium alloys have been reported in literature [57, 123, 139]. Evidence of numerous failure modes can be observed within this initiation region, including cleavage and fatigue striations within α grains. As well as ductile failure of β phase delineated by brittle facets assumed to be as a result of α_p.

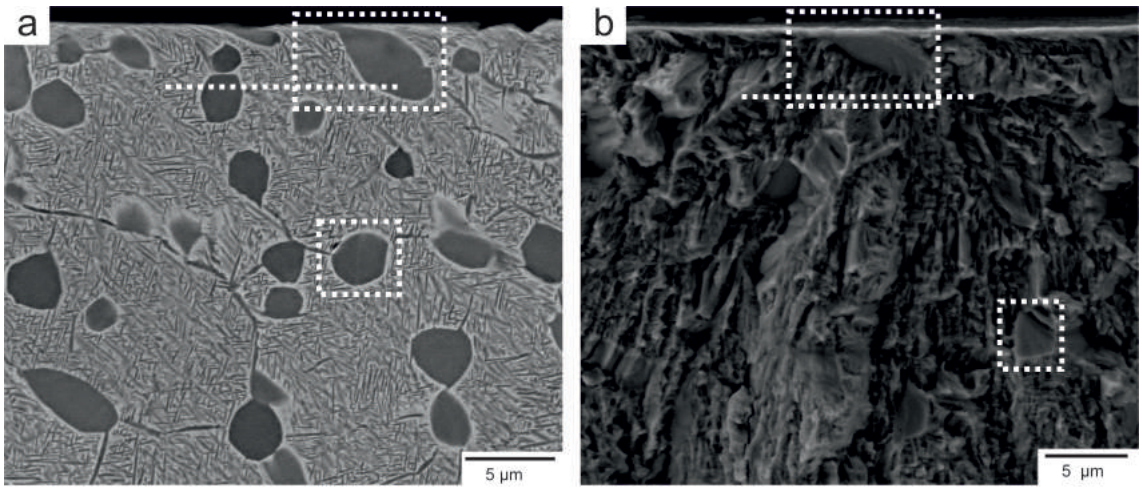

Figure 4.84: BSEI comparing the subsurface deformation as observed as a result of a. finish end milling and b. four point bend fatigue test failure.

When compared to subsurface analysis prior to fatigue testing, with BSEI on identical scales, the influence of machining can be interpreted from fractography as is shown in Fig.4.84. Microstructures of α_p can be easily distinguished along with the subsurface SPD and swept structures local to the machined surface. It is inferred from previous results in this thesis, sections 4.2 and 4.3 and in the literature [57, 123, 139] that this has occurred due the combination of factors.

- Preferential orientation of the crystallographic planes of the given α_p with respect to the orientation of the maximum induced stress as a result of machining.
- The proximity of the given α_p grain to the machined surface and thus the intensity of the applied tensile stress during fatigue testing.
- The location and orientation of this given α_p grain, which is subsequently dependant on the parent β grain orientation, due to the Burger's relationship.

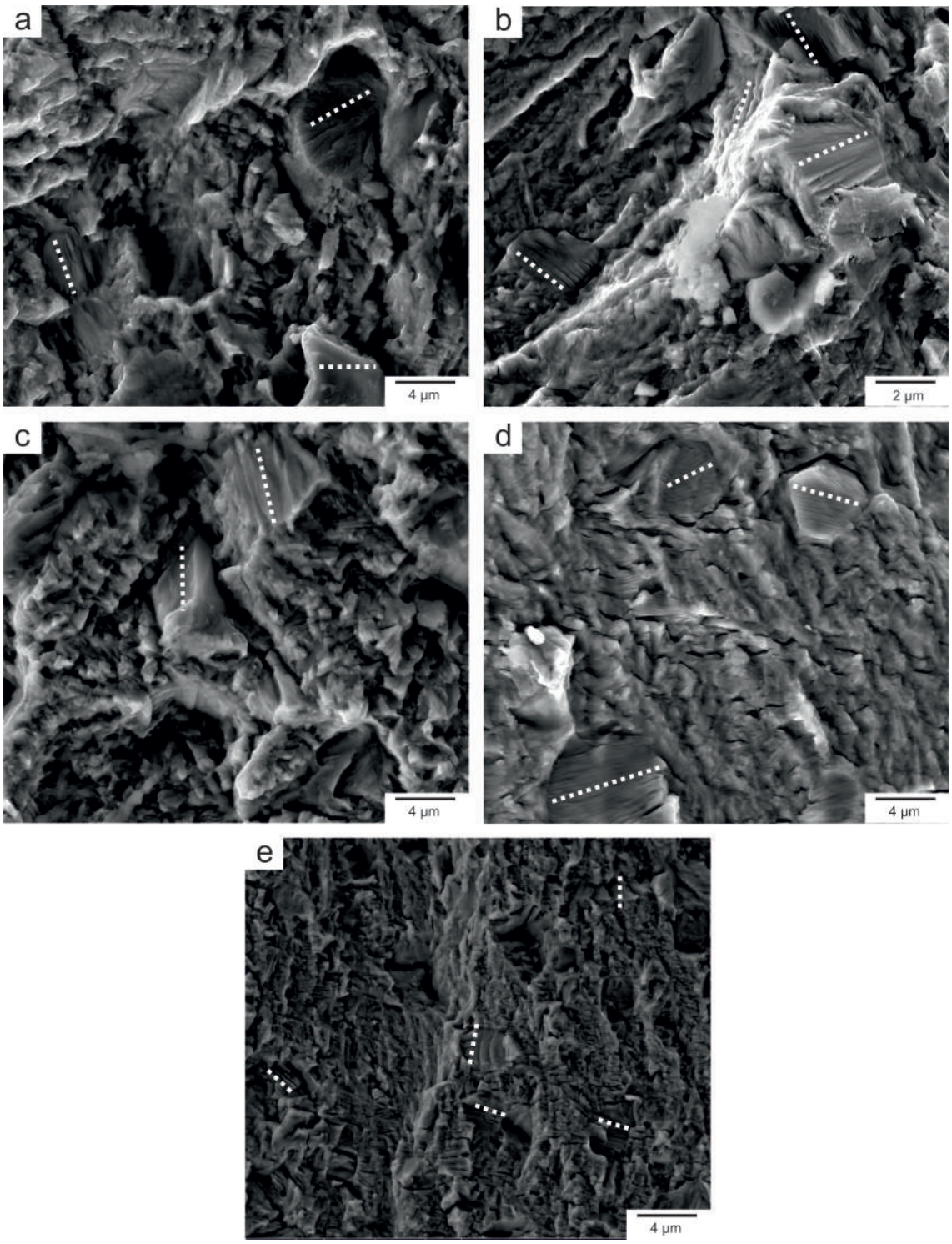

Figure 4.85: BSEI of α_p grains within the initiation and growth regions of the four point bend fatigue test fracture face with dominant slip directions identified.

Under high magnification BSEI within the upper 50 μm of the initiation zones presented in Fig.4.83, α_p grains present facets with an array of differently orientated slip lines, fatigue striations and micro cracks. Examples of such grains from both conditions are shown in Fig.4.85, with slip lines and micro-cracks highlighted with dashed white lines. Outside of this localised region, trans-granular brittle cleavage and slip plane activation could not be identified. Some α_p grains did however present evidence of fatigue striations. An observable behaviour that differentiated the two cutting conditions was an increased prevalence of micro-cracking presented

by condition 6 Fig.4.85a and e. However, this is difficult to accurately quantify. This is believed to be as a result of increased pre-existing activation of dislocation slip planes, SPD, Fig.4.73, 4.33 and 4.34, and increased localised residual stress Fig.4.74 as a result of machining prior to fatigue testing. Similar progressive damage accumulation through activation of slip planes resulting in strain localisation and eventual trans-granular fracture has been shown for Ti-5553 and other duplex titanium alloys during fatigue loading [57, 138–140].

4.4.7 Crack formation

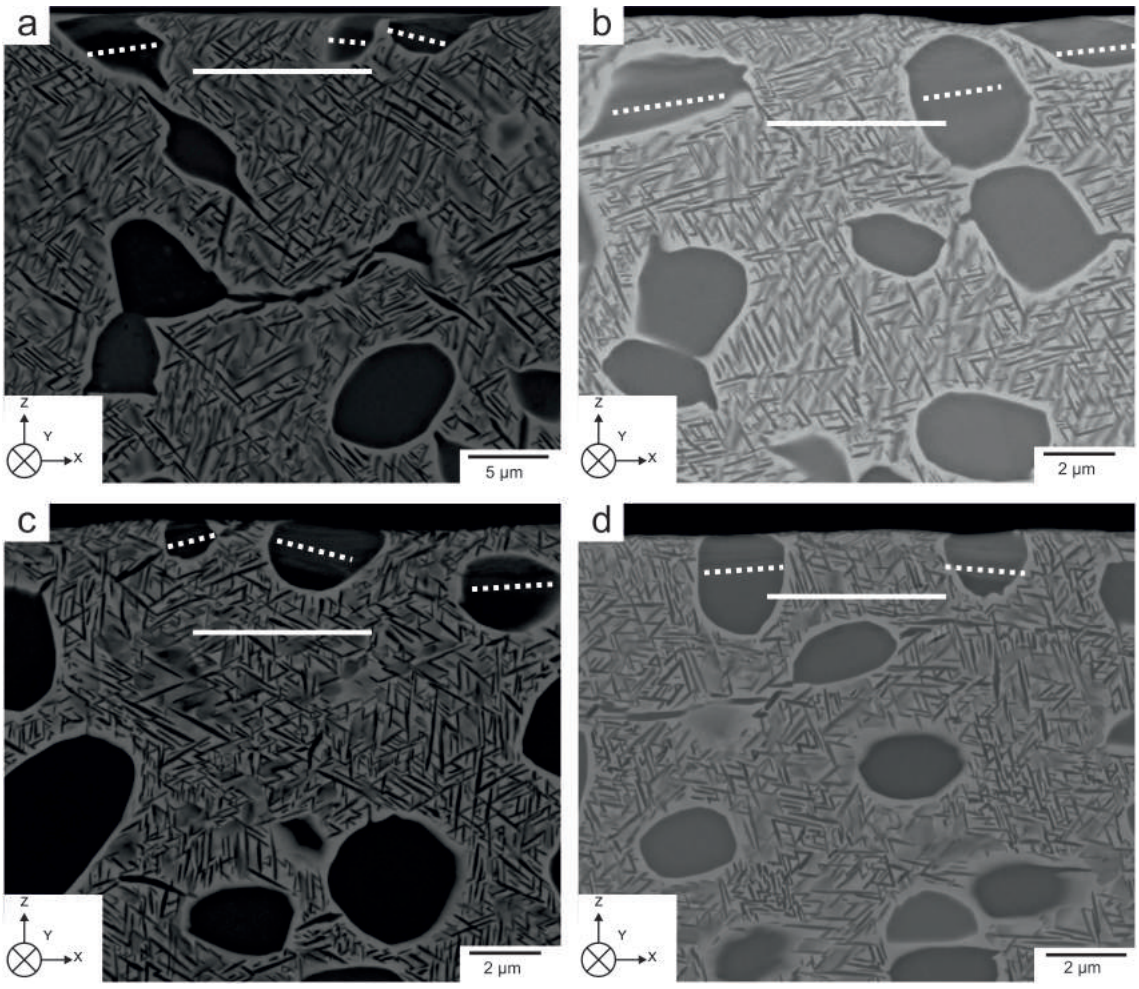

Figure 4.86: BSEI showing the observable maximum depth and the direction of dislocation slip as a result of finish end milling and subsequent four point bend fatigue testing for condition 1.

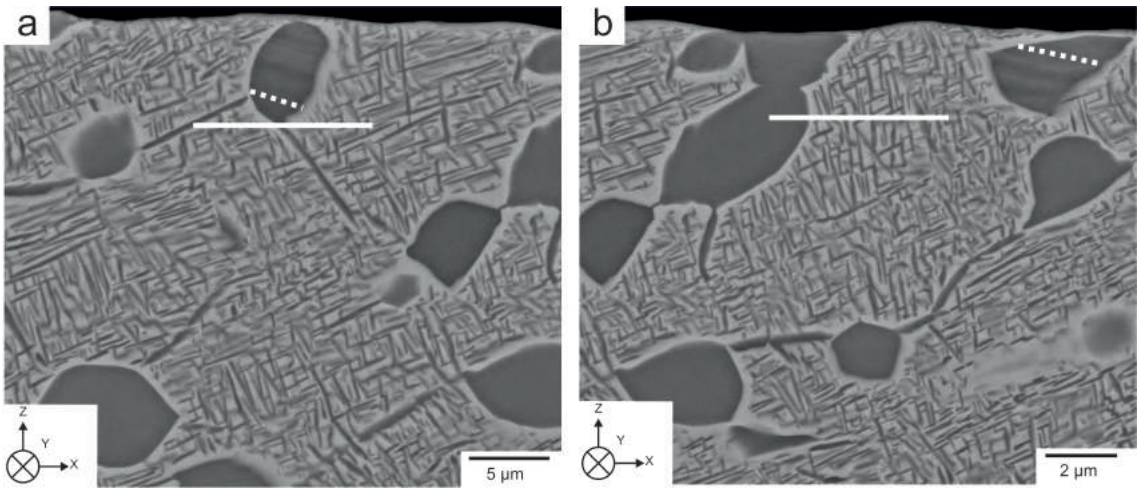

Figure 4.87: BSEI showing the observable maximum depth and the direction of dislocation slip as a result of finish end milling and subsequent four point bend fatigue testing for condition 6.

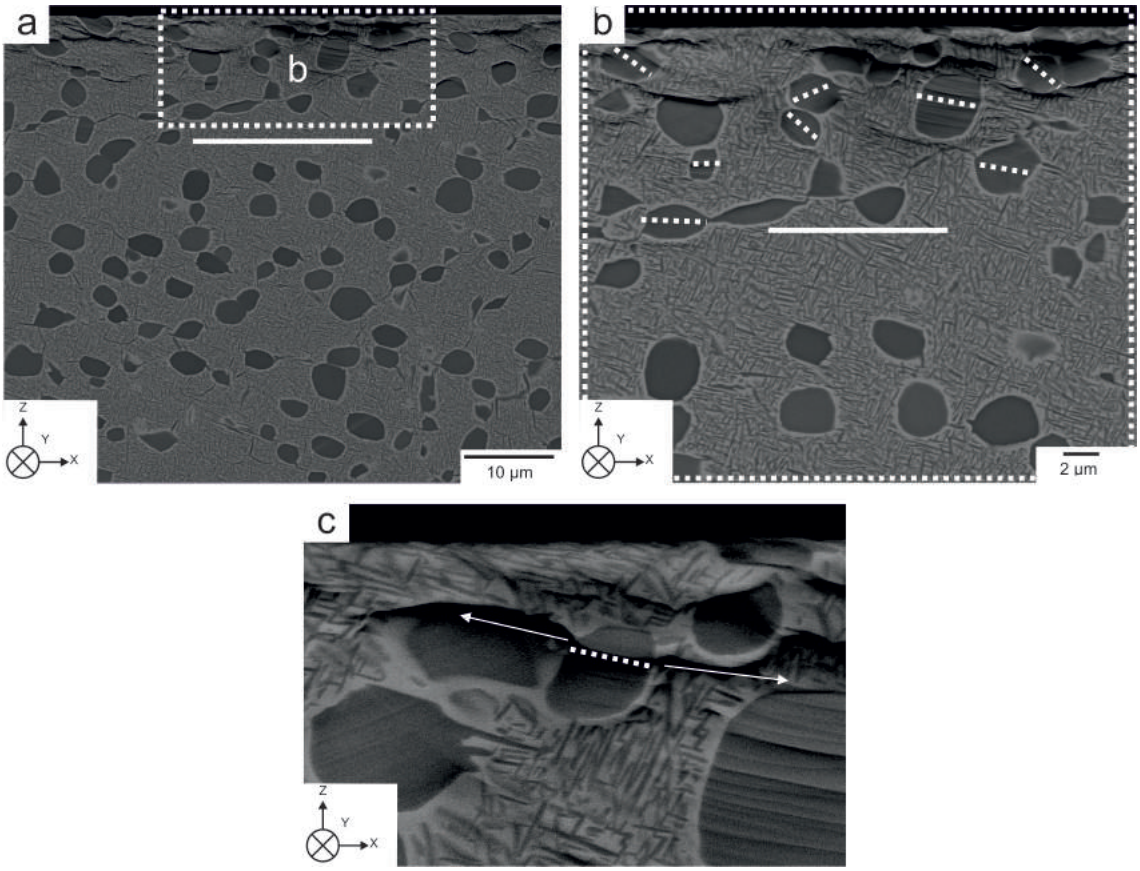

Figure 4.88: BSEI of severe plastic deformation, observable dislocation slip within α_p grains and microcracking along α/β grain boundaries as a result of finish end milling and subsequent four point bend fatigue testing.

In order to characterise the material condition prior to fatigue testing, subsurface microstructure was studied through BSEI of samples removed from just behind the fracture point as shown in Fig.3.23ii and iii. Examples of this analysis for conditions 1 and 6 are presented in Fig.4.86 and 4.87, respectively. Comparable depths of dislocation slip are present for both conditions. Similar conclusions can be drawn as

with the results from sections 4.2 and 4.3, in which increased SGR influences the intensity and quantity of dislocation slip present. There is also evidence of localisation of those α grains presenting slip planes relating to the preferential orientations of parent β grains. Slip lines are more readily observed in material subject to condition 6. The most significant instance of subsurface deformation as a result of machining and subsequent fatigue testing was found in material behind the fatigue fracture and is presented in Fig.4.88. High resolution BSEI, shows substantial and intense slip band formation in α_p grains in the upper 10 μm of the machining subsurface, Fig.4.88a and b. Fig.4.88, presents a glimpse into the progression, from machining induced deformation, through to the activation of dislocation slip, strain localisation and coalescence of micro-cracks in fatigue. Propagation of these micro-cracks persists along α/β grain boundaries as shown in Fig.4.88c. This suggests localisation, due to β orientation and subsequent α grain orientation, with respect to imposed stress from machining and subsequent localisation of tensile stress during fatigue testing.

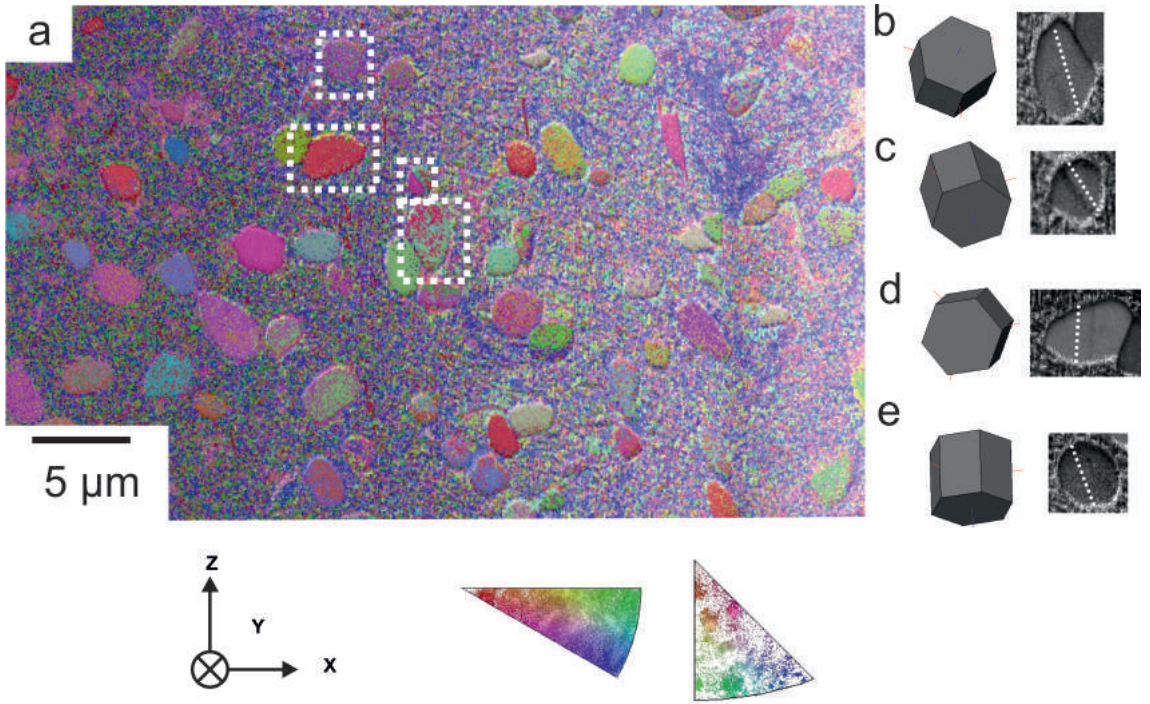

Figure 4.89: a.Noise reduced IPF OIM for cutting condition 6 in the Y orientation. b-e. BC images and corresponding 3D crystal orientation representations of α_p grains with strain induced dislocation slip directions presented as dashed white lines.

The intense subsurface deformation identified in Fig.4.88 was subject to EBSD to determine the direction and plane orientations of the intense dislocation slip present. Due to the intensity of the SPD, the resolution of indexed points was low, to counter this, a high magnification and small step size was utilised. Slip in the plane and direction was found in those α_p grains possessing no micro-cracking. Those α_p grains found to have initiated micro-cracking possessed dislocation slip in the $\{11\bar{2}0\}$ direction and the $\{000\bar{1}\}$ plane, as with the grain in Fig.4.88c. Initiation of basal cracks have been identified in fatigue behaviour of other titanium alloys [57, 123]. An example of a detailed subsurface EBSD IPF OIM is presented in Fig.4.89a, with 3D crystallographic orientations of α_p grains presenting dislocation slip lines in Fig.4.89b-e. This particular region of interest presented lower levels of strain which allowed for improved indexing when compared to Fig.4.88. Dislocation slip was found to have been activated along Pyramidal $\{\bar{1}101\}$ and $\{1\bar{2}1\bar{3}\}$ planes and Pristmatic $\{\bar{1}011\}$ and $\{\bar{1}010\}$ planes. It is believed under fatigue loading dislocation slip is activated along these crystallographic planes, those along basal planes initation subsurface micro-cracking which propagate eventual catastrophic fatigue failure.

Chapter 5

Conclusions

5.1 The effect of cutting parameters on the surface integrity and subsurface microstructure for finish milling of Ti-5Al-5Mo-5V-3Cr

Small scale testing methodologies were developed to accurately replicate complex finish end milling conditions employed in industrial machining activities by SLS. This technique allowed for an array of cutting conditions to be applied to material utilised directly from the manufacturing process. Condition monitoring and conventional non-destructive techniques were used to confirm the approach used, successfully produced milled surfaces representative of those produced in industry. No dynamic instability or major surface defects were observed during milling trials and thus, a robust experimental design has been developed. Building on existing literature [44, 45, 48, 49], advanced techniques such as BSEI and EBSD were used to characterise the metastable β titanium alloy Ti-5553. This investigation identified a strong Burgers relationship is maintained between the HCP α and BCC β phase. The two phases a significant disparity in grain size, a fact that influenced further material characterisation work. The influence of upstream thermomechanical processing was determined to be in-line with those previously discussed in Chapter 4.2. Stylus based techniques used to describe 2D surface roughness have been shown to be limited in their ability to accurately distinguish the influence of cutting conditions. 3D light micrograph techniques, an application not widely adopted outside of academia, has been shown for an industrial application to identify repeatable trends for increased cutting conditions. This research has also shown a conventional R_a metric, in both 2D and 3D, can be improved when considering more sensitive metrics such as R_q to distinguish these trends. The complex nature of a milled surface can only be accurately summarised when studied in 3D. Characterisation, through high magnification BSEI and EBSD, demonstrated that finish end milling of Ti-5553 introduces SPD layers in the near 2-5 μm of the surface. Within this SPD region, distortion of the microstructure has been shown to be determined by the direction of both tool rotation and tool direction. Localised surface defects, such as tearing and cavitation, within major feed marks, especially in the Y orientation were found at high f_z and SGR. Finish end milling at f_z above 0.22 mm/tooth and SGR found in conditions 6 and 7, were shown to activate slip planes within α_p grains. Grains presenting this deformation mode were shown to be localised in their proximity to the surface and SPD regions and non-uniform in slip band intensity. Instances of micro-cracking at isolated increases of f_z to 0.3 mm/tooth,

were found to initiate from intense slip bands within α_p grains and propagating along α/β grain boundaries. Propagation is retarded through impediment of crystallographically orientated "hard" α_s grains. Over the range of milling conditions investigated, a relationship between cutting forces and subsurface deformation was found. At high normal cutting forces, such as with increased V_c, increased propensity for sweeping of the microstructure occurs within the SPD region. At high major cutting forces, such as with increased f_z, a reduction in swept microstructure occurs. However, this coincides with increased propensity for induced dislocation slip within α_p grains. The true extent of subsurface deformation has been characterised through detailed EBSD. Finish end milling at high f_z and SGR activates dislocation slip in the pyramidal plane $1\bar{2}1\bar{3}(01\bar{1}\bar{1})$, prismatic plane $\bar{2}11\bar{3}(01\bar{1}0)$ and basal plane $\bar{2}110(000\bar{1})$. Through delineation techniques, no deformation twinning was found, this is believed to be due to the relatively fine α microstructures present in Ti-5553. Through strain contouring and dislocation slip observations, it was found that average and maximum subsurface deformation was induced to greater depths than is able to be determined through BSEI. β grains with their (001) planes orientated parallel to the tool direction and/or rotation, presented the greatest level of induced strain. Those grains subsequently presented the greatest propensity for dislocation slip in α_p grains. The induced deformation in the β phase therefore directly influences the true extent of α phase deformation. From this work, increases above intermediate levels of f_z (0.22 mm/tooth) would be detrimental to the in-service performance, through activation of deformation modes and increased surface roughness. However, complimentary increases in V_c up to 375 mm/min can result in significant reductions in cutting time and improved processing opportunities for SLS. An improved understanding of Ti-5553 and the effect of finish end milling has been achieved through this investigation. The techniques employed have also been utilised by several other researchers in both Masters, PhD and EngD projects, for a variety of topics ranging from mechanical engineering, condition monitoring and materials characterisation at The University of Sheffield and LMT Cachan in Paris and the industrial sponsor, SLS.

5.2 The effect of cutting parameters on tool wear for finish milling of Ti-5Al-5Mo-5V-3Cr

Through the application of small scale testing methodologies, elongated tool wear trials and a bespoke tool wear analytical technique, the influence of finish end milling on tool wear for Ti-5553 has be characterised. The effect of cutting parameters, as described in Chapter 4.3, on initial tool wear for small scale testing was deemed to be minimal. It was observed that isolated increased f_z resulted in a high propensity for built up edge (BUE) and re-deposited chips. Complimentary increases in V_c reduced the propensity for this phenomenon. For this chapter, a down-selection of four cutting conditions was chosen, based on the initial tool observations and the potential processing window determined from Chapter 4.2. Interrupted tool analysis was conducted, utilising a bespoke tool wear rig during elongated cutting trials. It was found that the steady state cutting nose and flank wear for condition 1, was a result of abrasive wear mechanisms, with a transition to adhesive wear mechanisms and increased tendency for crater wear after 2.5 hours of tool use. The same behaviour was seen but exacerbated, at significantly earlier durations of tool wear for isolated f_z and SGR increases. The influence of isolated increases in V_c

showed a substantial reduction of tool wear until 2 hours of use. Tools from the elongated tool wear trial were then used for milling of curved coupons, to allow for surface and subsurface characterisation. Increased feed and SGR has a significant influence on surface roughness in 3D. For isolated increases in f_z, the respective tool wear was found to be so significant intermittent tool engagement occurred, leading to an insufficient depth of cut (a_p) was produced. As with results in Chapter 4.2, cutting forces showed relationships with subsurface deformation behaviour. During early tool life, the same can be said for 3D roughness measurements trends. As with all cutting conditions, irrespective of tool wear, minimal variations in the Y orientated thrust cutting forces has been recorded and therefore, would be of no use for condition monitoring. Isolated increases in V_c produced progressively severe distortion to subsurface microstructures to intensifying depths. Isolated increases in f_z produced intense dislocation slip in α_p grains, throughout substantial regions of the subsurface to increasing depths as tool wear progressed. Due to limited resources for such a large sample size of coupons, EBSD was not carried out and the actual slip plane orientation could not be determined. The investigation carried out in this Chapter demonstrates the importance of tool wear and the economic influence in machinability studies. From this study, current cutting conditions employed by SLS can be exploited up to 2.5 hours, demonstrating that extended tool performance is achievable. Despite increased cutting conditions studied in this investigation previously deemed as suitable for production, significant limitations in tool wear have been identified. Along with these limitations, subsurface deformation and surface roughness was degrading rapidly with increased f_z. This results in the narrowing of the potential processing window within the boundaries of conditions 1, 2, 4 and 6. Increases in f_z should be complemented with increases in V_c, to aid in coolant delivery and chip evacuation.

5.3 The effect of machining induced deformation on fatigue performance for finish milling of Ti-5Al-5Mo-5V-3Cr

Low cost small scale four point bend fatigue testing was performed on finish end milled Ti-5553 in order to study the influence of SGR on fatigue performance. A custom built four point bend test rig was designed through mechanical hand calculations and FE analysis using the commercial software package Ansys. Machined coupons were characterised through a range of advanced techniques such as BSEI, EBSD and XRD residual stress analysis. Fatigue testing was conducted at R=0.1 in the low cycle fatigue regime with subsequent analysis of fracture behaviour and subsurface deformation activation. Increased SGR reduced the average low cycle fatigue life of finish end milled Ti-5553 from 100% and 42.63% cycles to failure. Initiation of fatigue failures occurred through quasi-cleavage of α_p grains at the upper finish end milled surface. No distinguishable initiation zone was observed, as is normally seen in conventional fatigue testing. However, a region determined to be structurally different from the remaining fracture face was deemed to present a region of fatigue crack initiation. Within a 250 μm in radius from the initiated α_p grain, mixed mode failure was observed. Within this region, α_p grains present micro-cracking on cleavage facets, along specific crystallographic planes. Fibrous ductile failure is consistent throughout the bulk β matrix. Failure then propagated within the final 5-10% of fatigue life through the bulk, progressing along crystal-

lographic orientations of the β grains with intergranular seizure along brittle α/β grain boundaries. Final catastrophic failure occurred within the final 500 μm of the lower edge, the region subjected to the greatest compressive stresses during fatigue testing. Material within the chamfered regions of the coupons presented gross plastic tearing, typically along α/β grain boundaries with necking along the interface between the chamfered and upper milled faces. Initiation is determined to be due to the severity of induced deformation from machining which activated deformation modes, such as dislocation slip along basal $\{11\bar{2}0\}$, prismatic $\{\bar{1}011\}$ and pyramidal $\{\bar{1}101\}$ planes. When compared to a non-machined condition, which presented limited residual stresses and no distinguishable activation of deformation modes, fatigue life has been elongated as a result of machining. The results suggest machining induced dislocation slip initiate fatigue cracking as due to tensile loading during fatigue testing. Stress localisation advances dislocation slip forming micro-cracking which coalesces and propagates along α/β grain boundaries. Fatigue cracks propagate in to the bulk microstructure in a ductile manner to eventual final brittle failure. These mechanisms compete against residual stresses induced from machining. If machining induced deformation modes can be mitigated against, fatigue life is maximised for machined Ti-5553. This test design has been proven to produce a wide reaching influence with potential applications to a range of study. On-going research is currently underway utilising this four point bend fatigue test to study the effect of other machining phenomena such as re-adhered chips with a range of aerospace alloys.

5.4 Summary

During this study, a detailed research programme has been undertaken to investigate the influence of industrial finish milling processes on the surface integrity, subsurface microstructure, tool wear and fatigue behaviour of an aerospace, metastable β titanium alloy, Ti-5553. At the conclusion of this research, it is worthwhile to contemplate the information discussed, the aims and objectives, as defined in Chapter 1. This work addresses the challenges surrounding process improvement for complex alloys within the aerospace industry. The techniques utilised in this work have the capability of reducing the duration, complexity and cost for such process improvement, while yielding a greater level of understanding than conventional techniques. The work combines skills and procedures utilised by the Mechanical Engineering and Materials Science disciplines and attempts to bridge the technological and theoretical gap between the two disciplines. The small scale, low cost methodologies employed, have accurately replicated complex industrial machining operations. This was achieved in a manner which is applicable to a range of aerospace alloys subject to an array deformational processes. Material taken directly from industrial production processes was first characterised and compared to the literature [24, 44, 48, 49]. Collaborative work was carried out with SLS to determine the machining operation that presented the greatest opportunity for improvement. This was determined to be finish end milling of curved surfaces. Condition monitoring and characterisation techniques employed by industry were then used to affirm that the small scale methodologies developed accurately replicated the industrial process. These testing designs allowed for the exploration of not only cutting parameters; V_c and f_z, but the application of worn tools to ascertain wear mechanisms. Industrial cutting operations were further simplified and applied to coupons subsequently subject to bespoke four point bend fatigue testing. This test design isolated the surface

roughness and subsurface deformation, resulting from finish end milling, to tensile fatigue stresses to interrogate fatigue mechanisms. Due to the flexibility and reliability, these testing techniques have been utilised in other studies at the University of Sheffield and LMT Cachan, for Masters, PhD and EngD studies. Through the consideration of surface integrity and subsurface microstructure on in-service performance, with the limiting factor of tool wear, beneficial improvements to the existing finish end milling process have been identified. With the current cutting parameters; of 300 m/min and 0.14 mm/tooth, it has been shown; surface integrity and subsurface microstructures can be maintained up to 2.5 hours of tool use. This will enable industry to optimise existing procedures. Theoretically, over the range of cutting parameters achievable on modern machining centres, substantial reductions in cutting time are achievable. However, a range of factors have limited this opportunity significantly. Surface roughness in machining, assessed conventionally by mechanical engineers through 2D amplitude parameters, R_a, initially suggests all cutting conditions are achievable. However, when the 3D surface, under higher magnification, is considered, this potential processing window is reduced. The behaviour observed in 3D roughness, shows good agreement with monitored cutting forces and tool wear. A relationship between the 3D roughness, cutting forces and subsurface microstructural response has been identified. For the isolated increase in V_c, minimal increases in 2D and 3D roughness are observed. Increases in the X orientated normal cutting force, manifests themselves in the increased propensity of distortion to the upper 3-5 μm of subsurface material. High V_c allow for improved coolant delivery and chip evacuation, the combination of which is believed to reduce localised temperatures and restrict the activation of adhesive tool wear mechanisms. Current cutting conditions induce conventional wear development, in which a transition from abrasive to adhesive wear mechanisms is seen, prior to rapid crater wear after 2.5 hours of tool use. The transition to adhesive wear mechanisms occur much more rapidly when tools are subject to increased f_z. Increased f_z results in evidence of BUE and crater wear, resulting in an intermittent cutting action and the deterioration of surface integrity. This dramatic increase in tool wear limits the industrial application of such cutting parameters and the potential processing window. Complimentary increases in V_c, with f_z, allow for improved coolant delivery and reduction of BUE, but substantial tool wear is produced at high SGR. Increased f_z, has shown to induce SPD and activation of dislocation slip planes within α_p. This behaviour coincides with increased surface roughness and Z orientated cutting forces. Advanced characterisation techniques such as BSEI and EBSD, have been utilised to interrogate induced deformation modes. Across all cutting conditions, no deformation twins were identified. Increased cutting parameters, namely feed and SGR, were shown to increase the propensity for activation of an array of slip planes including, basal $(000\bar{1})$, pyramidal $(01\bar{1}\bar{1})$ and prismatic $(01\bar{1}0)$. The average depth of induced deformation was found to increase with f_z and SGR. At 30-40 μm, EBSD uncovers at greater depth to deformation than has been previously seen through light microscopy or BSEI. The deformation response exhibited in the α phase is directly related to the induced strain within the β matrix due to crystallographic relationships resulting from downstream thermomechanical processing. Strain which exacerbated within β grains orientated with the (001) plane parallel to the tool direction. Those grains present an increased propensity for dislocation slip within primary α_p. Conditions outside of intermediate V_c and f_z, 375 m/min and 0.22 mm/tooth, are deemed to be outside of the usable processing window due to their influence on tool wear. From this, the upper limit of

SGR was selected along with the initial cutting conditions, for investigation of the fatigue behaviour. Through a custom four point bend fatigue test and advanced characterisation techniques, it was found increased SGR reduced fatigue life by up to 50%. Initiation of fatigue failures occurred through quasi-cleavage of primary α_p grains located within the SPD region, subject to the greatest tensile stress during testing. Through cross-sectional EBSD of fatigue tested Ti-5553, intense dislocation slip along basal $(11\bar{2}0)$, prismatic $(\bar{1}010)$ and pyramidal $(\bar{1}101)$ planes were identified. Micro-cracking along basal planes is believed to be a leading mechanism for fatigue cracking. Fatigue cracks which then propagate in to the bulk microstructure in a ductile manner, influenced by the crystallographic soft orientations of β grains and along brittle α/β grain boundaries culminating in final brittle failure. These mechanisms compete against residual stresses induced from machining processes. If machining induced deformation modes can be mitigated against, in-service performance and component life could therefore be improved. It can be postulated, that thermomechanical processing and crystallographic orientation have a significant underlying influence on the susceptibility to subsurface deformation during finish end milling of Ti-5553. Induced deformation, which in-turn, has a direct effect on fatigue performance. This research has shown, simple machinability trials and characterisation are not satisfactory to accurately determine suitable processing windows for manufacturing aerospace alloys. The techniques developed in this thesis allow for a comprehensive understanding of material response to machining and subsequent implication of this for in-service behaviour.

Chapter 6

Future Work

This investigation has addressed the aims and objectives originally outlined and has furthered the knowledge of machinability, tool wear mechanisms and fatigue performance for machined Ti-5553. Despite the development of improved techniques for interrogating high performance aerospace alloys, numerous topics for further study have emerged. Though most were considered, opportunities have arisen, to where exploitation would significantly further this research. In order to conclusively determine an improved processing window, an increased number of parametric cutting trials are required to add statistical confidence to the trends identified. There is a clear opportunity to include a third fundamental parameter to this processing window by introducing depth of cut. This will inevitably encourage increased cutting forces and subsequent induced deformation and tool wear as a result of increased material removal rates. In order to optimise material utilisation, individual coupons could be subject to multiple cutting parameters. The intention of this work was to develop small scale testing methodologies that could be applied to an array of variables. A clear opportunity here would be to apply these techniques to a full and comprehensive array of aerospace alloys such as Ti-64 and nickel superalloys. The approach also lends itself not only to ball nose finish end milling, but a variety of other commonly utilised machining strategies and tooling geometries or materials. This will improve the robustness of the design, offering statistical significance to the results, building on the work in the literature [20,24,95,104]. A transition from abrasive to adhesive wear mechanisms has been identified. Additional confirmation is required and would be achieved through the characterisation of cutting tools following cutting trials. It is proposed, that a combination of cross-sectional BSEI analysis and energy-dispersive X-ray spectroscopy (EDS), of both the machined alloys and cutting tools would satisfy this, as has been conducted in the literature [112, 113]. As introduced during fatigue testing, an opportunity exists for further FEA in this testing programme. The commercial packages; AdvantEdge and Deform could be used to model the cutting processes as is seen in the literature [82,141–143]. Results from which can be incorporated into the Ansys FE model produced, for further investigation into the relationship between subsurface deformation and fatigue behaviour. For a holistic understanding of this relationship, surface condition must also be considered. As a result of the high fidelity, this model can be exploited in a way to incorporate a geometric roughness and subsequent stress concentration factors, based on existing results of practical experimentation. To improve the accuracy of such simulations, it is suggested that a series of thermomechanical compression tests over a range of high strain rates are conducted to yield accurate material properties. The focus of this study was low cycle fatigue and as is clear

from the results in Chapter 7, the quantitative fatigue life differ between R=-1 and R=0.1 testing approaches. Therefore, it is pertinent to produce a full spectrum of cycles to failure over a range of applied stresses, for Ti-5553 and other prominent aerospace alloys. The dominant subsurface deformation mode identified during this study was the activation of dislocation slip within α_p grains. Due to the high levels of SPD and induced stress, EBSD often failed to provide satisfactory resolution for characterisation. The application of transmission electron microscopy (TEM), would be suitable to characterise the damage accumulation experienced in fatigue tested and material subject to worn tools. Such approaches have carried out in the literature [59, 127, 139]. Due to the complexity and lengthy material preparation required for TEM analysis, it is suggested that the range of material characterisation techniques be reduced. Due the alloys inherent fine microstructure, for Ti-5553, exclusion of surface microscopy and light microscopy would be acceptable. A regimen of BSEI, EBSD, XRD-residual stress analysis and TEM would become the focus of further study. A process of damage accumulation, accommodated as dislocation slip, as a result of machining, followed by subsequent strain localisation and crack initiation along these planes during fatigue testing has been postulated to be the fundamental fatigue mechanism. In order to satisfy this hypothesis, a series of interrupted four point bend fatigue tests are suggested. To determine precisely, the stages at which to cease a given fatigue test, condition monitoring techniques such as acoustic emission can be utilised. This will allow for in-situ micro-cracking to be identified. Finally, it is proposed EBSD analysis of α_p grains within the initiation zone of the fracture face should be considered. Such approaches have been defined in the literature [57, 123]. This will resolve the definitive mechanism driving fatigue failure and draw correlations between cutting parameters and fatigue performance.

References

[1] A. Rothman, "Airbus raises prospect of ditching A380 as orders vanish," 2014.

[2] Aibus, "Flying by numbers: Global market forecast 2015-2034," *Journal of Chemical Information and Modeling*, vol. 1, no. 1, 2015.

[3] Boeing, "Current market outlook 2015-2034," *Boeing*, vol. 1, no. 1, 2015.

[4] D. Banerjee and J. C. Williams, "Perspectives on titanium science and technology," *Acta Materialia*, vol. 61, no. 3, pp. 844–879, 2013.

[5] Boeing, "Boeing 787 dreamliner," 2015.

[6] Roskill, "Titanium: Market Outlook to 2018," tech. rep., 2013.

[7] Boeing, "Boeing rolls out first 787 dreamliner at increased production rate," 2014.

[8] C. S. Tang and J. D. Zimmerman, "Development and Supply Chain Risks : The Boeing 787 Case," vol. 10, pp. 74–87, 2009.

[9] Rueters, "Boeing makes planes heavier to save money," 2015.

[10] E. Kraft, *Summary of Emerging Titanium Cost Reduction Technologies*. No. January 2004, 2004.

[11] S. Seong, O. Younossi, and B. W. Goldsmith, "Titanium: Industrial base, price trends and technology initiatives," tech. rep., 2009.

[12] I. Jawahir, E. Brinksmeier, R. M'Saoubi, D. Aspinwall, J. Outeiro, D. Meyer, D. Umbrello, and a.D. Jayal, "Surface integrity in material removal processes: Recent advances," *CIRP Annals - Manufacturing Technology*, vol. 60, pp. 603–626, jan 2011.

[13] P. Crawforth, B. Wynne, S. Turner, and M. Jackson, "Subsurface deformation during precision turning of a near-alpha titanium alloy," *Scripta Materialia*, vol. 67, pp. 842–845, nov 2012.

[14] M. Thomas, S. Turner, and M. Jackson, "Microstructural damage during high-speed milling of titanium alloys," *Scripta Materialia*, vol. 62, pp. 250–253, mar 2010.

[15] Messier-Bugatti-Dowty, "World leader in aircraft landing systems."

[16] J. D. Cotton, R. D. Briggs, R. R. Boyer, S. Tamirisakandala, P. Russo, N. Shchetnikov, and J. C. Fanning, "State of the Art in Beta Titanium Alloys for Airframe Applications," *Jom*, vol. 67, no. 6, pp. 1281–1303, 2015.

[17] D. Eylon, A. Vassel, Y. Combres, R. R. Boyer, P. J. Bania, and R. W. Schutz, "Issues in the development of beta titanium alloys," *JOM*, vol. 46, no. 7, pp. 14–15, 1994.

[18] G. Lutjering and J. C. Williams, *Titanium*. Springer, 2007.

[19] C. Leyens and M. Peters, eds., *Titanium and Titanium Alloys*. Wiley-VCH, 2003.

[20] A. Ugarte, R. M'Saoubi, A. Garay, and P. Arrazola, "Machining Behaviour of Ti-6Al-4V and Ti-5553 Alloys in Interrupted Cutting with PVD Coated Cemented carbide," *Procedia CIRP*, vol. 1, pp. 202–207, 2012.

[21] M. Armendia, P. Osborne, A. Garay, J. Belloso, S. Turner, and P.-J. Arrazola, "Influence of Heat Treatment on the Machinability of Titanium Alloys," *Materials and Manufacturing Processes*, vol. 27, no. 4, pp. 457–461, 2012.

[22] P. Crawforth, "Towards a Micromechanistic Understanding of Imparted Subsurface Deformation During Machining of Titanium Alloys," no. September, p. 281, 2014.

[23] E. Ezugwu and Z. Wang, "Titanium alloys and their machinability," *Journal of Materials Processing Technology*, vol. 68, no. 3, pp. 262–274, 1997.

[24] P.-J. Arrazola, a. Garay, L.-M. Iriarte, M. Armendia, S. Marya, and F. Le Maître, "Machinability of titanium alloys (Ti6Al4V and Ti555.3)," *Journal of Materials Processing Technology*, vol. 209, pp. 2223–2230, mar 2009.

[25] H. Abdelaal, M. Nouari, and M. Elmansori, "Influence of thermal conductivity on wear when machining titanium alloys," *Tribology International*, vol. 42, pp. 359–372, feb 2009.

[26] a. Jawaid, C. Che-Haron, and a. Abdullah, "Tool wear characteristics in turning of titanium alloy Ti-6246," *Journal of Materials Processing Technology*, vol. 92-93, pp. 329–334, aug 1999.

[27] E. Ezugwu, J. Bonney, and Y. Yamane, "An overview of the machinability of aeroengine alloys," *Journal of Materials Processing Technology*, vol. 134, pp. 233–253, mar 2003.

[28] S. Zhang, J. F. Li, J. X. Deng, and Y. S. Li, "Investigation on diffusion wear during high-speed machining Ti-6Al-4V alloy with straight tungsten carbide tools," *International Journal of Advanced Manufacturing Technology*, vol. 44, no. 1-2, pp. 17–25, 2009.

[29] A. Ginting and M. Nouari, "Surface integrity of dry machined titanium alloys," *International Journal of Machine Tools Manufacture*, vol. 49, pp. 325–332, 2009.

[30] N. Corduan, T. Himbart, G. Poulachon, M. Dessoly, M. Lambertin, J. Vigneau, and B. Payoux, "Wear Mechanisms of New Tool Materials for Ti-6AI-4V High Performance Machining," *CIRP Annals - Manufacturing Technology*, vol. 52, no. 1, pp. 73–76, 2003.

[31] C. Che-Haron, *Tool life and surface integrity in turning titanium alloy*, vol. 118. dec 2001.

[32] J. A., S. S., and K. S., "Evaluation of wear mechanisms of coated carbide tools when face milling titanium alloy," *Journal of Materials Processing Technology*, vol. 99, no. 1, pp. 266–274, 2000.

[33] R. B. Da Silva, Á. R. MacHado, E. O. Ezugwu, J. Bonney, and W. F. Sales, "Tool life and wear mechanisms in high speed machining of Ti-6Al-4V alloy with PCD tools under various coolant pressures," *Journal of Materials Processing Technology*, vol. 213, no. 8, pp. 1459–1464, 2013.

[34] C. Che-Haron and a. Jawaid, "The effect of machining on surface integrity of titanium alloy Ti6Technology, vol. 166, pp. 188–192, aug 2005.

[35] J. Sun and Y. Guo, "A comprehensive experimental study on surface integrity by end milling Ti6Al4V," *Journal of Materials Processing Technology*, vol. 209, pp. 4036–4042, apr 2009.

[36] P. Crawforth, C. M. Taylor, and S. Turner, "The Influence of Alloy Chemistry on the Cutting Performance and Deformation Kinetics of Titanium Alloys during Turning," *Procedia CIRP*, vol. 45, pp. 151–154, 2016.

[37] M. S. Dargusch, M. X. Zhang, S. Palanisamy, A. J. M. Buddery, and D. H. StJohn, "Subsurface deformation after dry machining of grade 2 titanium," *Advanced Engineering Materials*, vol. 10, no. 1-2, pp. 85–88, 2008.

[38] R. M'Saoubi, T. Larsson, J. Outeiro, Y. Guo, S. Suslov, C. Saldana, and S. Chandrasekar, "Surface integrity analysis of machined Inconel 718 over multiple length scales," *CIRP Annals - Manufacturing Technology*, vol. 61, pp. 99–102, jan 2012.

[39] M. Suraratchai, J. Limido, C. Mabru, and R. Chieragatti, "Modelling the influence of machined surface roughness on the fatigue life of aluminium alloy," *International Journal of Fatigue*, vol. 30, pp. 2119–2126, dec 2008.

[40] R. Dewes, D. Aspinwall, W. Voice, P. Bowen, and D. Novovic, "The effect of machined topography and integrity on fatigue life," *International Journal of Machine Tools and Manufacture*, vol. 44, no. 2-3, pp. 125–134, 2004.

[41] a. Souto-Lebel, N. Guillemot, C. Lartigue, and R. Billardon, "Characterization and influence of defect size distribution induced by ball-end finishing milling on fatigue life," *Procedia Engineering*, vol. 19, pp. 343–348, jan 2011.

[42] N. Guillemot, C. Lartigue, R. Billardon, and B. K. Mawussi, "Prediction of the endurance limit taking account of the microgeometry after finishing milling," *International Journal on Interactive Design and Manufacturing (IJIDeM)*, vol. 4, pp. 239–249, oct 2010.

[43] H. M. Flower, "Microstructural development in relation to hot working of titanium alloys," *Materials Science and Technology*, vol. 6, no. 11, pp. 1082–1092, 1990.

[44] N. Jones, R. Dashwood, D. Dye, and M. Jackson, "Thermomechanical processing of Ti5Al5Mo5V3Cr," *Materials Science and Engineering A*, vol. A 490, p. 9, 2008.

[45] N. Jones, R. Dashwood, D. Dye, and M. Jackson, "The Flow Behavior and Microstructural Evolution of Ti-5Al-5Mo-5V-3Cr during Subtransus Isothermal Forging," *Metallurgical and Materials Transactions A*, vol. 40, pp. 1944–1954, jun 2009.

[46] R. Boyer, "An overview on the use of titanium in the aerospace industry," *Materials Science and Engineering: A*, vol. 213, pp. 103–114, aug 1996.

[47] R. Boyer and R. Briggs, "The Use of β Titanium Alloys in the Aerospace Industry," *Journal of Materials Engineering and Performance*, vol. 14, pp. 681–685, dec 2005.

[48] N. Jones and M. Jackson, "On mechanism of flow softening in Ti-5Al-5Mo-5V-3Cr," *Materials Science and Technology*, vol. 000, no. 000, p. 8, 2010.

[49] M. D. Richardson, "Microstructural and Mechanical Property Development in Metastable Beta Titanium Alloys," no. January 2016.

[50] M. Baili, V. Wagner, G. Dessein, J. Sallaberry, and D. Lallement, "An Experimental Investigation of Hot Machining with Induction to Improve Ti-5553 Machinability," *Applied Mechanics and Materials*, vol. 62, pp. 67–76, jun 2011.

[51] J. W. Foltz, B. Welk, P. C. Collins, H. L. Fraser, and J. C. Williams, "Formation of Grain Boundary α in β Ti Alloys: Its Role in Deformation and Fracture Behavior of These Alloys," *Metallurgical and Materials Transactions A*, vol. 42, pp. 645–650, jun 2010.

[52] Duerig, T. W. and J. C. Williams, ""Overview: microstructure and properties of beta titanium alloys." Beta Titanium Alloys in the 1980's," *TMS*, pp. 19–67, 1983.

[53] M. Thomas, "On the characterisation of subsurface deformation microstructures in aerostructural titanium alloys," p. 99, 2008.

[54] L. Wang, Y. Yang, P. Eisenlohr, T. R. Bieler, M. A. Crimp, and D. E. Mason, "Twin nucleation by slip transfer across grain boundaries in commercial purity titanium," *Metallurgical and Materials Transactions A: Physical Metallurgy and Materials Science*, vol. 41, no. 2, pp. 421–430, 2010.

[55] G. Dieter and D. Bacon, *Mechanical Metallurgy. SI Metric Edition.* McGraw-Hill, 2 ed., 1988.

[56] O. Engler and V. Randle, *Introduction to texture analysis; Macrotexture, microtexture and orientation mapping.* 2nd ed., 2010.

[57] F. Bridier, P. Villechaise, and J. Mendez, "Analysis of the different slip systems activated by tension in a alpha-beta titanium alloy in relation with local crystallographic orientation," *Acta Materialia*, vol. 53, no. 3, pp. 555–567, 2005.

[58] D. B. Williams and C. B. Carter, *The Transmission Electron Microscope.* 2009.

[59] G. J. Baxter, W. M. Rainforth, and L. Grabowski, "TEM observations of fatigue damage accumulation at the surface of near alpha Titanium alloy IMI 834," vol. 44, no. 9, pp. 3453–3463, 1996.

[60] J. Christian and S. Mahajan, "Deformation twinning," *Progress in Materials Science*, vol. 39, no. 1-2, pp. 1–157, 1995.

[61] D. H. Shin, I. Kim, J. Kim, Y. S. Kim, and S. L. Semiatin, "Microstructure development during equal-channel angular pressing of titanium," *Acta Materialia*, vol. 51, no. 4, pp. 983–996, 2003.

[62] G. G. E. Seward, S. Celotto, D. J. Prior, J. Wheeler, and R. C. Pond, "In situ SEM-EBSD observations of the hcp to bcc phase transformation in commercially pure titanium," *Acta Materialia*, vol. 52, no. 4, pp. 821–832, 2004.

[63] R. Msaoubi and L. Ryde, "Application of the EBSD technique for the characterisation of deformation zones in metal cutting," *Materials Science and Engineering: A*, vol. 405, pp. 339–349, sep 2005.

[64] S. Di Iorio, L. Briottet, E. F. Rauch, and D. Guichard, "Plastic deformation, damage and rupture of PM Ti-6Al-4V at 20 K under monotonic loading," *Acta Materialia*, vol. 55, no. 1, pp. 105–118, 2007.

[65] Z. Keshavarz and M. R. Barnett, "EBSD analysis of deformation modes in Mg3Al1Zn," *Scripta Materialia*, vol. 55, pp. 915–918, nov 2006.

[66] L. Germain, S. R. Dey, M. Humbert, and N. Gey, "Determination of parent orientation maps in advanced titanium-based alloys," *Journal of Microscopy*, vol. 227, no. 3, pp. 284–291, 2007.

[67] C. Cayron, B. Artaud, and L. Briottet, "Reconstruction of parent grains from EBSD data," *Materials Characterization*, vol. 57, no. 4-5, pp. 386–401, 2006.

[68] J. P. Davim, *Surface integrity in machining*. Springer, 2010.

[69] G. Gao, B. Wu, D. Zhang, and M. Luo, "Mechanistic identification of cutting force coefficients in bull-nose milling process," *Chinese Journal of Aeronautics*, vol. 26, no. 3, pp. 823–830, 2013.

[70] S. Engin and Y. Altintas, "Mechanics and dynamics of general milling cutters.," *International Journal of Machine Tools and Manufacture*, vol. 41, no. 15, pp. 2195–2212, 2001.

[71] D. K. Aspinwall, R. C. Dewes, E. G. Ng, C. Sage, and S. L. Soo, "The influence of cutter orientation and workpiece angle on machinability when high-speed milling Inconel 718 under finishing conditions," *International Journal of Machine Tools and Manufacture*, vol. 47, no. 12-13, pp. 1839–1846, 2007.

[72] K.-D. Bouzakis, P. Aichouh, and K. Efstathiou, "Determination of the chip geometry, cutting force and roughness in free form surfaces finishing milling, with ball end tools," *International Journal of Machine Tools and Manufacture*, vol. 43, pp. 499–514, apr 2003.

[73] M. Sima and T. Özel, "Modified material constitutive models for serrated chip formation simulations and experimental validation in machining of titanium alloy Ti6Al4V," *International Journal of Machine Tools and Manufacture*, vol. 50, pp. 943–960, nov 2010.

[74] M. R. Shankar, B. C. Rao, S. Lee, S. Chandrasekar, A. H. King, and W. D. Compton, "Severe plastic deformation (SPD) of titanium at near-ambient temperature," *Acta Materialia*, vol. 54, no. 14, pp. 3691–3700, 2006.

[75] B. Zou, M. Chen, C. Huang, and Q. An, "Study on surface damages caused by turning NiCr20TiAl nickel-based alloy," *Journal of Materials Processing Technology*, vol. 209, no. 17, pp. 5802–5809, 2009.

[76] R. Pawade, S. Joshi, P. Brahmankar, and M. Rahman, "An investigation of cutting forces and surface damage in high-speed turning of Inconel 718," *Journal of Materials Processing Technology*, vol. 192, pp. 139–146, 2007.

[77] A. Souto-lebel, N. Guillemot, C. Lartigue, and R. Billardon, "Procedia Engineering Characterization and influence of defect size distribution induced by ball-end finishing milling on fatigue life," vol. 00, pp. 3–8, 2012.

[78] K. Moussaoui, M. Mousseigne, J. Senatore, and R. Chieragatti, "The effect of roughness and residual stresses on fatigue life time of an alloy of titanium," *International Journal of Advanced Manufacturing Technology*, vol. 78, no. 1-4, pp. 557–563, 2015.

[79] H. Itoga, K. Tokaji, M. Nakajima, and H. N. Ko, "Effect of surface roughness on step-wise S-N characteristics in high strength steel," *International Journal of Fatigue*, vol. 25, no. 5, pp. 379–385, 2003.

[80] M. R. Bayoumi and A. K. Abdellatif, "Effect of surface finish on fatigue strength," *Engineering Fracture Mechanics*, vol. 51, no. 5, pp. 861–870, 1995.

[81] D. Ardi, Y. Li, K. Chan, L. Blunt, and M. Bache, "The Effects of Machined Topography on Fatigue Life of a Nickel based Superalloy," *Procedia CIRP*, vol. 13, pp. 19–24, 2014.

[82] J. P. Davim, *Surface integrity in Machining*. Springer, 2010.

[83] A. Cox, T. Sa, and M. Jackson, "The effect of finish milling on the surface integrity and subsurface microstructure in Ti-5AL-5Mo-5V-3Cr," pp. 299–304, 2015.

[84] N. Tayebi and A. A. Polycarpou, "Modeling the effect of skewness and kurtosis on the static friction coefficient of rough surfaces," *Tribology International*, vol. 37, no. 6, pp. 491–505, 2004.

[85] D. Ulutan and T. Ozel, "Machining induced surface integrity in titanium and nickel alloys: A review," *International Journal of Machine Tools and Manufacture*, vol. 51, pp. 250–280, mar 2011.

[86] K. L. Johnson, "Contact Mechanics," 1985.

[87] Y. Quinsat, L. Sabourin, and C. Lartigue, "Surface topography in ball end milling process: Description of a 3D surface roughness parameter," *Journal of Materials Processing Technology*, vol. 195, pp. 135–143, jan 2008.

[88] Y. Quinsat, S. Lavernhe, and C. Lartigue, "Characterization of 3D surface topography in 5-axis milling," *Wear*, vol. 271, pp. 590–595, jun 2011.

[89] J. P. Velásquez, a. Tidu, B. Bolle, P. Chevrier, and J.-J. Fundenberger, "Subsurface and surface analysis of high speed machined Ti6Al4V alloy," *Materials Science and Engineering: A*, vol. 527, no. 10-11, pp. 2572–2578, 2010.

[90] S. Jeelani and K. Ramakrishnan, "Subsurface plastic deformation in machining annealed 181982.

[91] J. A. Bailey and S. Jeelani, "Determination of subsurface plastic strain in machining using an embossed grid," *Wear*, vol. 36, no. 2, pp. 199–206, 1976.

[92] A. Gente, H. W. Hoffmeister, and C. J. Evans, "Chip Formation in Machining Ti6Al4V at Extremely High Cutting Speeds," *CIRP Annals - Manufacturing Technology*, vol. 50, no. 1, pp. 49–52, 2001.

[93] C. Huang, T. G. Murthy, M. R. Shankar, R. M'Saoubi, and S. Chandrasekar, "Temperature rise in severe plastic deformation of titanium at small strain-rates," *Scripta Materialia*, vol. 58, no. 8, pp. 663–666, 2008.

[94] M. Cotterell and G. Byrne, "Characterisation of chip formation during orthogonal cutting of titanium alloy Ti-6Al-4V," *CIRP Journal of Manufacturing Science and Technology*, vol. 1, no. 2, pp. 81–85, 2008.

[95] M. Armendia, A. Garay, L.-M. Iriarte, and P.-J. Arrazola, "Comparison of the machinabilities of Ti6Al4V and TIMETAL® 54M using uncoated WCCo tools," *Journal of Materials Processing Technology*, vol. 210, pp. 197–203, jan 2010.

[96] S. Sun, M. Brandt, and M. Dargusch, "Characteristics of cutting forces and chip formation in machining of titanium alloys," *International Journal of Machine Tools and Manufacture*, vol. 49, pp. 561–568, jun 2009.

[97] J. P. Davim, *Machining Fundamentals and Recent Advances*. Springer, 2008.

[98] J. Fanning, "Properties of TIMETAL 555 (Ti-5Al-5Mo-5V-3Cr-0.6Fe)," *Journal of Materials Engineering and Performance*, vol. 14, pp. 788–791, dec 2005.

[99] P.-J. Arrazola, L. M. Iriarte, and M. Armendia, "Physical and mechanical aspects of Ti alloys machining: Outlook," tech. rep., Faculty of Engineering Mondragon University, 2012.

[100] D. Yan, T. Hilditch, H. Kishawy, and G. Littlefair, "On Quantifying the Strain Rate During Chip Formation When Machining Aerospace Alloy Ti-5553," *Procedia CIRP*, vol. 8, pp. 122–127, jan 2013.

[101] K. Firm, R. Boyer, and G. Welsch, "Materials Properties Handbook: Titanium Alloys," *ASM International: Materials Park, OH*, p. xxii 1176, 1994.

[102] W.-S. Lee and C.-F. Lin, "High-temperature deformation behaviour of Ti6Al4V alloy evaluated by high strain-rate compression tests," *Journal of Materials Processing Technology*, vol. 75, pp. 127–136, mar 1998.

[103] C. MacHai and D. Biermann, "Machining of Beta-titanium-alloy Ti-10V-2Fe-3Al under cryogenic conditions: Cooling with carbon dioxide snow," *Journal of Materials Processing Technology*, vol. 211, no. 6, pp. 1175–1183, 2011.

[104] R. M'Saoubi, D. Axinte, S. L. Soo, C. Nobel, H. Attia, G. Kappmeyer, S. Engin, and W.-M. Sim, "High performance cutting of advanced aerospace alloys and composite materials," *CIRP Annals - Manufacturing Technology*, 2015.

[105] E. O. Ezugwu, R. B. Da Silva, J. Bonney, and . R. MacHado, "Evaluation of the performance of CBN tools when turning Ti-6Al-4V alloy with high pressure coolant supplies," *International Journal of Machine Tools and Manufacture*, vol. 45, no. 9, pp. 1009–1014, 2005.

[106] Z. G. Wang, Y. S. Wong, and M. Rahman, "High-speed milling of titanium alloys using binderless CBN tools," *International Journal of Machine Tools and Manufacture*, vol. 45, no. 1, pp. 105–114, 2005.

[107] W. Min and Z. Youzhen, "Diffusion wear in milling titanium alloys," *Materials Science and Technology*, vol. 0836, no. April 2016, 2013.

[108] D. Jianxin, L. Yousheng, and S. Wenlong, "Diffusion wear in dry cutting of Ti-6Al-4V with WC/Co carbide tools," *Wear*, vol. 265, no. 11-12, pp. 1776–1783, 2008.

[109] J. Taylor, "The tool wear-time relationship in metal cutting," *International Journal of Machine Tool Design and Research*, vol. 2, no. 2, pp. 119–152, 1962.

[110] Y. Su, N. He, L. Li, and X. Li, "An experimental investigation of effects of cooling/lubrication conditions on tool wear in high-speed end milling of Ti-6Al-4V," *Wear*, vol. 261, pp. 760–766, oct 2006.

[111] a. N. Amin, A. F. Ismail, and M. Nor Khairusshima, "Effectiveness of uncoated WCCo and PCD inserts in end milling of titanium alloyTi6Al4V," *Journal of Materials Processing Technology*, vol. 192-193, pp. 147–158, oct 2007.

[112] O. Hatt, H. Larsson, F. Giuliani, P. Crawforth, B. Wynne, and M. Jackson, "Predicting Chemical Wear in Machining Titanium Alloys Via a Novel Low Cost Diffusion Couple Method," *Procedia CIRP*, vol. 45, pp. 219–222, 2016.

[113] O. Hatt, P. Crawforth, and M. Jackson, "On the mechanism of tool crater wear during titanium alloy machining," *Wear*, vol. 374-375, pp. 15–20, 2017.

[114] V. S. Sharma, M. Dogra, and N. Suri, "Cooling techniques for improved productivity in turning," *International Journal of Machine Tools and Manufacture*, vol. 49, pp. 435–453, may 2009.

[115] W. Callister and D. Rethwisch, *Materials science and engineering: an introduction*, vol. 94. 2007.

[116] R. Stephens, R. Fatemi, and H. Fuchs, *Metal Fatigue in Engineering*. New York: John Wiley Songs, 2nd ed., 2000.

[117] K. S. Chan, "Roles of microstructure in fatigue crack initiation," *International Journal of Fatigue*, vol. 32, pp. 1428–1447, sep 2010.

[118] E. Sackett, L. Germain, and M. Bache, "Crystal plasticity, fatigue crack initiation and fatigue performance of advanced titanium alloys," *International Journal of Fatigue*, vol. 29, pp. 2015–2021, sep 2007.

[119] G. T. Cashman, "A review of Competing Modes fatigue behavior," *International Journal of Fatigue*, vol. 32, no. 3, pp. 492–496, 2010.

[120] J. Huang, Z. Wang, and K. Xue, "Cyclic deformation response and micromechanisms of Ti alloy Ti5Al5V5Mo3Cr0.5Fe," *Materials Science and Engineering: A*, vol. 528, pp. 8723–8732, nov 2011.

[121] A. Drechsler, T. Dorr, and L. Wagner, "Mechanical surface treatments on Ti10V2Fe3Al for improved fatigue resistance," *Materials Science and Engineering: A*, vol. 243, pp. 217–220, 1998.

[122] V. A. Joshi, *Titanium Alloys: An atlas of structures and fracture features*. Taylor Francis, 2006.

[123] F. Bridier, P. Villechaise, and J. Mendez, "Slip and fatigue crack formation processes in an α/β titanium alloy in relation to crystallographic texture on different scales," *Acta Materialia*, vol. 56, pp. 3951–3962, sep 2008.

[124] S. K. Jha, C. J. Szczepanski, R. John, and J. M. Larsen, "Deformation heterogeneities and their role in life-limiting fatigue failures in a two-phase titanium alloy," *Acta Materialia*, vol. 82, no. 2015, pp. 378–395, 2015.

[125] M. R. Bache, W. J. Evans, and H. M. Davies, "Electron back scattered diffraction (EBSD) analysis of quasi-cleavage and hydrogen induced fractures under cyclic and dwell loading in titanium alloys ," *Journal of Materials Science*, vol. 32, no. 13, pp. 3435–3442, 1997.

[126] A. L. Pilchak, R. E. A. Williams, and J. C. Williams, "Crystallography of fatigue crack initiation and growth in fully lamellar Ti-6Al-4V," *Metallurgical and Materials Transactions A: Physical Metallurgy and Materials Science*, vol. 41, no. 1, pp. 106–124, 2010.

[127] P. O. Tympel, T. C. Lindley, E. A. Saunders, M. Dixon, and D. Dye, "Influence of complex LCF and dwell load regimes on fatigue of Ti-6Al-4V," *Acta Materialia*, vol. 103, no. 2016, pp. 77–88, 2016.

[128] S. K. Jha, C. J. Szczepanski, P. J. Golden, W. J. Porter, and R. John, "Characterization of fatigue crack-initiation facets in relation to lifetime variability in Ti-6Al-4V," *International Journal of Fatigue*, vol. 42, pp. 248–257, 2012.

[129] S. K. Jha, J. M. Larsen, and A. H. Rosenberger, "Towards a physics-based description of fatigue variability behavior in probabilistic life-prediction," *Engineering Fracture Mechanics*, vol. 76, no. 5, pp. 681–694, 2009.

[130] K. S. Ravi Chandran, P. Chang, and G. T. Cashman, "Competing failure modes and complex S-N curves in fatigue of structural materials," *International Journal of Fatigue*, vol. 32, no. 3, pp. 482–491, 2010.

[131] S. K. Jha and K. S. R. Chandran, "An unusual fatigue phenomenon: Duality of the S-N fatigue curve in the Beta titanium alloy Ti-10V-2Fe-3Al," *Scripta Materialia*, vol. 48, no. 8, pp. 1207–1212, 2003.

[132] C.-f. Yao, D.-x. Wu, Q.-c. Jin, X.-c. Huang, J.-x. Ren, and D.-h. Zhang, "Influence of high-speed milling parameter on 3D surface topography and fatigue behavior of TB6 titanium alloy," vol. 23, pp. 650–660, 2013.

[133] Y. Guo, R. M'Saoubi, and S. Chandrasekar, "Control of deformation levels on machined surfaces," *CIRP Annals - Manufacturing Technology*, vol. 60, pp. 137–140, jan 2011.

[134] N. Guillemot, M. Winter, A. Souto-Lebel, C. Lartigue, and R. Billardon, "3D heat transfer analysis for a hybrid approach to predict residual stresses after ball-end milling," *Procedia Engineering*, vol. 19, pp. 125–131, 2011.

[135] S. As, B. Skallerud, B. Tveiten, and B. Holme, "Fatigue life prediction of machined components using finite element analysis of surface topography," *International Journal of Fatigue*, vol. 27, pp. 1590–1596, oct 2005.

[136] D. Novovic, R. Dewes, D. Aspinwall, W. Voice, and P. Bowen, "The effect of machined topography and integrity on fatigue life," *International Journal of Machine Tools and Manufacture*, vol. 44, pp. 125–134, feb 2004.

[137] S. As, B. Skallerud, and B. Tveiten, "Surface roughness characterization for fatigue life predictions using finite element analysis," *International Journal of Fatigue*, vol. 30, no. 2008, pp. 2200–2209, 2008.

[138] B. Voillot, R. Billardon, J. L. Lebrun, and F. Hild, "Validation of XRD Stress Analyses Combining in-situ Tests and Integrated Peak Processing," vol. 2, pp. 91–96, 2016.

[139] D. Qin, Y. Li, S. Zhang, and L. Zhou, "On the tensile embrittlement of lamellar Ti-5Al-5V-5Mo-3Cr alloy," *Journal of Alloys and Compounds*, vol. 663, pp. 581–593, 2016.

[140] G. J. Baxter, W. M. Rainforth, and L. Grabowski, "TEM observations of fatigue damage accumulation at the surface of near alpha Titanium alloy IMI 834," vol. 44, no. 9, pp. 3453–3463, 1996.

[141] K. Zhang, K. Yang, A. Huang, X. Wu, and C. Davies, "Fatigue crack initiation in as forged Ti6Al4V bars with macrozones present," *International Journal of Fatigue*, vol. 80, no. 2015, pp. 288–297, 2015.

[142] M. Calamaz, D. Coupard, and F. Girot, "A new material model for 2D numerical simulation of serrated chip formation when machining titanium alloy Ti6Al4V," *International Journal of Machine Tools and Manufacture*, vol. 48, pp. 275–288, mar 2008.

[143] D. Umbrello, "Finite element simulation of conventional and high speed machining of Ti6Al4V alloy," *Journal of Materials Processing Technology*, vol. 196, pp. 79–87, jan 2008.

[144] T. Özel, "The influence of friction models on finite element simulations of machining," *International Journal of Machine Tools and Manufacture*, vol. 46, pp. 518–530, apr 2006.